Zentrum für Sonnenenergie- und Wasserstoffforschung Baden-Württemberg
Akkumulatoren Materialforschung

Universität Ulm
Fakultät für Naturwissenschaften

Synthesis, Structural Investigation and Surface Modification of Spherical, Co-free Li-rich Layered Oxides under Consideration of their Up-Scaling to kg-Scale

Dissertation

zur Erlangung des Doktorgrades Dr. rer. nat.

der Fakultät für Naturwissenschaften der Universität Ulm

vorgelegt von

Florian Dominik Klein

aus Esslingen am Neckar

2023

Amtierender Dekan der Fakultät der Naturwissenschaften:
Prof. Dr. Kay-Eberhardt Gottschalk

1. Gutachter: Prof. Dr. Mika Lindén

2. Gutachter: Prof. Dr. Markus Hölzle

Tag der Promotion: 20.10.2023

Abstract

Li-rich layered oxides (LRLO) is one of the next-generation cathode material classes. During synthesis, a higher amount of Li^+ source compared to NMC materials is required, which can be the origin of surface residues and inhomogeneities within the secondary particles after thermal annealing. Therefore, it is important to understand the structural Li^+ incorporation from the atomic up to the µm-scale, and to improve the properties of the near-surface region such as the Li^+ diffusivity.

In the first part of this work, $LiNi_{0.5}Mn_{0.5}O_2$ was investigated with respect to its Li^+ stoichiometry ($Li_{1+x}(Mn_{0.5}Ni_{0.5})_{1-x}O_2$, $0 \leq x \leq 0.16$). The incorporation of excess Li^+ ions induced $LiMn_6$ superstructure ordering in the TM layer, and local phase segregation on the µm length-scale for high Li^+ excesses ($x = 0.16$). For moderate Li^+ excesses, a homogeneous particle microstructure was found. The structural homogeneity was also mirrored in the electrochemical performance, and $Li_{1.07}(Mn_{0.5}Ni_{0.5})_{0.93}O_2$ was identified as the most stable material within the investigated series, with a discharge capacity of 173 mAh g^{-1} (658 Wh kg^{-1}). The study thus highlights the importance of a comprehensive structural characterization of battery materials in order to establish true structure-activity relationships.

The second part of the thesis was focused on the understanding of the near-surface region of $Li_{1.2}Mn_{0.6}Ni_{0.2}O_2$. Impurities from the co-precipitation and surface residues like carbonates can clog pores after thermal lithiation of the precursor. Different treatment procedures were applied to $Li_{1.2}Mn_{0.6}Ni_{0.2}O_2$: pH-neutral and acidic treatments of various strength. The proton concentration of the washing solution and the temperature of the annealing steps were identified as critical parameters. Whereas water and nitric acid treatment formed a spinel-like near-surface region and removed the impurities, citric acid treatment introduced an oxygen-deficient near-surface region in combination with a carbon-containing surface coating after thermal annealing. Taken together, these studies led to significantly improved electrochemical performance of the materials, and showed that the formal oxygen content in the materials depends strongly on the synthesis route.

Overall, this work showed that Li^+ distribution during the thermal annealing is a highly critical parameter with respect to homogeneity on particle level and that the electrochemical performance of LRLO is very sensitive to the selected surface modification strategy. The

combination of all three approaches led to an in-depth understanding of performance relevant parameters and were the basis for the development of a scalable synthesis route, which was confirmed with the successful production of a 5 kg batch of $Li_{1.2}Mn_{0.6}Ni_{0.2}O_2$. The scaled-up synthesis yielded materials with characteristics closely mirroring those of corresponding material synthesized as small batch syntheses.

Table of Contents

Abstract I

Table of Contents III

Abbreviations V

List of Figures VII

1. Introduction 1

1.1. State-of-the-art Li-Ion Batteries 2

1.1.1. Overview 2

1.1.2. Cathode materials for Li-Ion Batteries 5

1.1.3. Co-free layered oxides as an alternative to NMC materials 8

1.2. Li-rich layered oxide materials 10

1.2.1. Structure and the related anionic redox mechanism 10

1.2.2. Synthesis of LRLO 14

1.2.3. Influence of the secondary particle architecture 15

1.2.4. Surface modification of LRLO 17

2. Objectives 20

3. Results and Discussion 21

3.1. Towards a deeper structural understanding of thermal lithiation and post-processing procedures during synthesis of spherical LRLO materials 22

3.1.1. Structural effects induced by Li^+ excess 22

3.1.2. Surface modification strategies to improve electrochemical performance of spherical HE-NMx materials 24

3.1.3. Connecting the dots - Causes and structural effects of the applied surface modification 27

3.2. Up-scaling of HE-NMx into the kg-scale 30
3.2.1. Experimental 32
3.2.2. Characterization of the 5 kg HE-NMx material and comparison with the powder obtained from small-scale synthesis 32
4. Summary and Outlook 36
5. Zusammenfassung und Ausblick 40
6. References 44
7. Appendix i
7.1. Acknowledgements i
7.2. Publications and Conference Contributions iii
7.2.1. Conference Contributions iii
7.2.2. List of Publications iv
7.3. Curriculum Vitae v
7.4. Declaration of Authorship vii
7.5. Reprints of Publications viii

Abbreviations

Abbreviation	Unit	Full form
BEV		Battery electric vehicle
C	mAh g^{-1}	Specific capacity
ccp		Cubic close packed
CEI		Cathode electrolyte interphase
CS		Cross-section
CSTR		Continuously stirred tank reactor
DEC		Diethyl carbonate
DEMS		Differential electrochemical mass spectrometry
DMC		Dimethyl carbonate
EC		Ethylene carbonate
EMC		Ethyl methyl carbonate
FEC		Fluoroethylene carbonate
GIC		Graphite intercalation compounds
e.g.		For example
hcp		Hexagonal close packed
HE-NMC		Li- and Mn-rich layered oxides
HE-NMx		Co-free Li- and Mn-rich layered oxides
ICP-OES		Inductively coupled plasma – optical emission spectroscopy
LFP		Lithium iron phosphate, $LiFePO_4$
LFMP		Lithium iron manganese phosphate
LIB		Lithium-ion battery
LiTFSI		Lithium bis(trifluoromethanesulfonyl)imide
LMNO		Lithium manganese nickel oxide, $LiNi_{0.5}Mn_{1.5}O_4$ (spinel)
LMO		Lithium manganese oxide, $LiMn_2O_4$ (spinel)
LRLO		Li- and Mn-rich layered oxide
LS		layered-to-spinel (transformation)
LTO		Lithium titanate, $Li_4Ti_5O_{12}$
Ni-MH		Nickel-metal hydride battery

Abbreviation	Unit	Full form
NMC		Layered Li-Ni-Mn-Co oxide
NMx		Co-free layered Li-Ni-Mn oxide
RT		Room temperature
SEI		Solid electrolyte interphase
SEM		Scanning electron microscopy
SOC		State of charge
TEM		Transmission electron microscopy
TM		Transition metal
TGA		Thermogravimetric analysis
VC		Vinylene carbonate
XPS		X-ray photoelectron spectroscopy
XRD		Powder X-ray diffraction

List of Figures

Figure 1.1. Final Energy consumption prediction (a) per sector and (b) energy carrier in the European Union (EU27), Norway, Switzerland and the United Kingdom (+3). 1

Figure 1.2. Schematic configuration of a state-of-the-art Li-ion cell..... 3

Figure 1.3. Overview over the most prominent cathode material structures in LIBs and their relationship based on similar structure units. 6

Figure 1.4. Exemplary voltage profiles of an olivine $LiFePO_4$ (black), an ordered high-voltage spinel $LiNi_{0.5}Mn_{1.5}O_4$ (red), a Co- containing Ni-rich layered oxide $LiNi_{0.8}Mn_{0.1}Co_{0.1}O_2$ (blue), a Co-free layered oxide $LiNi_{0.5}Mn_{0.5}O_2$ (green), and a Li-rich layered oxide $Li_{1.2}Mn_{0.54}Ni_{0.13}Co_{0.13}O_2$ 7

Figure 1.5. Overview over the structure and the electrochemistry of HE-NMC 11

Figure 1.6. Origin of the preferred O oxidation along the Li–O–Li configuration 12

Figure 1.7. Schematic illustration of the industrial production process of (a) lithium transition metal oxides like $LiTMO_2$, $LiTM_2O_4$, or Li-rich layered oxides $Li_{1+x}TM_{1-x}O_2$ (TM = Ni, Co, Mn, Al and $0 < x < 0.2$) and (b) phospho-olivine based materials $LiTMPO_4$ (TM = Fe, Ni, Co, Mn)..... 15

Figure 1.8. Schematic overview over the different length scales in a spherical secondary LRLO particle and their most important parameters..... 16

Figure 1.9. Schematic illustration of the surface reconstruction during the post-treatment steps. 18

Figure 3.1. Schematic compositional diagram of the Li-Mn-Ni-O ternary system (Li + Mn + Ni = 1) with selected structures: $Li(Ni_{1-y}Mn_y)O_2$ ($0 \le y \le 0.5$, red), $z\ Li_2MnO_3 \bullet (1-z)\ LiMn_{0.5}Ni_{0.5}O_2$ ($0 \le z \le 0.5$, green) and $Li_{1+x}(Mn_{0.5}Ni_{0.5})_{1-x}O_2$ ($0 \le x \le 0.2$, black). 23

Figure 3.1. Fitted peak position of the A_{1g} vibration band for different amount of Li^+ excess: $Li_{1.00}$, $Li_{1.07}$, $Li_{1.10}$ and $Li_{1.16}$. 24

Figure 3.2. Specific discharge capacity of C/10 cycling (first cycle C/20): pristine (untreated, black), W300 (green), A300 (dark blue), W900 (light green) and A900 (blue). 25

Figure 3.3. Specific discharge capacities obtained during long-term cycling tests of C0 (black), C1 (red), C2 (blue), and C3 (green) at room temperature (RT)..... 27

Figure 3.4. Schematic overview about the different process steps in the developed, scalable synthesis route. 31

Figure 3.5. Structural and morphological characterization of the 5 kg batch (green) compared with the sample C0 (black).. 33
Figure 3.6. Electrochemical characterization of the 5 kg batch. 34
Figure 3.7. Long-term cycling data of the 5 kg batch at 1C. 34

1. Introduction

Since the beginning of the industrialization, the annual emission of greenhouse gases strongly increased, leading to a continuous rise of the global mean temperature of around 1°C in 2016 compared to pre-industrial levels. Furthermore, the last seven years (2015-2021) were the seven warmest years on record.[1] To mitigate the negative effects of the climate change and to limit the further increase of the global mean temperature, greenhouse gas emission (*e.g.*, CO_2) and the total energy consumption must be strongly reduced.[2] Technical optimization and innovation, electrification as well as a transformation of the energy mix are the most prominent strategies of decarbonization.[2] These changes can lead to a decrease of the total energy consumption in the European Union, Norway, Switzerland, and United Kingdom (EU27+3) from 13,200 TWh (2020) to 11,019 TWh (2030), which is spread over all sectors but accentuated for the transport sector (Figure 1.1a).[2] The latter strongly benefits from the ongoing transformation from combustion engines to battery electric vehicles (BEV) in the passenger and heavy-duty transport, which will strongly increase the demand for electricity (Figure 1.1b).[2,3]

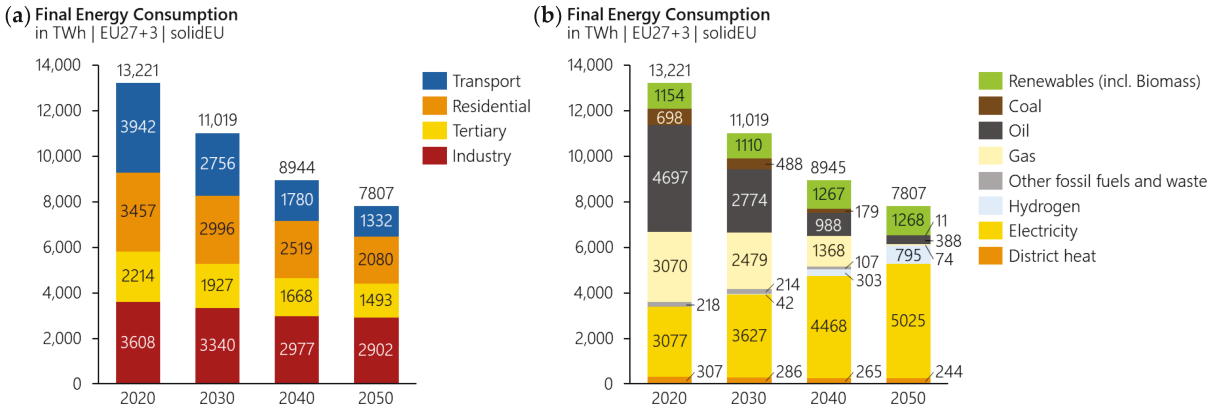

Figure 1.1. Final Energy consumption prediction (a) per sector and (b) energy carrier in the European Union (EU27), Norway, Switzerland and the United Kingdom (+3). Reproduced and modified from A. Guminski, C. Fiedler, S. Kigle, C. Pellinger, P. Dossow, K. Ganz, F. Jetter, T. Kern, T. Limmer, A. Murmann, J. Reinhard, T. Schmidt-Achert, S. von Roon, *eXtremOS Summary Report, Modeling Kit and Scenarios for Pathways towards a Climate Neutral Europe,* München: Forschungsstelle für Energiewirtschaft e.V. **2021,** DOI: 10.34805/FFE-24-21, with permission from the authors. Copyright (2021) by the authors.[4]

The transformation of the transport sector is driven by the fast developments of the key technology, the Li-ion battery (LIB).[2] Its success story began in 1991 with its commercialization by Sony, accompanied with a continuous growth in various fields of application like electronics (*e.g.*, notebooks and cell phones).[5] Later on, the LIB drew

increasingly interest of the automotive industry due to its high energy density and specific energy and is currently the state-of-the-art technology here.[6] Due to its high societal interest, this revolution in energy storage was honored by the Nobel Committee for Chemistry in 2019 with the Nobel Prize for M. Stanley Whittingham, Akira Yoshino and John B. Goodenough for their research in this topic that significantly contributed to the successful development and commercialization of the LIB technology.[7]

The estimated growth of the BEV market will increase the LIB demand in the next years drastically, which will be also accompanied with an increased demand of required raw materials like Li, Mn, Ni, Co, and graphite.[8] A strong environmental, political and ethical impact is expected. Particularly, Co is very critical as it is currently the most expensive element in commercial LIBs and is associated with child labor, hazardous working conditions and high toxicity.[9-11] According to this circumstances, it is very important to find adequate Co-free alternative cathode materials and compositions based on earth-abundant materials to reduce both the costs and the environmental footprint of the LIB.[11]

1.1. State-of-the-art Li-Ion Batteries

1.1.1. Overview

In general, a battery is used as a storage device and consist of two or more electrochemical cells (either connected in parallel or in series), which can convert chemically stored energy into electrical energy and dependent on the system also vice versa.[12] The prerequisite for the conversion is that both chemical reactions occurring at both electrodes of the cell are spatially separated to prohibit the direct electron transfer and that the electrodes are connected over an external electrical circuit with each other.[13] Furthermore, a negative Gibbs energy to guarantee a spontaneous discharge reaction of the battery is obligatory.[13,14] An electrochemical cell has a positive and a negative electrode.[15] The negative electrode has a lower potential compared to the positive electrode and is able to reduce the active material at the positive electrode during discharging while it is oxidized.[14] Therefore, the negative electrode is denoted as anode and the positive electrode as cathode, respectively.[15] In rechargeable batteries, the redox-processes are inverted upon charging, which changes the assignment of anode and cathode in terms of electrochemistry.[16] For simplification, the terms anode and cathode are typically used in the battery community as well as in this work

independent of the current direction to describe the electrodes based on the discharge reaction (negative electrode: anode, positive electrode: cathode).[14]

The batteries on the market can be divided in primary and secondary batteries.[12] Primary batteries such as alkaline-manganese batteries can be discharged only for one time and have to be disposed afterwards.[17] Secondary batteries such as lead-acid, nickel-metal hydride (Ni-MH), and Li-ion batteries belong to the rechargeable batteries, which can be (dis-)charged for many times.[12] Compared with lead-acid or Ni-MH batteries, LIBs have a strongly increased energy density.[18]

A complete Li-ion cell is composed of two electrodes, anode and cathode, soaked with an aprotic electrolyte and isolated by a separator (Figure 1.2).[19] Most of the commonly used active materials on both electrodes are insertion compounds working as Li^+ host matrix.[20] During charging of the cells, electrons are transferred from the positive to the negative electrode over an external circuit.[19] To achieve charge neutrality, Li^+ ions are simultaneously deintercalated from the cathode material and solvated by the electrolyte molecules. Subsequently, they diffuse through the separator to the anode and after desolvation, the ions are intercalated into the anode active material.[19,21,22] During discharge, the same mechanism occurs in the opposite direction, which is why it is often called “rocking-chair principle”.[23-25]

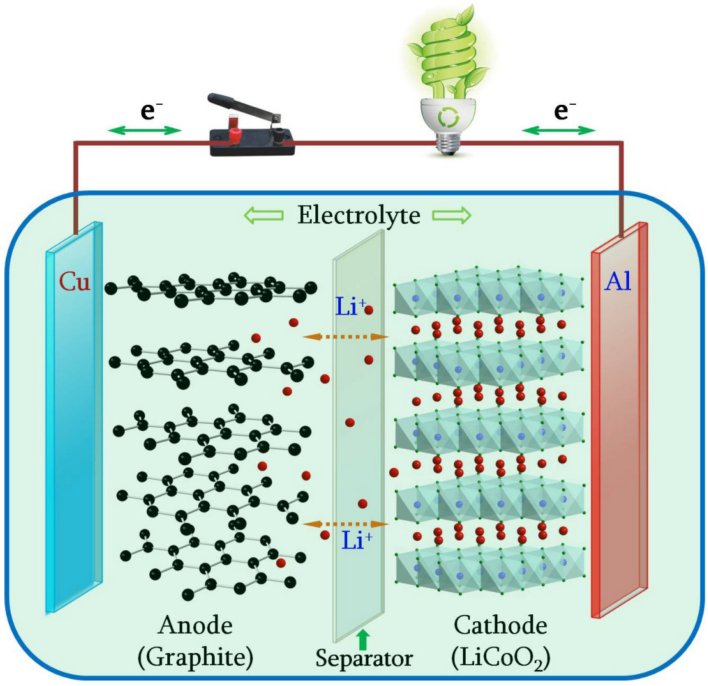

Figure 1.2. Schematic configuration of a state-of-the-art Li-ion cell consisting of aluminum foil coated with Li^+ containing host matrix and a cupper foil coated with graphite. Both electrodes are separated by a separator and soaked with electrolyte. Reproduced from C. Liu, Z. G. Neale, G. Cao, *Mater. Today* **2016**, *19*, 109 **DOI:** 10.1016/j.mattod.2015.10.009, under CC BY-NC-ND 4.0 (https://creativecommons.org/licenses/by-nc-nd/4.0/).[19]

This concept allows a reversible energy storage. For practical application, high reversibility of the (de-)intercalation process and good electrochemical performance are key factors.[26] The half-cell reactions can be described for a typical LIB composed of a graphite anode and a $LiTMO_2$ (TM = Mn, Ni, Co) cathode by the equations (1) - (3):[20]

$$\text{Cathode:} \quad LiTMO_2 \underset{\text{Discharge}}{\overset{\text{Charge}}{\rightleftharpoons}} Li_{1-x}TMO_2 + x\,Li^+ + x\,e^- \qquad (1)$$

$$\text{Anode:} \quad C_n + x\,Li^+ + x\,e^- \underset{\text{Discharge}}{\overset{\text{Charge}}{\rightleftharpoons}} Li_xC_n \qquad (2)$$

$$\text{Total:} \quad LiTMO_2 + C_n \underset{\text{Discharge}}{\overset{\text{Charge}}{\rightleftharpoons}} Li_xC_n + Li_{1-x}TMO_2 \qquad (3)$$

Due to the multitude of cathode (see section 1.1.2) and anode materials, which differ among others in the chemical composition, the redox-centers and their electrochemical performance, LIBs can be individually configured depending on the application and the technical requirements.[27]

Graphite is the mostly used anode active material in LIBs and a typical intercalation compound.[28] During lithiation of the graphite, the Li^+ ions are intercalated between the graphene sheets, which results in the formation of graphite intercalation compounds (GIC) with different lithium contents up to a final composition of LiC_6 under standard conditions.[20] The potential curve is shaped by the formation of different equilibria between two GIC, leading to four plateaus in the potential range of 0 - 0.25 V vs. Li^+/Li.[29] Furthermore, the low working potential leads to the partial reduction of the electrolyte solvents at the graphite surface and the formation of a stable solid electrolyte interface (SEI), which protects the material from faster degradation.[14] Generally, graphite is characterized by a low working potential, high specific capacity (C_{theo} = 372 mAh g^{-1}), good reversibility, and higher safety compared to lithium metal.[30,31]

Besides graphite, there are different other anode material classes, like conversion-type TM or alloying compounds.[32,33] Lithium titanate ($Li_4Ti_5O_{12}$, LTO) is an 3D insertion material with a flat potential plateau, negligible volume change (zero-strain), long-term cycling stability, and excellent rate capability.[34] However, it suffers from a low specific capacity (C_{theo} = 175 mAh g^{-1}) and a high working potential (1.55 V vs. Li^+/Li), which results in a low

specific energy on cell level.[28,35] Compared to LTO, Si as an alloying compound has a very high specific capacity (C_{theo} = 3579 mAh g^{-1} at RT, $Li_{15}Si_4$) and a low working potential (≈ 0.4 V vs. Li^+/Li).[36,37] Unfortunately, low conductivity and a volume expansion of up to 300 % between unlithiated and fully lithiated state strongly affect its lifetime: the continuous volume breathing during lithiation and delithiation causes cracking, continuously formation of new solid electrolyte interphase (SEI), and consequently a very fast capacity fade during cycling.[38,39] High specific and volumetric energies can be obtained for full cells, when mixing the Si with graphite.[36,39] Commercial cells nowadays use about < 6 - 8 % of Si in graphite electrodes.[40]

The main task of the electrolyte is the transport of Li^+ between the electrodes to maintain charge neutrality.[26] Standard liquid electrolytes are mixtures of organic, aprotic solvents, conductive salts (*e.g.*, $LiPF_6$ or LiTFSI), and SEI forming additives (*e.g.*, fluoroethylene carbonate (FEC) or vinylene carbonate (VC)).[26,41,42] The solvent is typically a mixture of different aliphatic carbonates: linear carbonates (*e.g.*, dimethyl carbonate (DMC), ethyl methyl carbonate (EMC) or diethyl carbonate (DEC)) and cyclic carbonates (*e.g.*, ethylene carbonate EC).[27] The combination of both, linear and cyclic carbonates, strongly influences the viscosity and the dielectric constant of the mixtures, which effects the solubility of the conductive salts and the mobility of the Li^+ ions, respectively.[43] Therefore, the choice of the electrolyte is very important and has to be adapted with respect to the configured system.[21] The separator is permeable for the electrolyte and the Li^+ ions.[44] It consists of a polyolefin foil that separates the half-cell reactions and prevents short-circuits in the cell.[45] To increase the mechanical and thermal stability as well as the wettability of the separator, the foils can be coated with ceramic materials.[44,46]

1.1.2. Cathode materials for Li-Ion Batteries

Cathode materials, the source of the electrochemical active Li^+, are beside the anode materials the second redox active part and a key component of a LIB, influencing the energy density, the voltage curve, the application, and the costs of the battery.[11,47] State-of-the-art cathode active materials belong to the group of insertion type materials and can be divided into different types of crystal structures (typically TM = Mn, Ni, Co, or Fe) – layered ($LiTMO_2$), spinel ($LiTM_2O_4$) and phosphate-based olivine structures ($LiTMPO_4$).[48] The TM-compounds form a stable host matrix for the Li^+ ions. It ensures stable cycling behavior, but limits the usable

specific capacity due to its mass and the Li^+ diffusivity.[19] An overview of these structures is given in Figure 1.3.[48]

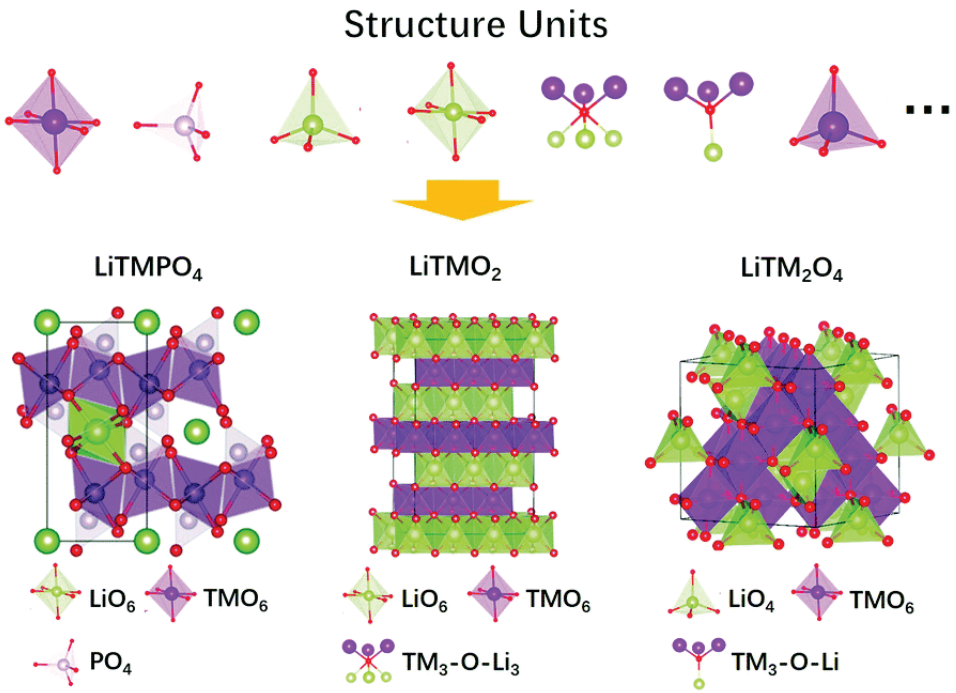

Figure 1.3. Overview over the most prominent cathode material structures in LIBs and their relationship based on similar structure units. Reproduced from L. Yang, K. Yang, J. Zheng, K. Xu, K. Amine and F. Pan, *Chem. Soc. Rev.*, **2020**, 49, 4667 DOI: 10.1039/D0CS00137F with permission from the Royal Society of Chemistry. Copyright (2020) The Royal Society of Chemistry.[48]

Materials with a phosphor-olivine structures, like $LiFePO_4$ (lithium iron phosphate, LFP), are based on a distorted hexagonal close-packed (hcp) oxide array with Li^+ and Fe^{2+} in half of the octahedral sites and P in one-eighth of the tetrahedral sites (space group *Pnma*).[49] Besides Fe, different other TM have been investigated like Ni, Co, Mn or V.[50-52] The incorporation of TM-O-P-bonds increases the stability of the oxide ions against oxidation during overcharging and results in a higher redox potential of the TMs compared to the TM-O lattice due to inductive effect of P.[21,53] The phosphor-olivine structure provides only one-dimensional Li^+ diffusion channels in the structure, which reduce in combination with the low electrical conductivity the electrochemical performance of the material.[47,50,54] The conductivity issues are counteracted by nano-sizing of the LFP and carbon coating that even allows its utilization in high power applications.[52,55,56] LFP operates at a flat voltage plateau at ≈ 3.4 V vs. Li^+/Li, which is attributed to a two-phase reaction mechanism between LFP and $FePO_4$ (Figure 1.4). It is possible to utilize almost one Li^+ per formula unit with a theoretical capacity of C_{theo} = 170 mAh g^{-1}.[55,57] A similar characteristic flat voltage curve is reported for AB_2X_4 spinel

type materials like $LiMn_2O_4$ (lithium manganese oxide, LMO, ≈ 4.1 V vs. Li^+/Li) with a theoretical specific discharge capacity of C_{theo} = 148 mAh g^{-1}.[58] The structure is based on a cubic close packed (ccp) oxide sub-lattice with $Mn^{3+/4+}$ ions occupying the half of the octahedral and Li^+ ions one-eight of the tetrahedral sites (space group: *Fd$\bar{3}$m)*.[49]

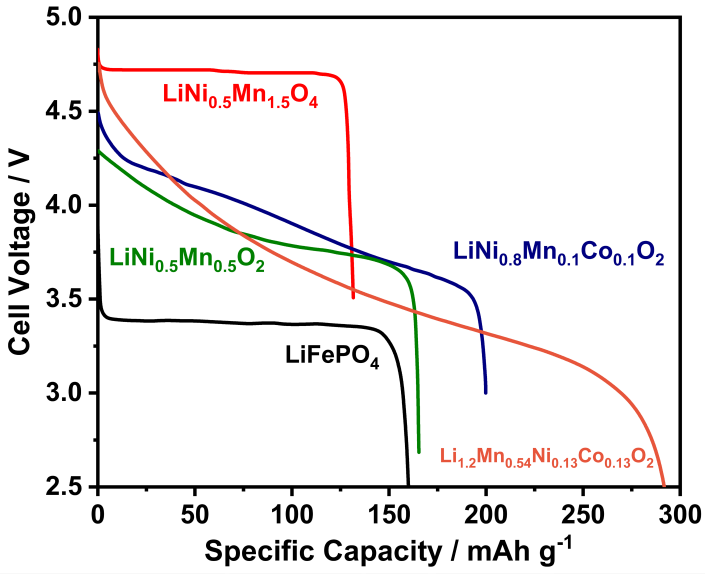

Figure 1.4. Exemplary voltage profiles of an olivine $LiFePO_4$ (black), an ordered high-voltage spinel $LiNi_{0.5}Mn_{1.5}O_4$ (red), a Co- containing Ni-rich layered oxide $LiNi_{0.8}Mn_{0.1}Co_{0.1}O_2$ (blue), a Co-free layered oxide $LiNi_{0.5}Mn_{0.5}O_2$ (green), and a Li-rich layered oxide $Li_{1.2}Mn_{0.54}Ni_{0.13}Co_{0.13}O_2$ with Li metal as counter electrode. The figure is based on different publications.[52,59-62]

In the beginning of the delithiation, a first order phase transition takes place, which can be described as solid solution reaction and is extended to a stoichiometry of approximately $Li_{0.6}Mn_2O_4$.[63] During further delithiation, two topotactic biphasic reactions occur with an intermediate phase of $Li_{0.5}Mn_2O_4$ and the final phase of λ-MnO_2.[63,64] The relithiation is mechanistically similar but the solid solution behavior is associated with the Li^+-poor λ-MnO_2 phase and not with the Li^+-rich phase.[63] The LMO material suffers from a limited specific discharge capacity. To increase the specific energy, the Mn^{3+} ions can be partially exchanged with another redox-active TM, *e.g.*, Co (5.1 V vs. Li^+/Li), Fe (4.9 V vs. Li^+/Li), or Ni (4.7 V vs. Li^+/Li).[62,65-67] The high-voltage $LiNi_{0.5}Mn_{1.5}O_4$ spinel (lithium manganese nickel oxide, LMNO) is the most promising candidate of this group in terms of electrochemical performance and costs.[27] Depending on the synthesis conditions and the stoichiometry, the Ni^{2+} ions in LMNO can be located at specific sites, which results in a higher order (space group: *$P4_332$*) and superstructure reflections in the X-ray powder diffraction (XRD) pattern. The synthesis conditions with regards to oxygen deficient structures and the ratio between

ordered and disordered phase have a critical impact on the real structure (*P4$_3$32* vs. *Fd$\bar{3}$m*), potential characteristic, the structural conversion mechanism and aging behavior of the material.[62,68-70] For commercial use, several issues, limiting the cycle life of a LMNO containing cell, still have to be solved mainly related to the electrolyte instability of this high operational voltage material, which results in Mn dissolution, chemical cross-talk and poisoning of the negative electrode.[27,58,70]

The currently most important class of materials from a commercial point of view are the layered transition metal oxides $LiTMO_2$ (C_{theo} ≈ 275 - 280 mAh g^{-1}).[71] The $LiTMO_2$ structure is generally based on a ccp framework of oxide ions with fully occupied octahedral sites by Li and TM ions and isostructural to the α-$NaFeO_2$ type with the space group *R$\bar{3}$m*.[72-74]. The layers are built on alternately stacked planes of edge-sharing [LiO_6] or [TMO_6] octahedra (see Figure 1.3).[71] In 1958, $LiCoO_2$ (lithium cobalt oxide, LCO) was synthesized and structurally characterized as a layered material.[75] Later on, Goodenough's group investigated LCO for the first time in 1980 as a possible Li-ion intercalation compound.[76] In 1990, another important layered cathode material, $LiNiO_2$ (lithium nickel oxide, LNO), was proposed by Dahn *et al*., which suffers from several stability issues during synthesis and cycling.[77-80] Therefore, the partial replacement of the Ni ions by other transition metal oxides like Mn, Co, and Al was studied intensively.[81] Fundamental work was published in 2001 by several groups about $Li(Ni_xCo_{1-2x}Mn_x)O_2$ (*x* = 1/4, 3/8, Dahn and Lu, lithium nickel manganese cobalt oxide, NMC), $LiNi_{1/3}Mn_{1/3}Co_{1/3}O_2$ (NMC-111) and $LiNi_{0.5}Mn_{0.5}O_2$ (both Ohzuku and Makimura).[82-84] Similar investigations are reported for simultaneous Co and Al doping, which resulted in the commercial available $LiNi_{0.8}Co_{0.15}Al_{0.05}O_2$ (lithium nickel cobalt aluminum oxide, NCA).[85-88] A higher Ni content implies generally a higher capacity.[89] Based on a deeper understanding of the materials, optimization of both cost and energy density led to an increase of the Ni content of the NMC materials from NMC-111 through NMC-532 and NMC-622 to NMC-811 in the past years. The trend of developing materials with even higher nickel content is ongoing.[27,73,74]

1.1.3. Co-free layered oxides as an alternative to NMC materials

The rising demand for battery materials with high Ni-content may drive into Ni supply risks.[27] Furthermore, the impact of the critical and expensive element Co has to be eliminated in the future in order to reduce costs. From a compositional point of view, LFP, lithium iron manganese phosphate (LFMP), LMNO and Li-rich layered oxides (section 1.2) are very

promising candidates, as they are Co-free and have strongly reduced Ni-content compared to the currently applied Ni-rich NMC materials. Co-free stoichiometric layered oxides represent another important cathode material class usually operating within the stability window of the typical electrolytes and provide higher specific discharge capacities.[27,60,90] For example, Ohzuku and Makimura reported that the elimination of Co and decrease of Ni content is possible with a stable discharge capacity of around 200 mAh g^{-1} for the layered oxide $LiNi_{0.5}Mn_{0.5}O_2$.[91] This material is part of the Co-free solid solution series $Li(Ni_{1-y}Mn_y)O_2$ ($0 \leq y \leq 0.5$, Co-free lithium nickel manganese oxide, NMx).[72,92,93] The substitution of Ni with Mn in NMx stabilizes the host matrix due to the presence of electrochemical inactive Mn^{4+} ions in the structure.[60] Simultaneously, each Mn^{4+} reduces an equivalent number of Ni^{3+} to Ni^{2+} in order to maintain charge neutrality.[94,95] The substitution of Ni with Mn under maintenance of the layered α-$NaFeO_2$ structure is thermodynamically limited to $y = 0.5$. A higher Mn content ($y > 0.5$) leads to the presence of Jahn-Teller active Mn^{3+} ions, a distortion of the lattice and the formation of phases with different structures.[72,93,96] Consequently, $LiNi_{0.5}Mn_{0.5}O_2$ has the highest possible Mn content in the NMx solid solution and contains predominantly Ni^{2+} and Mn^{4+} ions, which maximize the structural stabilization.[60,97] A high Ni^{2+} content and the similar ionic radii of Ni^{2+} and Li^+ (0.69 Å vs. 0.76 Å) are the general driving force for a pronounced Li/Ni displacement in the lattice (≈ 8 – 10 %).[91,93,98] Based on first-principle calculations, the formation of a flower-like cluster in the transition metal layer of $LiNi_{0.5}Mn_{0.5}O_2$ is discussed as thermodynamically favored and contributes to the increased Li/Ni displacement.[99,100] Several groups reported experimental evidence for the ordering in $LiNi_{0.5}Mn_{0.5}O_2$ and suppose that the superstructure has a positive influence on the electrochemical performance of the material due to the accessibility of the Li^+ inside the TM layer.[101-103] However, the high amount of Ni^{2+} in the Li^+ layer results in lower Li^+ diffusion kinetics, and therefore lower electrochemical performance.[60,104-107]

The voltage curve of $LiNi_{0.5}Mn_{0.5}O_2$ is characterized by a sloping voltage change, similar to the above-mentioned layered $LiTMO_2$ oxides, based on the $Ni^{2+/4+}$ redox couple between 2.5 and 4.6 V vs. Li^+/Li (Figure 1.4).[19,108] Its initial discharge capacity varies between 150 and 200 mAh g^{-1} and is strongly dependent on the synthesis route: in particular from the annealing steps,[109-112] from the annealing temperature,[111,113-116] and from the Li^+/TM ratio.[109,111,116-122] Different groups stated that Li^+ excess is able to decrease the Li/Ni cation disordering.[111,117] Furthermore, Myung *et al.* proved the successful incorporation of the Li^+

excess into the lattice with neutron diffraction.[120] Until now, the structural influence of the Li^+ excess and the formation of Li-rich layered oxide domains is still under scientific debate.[117,120]

1.2. Li-rich layered oxide materials

1.2.1. Structure and the related anionic redox mechanism

It was already indicated at the end of the last paragraph that it is possible to incorporate more Li^+ into the layered cathode materials than the stoichiometric amount of typical layered oxides (Li^+/TM = 1). The so-called Li-rich layered oxides (LRLO, HE-NMC) can be seen as an own class of layered materials with the general formula $x\ Li_2MnO_3 \cdot (1\text{-}x)\ LiNi_{1-y-z}Mn_yCo_zO_2$ ($y + z \leq 1$). They can provide exceptionally high reversible capacities (over 250 mAh g^{-1}) in combination with average discharge voltages over 3.5 V vs. Li^+/Li and are compositionally dominated by Mn, which is more earth-abundant than Co or Ni.[123-125] For similar Co-free structures (HE-NMx) between the endmembers $LiNi_{0.5}Mn_{0.5}O_2$ and Li_2MnO_3, lower reversible discharge capacities of typically 220-240 mAh g^{-1} are reported.[126-128] The detailed structure of LRLO is still under scientific debate since more than 20 years.[124] There are two preferred models to describe the structure: a nanocomposite of Li_2MnO_3 and $LiTMO_2$ or a solid solution (for example $Li_{1.2}Mn_{0.54}Ni_{0.13}Co_{0.13}O_2$).[126,129-132] Depending on the applied analysis method and the investigated materials, both models are scientifically supported.[124] The solid solution character of the LRLO is based on the similar crystal lattices of monoclinic Li_2MnO_3 (*C/2m*) and trigonal $LiTMO_2$ ($R\bar{3}m$).[133] Therefore, the Li_2MnO_3 lattice can also be described as an α-$NaFeO_2$ type structure (Figure 1.5a) with additional honeycomb ordering in the TM layer (Figure 1.5b), which is reported as the reason for the additional reflections between 20 and 25° 2θ (Cu-K_α) in the LRLO XRD pattern.[124] Their asymmetric shape (Figure 1.5d inset) is described to indicate the presence of stacking faults.[103,134,135] The intensity of the superstructure reflections varies strongly with the composition of the LRLO material.[135]

Generally, the main reasons for the ordered arrangement in the TM layer are the optimization of the charge distribution and the minimization of structural strain (*e.g.*, 0.76 (Li^+) vs. 0.53 Å (Mn^{4+})[98]) due to the Li^+ ions in the TM layer being mainly surrounded by Mn^{4+} ions (Figure 1.5b).[130,133,134] The presence of Li^+ in the TM layer strongly influences the electrochemical characteristics of the LRLOs.[136] Compared to the stoichiometric layered materials with only cationic redox active species, LRLOs benefit from the combination of both

cationic and anionic redox reactions.[90] This is very obvious during the first cycle. Typical NMC or NMx materials have a characteristic sloping voltage profile.[19] In contrast, the voltage curves of LRLOs start with a slope (cationic redox), which turns into a plateau at a voltage of approximately 4.5 V during the initial delithiation (Figure 1.5c). The plateau is assigned to the activation of Li_2MnO_3 domains (O-redox).[137] The end of the plateau is accompanied by an irreversible O_2 release, being one typical drawback of the O-redox process in LRLOs.[138]

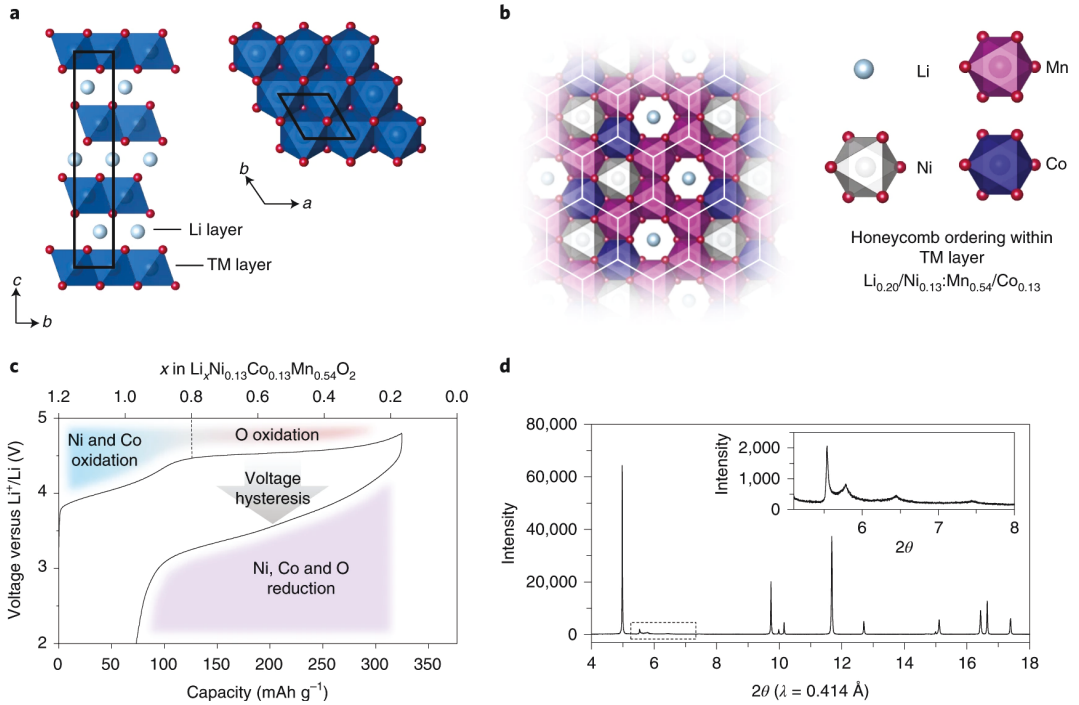

Figure 1.5. Overview over the structure and the electrochemistry of HE-NMC: a) layered *R*$\bar{3}$*m* crystal structure of HE-NMC, b) an exemplary configuration of the in-plane honeycomb-ordering of Li, Mn, Ni and Co in the TM layer, c) Initial charge-discharge cycle for $Li_{1.2}Ni_{0.13}Co_{0.13}Mn_{0.54}O_2$, and d) synchrotron XRD pattern with additional reflections from honeycomb ordering (inset).[134] Reproduced from R. A. House, G. J. Rees, M. A. Pérez-Osorio, J.-J. Marie, E. Boivin, A. W. Robertson, A. Nag, M. Garcia-Fernandez, K.-J. Zhou, P. G. Bruce, *Nat. Energy* **2020**, *5*, 777, DOI: 10.1038/s41560-020-00697-2 with permission from Springer Nature. Copyright (2020) The Authors, under exclusive license to Springer Nature Limited.

So far, the mechanism of the O-redox and the activation during the first delithiation is not yet fully understood. In the beginning, the group of Bruce supposed a Li^+-H^+ exchange mechanism as a possible reason for the electrochemical activity of Li_2MnO_3, but later on it was revealed as a parasitic side reaction at elevated cut-off voltages up to 4.8 V.[139-142] The lattice oxygen extraction mechanism proposed by Dahn's group was substantiated further with the detection of O_2 release at the end of the initial delithiation and an increase of the TM/O ratio in LRLO material.[104,138,142,143] Furthermore, several other possibilities, like TM over-oxidation or reversible redox of bulk lattice oxygen, were debated.[144-146] The current understanding based

on a broad variety of experimental and theoretical results is the combination of cationic and anionic redox reactions.[144,147] To utilize the anionic O-redox contribution, the materials must fulfill some structural requirements. Based on theoretical calculations, the group of Ceder suggested that the local environment of the oxide ions is highly important for the O-redox.[136] In a perfect $LiTMO_2$ lattice without Li/Ni disordering, each oxide ion is coordinated by three TM and three Li^+ ions forming three Li-O-TM configurations (Figure 1.6a).[136] The O 2*p* and the TM *d* orbitals are overlapping with each other, which results in bonding and anti-bonding orbitals, respectively. In the resulting band structure (Figure 1.6b), the bands are dominated either by the TM contribution (grey) or by the O contribution (red).[148] The Fermi level is typically located in the e_g* or the non-bonding t_{2g} band. Therefore, the electrons of the redox process are provided primarily from the TM during delithiation of $LiTMO_2$, although the generated holes can be also delocalized to a certain extent on the oxide ions.[149]

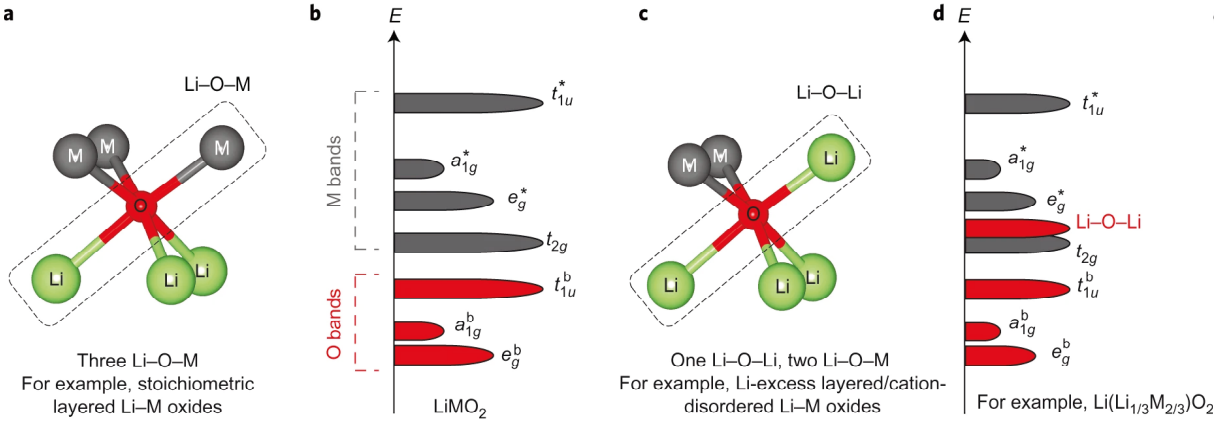

Figure 1.6. Origin of the preferred O oxidation along the Li–O–Li configuration: a) local octahedral coordination of an oxide ion in stoichiometric $LiTMO_2$ with three Li-O-TM configurations, b) schematic of the band structure in stoichiometric $LiTMO_2$, c) local octahedral coordination of an oxide ion in LRLO with two Li-O-TM and one Li-O-Li configurations, and d) schematic of the band structure in LRLO.[136] Reproduced from D.-H. Seo, J. Lee, A. Urban, R. Malik, S. Kang, G. Ceder, *Nat. Chem.* **2016**, *8*, 692, DOI: 10.1038/nchem.2524 with permission from Springer Nature. Copyright (2016), Nature Publishing Group.

In LRLOs, one of the Li-O-TM configurations is exchanged with a Li-O-Li configuration due to the presence of Li^+ into the TM layer (Figure 1.6c). The overlap between the Li 2*s* orbitals and the O 2*p* orbital is relatively small. This results in a weak Li-O bonding. Additionally, the O 2p orbital of the Li-O-Li configuration is excluded from the O-TM hybridization due to the missing TM orbitals leading to a non-bonding (orphaned) O 2p orbital. As a consequence, the electron density around this oxide ion increases significantly. The density of states of the orphaned orbital in the band structure increases with the number of Li-O-Li configurations in the lattice.[136] Typically, the non-bonding band is energetically localized between the bonding

states and the antibonding states in the band structure (Figure 1.6d) and depends strongly on the incorporated TMs and their TM-O covalence. The location of the band and the overlap with the TM states decides upon the occurring redox processes in the material, whether it is a cationic or anionic redox reaction or a combination of both.[136] This consideration is used to adjust the material properties and the reversibility of the O-redox.[150]

The reversibility of the O-redox is strongly dependent on the stabilization of the reduction products of the oxide ions.[151] Several groups reported that highly covalent TM-O bonds are able to stabilize peroxide O_2^- species in the structure and to limit their further reduction to molecular O_2.[151-154] So far, it is still under debate, if the same mechanism occurs in HE-NMC/HE-NMx materials with strongly reduced reversibility due to the lower covalence of the TM-O bond.[136,151] Besides the peroxide species, there is another alternative mechanism proposed, which is the disproportionation of nominally O^- species into oxide (O^{2-}) and molecular O_2 under TM migration in the structure.[61,134] According to the group of Bruce, the O_2 molecules arising in the bulk are most likely trapped in the lattice and can be used during re-lithiation of the structure, whereas the O_2 molecules arising in the surface-near region get lost via gas release.[134,155] As a consequence of the latter, surface densification from layered via spinel-like to rock-salt structure and electrolyte oxidation is strongly pronounced for LRLO materials during the initial cycle and reported as the cause for the high irreversible initial capacity loss.[155-159]

LRLO materials suffer additionally from voltage fade and have a large voltage hysteresis. Both are related to the anionic redox reaction.[160] The voltage hysteresis is associated with a reversible TM migration resulting in a large difference between the reduction and the oxidation potential of the anionic redox reaction.[134,147] The voltage fade is typically dominated by the progressive irreversible TM migration during cycling from partial oxygen loss in the structure and the subsequent layered-to-spinel (LS) transformation.[128,161] It is reported that the layered $R\bar{3}m$ phase transforms into a defect spinel-like LT-$LiCoO_2$ type ($Fd\bar{3}m$) and finally into a disordered rock-salt structure ($Fm\bar{3}m$) during cycling.[128] This is clearly indicated in the voltage profile by the formation of a plateau at around 2.7 V vs. Li^+/Li, which can be ascribed to the $Mn^{3+/4+}$ redox couple.[161,162] Typical countermeasures against the issues appearing with the oxygen redox process are the modification of the electrolyte,[163-165] doping of the bulk to stabilize the host structure and to reduce TM migration at high degree of delithiation,[124,150,166-168] or different kind of surface modification.[124]

1.2.2. Synthesis of LRLO

In general, the typical routes used for the synthesis of Li^+-containing TM oxides for application in LIBs can be used also for the synthesis of LRLO materials. Many scientific publications focusing on layered Li-containing oxide cathode materials use synthesis routes, which are difficult to scale up and are highly cost intensive for industrial application.[169,170] They typically include steps such as high-energy ball milling, use of dense pellets for calcination, sol-gel chemistry, combustion methods, or freeze drying.[135,161,166,171-174] For example, a very often applied route for the synthesis of LRLO materials for example uses small-sized, irregular precursor particles exhibiting a high surface area, which are pressed into pellets together with a Li^+ source. This guarantees excellent contact between both, Li^+ source and precursor, as well as short diffusion pathways.[175] Additionally, the use of pellets minimizes Li^+ loss during thermal annealing, and leads to very homogeneous products, being its main advantage.[176] On the other hand, this method is difficult to transfer into larger scale, because the densely sintered pellets have to be grinded afterwards in a time-consuming process into powder again. This step can introduce defects into the lattice, decreasing the overall performance of the materials.[177] Furthermore, the defined adjustment of particle size distribution, surface area, and tap density – all parameters of high relevance for processing – is not possible.[169,178]

In technically applied large-scale production routes of battery materials, secondary particles with spherical shape are preferred. The spherical morphology can be introduced with different methods and is dependent on the material class. Typical synthesis routes of Li-TM-oxides and the phosphor-olivine based materials are illustrated in Figure 1.7.[179]

The spherical precursor particles for Li-TM-oxides are typically prepared via the co-precipitation route in a continuously stirred tank reactor (CSTR), in which a TM salt solution (*e.g.*, $TMSO_4$), a precipitation agent (*e.g.*, NaOH or Na_2CO_3), and a complexing agent (*e.g.*, NH_4OH) are added dropwise under vigorously stirring.[180] Different parameters like, *e.g.*, the stirring speed, the pH of the suspension, the concentration of the complexing agent, the reactor geometry, and the temperature strongly influence the properties of the precursor and partially of the final product (*e.g.*, tap density, primary particle size, particle size distribution, morphology, and porosity) and have to be therefore selected very carefully.[176,181-184] After the precipitation, the precursor is filtrated and washed, to remove the neutral salts and other soluble components, dried and sieved.[180] Filtration and washing particularly benefit from the

spherical particle morphology that strongly reduces the clogging of the filter compared to sub-micrometer particles with irregular morphology.

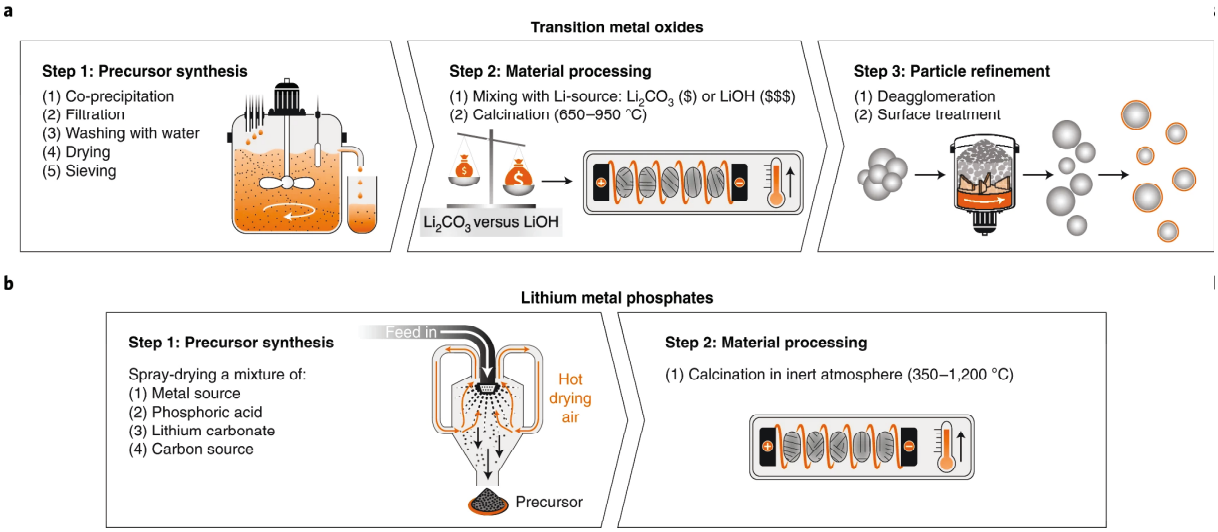

Figure 1.7. Schematic illustration of the industrial production process of (a) lithium transition metal oxides like $LiTMO_2$, $LiTM_2O_4$, or Li-rich layered oxides $Li_{1+x}TM_{1-x}O_2$ (TM = Ni, Co, Mn, Al and $0 < x < 0.2$) and (b) phospho-olivine based materials $LiTMPO_4$ (TM = Fe, Ni, Co, Mn).[179] Reproduced from R. Schmuch, R. Wagner, G. Hörpel, T. Placke, M. Winter, *Nat. Energy* **2018**, *3*, 267, DOI: 10.1038/s41560-018-0107-2 with permission from Springer Nature. Copyright (2018) Springer Nature.

In the next step, the precursor is mixed with a stoichiometric amount of a lithium salt (*e.g.*, LiOH or Li_2CO_3) and subsequently calcined in a furnace at temperatures between 650°C and 1000°C.[179,185] Finally, the as-received product is deagglomerated and can be post-treated to remove residues from the surface or to apply a surface coating.[179] Both are used to optimize the stability of the material particularly at the cathode electrolyte interface and to improve the electrochemical performance (see 1.2.4).[186,187]

1.2.3. Influence of the secondary particle architecture

The utilization of spherical secondary particles on industrial scale has further benefits besides the higher tap density and scalability compared to materials with irregular secondary particle shapes. For example, the particle surface can be minimized to reduce the amount of side-reactions. Furthermore, the sphericity provides improved processability during electrode manufacturing.[178] Nevertheless, a defined secondary particle structure increases the complexity of the synthesis procedure drastically, because the change of one parameter might simultaneously affect other parameters on different length-scales inside the secondary particle structure. The latter are described schematically in Figure 1.8 together with their most important properties.

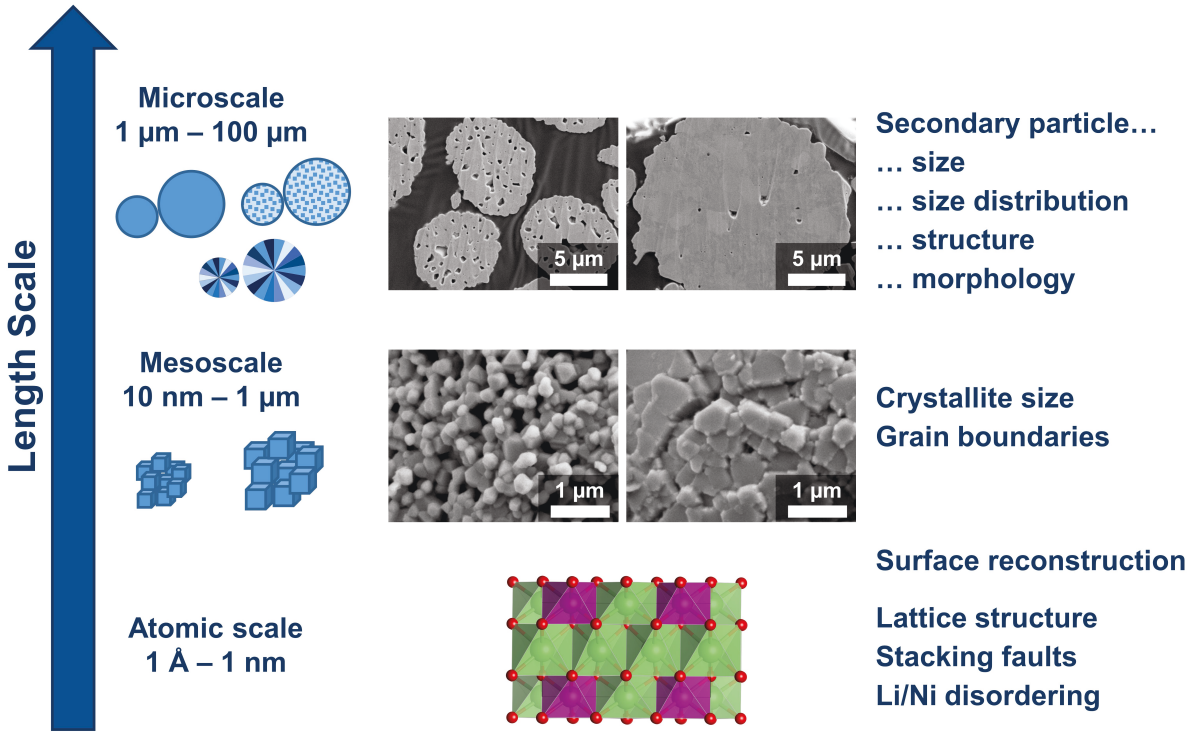

Figure 1.8. Schematic overview over the different length scales in a spherical secondary LRLO particle and their most important parameters, which can affect each other. The classification of the length-scales is based on Wang *et al*.[184]

The origin of the fundamental electrochemical material properties, *e.g.*, the energy required for (de-)lithiation from the host lattice, which is directly correlated to the electrochemical potential, is located on the atomic length scale.[19] The fundamental function is based on three main factors: a) the presence of a suited redox-pair, embedded in a b) Li^+ containing host-structure with c) suitable Li^+ diffusion pathways.[19] Furthermore, different kind of defects and structural disorder are able to influence the site energy of the electrochemical active ions.[19] A detailed discussion about structural details of LRLO materials is presented in section 1.2.1.

On the length-scale of the primary particles, the crystallite size and possible phase segregation are important properties, which can strongly influence the electrochemical performance of the material as well.[188,189] A small crystallite size provides faster diffusion kinetics due to shorter diffusion pathways and is able to improve the rate capability of the material.[190] Particularly in LRLO particles, a smaller crystallite size also increases the specific surface area of the particles, which leads to an increased activation of the Li_2MnO_3 domains and higher discharge capacity, but also to a faster degradation of the material due to the elevated oxygen loss and hence a higher rate of side reactions.[61,190]

The microscale is another length-scale of importance for the performance of a given cathode material. It includes, *e.g.*, the microstructure, the size and the morphology of the secondary particles. Typical microstructures of Li^+-containing layered oxide secondary particles are based on primary particles oriented either randomly or radially.[191] Furthermore, core-shell particles with different TM ratios inside the secondary particle structure are also possible.[192,193] The morphology of the secondary particles, *e.g.*, spherical or irregular, can be also varied.[61] House *et al.* reported that spherical particles have a lower surface to bulk ratio and therefore less oxygen loss at the surface of LRLO material when compared to the same but irregular shaped material, leading to increased discharge capacities.[61] In combination with the understanding of the redox mechanism on atomic scale, these results indicated that the irreversible oxygen release and the activation of the Li_2MnO_3 domains have to be considered in the design of the particle microstructure. LRLO materials with spherical secondary particle architecture have typically lower tap density (< 2.0 g cm^{-3}) compared to NMC materials.[169,170] Currently the porosity as well as the surface area of the particles are reported to be critical parameters for LRLO, which have to be improved further in the future.[194] Similar to the electrochemical (de-)lithiation of the material, the secondary particle architecture provides longer diffusion pathways from the outer to the inner part of the spheres compared to small particles with irregular morphology. The same effect can be assumed during synthesis for the thermal lithiation of the precursor. This can lead to inhomogeneities within the secondary particles and defects in the crystal lattice during synthesis, particularly in technically applied synthesis routes with less contact between Li^+ source and precursor.[195] A precise control of the calcination conditions is therefore very important.

1.2.4. Surface modification of LRLO

As indicated above, the particle surface of LRLO materials has a significant influence on their electrochemical performance and is associated with irreversible oxygen loss and layer-to-spinel transformation. Several groups investigated the influence of the TM composition in the materials on the particle surface or reported strategies for surface modification during the synthesis procedure.[196,197] Surface modifications are typically divided into two groups: a) the formation of reconstruction layers, and b) the application of surface coatings.[159,196]

Surface reconstruction layers are implemented to prevent the TM migration and the beginning of structural degradation processes in the surface-near region. They form an intergrown phase

with the bulk guarantying a good phase compatibility.[196] The most popular approach is the formation of a spinel-like layer or the implementation of O-vacancies.[198]

Spinel-like structures with their 3D-diffusion channels and high-voltage stability are able to improve the Li^+ diffusivity at the cathode electrolyte interphase (CEI) and to reduce the gassing.[199] Typically used synthesis routes are a combination of a chemical treatment, forming a Li^+-deficient structure in the surface-near region, and a subsequent heat-treatment step that induces a structural reorganization (Figure 1.9). For the chemical treatment step, the use of a wide variety of chemicals were reported in the past: oxidizing or reducing agents like N_2H_4, SO_2, and $Na_2S_2O_8$,[200-203] as well as mineral or organic acids,[204-212] or H_2O.[213] Furthermore, both, the duration of the treatment and the TM dissolution at lower pH values, have to be considered to avoid damage of the bulk structure.[211,212,214]

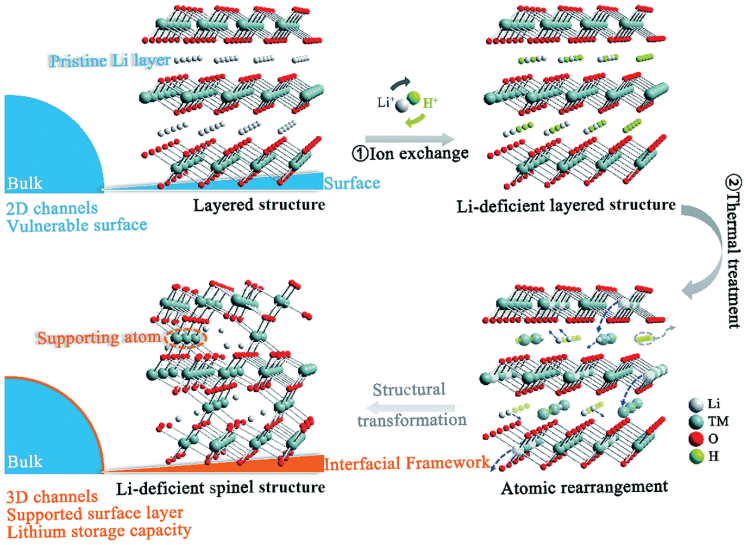

Figure 1.9. Schematic illustration of the surface reconstruction during the post-treatment steps.[199] Reproduced from Y. Zheng, L. Chen, Y. Su, J. Tan, L. Bao, Y. Lu, J. Wang, R. Chen, S. Chen, F. Wu, *J. Mater. Chem. A* **2017**, *5*, 24292, DOI: 10.1039/C7TA08735G with permission from the Royal Society of Chemistry. Copyright (2017), the Royal Society of Chemistry.

The introduction of O-vacancies in the surface-near region under preservation of the layered structure is reported to be very challenging.[196] For example, Nakamura *et al.* reported that an oxygen deficiency in the structure higher than $\delta \approx 0.042$ in $Li_{1.2}Mn_{0.6}Ni_{0.2}O_{2-\delta}$ leads to the decomposition in Ni_6MnO_8 and a Li-Mn enriched layered oxide.[215] Oxygen-deficient structures in the surface-near region can reduce the oxygen partial pressure at the surface, which can strongly decrease the irreversible release of O_2, and thus reducing the amount of side reactions with the electrolyte forming less CEI. Consequently, the initial Coulombic efficiency also increases.[123] Furthermore, first principle calculations indicated that the energy

barriers of the Li^+ diffusion strongly decrease with a higher concentration of O-vacancies leading to improved kinetics.[216] Most of these interphase modifications are using gas-solid interphase reactions with CO_2 to introduce O-vacancies in the surface-near region.[123,217,218] A completely different approach is the use of a carbon source to introduce both, a carbon coating layer and O-deficiencies.[219-221]

The second modification strategy is to coat the particle surface with a protective layer. Surface coatings are used to avoid the direct contact between the electrolyte and the particle surface, which prevents electrolyte oxidation, oxygen loss, structural transformations, as well as TM dissolution and migration.[159] A wide variety of coatings have been already applied like for example phosphates,[187,222-225] oxides,[226-228] fluorides,[187,229] or carbon-containing materials.[198,219-221,230-236] C-containing coatings are typically applied via a two-step procedure, including the deposition of a precursor like urea,[198] graphene oxide,[221] different polymers,[231,233,234] or organic acids,[219,237] and a subsequent low temperature treatment, mostly under inert conditions, in which the precursor is converted into the final coating. Due to the reductive character of the carbon, a carbothermal reduction reaction of the LRLO material is possible and therefore in most of the publications, a simultaneous formation of spinel-like structures or O-vacancies in the surface-near region, which typically improve the electrochemical performance, is observed.[220,231]

2. Objectives

Application-oriented synthesis routes towards electrode materials are essential for investigations under more realistic operation conditions. Particularly due to the high Li^+/TM ratio of LRLOs and the spherical morphology of the precursor, limited Li^+ diffusion, less contact between precursor and Li^+ source, as well as Li^+ evaporation can lead to compositional inhomogeneities in the secondary particles and to the formation of surface impurities from residual Li^+ species. Both effects may result in loss of electrochemical performance. Furthermore, in addition to the precursor synthesis, the post-processing, particularly in relation to the calcination process, is highly important for the performance of the material, and needs to be part of the overall up-scaling optimization.

Therefore, the aim of this work was to understand the Li^+ incorporation into LRLO materials for particles exhibiting a spherical secondary particle morphology in more detail. In a second step, procedures to remove surface impurities and to improve the electrochemical performance should be investigated with specific focus on different post-treatment procedures. All reaction steps should be scalable (kg-scale), in order to provide enough material for pilot-scale, double-sided electrode processing.

A fundamental understanding of the changes in the material upon lithiation and post-processing is only possible with in-depth material characterization. Thus, a second important objective of this work was the implementation, adaption, and specific combination of established characterization methods, which are able to resolve homogeneity effects on the particle and the atomic levels.

3. Results and Discussion

Two Co-free materials were selected: $Li_{1.2}Mn_{0.6}Ni_{0.2}O_2$ (x = 0.5), which is part of HE-NMx materials with the general formula $x\ Li_2MnO_3 \cdot (1\text{-}x)\ LiNi_{0.5}Mn_{0.5}O_2$, and the corresponding stoichiometric end-member $LiMn_{0.5}Ni_{0.5}O_2$. The most important findings of this work have already been published in peer-reviewed scientific journals. The publications are attached at the end of the thesis, where they are reprinted in the original format together with their supporting information (see Reprints of Publications). All three publications deal with the principle challenges related to LRLO, their understanding, and the importance of surface modification methods for this material class. In this chapter, the publications (P1-P3) are discussed from a wider perspective to put the results in the broader context of cathode materials.

P1) Enhanced electrochemical capacity of spherical Co-free $Li_{1.2}Mn_{0.6}Ni_{0.2}O_2$ particles after a water and acid treatment and its influence on the initial gas evolution behavior

F. Klein, J. Bansmann, Z. Jusys, C. Pfeifer, P. Scheitenberger, M. Mundszinger, D. Geiger, J. Biskupek, U. Kaiser, R. J. Behm, M. Lindén, M. Wohlfahrt-Mehrens, P. Axmann, *ChemSusChem* **2022**, *15*, e202201061, DOI: 10.1002/cssc.202201061.

P2) Effect of Three-in-One Surface Modification of Spherical, Co-Free Li-Rich Cathode Material for Li-Ion Batteries ($Li_{1.2}Mn_{0.6}Ni_{0.2}O_2$) with Citric Acid

F. Klein, C. Pfeifer, J. Bansmann, Z. Jusys, R. J. Behm, M. Wohlfahrt-Mehrens, M. Lindén, P. Axmann, *J. Electrochem. Soc.* **2022***, 169,* 120533, DOI: 10.1149/1945-7111/acaa5c.

P3) In-depth structural characterization of the influence of Li^+ excess on spherical, Co-free layered $LiMn_{0.5}Ni_{0.5}O_2$ cathode material using correlative Raman-SEM microscopy

F. Klein, C. Pfeifer, P. Scheitenberger, L. F. Pfeiffer, D. Zimmer, M. Wohlfahrt-Mehrens, M. Lindén, P. Axmann, *J. Mater. Chem. A* **2023**, *11*, 5135, DOI: 10.1039/D2TA05957F.

3.1. Towards a deeper structural understanding of thermal lithiation and post-processing procedures during synthesis of spherical LRLO materials

3.1.1. Structural effects induced by Li^+ excess

Li^+ diffusion kinetics during the thermal lithiation process is a critical factor for layered Li-TM-oxide materials, and can affect the homogeneity of the Li^+ incorporation on the particle level.[195] A higher fraction of Li^+ salt compared to NMx materials is required for the synthesis of LRLO due to their increased Li^+/TM ratio. If the Li^+ ions need too much time to penetrate into the secondary particles to form the LRLO lattice, the excess Li^+ can accumulate on the surface and form a Li^+-containing melt around the particles. This leads to further challenges during the up-scaling process. The presence of a Li^+-containing melt can lead to sintering of the spherical secondary particles to form larger aggregates, which subsequently need to be milled for adjustment of the particle size distribution to meet the technical requirements. Furthermore, the initial morphology might change significantly during such a process.

To avoid these issues, the synthesis process must be understood not only on the atomic level, but also on the particle level. As described by the general formula of HE-NMx materials $x\ Li_2MnO_3 \cdot (1\text{-}x)\ LiNi_{0.5}Mn_{0.5}O_2$, the structural incorporation of Li^+ ions into the TM layer is accompanied with a higher Mn content in the structure to provide Mn for the formation of the $LiMn_6$ superstructure (Figure 3.1, green line). $LiNi_{0.5}Mn_{0.5}O_2$ was selected to investigate the incorporation of the excess Li^+ without increasing simultaneously the Mn fraction in the material. Various effects of excess Li^+ on structural and morphological level of spherical $Li_{1+x}(Ni_{0.5}Mn_{0.5})_{1-x}O_2$ ($0 \leq x \leq 0.2$, Figure 3.1, black line) were studied, and reported in publication P3.

Structural investigations indicated a complete incorporation of the excess Li^+ into the primary particles. One effect of the excess Li^+ on structural level was the decrease of the Li^+/Ni^{2+} displacement in the material. In order to stabilize Li^+ on TM positions in the TM layer, a Mn-rich direct surrounding close to the $LiMn_6$ superstructure is necessary for charge balance. This induced phase separation at high Li^+ excess (approximately $x > 0.10$) into large homogeneous crystallites with slightly increased Ni-content, and areas of randomly oriented small Li-Mn-rich crystallites surrounded by Ni-rich layered compounds along the grain boundaries. This process was facilitated due to the high synthesis temperatures required for this material class and the

related mobility of the ions. Furthermore, the presence of a Li^+ salt melt resulted in the densification of the particle morphology. For moderate Li^+ excess ($x \approx 0.07 – 0.10$), a higher initial discharge capacity and an improved capacity retention was observed.

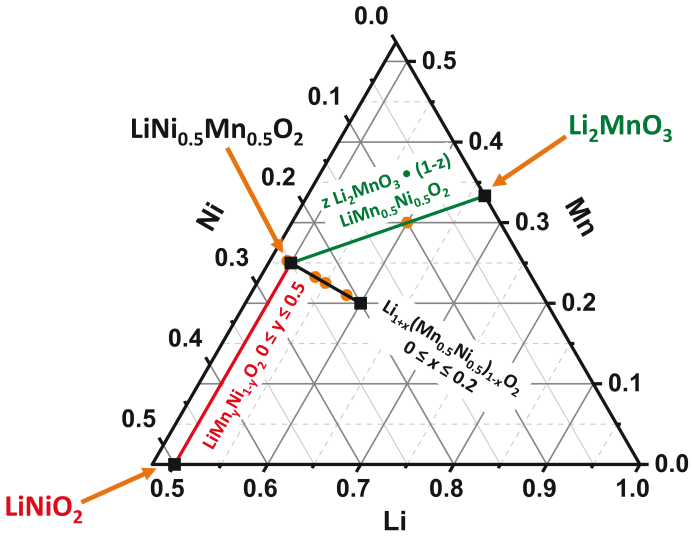

Figure 3.1. Schematic compositional diagram of the Li-Mn-Ni-O ternary system (Li + Mn + Ni = 1) with selected structures: $Li(Ni_{1-y}Mn_y)O_2$ ($0 \le y \le 0.5$, red), $z\ Li_2MnO_3 \bullet (1\text{-}z)\ LiMn_{0.5}Ni_{0.5}O_2$ ($0 \le z \le 0.5$, green) and $Li_{1+x}(Mn_{0.5}Ni_{0.5})_{1-x}O_2$ ($0 \le x \le 0.2$, black). The elemental composition of the powders investigated in the thesis are marked with an orange dot. Reproduced and modified from F. Klein, C. Pfeifer, P. Scheitenberger, L. F. Pfeiffer, D. Zimmer, M. Wohlfahrt-Mehrens, M. Lindén, P. Axmann, *J. Mater. Chem. A* **2023**, *11*, 5135, DOI: 10.1039/D2TA05957F, under CC BY 3.0 license (https://creativecommons.org/licenses/by/3.0/).[P3]

The structural changes depending on the Li^+ content were not fully resolvable by XRD due to the structural similarity of the segregated phases. Therefore, a combination of SEM, EDX, and Raman microscopy were used to study the homogeneity at the microscale, as reported in P3. Correlative Raman-SEM microscopy of particle cross-sections provided local chemical, structural and morphological information, which allowed to investigate in-detail the above-mentioned structural variations within the secondary particles. It was shown, that the shift of the Raman vibration band at approximately 600 cm^{-1} was dependent on the Li^+ fraction in the TM layer (Figure 3.2) and correlated with the local Mn/Ni ratio in the samples.

In order to obtain the highest measurement quality and resolution, the sample preparation process, used for correlative SEM-Raman microscopy was adapted and optimized during this thesis. This included the use of embedded particle cross-sections (CS), which were polished with a broad Ar^+ ion beam, instead of loose powders, and the adaption of the Raman sample stage to house the SEM sample holder. The use of the cross-sections allowed a fast re-localization of the investigated area, a good correlation of the microscope images, and an improved signal-to-noise ratio due to the flat and fresh polished surface of the particles.

Furthermore, for devices without autofocus, a flat sample topography is obligatory for enabling the possibility of a large area scan without losing focus. The preparation method was further applied to fresh and aged electrodes in publication P2.

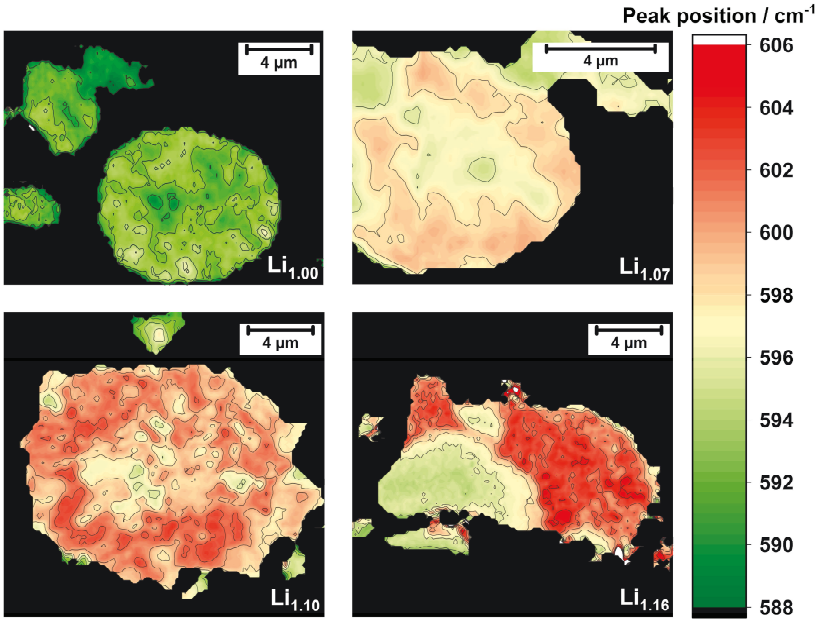

Figure 3.2. Fitted peak position of the A_{1g} vibration band for different amount of Li^+ excess: $Li_{1.00}$, $Li_{1.07}$, $Li_{1.10}$ and $Li_{1.16}$. Reproduced from F. Klein, C. Pfeifer, P. Scheitenberger, L. F. Pfeiffer, D. Zimmer, M. Wohlfahrt-Mehrens, M. Lindén, P. Axmann, *J. Mater. Chem. A* **2023**, *11,* 5135, DOI: 10.1039/D2TA05957F under CC BY 3.0 license (https://creativecommons.org/licenses/by/3.0/).[P3]

3.1.2. Surface modification strategies to improve electrochemical performance of spherical HE-NMx materials

Chemical impurities can have a strong influence on the electrochemical performance of LRLO materials. For synthesis of the carbonate precursor described in publication P1, Na_2CO_3 was used as precipitation agent during synthesis. Despite of applying extensive washing procedures of the precursor, Na^+ impurities remained in the material, resulting in poor electrochemical performance. A slow activation, indicated by a progressive increase of the discharge capacity during cycling, was observed, together with a low initial specific discharge capacity (Figure 3.3, black dots). A structural incorporation of Na^+ into the TM carbonate precursor was reported also in a patent letter of Umicore, and was suggested to have a negative impact on the electrochemical performance.[238] Furthermore, the effective reduction of the Na^+ content in the TM carbonate precursor during precursor post-treatment was reported by the authors as cost and time intensive and therefore not suited for technical application.[238] Raman spectroscopy and carbonate titration of the as-synthesized HE-NMx

material in publication P1 proved the presence of significant amounts of Na_2CO_3 impurities in the final product. Due to the high solubility of Na_2CO_3 in aqueous media, different post-treatment procedures with water (W, green colored dots in Figure 3.3) or diluted nitric acid (A, blue colored dots in Figure 3.3), and a subsequent annealing at 300°C or 900°C were systematically investigated in P1. All post-treatments were able to eliminate Na^+ impurities and Li^+ residues from the as-synthesized material. Furthermore, the electrochemical testing of the post-treated samples annealed at 300°C showed direct activation to full capacity. They reached their maximum capacity during the first cycle with significantly increased values compared to untreated material (Figure 3.3). High annealing temperatures were proven to be detrimental, as the samples post-treated at 900°C were strongly deactivated. The post-treatment effect increased with higher proton concentration of the treatment solution. For the acid treated sample, thermal deactivation was due to the formation of rock-salt structures. For a more detailed analysis including long-term cycling data, and a discussion of possible activation and passivation mechanisms, including the influence of the formation of spinel-like phases and phase-segregation, the interested reader is referred to publication P1 (Reprints of Publications).

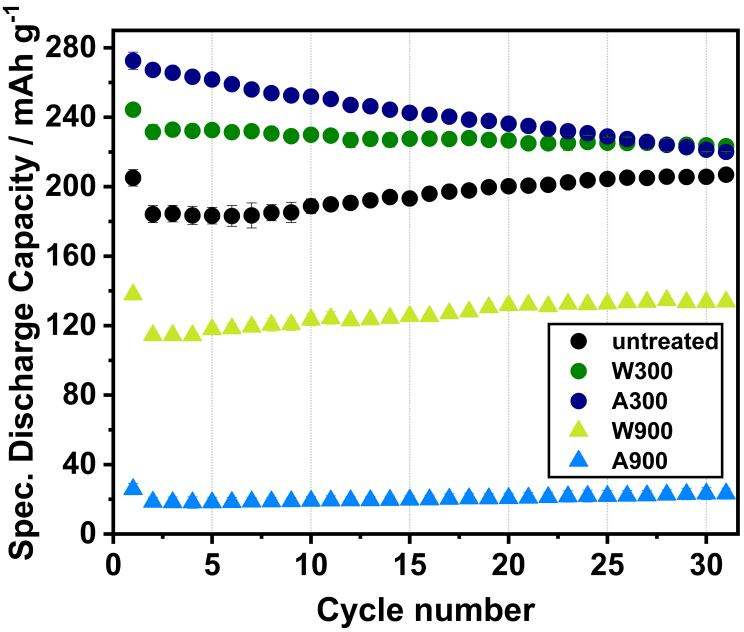

Figure 3.3. Specific discharge capacity of C/10 cycling (first cycle C/20): pristine (untreated, black), W300 (green), A300 (dark blue), W900 (light green) and A900 (blue). Adapted and modified from F. Klein, J. Bansmann, Z. Jusys, C. Pfeifer, P. Scheitenberger, M. Mundszinger, D. Geiger, J. Biskupek, U. Kaiser, R. J. Behm, M. Lindén, M. Wohlfahrt-Mehrens, P. Axmann, *ChemSusChem* **2022**, *15*, e202201061, DOI: 10.1002/cssc.202201061, under CC BY 4.0 license (https://creativecommons.org/licenses/by/4.0/).[P1]

From a technical point of view, the results of the study indicated that an acidic treatment is a well-suited method for enabling higher initial discharge capacities. Furthermore, it could be proven that the modification of the near-surface region of the primary particles was one highly important factor in the improvement of the electrochemical performance of the LRLO material. Combined with its high activity, however, the acidic treated material was less stable during cycling and showed a progressive capacity loss, which was assigned to structural changes in the near-surface region of material A300 (dark blue dots in Figure 3.3). This indicated that a chemically softer post-treatment route was necessary.

In publication P2, a new concept was applied, which combined softer acidic pre-treatment with additional surface modification, *e.g.*, a surface coating. Surface coatings are able to improve the CEI of LRLO, particularly for the high upper cut-off voltages (U > 4.6V) and to reduce the side-reactions with the electrolyte (see section 1.2.4).[124] The three-in-one treatment procedure combined the washing of the HE-NMx material with the application of a surface coating on the particle surface, and the partial reduction of its near-surface region, without adding further costly synthesis steps. Based on the results of publication P1, the proton concentration can be most likely used to adjust how aggressively the material is treated during the aqueous step of the post-treatment procedure. The application of a carbon coating was chosen due to the variety of precursor molecules with different acidity and its reductive properties to form an oxygen-deficient near-surface region. The final carbon-containing deposits formed *in-situ* on the surface of the primary particles during the annealing step.

Based on the above, citric acid (CA) was selected as a carbon precursor as it is a weak organic acid.[239-242] In parallel, a Na^+-free precursor synthesis route was developed to eliminate the influence of Na^+ ions during the crystallite growth. The corresponding lithiated Na^+-free HE-NMx material was used as a new base material. The sample names follow their CA/HE-NMx ratios: C0 (0 wt%), C1 (0.88 wt%), C2 (1.76 wt%), and C3 (2.95 wt%). The results of a wide variety of structural and chemical analysis methods, *e.g.*, XPS, Raman spectroscopy, and SEM, indicated that most likely a carbothermal reduction of the HE-NMx with the carbon-containing species took place in the near-surface region. Li_2CO_3 was formed as a by-product of this reaction. An oxygen-deficient spinel-like phase, which was reported to have increased Li^+ diffusivity, and a carbon-containing surface species were proved, which confirmed the successful implementation of this post-treatment route.[198,243] The materials showed a

progressive electrochemical activation, reaching specific discharge capacities of up to 247 mAh g^{-1} (C/10, RT, after 100 cycles, Figure 3.4). Overall, the coated materials from this combined treatment, showed improved performance compared to carbon-free specimen. A more detailed discussion of the results is given in the full-text of publication P2 (Reprints of Publications).

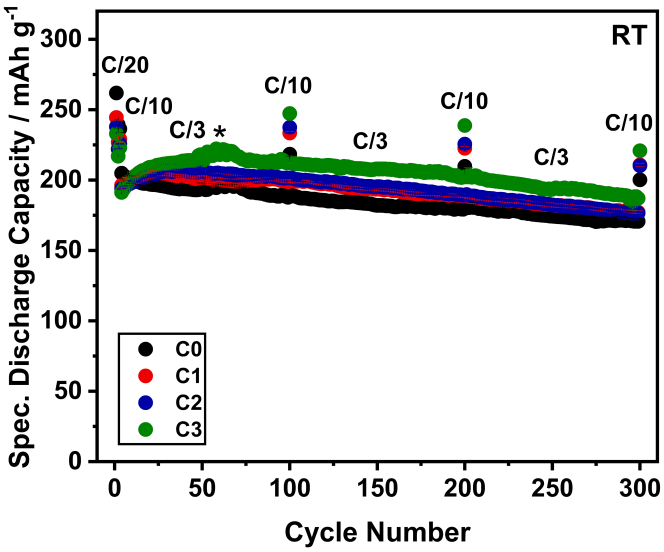

Figure 3.4. Specific discharge capacities obtained during long-term cycling tests of C0 (black), C1 (red), C2 (blue), and C3 (green) at room temperature (RT). The peaks of C3 and C0 marked with a star (*) are artefacts from temporarily slightly increased RT (ΔT ≈ 3 °C). Reprinted and modified from F. Klein, C. Pfeifer, J. Bansmann, Z. Jusys, R. J. Behm, M. Wohlfahrt-Mehrens, M. Linden, P. Axmann, *J. Electrochem. Soc.* **2022**, *169*, 120533, DOI: 10.1149/1945-7111/acaa5c, under CC BY 4.0 license (https://creativecommons.org/licenses/by/4.0/).[P2]

3.1.3. Connecting the dots - Causes and structural effects of the applied surface modification

Surface coating strategies always address specific properties of the bulk material: The publication about the incorporation of Li^+ ions (P3) gave not only insights into the influence of excess Li^+ on $LiMn_{0.5}Ni_{0.5}O_2$, but can be seen as a model study for the discussion of possible structural changes at the surface of HE-NMx materials in general. If the observed phase separation model induced by excess Li^+ is applied on $Li_{1.2}Mn_{0.6}Ni_{0.2}O_2$ (Li^+/TM = 1.50), a complete phase separation into $LiNiO_2$ and Li_2MnO_3 is expected for the composition $Li_{1.273}Mn_{0.545}Ni_{0.182}O_2$ (Li^+/TM = 1.75). Spherical particle morphology and the high amount of Li^+ source might facilitate a local Li^+ excess on the surface of spherical LRLO during calcination. Consequently, phase separation in the surface-near region of the primary particles is likely to occur at the beginning of the thermal lithiation process, and thus having a negative influence on the electrochemical performance. In parallel, Li^+ can evaporate as Li_2O at high

temperatures, which has been proven by chemical analysis.[244,245] This evaporation is able to induce local Li^+ deficiencies, which together with a possible local Mn-Ni segregation results in surface densification to form an inhomogeneous, dense, rock salt containing near-surface region. For example, Boivin *et al.* reported the formation of an up to 4 nm thick disordered, surface rock-salt phase in $Li_{1.2}Mn_{0.6}Ni_{0.2}O_2$ after thermal lithiation of the precursor, which corresponded to approximately 20 % of the crystallite volume in crystallites with 100 nm diameter.[197] This underlined the importance of the surface modifications for HE-NMx materials to modify the dense layer and to improve the diffusivity of the Li^+ ions into the particle during electrochemical operation.

In order to shed more light on the chemical modification of the surface-near region, the latter was modified using a variety of the as-synthesized materials (HE-NMx out of different precursors with similar Ni-Mn-stoichiometry either with or without Na^+ impurities), and treatment procedures in the studies P1 and P2. The same sample codes as those used in P1 and P2 were used, W300 and A300 (P1), as well as C0-C3 (P2). The materials W300 and C0 were both initially treated with water. Whereas C0 was annealed at 400°C under Ar atmosphere, W300 was heated up to 300°C under air. Both materials were free from impurities, and were therefore used as reference materials within their group of samples. All XRD patterns of W300, A300, and C0-C3 had typical reflections of HE-NMx materials including the superstructure reflections. No additional shoulders, which are indicators for the presence of spinel-like phases, were observed.[246] This indicated that the influence of the applied post-treatment steps on the long-range ordering of the bulk was small. Similar results were also observed for the expansion of the unit cells. Both lattice parameters increased with the acidic treatment from C0 (W300) to C3 (A300), for example the *c*-parameter from 14.260 Å (14.258 Å) to 14.270 Å (14.274 Å). For A300, the increase in the lattice parameter values was more pronounced compared to C3. Generally speaking, the lattice expansion was most probably caused by the partial reduction of Mn^{4+} into Mn^{3+}, which went along with an elongation of the TM-O bonds. The local structural deviations and the short-range ordering were investigated by Raman spectroscopy. In both cases, the spectra had an additional shoulder at ≈ 650 cm^{-1} indicating the presence of spinel-like structures, which could not be seen by XRD.[130,247,248]

Additional characterization was carried out by XPS and cerimetry measurements. Whereas the Mn^{3+}/Mn^{4+} ratio derived from the Mn XPS spectra increased only to a minor degree from

W300 to A300, Mn^{3+} dominated the spectra of C3. The stronger reduction of the HE-NMx near-surface region in C3 resulted most likely from the carbothermal reduction reaction with the *in-situ* formed carbon species on the surface. This assumption was supported by an increase of the carbonate signal in the C 1s spectra and total inorganic carbon analysis. Furthermore, a broadening of the Li 1s spectrum as it was observed for A300 and indicated the presence of a spinel-like environment for some of the Li^+ ions, was not found in the series C1-C3.[249] This was explained by the calculated formal oxygen stoichiometry ($Li_{1.2}Mn_{0.6}Ni_{0.2}O_{2+\delta}$) experimentally obtained from cerimetry, complexometric titration and ICP-OES. Compared to W300 and C0 with stoichiometric formal oxygen content ($\delta = 0$), the formal oxygen stoichiometry in A300 was higher, whereas it was lower for C1-C3. An overstoichiometric formal oxygen content ($\delta > 0$) indicated the presence of either spinel ($LiTM_2O_4$), Ni_6MnO_8 rock-salt structures, or both. In contrast, substoichiometric formal oxygen content ($\delta < 0$) indicated vacancies in the structure, which is in accordance with the reported results of comparable C-containing coating procedures.[198,235] As a result, the structural characterization showed that it is possible to control the structural properties of the near-surface region with the choice of the post treatment route. Furthermore, it was shown that the increase of the lattice parameters did not allow the differentiation between a formal oxygen over- and substoichiometry, respectively, but a qualitative indication for the partial reduction of the Mn^{4+} ions into the trivalent state.

The effect of the different formal oxygen stoichiometries helped to additionally understand the different electrochemical performance, gassing behavior, and aging of A300 and C1-C3. As reported in P1, the specific discharge capacity of A300 was initially high (272 mAh g^{-1}, C/20), but strongly decreased continuously upon cycling. The O_2 evolution rate increased from W300 to A300, which indicated a more distinct electrochemical activation, and the potential curve of A300 behaved slightly different from W300. Both were ascribed to the Mn-Ni segregation in the material, which resulted in a higher fraction of Li_2MnO_3 domains in the lattice.

Compared to that, the vacancy-containing materials C1-C3 started with low initial discharge capacities, followed by a progressive electrochemical activation. After complete activation, a high specific discharge capacity was reached (247 mAh g^{-1} after 100 cycles, C/10). Cycling at elevated temperatures and the gassing behavior of the materials let suppose that the activation process in the beginning is not only dominated by the vacancies, but also most likely influenced by the decomposition of Li_2CO_3 impurities formed during the post-treatment. The

O_2 evolution rate during the initial delithiation was already strongly reduced for C1 and no longer detectable for C3, which is the reverse effect observed for the acid treated A300. Similar results were reported for example by Qiu *et al.*, who introduced oxygen vacancies in HE-NMC material.[123] Furthermore, the increase of the O_2 evolution rate from W300 to A300 is likely an indication for the continuation of the structural degradation from the post-treatment during electrochemical cycling.

Overall, both publications, P1 and P2, clearly proved the strong impact of the applied post-treatment procedures on the electrochemical performance and the structural stability of the materials. The formal oxygen stoichiometry of the investigated powders was identified as an adequate indicator to differentiate between the spinel-like phase in A300 and the vacancies-containing samples C1-C3. Unfortunately, based on the XRD patterns and the refined lattice parameters, neither a differentiation between over- and substoichiometric formal oxygen content in the powders nor a direct correlation with the electrochemical performance of the materials was possible. The electrochemical performances of A300 and C1-C3 were barely comparable. The structure of A300 was already destabilized during its more aggressive post-treatment, and therefore this material aged differently to C1-C3. Compared to A300, the post-treatment with CA laid the foundations for the progressive activation of C1-C3, which likely helped to improve the electrochemical performance at room temperature. The structural transformation into spinel-like phases during long-term cycling was not suppressed in the investigated materials by the vacancies in the structure.

3.2. Up-scaling of HE-NMx into the kg-scale

The main part of the thesis dealt with the deeper understanding of the HE-NMx material on particle level (P1-P3). The necessary synthesis steps of the scalable synthesis route were identified there for $Li_{1.2}Mn_{0.6}Ni_{0.2}O_2$ and particularly optimized before in the smaller scale of up to approximately 100 g. The basic material without post-treatment in the CA post-treatment publication for example was already lithiated and annealed in a batch size of 130 g (P2). However, it was fundamental to prove that the developed synthesis route is indeed scalable.

In Figure 3.5, the single synthesis steps for the up-scaled material are summarized and supplemented with the key process parameters for the successful scale-up. The advantages

of using spherical precursor from continuous co-precipitation reaction in a CSTR were already discussed in the section 1.2.2. For the next two steps of the synthesis, lithiation and annealing, the precursor was mixed with the Li^+ source and water to form a highly viscous slurry, which was subsequently dried before the thermal annealing. The wet impregnation was able to distribute the Li^+ source more uniformly in the sample and on the surface of the primary particles of the precursor. This strongly reduced the diffusion pathways during the subsequent annealing step and allowed more homogeneous reaction conditions. The use of large flat saggars avoided the formation of agglomerates in the sample, because a local segregation and accumulation of the melted Li^+ source at the bottom, as observed in high cylindrical crucibles, cannot occur to this extent. An additional important advantage of the flat saggars was the improved access of the oven atmosphere to each particle due to the lower filling level compared to a cylindrical crucible with small base area and high filling level.

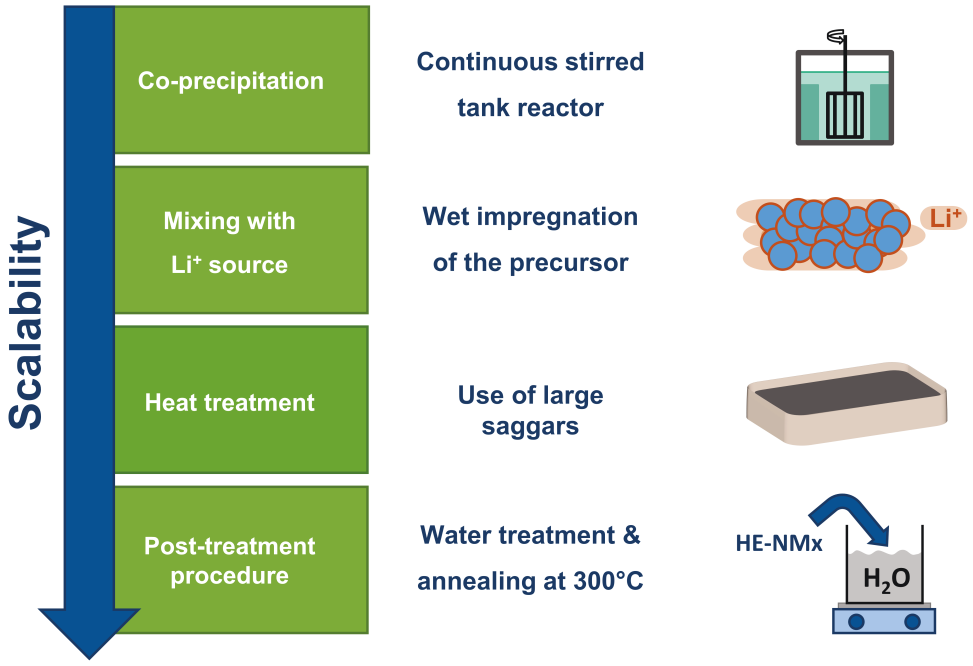

Figure 3.5. Schematic overview about the different process steps in the developed, scalable synthesis route. The drawing in the bottom right corner is modified from F. Klein, J. Bansmann, Z. Jusys, C. Pfeifer, P. Scheitenberger, M. Mundszinger, D. Geiger, J. Biskupek, U. Kaiser, R. J. Behm, M. Lindén, M. Wohlfahrt-Mehrens, P. Axmann, *ChemSusChem* **2022**, *15*, e202201061, DOI: 10.1002/cssc.202201061, under CC BY 4.0 license (https://creativecommons.org/licenses/by/4.0/).[P1]

The last step of the synthesis, the post-treatment procedure, was important to remove possible surface impurities and to manipulate the surface of the material with respect to the electrochemical performance and the aging of the material. The scale-up was conducted in

parallel to the investigation of possible surface coatings on the HE-NMx material, which was the reason why the water treatment was applied to the 5 kg of material.

3.2.1. Experimental

The 5 kg batch was synthesized similar to the synthesis route with aqueous post-treatment of publication P1. There are some deviations from the original synthesis route reported there, in particular due to the progress of the precursor synthesis and the larger batch size. As a precursor material, a Na^+-free TM carbonate precursor was used (P2). The precursor synthesis was performed following the continuous co-precipitation process, while the sample was divided into batches of around 1 kg sample size for the lithiation, annealing and the post-treatment procedure due to the limiting size of the oven. Furthermore, the amount of ultrapure H_2O was reduced for the post-treatment step (HE-NMx:$H_2O \approx 1:2.5$). The experimental details of the structural, morphological and electrochemical characterization can be found in P2.

3.2.2. Characterization of the 5 kg HE-NMx material and comparison with the powder obtained from small-scale synthesis

The up-scaled material was characterized by XRD, SEM, and electrochemistry to verify its quality. The structural and morphological characterization results are summarized in Figure 3.6. The material C0 of publication P2 was used in order to compare the material from small with the kg-scale, because both materials are based on the Na^+-free precursor. The XRD pattern of the 5 kg batch was similar to the pattern of C0 and can be indexed to the space group $R\bar{3}m$ with superstructure reflections of the honeycomb ordering (Figure 3.6a).[250,251] Furthermore, reflections of impurity phases were not observed and the layered structure was well pronounced, which was indicated for example by the splitting of the (006) and (102) as well as of the (108) and (110) reflections.[107]

The lattice parameters were determined via Rietveld refinement with TOPAS V6 and the structural model of Fell et al. for $Li_{1.2}Mn_{0.6}Ni_{0.2}O_2$.[252] The lattice parameters a = 2.862 Å and c = 14.255 Å were comparable to the lattice parameters of C0 (a = 2.862 Å and c = 14.260 Å) and W300 (a = 2.859 Å and c = 14.258 Å), particularly the a parameters were in very good mutual agreement. The SEM image of the up-scaled powder showed spherical secondary particles with a diameter of approximately 10 µm and smaller (Figure 3.6d). The fraction of

smaller particles and the particle morphology was similar those observed for C0 particles (Figure 3.6c).

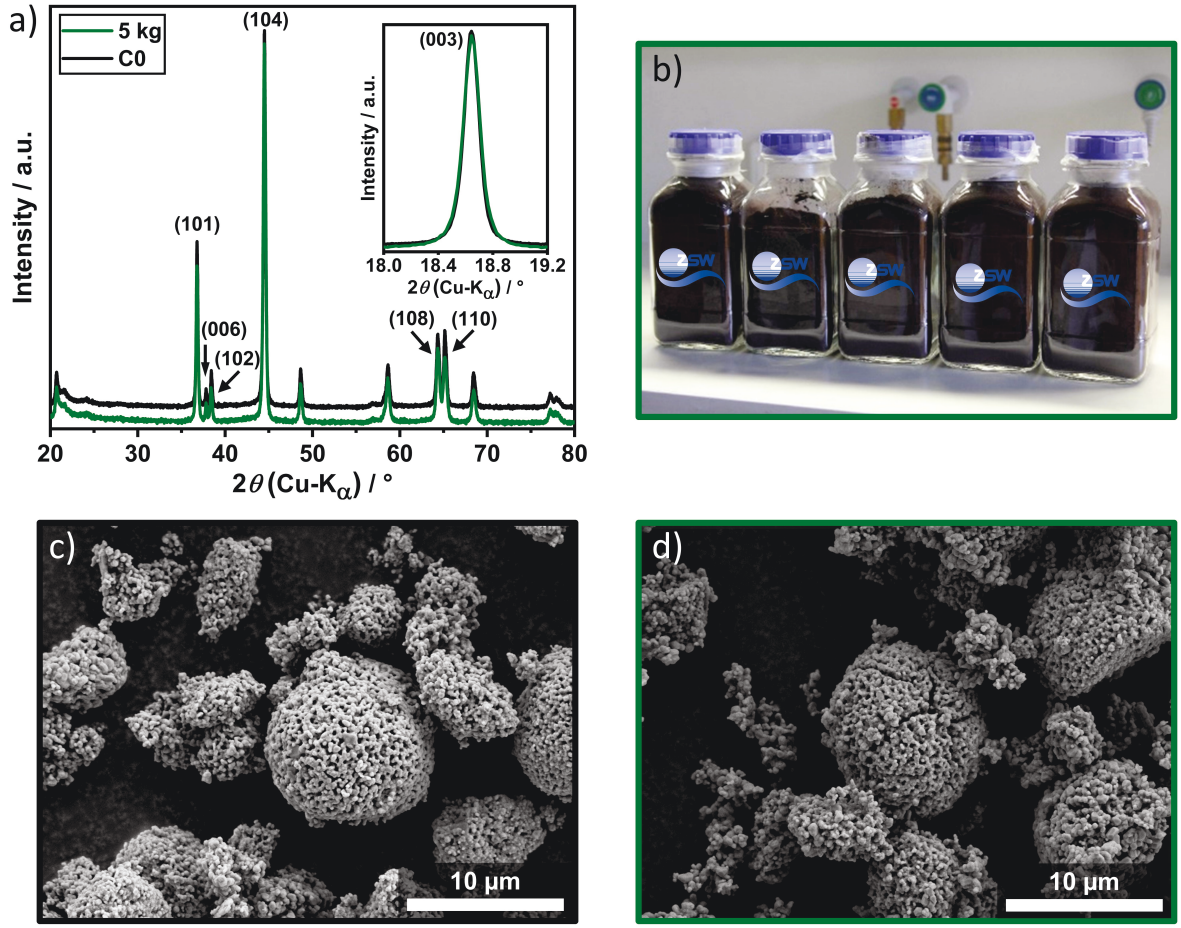

Figure 3.6. Structural and morphological characterization of the 5 kg batch (green) compared with the sample C0 (black). (a) Overview over the XRD pattern and the 003 reflection (inlet). The data of C0 are based on F. Klein *et al*.[P2], (b) image of the bottled powder, and comparison of the particle morphology using SEM images of (c) C0 and (d) 5 kg batch.

The electrochemical characterization results in half-cell configuration against Li metal in a voltage range between 2.5 and 4.8 V showed slightly higher initial discharge capacity of 246 mAh g^{-1} for the up-scaled sample (Figure 3.7a). The first cycle voltage profile showed the typical characteristics of LRLO materials with a pronounced flat voltage plateau in the second part of the delithiation step (Figure 3.7b).[134] The voltage profiles let assume that both materials were activated similarly during delithiation, but the up-scaled material benefitted from a smaller initial irreversible capacity loss due to an increased capacity between 3.5 and 2.5 V. This voltage window was assigned to the O-reduction, which let assume that the up-scaled sample was chemically activated to a slightly higher degree during the post-treatment step compared to the small scale reference.[147] The discharge capacities of C0 and the 5 kg

material matched each other after 5 - 10 cycles and showed a similar behavior during subsequent cycling. A comparison of rate capability showed higher performance for the up-scaled material.

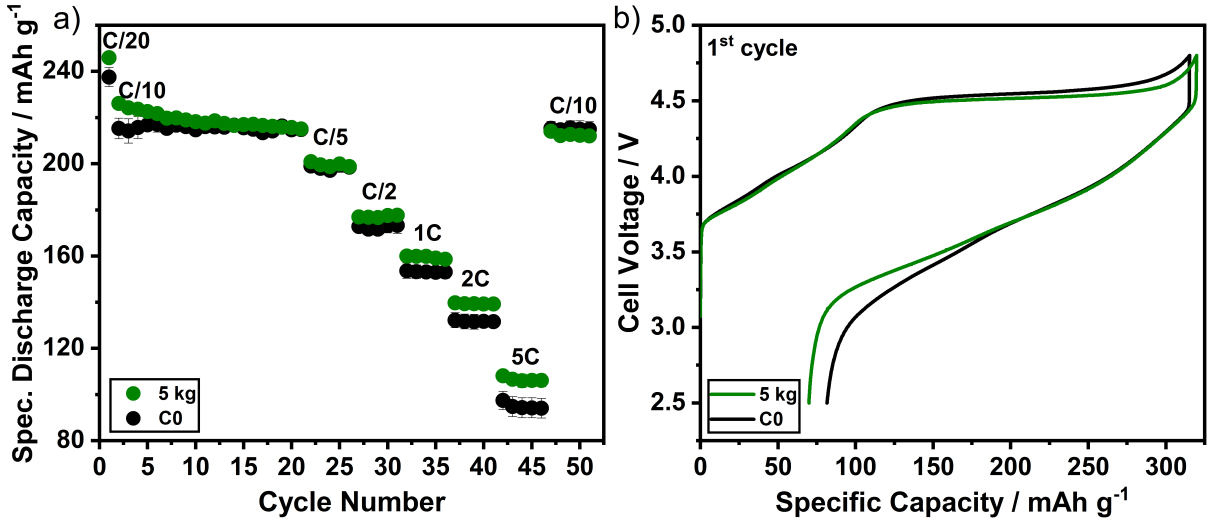

Figure 3.7. Electrochemical characterization of the 5 kg batch (green): (a) specific discharge capacity over cycling including a rate capability test and (b) voltage curve of the initial cycle. As a baseline material with smaller batch size, the data of C0 were used based on F. Klein *et al.* [P2]

The long-term cycling stability of the up-scaled material at 1C is presented in Figure 3.8. During the first 100 cycles, the discharge capacity dropped to 90 % state of health (SoH, Figure 3.8a), followed by a nearly linear decrease of the capacity during further cycling, and reached the technical end-of-life (80 % SoH) after approximately 500 cycles. After 1000 cycles, the electrode still had 60 % of the initial 1C capacity left.

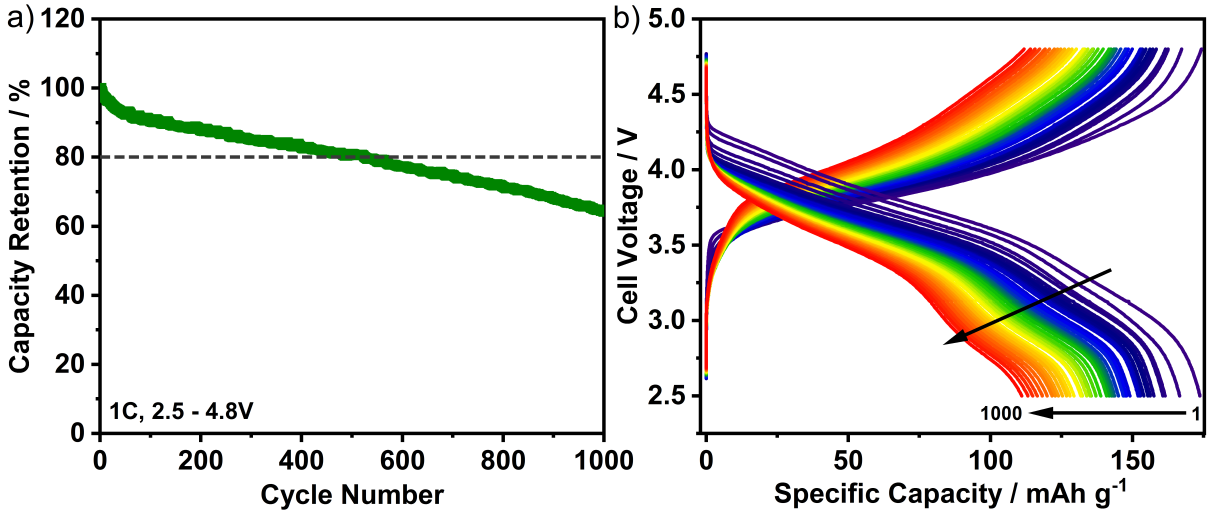

Figure 3.8. Long-term cycling data of the 5 kg batch at 1C (1C ≙ 250 mA g^{-1}): (a) state of health over cycles and (b) voltage profiles of every 25th cycle.

The capacity drop during the initial cycles of the experiment can be explained with the help of the voltage profiles (Figure 3.8b). Particularly in the first 100 cycles, a strong increase of the

overpotential directly in the beginning of the lithiation was observed, which could be associated with, *e.g.*, the formation of a CEI or a lower O-redox activity due to kinetic limitations. Other aging phenomena dominated most likely the nearly linear part of the capacity retention, for example the layered-to-spinel transformation, indicated by the black arrow in Figure 3.8b, and the increased capacity during delithiation between 3.2 and 3.75 V, representing the $Mn^{3+/4+}$ redox couple.

Overall, the characterization of the up-scaled material indicated that all investigated properties are predominantly similar with the powder from smaller scale synthesis. This was possible due to the combined approach of generating an in-depth scientific understanding of the structural and morphological effects controlling the electrochemical performance for this class of materials and the transfer of the generated knowledge into application oriented scale-up process. Therefore, this study clearly underlined the scalability of the developed synthesis route. The synthesized HE-NMx material will be used to investigate its electrochemical properties in more technical relevant cell designs, like pouch or cylindrical cells.

4. Summary and Outlook

Li-rich layered oxides is one promising class of next-generation cathode materials that reduces the demand for the critical transition metals Co and Ni, and simultaneously provides high discharge capacities originating from the participation of both cationic and anionic redox pairs. The electrochemical performance of the anionic redox reaction with its electrochemical first cycle activation-mechanism is particularly sensitive to the change of the surface to volume ratio. Furthermore, a higher amount of Li^+ source during the synthesis compared to NMC materials is required, which can be the origin of surface residues and inhomogeneities within the secondary particles. In combination with the technical requirement of dense particle architectures and suited particle size distribution to increase the volumetric density of the final battery, all parameters mentioned above have to be taken into consideration during scalable synthesis route development of LRLO materials with spherical secondary particle morphologies.

In the first part of this work, $LiNi_{0.5}Mn_{0.5}O_2$ was investigated with respect to its Li^+ stoichiometry ($Li_{1+x}(Mn_{0.5}Ni_{0.5})_{1-x}O_2$, $0 \leq x \leq 0.16$) to generate a deeper understanding of the Li^+ incorporation process into the precursor material consisting of spherical secondary particles. It was shown that most of the excess Li^+ was incorporated into the HE-NMx structure, particularly at low-to-moderate Li^+-excesses. This caused $LiMn_6$ superstructure ordering in the TM layer with arising superstructure reflections in the XRD pattern. A detailed analysis of the materials with correlative microscopy combining SEM, EDX, and Raman microscopy proved that the Li-Mn ordering induced a local phase segregation on microstructural length-scale for high Li^+ excess ($x = 0.16$) into a) large homogeneous crystallites with slightly increased Ni-content, and b) areas of randomly oriented small Li-Mn-rich crystallites surrounded by Ni-rich layered compounds along the grain boundaries. For moderate Li^+ excesses, a more homogenous particle microstructure was found. The phase segregation was interpreted as a kinetically hindered Li^+ incorporation into the dense spherical precursor architecture combined with the formation of a Li^+-containing melt around the spheres during heat-treatment, which led to further densification of the final secondary particles. $Li_{1.07}(Mn_{0.5}Ni_{0.5})_{0.93}O_2$ was identified as the most stable material within the investigated series with a discharge capacity of 173 mAh g^{-1} (658 Wh kg^{-1}).

The results obtained for $LiNi_{0.5}Mn_{0.5}O_2$ are highly relevant as well for other LRLO materials with higher Li and Mn contents as well. In particular, in the beginning of the thermal lithiation process, an optimized precursor particle architecture can help to facilitate Li^+ access into the core of the particles, and reduce segregation in the near-surface region.

The second part of the thesis was focused on the understanding of the near-surface region of $Li_{1.2}Mn_{0.6}Ni_{0.2}O_2$. Impurities from the coprecipitation of precursor and surface residues after the calcination like carbonates in the final product, resulting in a low initial discharge capacity and extended activation during cycling. Different post-treatment procedures were investigated for the removal of the Na^+ and surface impurities. The materials were washed in a first step with water or diluted acid, and subsequently treated at either 300°C or 900°C under air. The treatments strongly affected the electrochemical performance of the materials: a) samples calcined at 900°C were deactivated, whereas b) samples calcined at 300°C showed improved performance. The acid treated, deactivated material showed phase separation into Li-Mn-enriched layered oxide and Ni_6MnO_8 rock-salt structures. The latter was mainly located at the grain boundaries and most probably blocked the Li^+ diffusion pathways. Materials that had undergone low temperature treatment exhibited high initial discharge capacities of up to 270 mAh g^{-1} (C/20). Generally, the proton concentration during washing was found to be a highly critical parameter: while the acid treated sample was initially strongly activated during cycling, it suffered from pronounced capacity fade. This was explained by a higher TM leaching during acid treatment, leading to local Mn- and Ni-enrichments and a spinel-like phase in the surface-near region. The water treated sample showed moderate capacity increase with stable cycling behavior.

The generated knowledge was transferred into the implementation of a surface carbon coating on the particles. The treatment of a HE-NMx material without Na^+-impurities with less aggressive citric acid solution increased the specific discharge capacity, and controlled the structure of the primary particle near-surface region. Furthermore, the deposited CA coating could be transformed to carbon upon heat-treatment, resulting in a protective surface coating with increased electric conductivity. Chemical and structural characterization confirmed the formation of the carbon-containing coating as well as the formation of an oxygen-deficient near-surface region in the primary LRLO particles. The post-treated materials showed improved electrochemical performance compared to the untreated material after a progressive activation of the Li_2MnO_3 domains and reached discharge capacities of up to

247 mAh g^{-1} at RT and up to 276 mAh g^{-1} at 40°C (both C/10). Slightly increased voltage fading for materials with higher CA/LRLO ratio was attributed to a faster layered-to-spinel transformation probably caused by the structural changes during post-treatment. However, the improved capacity overcompensated for the voltage fade during cycling resulted in higher specific energies for all treated materials.

Both post-treatment studies showed that the surface modification has a strong influence on the electrochemical performance and the structural stability of LRLO materials. Dependent on the choice of the post-treatment procedure, either formal oxygen deficiency or oxygen excess can be introduced into the surface-near region in a controlled way. A direct correlation between the formal oxygen stoichiometry, the structural information from XRD and the electrochemical performance was, however, not observed.

The scalability of the developed synthesis routes was demonstrated with a scaled-up synthesis yielding 5 kg of HE-NMx material that exhibited an initial discharge capacity of 246 mAh g^{-1}, and a capacity retention of 80 % after approximately 500 cycles at 1C.

Overall, this worked showed that the Li^+ distribution during the thermal annealing is a very critical parameter with respect to chemical and structural homogeneity on the particle level. The chemical homogeneity was directly mirrored in the electrochemical performance of LRLO-based cathode materials and is therefore of high relevance in application-oriented synthesis.

It was shown that the electrochemical performance and the structural stability of the LRLO during cycling were highly sensitive to the applied surface modification conditions. Furthermore, correlative SEM-Raman microscopy was adapted to identify structural inhomogeneities inside the secondary particles and to evaluate aging mechanisms. Finally, the scalability of the applied synthesis route was confirmed.

The up-scaled material will be used in the future for investigating the HE-NMx material in application-oriented cell designs. The high amount of synthesized material allows producing of double-side coated pilot-line electrodes for the assembly of multi-layered pouch cells. For example, it is important to better understand the balancing of anode and cathode for this class of material with respect to the high initial irreversible capacity loss.

From a material perspective, the study opened the way to further improvement by generating many new questions, which can target the further optimization of the lithiation process during calcination. This specifically addresses particle architecture as well as chemistry. The secondary particle architecture has to be further optimized with the goal of physically dense

and high electrochemical activity to achieve maximum volumetric energy density. Such development will include optimization of the anisotropy and size of primary particles, secondary particle density as well as particle size distribution. Further mechanistic understanding of the thermal lithiation process with respect to the Li^+ accessibility into the spherical precursor particles is necessary in order to identify the ideal precursor properties such as an optimal porosity or their chemical composition (*e.g.*, carbonate-based or hydroxide based) to obtain homogeneous LRLO materials.

5. Zusammenfassung und Ausblick

Li-reiche Schichtoxide gehören zu einer der vielversprechenden, zukünftigen Kathodenmaterialklassen für Li-Ionen Batterien. Mit Hilfe dieser Materialien kann der Bedarf an kritischen und teuren Übergangsmetallen wie Co oder Nickel minimiert werden. Durch die gleichzeitige Nutzbarkeit von kationischen und anionischen Redoxreaktionen, zeichnet sich die Materialklasse durch hohe spezifische Entladekapazitäten aus. Die elektrochemische Leistungsfähigkeit der anionischen Redoxreaktion ist sehr empfindlich gegenüber dem Verhältnis aus Oberfläche und Volumen der Materialien. Zusätzlich wird während der Synthese der LRLO-Materialien eine größere Menge an Li^+-Salzen benötigt als bei der Synthese von herkömmlichen Schichtoxiden wie zum Bespiel NMCs. Dies kann zu Oberflächen-verunreinigungen und Inhomogenitäten innerhalb der Sekundärpartikel führen. Aus technischer Sicht sollten die oben genannten Parameter bei der Entwicklung von skalierbaren Syntheserouten für LRLO-Materialen mit sphärischer Sekundärpartikelmorphologie neben einer geeigneten Partikelgrößenverteilung und einer möglichst hohen Dichte der Partikelarchitektur berücksichtigt werden.

Im ersten Teil der Arbeit wurde der Einfluss eines Li^+-Überschusses auf das System $Li_{1+x}(Mn_{0.5}Ni_{0.5})_{1-x}O_2$ $(0 \leq x \leq 0.16)$ untersucht, um ein tieferes Verständnis des Li^+-Einbauprozesses in die Sekundärpartikelarchitektur zu erhalten. Es wurde gezeigt, dass der Li^+-Überschuss hauptsächlich in die Übergangsmetallschicht der HE-NMx Struktur eingebaut wurde und sich dort $LiMn_6$-Überstrukturen ausbildeten. Letztere wurden mittels Pulverdiffraktometrie nachgewiesen.

In einer detaillierten Untersuchung der Partikelmikrostruktur mittels korrelativer Mikroskopie aus SEM, EDX und Raman-Mikroskopie konnte eine durch die Ausbildung von $LiMn_6$-Clustern induzierte, lokale Phasensegregation im Mikrometerbereich für die Probe mit dem höchsten Li^+-Überschuss ($x = 0.16$) nachgewiesen werden. In der Mikrostruktur konnte zwei dominierende Strukturen identifiziert werden: a) große, homogene Kristallite mit leicht erhöhtem Ni-Gehalt und b) Regionen mit zufällig angeordneten Li-Mn-reichen Kristalliten, deren Korngrenzen von Ni-reichen Schichtoxiden dominiert wurden. Eine wesentlich homogenere Mikrostruktur bildete sich bei moderaten Li^+-Überschüssen aus. Die Ursache der Phasensegregation und der Verdichtung der Partikelmikrostruktur wurde auf einen

verzögerten Li^+-Einbau in den dichten Hydroxid-Präkursor und der daraus resultierenden Li^+-enthaltenden Schmelze außerhalb der sphärischen Partikel zurückgeführt. $Li_{1.07}(Mn_{0.5}Ni_{0.5})_{0.93}O_2$ wies die höchste elektrochemische Stabilität und eine spezifische Entladekapazität von 173 mAh g^{-1} (658 Wh kg^{-1}) in der Gruppe der untersuchten Materialien auf.

Die Ergebnisse aus der Untersuchung von $LiNi_{0.5}Mn_{0.5}O_2$ sind ebenfalls sehr wichtig für andere LRLO-Materialien mit höheren Li- und Mn-Stöchiometrien. Die Studie zeigte, dass besonders zu Beginn des thermischen Lithiierungsprozesses ein lokaler Li^+-Überschuss durch einen optimierten Zugang der Li^+-Ionen in die Sekundärpartikelstruktur vermieden werden sollte, um eine mögliche lokale Phasensegregation insbesondere an der Oberfläche der Partikel zu vermeiden.

Der zweite Teil dieser Arbeit konzentrierte sich auf das tiefere Verständnis der oberflächennahen Regionen von $Li_{1.2}Mn_{0.6}Ni_{0.2}O_2$. Verunreinigungen aus der Präkursor-Fällungsreaktion und Oberflächenverunreinigungen nach der Kalzinierung, wie beispielsweise Carbonate, führten zu einer geringen, initialen spezifischen Entladekapazität und einer verzögerten, schrittweisen Aktivierung des Materials während des Zyklisierens. Um die Na^+-Ionen und andere Oberflächenverunreinigungen zu entfernen, wurden verschiedene Nachbehandlungen angewendet. In einem ersten Schritt wurde das synthetisierte Material mit Reinstwasser bzw. verdünnter Salpetersäure gewaschen und anschließend bei 300°C bzw. 900°C nochmals an Luft kalziniert. Durch die Nachbehandlungen variierten die elektrochemischen Eigenschaften der Materialien deutlich: Während die bei 900°C nachbehandelten Materialien deaktiviert wurden, zeigten die bei 300°C nachbehandelten Materialien eine verbesserte, elektrochemische Leistungsfähigkeit. In der Struktur der säurebehandelten, deaktivierten Probe konnte eine Phasenseparation in Li-Mn-reichere Schichtoxide und Ni_6MnO_8 nachgewiesen werden. Die Ergebnisse lassen darauf schließen, dass die Kochsalzstruktur von Ni_6MnO_8 höchstwahrscheinlich die Li^+-Diffusionswege blockierte. Die bei 300°C behandelten Materialien erreichten hingegen spezifische Entladekapazitäten von bis zu 270 mAh g^{-1} (C/20). Durch die Studie wurde die Protonenkonzentration während des Waschens als kritischer Parameter identifiziert. Beispielsweise wurde die säurebehandelte Probe chemisch stark aktiviert, gleichzeitig zeigte sie jedoch eine erhöhte elektrochemische Instabilität. Dies konnte anhand der Ausbildung von lokalen Mn- und Ni-Anreicherungen und einer Spinell-ähnlichen Struktur in den

oberflächennahen Regionen der Primärpartikel erklärt werden, welche durch eine ausgeprägtere Auslaugung der Übergangsmetallionen aus der Struktur während der Säurebehandlung und der anschließenden Kalzinierung entstehen konnten. Die wasserbehandelte Probe zeigte einen moderaten Anstieg der spezifischen Entladekapazität und ein stabiles Zyklisierungsverhalten.

Das in dieser Studie gewonnene Wissen wurde in einer zweiten Studie mit der Aufbringung einer kohlenstoffhaltigen Oberflächenbeschichtung kombiniert. Dazu wurde ein HE-NMx-Material ohne Na^+-Verunreinigungen in einem weniger aggressiven Verfahren mit Zitronensäure behandelt. Die Behandlung wirkte sich positiv auf die Entladekapazität aus und ermöglichte eine kontrollierte Modifikation der Oberflächenchemie der Primärpartikel sowie die Abscheidung einer schützenden Oberflächenbeschichtung. Die chemische und strukturelle Charakterisierung bestätigte die Bildung einer kohlenstoffhaltigen Beschichtung sowie einer sauerstoffdefizitären, oberflächennahen Region in den Primärpartikeln. Die nachbehandelten HE-NMx Materialien zeigten eine verbesserte elektrochemische Leistungsfähigkeit nach der vollständigen, schrittweisen Aktivierung der Li_2MnO_3-Domänen im Vergleich zum unbehandelten Material und erreichten spezifische Entladekapazitäten von bis zu 247 mAh g^{-1} bei RT und bis zu 276 mAh g^{-1} bei 40°C (beide C/10). Der leicht erhöhte Spannungsabfall bei den Materialien mit höherem Zitronensäure/HE-NMx-Anteil während des Zyklisierens konnte auf eine schnellere Transformation vom Schichtoxid in eine Spinell-artige Struktur zurückgeführt werden, die wahrscheinlich von den strukturellen Änderungen während der Nachbehandlung hervorgerufen wurde. Die höhere Nutzbarkeit der Materialien und die damit verbundene höhere Entladekapazität kompensierte jedoch den erhöhten Spannungsabfall und sorgte damit für eine Steigerung der spezifischen Energie für alle in dieser Studie behandelten Materialien.

Beide Studien demonstrierten den großen Einfluss von Oberflächenmodifikationen auf die strukturelle Stabilität und die elektrochemische Leistungsfähigkeit von LRLO-Materialien haben. Weiterhin konnte gezeigt werden, dass über die Auswahl der Syntheseroute kontrolliert werden kann, ob die oberflächennahen Regionen entweder formal sauerstoffdefizitär oder sauerstoffreich sind. Eine direkte Korrelation zwischen der formalen Sauerstoffstöchiometrie, den strukturellen Informationen aus den Ergebnissen der Pulverdiffraktometrie und den elektrochemischen Eigenschaften konnte für die untersuchten Proben nicht beobachtet werden.

Die Skalierbarkeit der entwickelten Syntheserouten wurde durch die erfolgreiche Synthese von 5 kg HE-NMx-Material demonstriert, welches eine initiale Entladekapazität von 246 mAh g^{-1} und einen Erhalt von 80 % der Ausgangskapazität nach circa 500 Zyklen bei 1C aufweisen konnte.

In dieser Arbeit wurde gezeigt, dass die Li^+-Verteilung während der thermischen Lithiierung einen kritischen Parameter darstellt, der insbesondere die chemische und strukturelle Homogenität auf Partikelebene beeinflussen kann. Die chemische Homogenität spiegelte sich zudem direkt in der elektrochemischen Performance der HE-NMx-Materialien wieder. Die elektrochemischen Eigenschaften und die strukturelle Stabilität der HE-NMx-Materialien während des Zyklisierens sind zudem stark abhängig von den angewendeten Oberflächen-modifikationsstrategien. Korrelative SEM-Raman Mikroskopie wurde für die hauseigenen Geräte entwickelt und zur Identifizierung von möglichen strukturellen Inhomogenitäten in den Sekundärpartikeln und für die Alterungsanalyse genutzt. Abschließend wurde die Skalierbarkeit der verwendeten Syntheserouten bestätigt.

Das hochskalierte HE-NMx-Material wird nun in einem nächsten Schritt genutzt, um es in anwendungsnahen Zelltypen zu untersuchen. Die hergestellte Menge an Material erlaubt die Produktion von doppelseitig-beschichteten Elektroden auf einer kleineren Pilotanlage, um im Anschluss mehrfach gestapelte Pouch-Zellen zu bauen. Dieser Schritt ist besonders für die Materialentwicklung wichtig und beinhaltet zum Beispiel die Optimierung der Balancierung zwischen Anode und Kathode im Hinblick auf den initialen, hohen und irreversiblen Kapazitätsverlust von HE-NMx-Materialien.

Auf Materialebene sind neue Fragen in Bezug auf die weitere Optimierung des thermischen Lithiierungsprozesses hinzugekommen, die in Zukunft beantwortet werden müssen. Diese fokussieren sich in erster Linie auf die Partikelarchitektur und die verwendete chemische Zusammensetzung. Die Partikelarchitektur muss zur Erhöhung der Klopfdichte der Materialien weiter optimiert werden. Dies impliziert ebenfalls den Einfluss der Sekundärpartikeldichte, der Primärpartikelgröße und die Anisotropie der Kristallite. Eine weitergehende, mechanistische Untersuchung der thermischen Lithiierung in Bezug auf die Li^+-Zugänglichkeit in die Sekundärstruktur von sphärischen Präkursorpartikeln ist ebenfalls von Belang, um die idealen Präkursoreigenschaften für homogene LRLO-Materialien zu erforschen. Dazu gehören beispielsweise eine optimale Porosität des Präkursors oder dessen chemische Zusammensetzung (z.B. Karbonat- oder Hydroxid-basierte Materialien).

6. References

[1] *State of the Global Climate 2021,* World Meteorological Organization (Ed.) **2022,** ISBN: 978-92-63-11290-3, https://library.wmo.int/doc_num.php?explnum_id=11178 (visited on 10/24/2022).

[2] S. Kigle, M. Ebner, A. Guminski, *Energies* **2022**, *15*, 1334, DOI: 10.3390/en15041334.

[3] H.-K. Bartholdsen, A. Eidens, K. Löffler, F. Seehaus, F. Wejda, T. Burandt, P.-Y. Oei, C. Kemfert, C. Hirschhausen, *Energies* **2019**, *12*, 2988, DOI: 10.3390/en12152988.

[4] A. Guminski, C. Fiedler, S. Kigle, C. Pellinger, P. Dossow, K. Ganz, F. Jetter, T. Kern, T. Limmer, A. Murmann, J. Reinhard, T. Schmidt-Achert, S. von Roon, *eXtremOS Summary Report,* Forschungsstelle für Energiewirtschaft e.V. (Ed.) **2021,** DOI: 10.34805/FFE-24-21 (visited on 10/24/2022).

[5] A. Yoshino, *Angew. Chem. Int. Ed.* **2012**, *51*, 5798, DOI: 10.1002/anie.201105006.

[6] D. A. Corrigan, *Electrochem. Soc. Interface* **2022**, *31*, 63, DOI: 10.1149/2.F09223IF.

[7] D. Castelvecchi, E. Stoye, *Nature* **2019**, *574*, 308, DOI: 10.1038/d41586-019-02965-y.

[8] J. Dunn, M. Slattery, A. Kendall, H. Ambrose, S. Shen, *Environ. Sci. Technol.* **2021**, *55*, 5189, DOI: 10.1021/acs.est.0c07030.

[9] Y. Zhao, O. Pohl, A. I. Bhatt, G. E. Collis, P. J. Mahon, T. Rüther, A. F. Hollenkamp, *Sustain. Chem.* **2021**, *2*, 167, DOI: 10.3390/suschem2010011.

[10] S. Lee, A. Manthiram, *ACS Energy Lett.* **2022**, *7*, 3058, DOI: 10.1021/acsenergylett.2c01553.

[11] B. E. Murdock, K. E. Toghill, N. Tapia-Ruiz, *Adv. Energy Mater.* **2021**, *11*, 2102028, DOI: 10.1002/aenm.202102028.

[12] M. J. Smith, F. M. Gray, *J. Chem. Educ.* **2010**, *87*, 162, DOI: 10.1021/ed800053u.

[13] K. Schmidt-Rohr, *J. Chem. Educ.* **2018**, *95*, 1801, DOI: 10.1021/acs.jchemed.8b00479.

[14] M. Winter, R. J. Brodd, *Chem. Rev.* **2004**, *104*, 4245, DOI: 10.1021/cr020730k.

[15] C. H. Hamann, W. Vielstich, *Elektrochemie*, Wiley-VCH-Verlag GmbH & Co. KGaA, Weinheim, **2005**.

[16] C. Julien, A. Mauger, A. Vijh, K. Zaghib, *Lithium Batteries*, Springer International Publishing, **2016**.

[17] J. Song, K. Xu, N. Liu, D. Reed, X. Li, *Mater. Today* **2021**, *45*, 191, DOI: 10.1016/j.mattod.2020.12.003.

[18] Y. Liang, C.-Z. Zhao, H. Yuan, Y. Chen, W. Zhang, J.-Q. Huang, D. Yu, Y. Liu, M.-M. Titirici, Y.-L. Chueh, H. Yu, Q. Zhang, *InfoMat* **2019**, *1*, 6, DOI: 10.1002/inf2.12000.

[19] C. Liu, Z. G. Neale, G. Cao, *Mater. Today* **2016**, *19*, 109, DOI: 10.1016/j.mattod.2015.10.009.

[20] M. Winter, J. O. Besenhard, M. E. Spahr, P. Novák, *Adv. Mater.* **1998**, *10*, 725, DOI: 10.1002/(SICI)1521-4095(199807)10:10<725::AID-ADMA725>3.0.CO;2-Z.

[21] J. M. Tarascon, M. Armand, *Nature* **2001**, *414*, 359, DOI: 10.1038/35104644.

[22] Y. Makimura, T. Ohzuku in *Encyclopedia of electrochemical power sources* (Ed.: J. Garche), Elsevier, Amsterdam, **2009**, pp. 249–257.

[23] M. Lazzari, B. Scrosati, *J. Electrochem. Soc.* **1980**, *127*, 773, DOI: 10.1149/1.2129753.

[24] B. Scrosati, *J. Electrochem. Soc.* **1992**, *139*, 2776, DOI: 10.1149/1.2068978.

[25] A. Mauger, C. M. Julien, J. B. Goodenough, K. Zaghib, *J. Electrochem. Soc.* **2020**, *167*, 70507, DOI: 10.1149/2.0072007JES.

[26] K. Xu, *Chem. Rev.* **2004**, *104*, 4303, DOI: 10.1021/cr030203g.

[27] M. Armand, P. Axmann, D. Bresser, M. Copley, K. Edström, C. Ekberg, D. Guyomard, B. Lestriez, P. Novák, M. Petranikova, W. Porcher, S. Trabesinger, M. Wohlfahrt-Mehrens, H. Zhang, *J. Power Sources* **2020**, *479*, 228708, DOI: 10.1016/j.jpowsour.2020.228708.

[28] H. Zhang, Y. Yang, H. Xu, L. Wang, X. Lu, X. He, *InfoMat* **2022**, *4*, e12228, DOI: 10.1002/inf2.12228.

[29] M. Heß, P. Novák, *Electrochim. Acta* **2013**, *106*, 149, DOI: 10.1016/j.electacta.2013.05.056.

[30] S. J. An, J. Li, C. Daniel, D. Mohanty, S. Nagpure, D. L. Wood, *Carbon* **2016**, *105*, 52, DOI: 10.1016/j.carbon.2016.04.008.

[31] J. R. Dahn, T. Zheng, Y. Liu, J. S. Xue, *Science* **1995**, *270*, 590, DOI: 10.1126/science.270.5236.590.

[32] P. U. Nzereogu, A. D. Omah, F. I. Ezema, E. I. Iwuoha, A. C. Nwanya, *Appl. Surf. Sci. Adv.* **2022**, *9*, 100233, DOI: 10.1016/j.apsadv.2022.100233.

[33] C.-M. Park, J.-H. Kim, H. Kim, H.-J. Sohn, *Chem. Soc. Rev.* **2010**, *39*, 3115, DOI: 10.1039/B919877F.

[34] A. Ghosh, F. Ghamouss, *Front. Mater.* **2020**, *7,* DOI: 10.3389/fmats.2020.00186.

[35] X. Sun, P. V. Radovanovic, B. Cui, *New J. Chem.* **2015**, *39*, 38, DOI: 10.1039/C4NJ01390E.

[36] P. Li, H. Kim, S.-T. Myung, Y.-K. Sun, *Energy Storage Mater.* **2021**, *35*, 550, DOI: 10.1016/j.ensm.2020.11.028.

[37] J. Li, J. R. Dahn, *J. Electrochem. Soc.* **2007**, *154*, A156, DOI: 10.1149/1.2409862.

[38] K. Feng, M. Li, W. Liu, A. G. Kashkooli, X. Xiao, M. Cai, Z. Chen, *Small* **2018**, *14*, 1702737, DOI: 10.1002/smll.201702737.

[39] F. Luo, B. Liu, J. Zheng, G. Chu, K. Zhong, H. Li, X. Huang, L. Chen, *J. Electrochem. Soc.* **2015**, *162*, A2509-A2528, DOI: 10.1149/2.0131514jes.

[40] G. G. Eshetu, H. Zhang, X. Judez, H. Adenusi, M. Armand, S. Passerini, E. Figgemeier, *Nat. Commun.* **2021**, *12*, 5459, DOI: 10.1038/s41467-021-25334-8.

[41] S. S. Zhang, *J. Power Sources* **2006**, *162*, 1379, DOI: 10.1016/j.jpowsour.2006.07.074.

[42] X. Fan, C. Wang, *Chem. Soc. Rev.* **2021**, *50*, 10486, DOI: 10.1039/d1cs00450f.

[43] J. Kalhoff, G. G. Eshetu, D. Bresser, S. Passerini, *ChemSusChem* **2015**, *8*, 2154, DOI: 10.1002/cssc.201500284.

[44] P. Arora, Z. J. Zhang, *Chem. Rev.* **2004**, *104*, 4419, DOI: 10.1021/cr020738u.

[45] M. F. Lagadec, R. Zahn, V. Wood, *Nat. Energy* **2019**, *4*, 16, DOI: 10.1038/s41560-018-0295-9.

[46] A. Li, A. C. Y. Yuen, W. Wang, I. M. de Cachinho Cordeiro, C. Wang, T. B. Y. Chen, J. Zhang, Q. N. Chan, G. H. Yeoh, *Molecules* **2021**, *26,* DOI: 10.3390/molecules26020478.

[47] N. Nitta, F. Wu, J. T. Lee, G. Yushin, *Mater. Today* **2015**, *18*, 252, DOI: 10.1016/j.mattod.2014.10.040.

[48] L. Yang, K. Yang, J. Zheng, K. Xu, K. Amine, F. Pan, *Chem. Soc. Rev.* **2020**, *49*, 4667, DOI: 10.1039/d0cs00137f.

[49] C. Julien, A. Mauger, K. Zaghib, H. Groult, *Inorganics* **2014**, *2*, 132, DOI: 10.3390/inorganics2010132.

[50] K. Zaghib, A. Guerfi, P. Hovington, A. Vijh, M. Trudeau, A. Mauger, J. B. Goodenough, C. M. Julien, *J. Power Sources* **2013**, *232*, 357, DOI: 10.1016/j.jpowsour.2012.12.095.

[51] D. Shanmukaraj, R. Murugan, *Ionics* **2004**, *10*, 88, DOI: 10.1007/BF02410312.

[52] A. Mauger, C. Julien, *Batteries* **2018**, *4*, 39, DOI: 10.3390/batteries4030039.

[53] A. K. Padhi, K. S. Nanjundaswamy, C. Masquelier, S. Okada, J. B. Goodenough, *J. Electrochem. Soc.* **1997**, *144*, 1609, DOI: 10.1149/1.1837649.

[54] D. Morgan, A. van der Ven, G. Ceder, *Electrochem. Solid-State Lett.* **2004**, *7*, A30, DOI: 10.1149/1.1633511.

[55] F. Yu, L. Zhang, Y. Li, Y. An, M. Zhu, B. Dai, *RSC Adv.* **2014**, *4*, 54576, DOI: 10.1039/C4RA10899J.

[56] M. L. Trudeau, D. Laul, R. Veillette, A. M. Serventi, A. Mauger, C. M. Julien, K. Zaghib, *J. Power Sources* **2011**, *196*, 7383, DOI: 10.1016/j.jpowsour.2011.04.003.

[57] M. Hadouchi, T. Koketsu, Z. Hu, J. Ma, *Battery Energy* **2022**, *1*, 20210010, DOI: 10.1002/bte2.20210010.

[58] Y. Huang, Y. Dong, S. Li, J. Lee, C. Wang, Z. Zhu, W. Xue, Y. Li, J. Li, *Adv. Energy Mater.* **2021**, *11*, 2000997, DOI: 10.1002/aenm.202000997.

[59] M. Dalkilic, A. Schmidt, T. D. Schladt, P. Axmann, M. Wohlfahrt-Mehrens, M. Lindén, *J. Electrochem. Soc.* **2022**, *169*, 120501, DOI: 10.1149/1945-7111/aca360.

[60] Y.-K. Sun, D.-J. Lee, Y. J. Lee, Z. Chen, S.-T. Myung, *ACS Appl. Mater. Interfaces* **2013**, *5*, 11434, DOI: 10.1021/am403684z.

[61] R. A. House, H. Y. Playford, R. I. Smith, J. Holter, I. Griffiths, K.-J. Zhou, P. G. Bruce, *Energy Environ. Sci.* **2022**, *15*, 376, DOI: 10.1039/D1EE02237G.

[62] P. Axmann, G. Gabrielli, M. Wohlfahrt-Mehrens, *J. Power Sources* **2016**, *301*, 151, DOI: 10.1016/j.jpowsour.2015.10.010.

[63] M. Bianchini, F. Fauth, E. Suard, J. B. Leriche, C. Masquelier, L. Croguennec, *Acta Cryst. B* **2015**, *71*, 688, DOI: 10.1107/S2052520615017199.

[64] J. Sottmann, V. Pralong, N. Barrier, C. Martin, *J. Appl. Crystallogr.* **2019**, *52*, 485, DOI: 10.1107/S1600576719000773.

[65] K. Amine, H. Tukamoto, H. Yasuda, Y. Fujita, *J. Power Sources* **1997**, *68*, 604, DOI: 10.1016/S0378-7753(96)02590-6.

[66] H. Kawai, M. Nagata, H. Kageyama, H. Tukamoto, A. R. West, *Electrochim. Acta* **1999**, *45*, 315, DOI: 10.1016/S0013-4686(99)00213-3.

[67] M. P. Pico, I. Álvarez-Serrano, M. L. López, M. L. Veiga, *Dalton Trans.* **2014**, *43*, 14787, DOI: 10.1039/c4dt01809e.

[68] L. Wang, H. Li, X. Huang, E. Baudrin, *Solid State Ion.* **2011**, *193*, 32, DOI: 10.1016/j.ssi.2011.04.007.

[69] H. Sun, A. Hu, S. Spence, C. Kuai, D. Hou, L. Mu, J. Liu, L. Li, C. Sun, S. Sainio, D. Nordlund, W. Luo, Y. Huang, F. Lin, *Adv. Funct. Mater.* **2022**, *32*, 2112279, DOI: 10.1002/adfm.202112279.

[70] G. Liang, V. K. Peterson, K. W. See, Z. Guo, W. K. Pang, *J. Mater. Chem. A* **2020**, *8*, 15373, DOI: 10.1039/D0TA02812F.

[71] J. H. Yang, H. Kim, G. Ceder, *Molecules* **2021**, *26*, 3173, DOI: 10.3390/molecules26113173.

[72] E. Rossen, C. Jones, J. R. Dahn, *Solid State Ion.* **1992**, *57*, 311, DOI: 10.1016/0167-2738(92)90164-K.

[73] M. M. Thackeray, K. Amine, *Nat. Energy* **2021**, *6*, 933, DOI: 10.1038/s41560-021-00860-3.

[74] C. M. Julien, A. Mauger, *Energies* **2020**, *13*, 6363, DOI: 10.3390/en13236363.

[75] W. D. Johnston, R. R. Heikes, D. Sestrich, *J. Phys. Chem. Solids* **1958**, *7*, 1, DOI: 10.1016/0022-3697(58)90175-6.

[76] K. Mizushima, P. C. Jones, P. J. Wiseman, J. B. Goodenough, *Mater. Res. Bull.* **1980**, *15*, 783, DOI: 10.1016/0025-5408(80)90012-4.

[77] J. R. Dahn, U. von Sacken, C. A. Michal, *Solid State Ion.* **1990**, *44*, 87, DOI: 10.1016/0167-2738(90)90049-W.

[78] W. Li, J. Reimers, J. R. Dahn, *Solid State Ion.* **1993**, *67*, 123, DOI: 10.1016/0167-2738(93)90317-V.
[79] C. Delmas, J. P. Pérès, A. Rougier, A. Demourgues, F. Weill, A. Chadwick, M. Broussely, F. Perton, P. Biensan, P. Willmann, *J. Power Sources* **1997**, *68*, 120, DOI: 10.1016/S0378-7753(97)02664-5.
[80] M. Bianchini, M. Roca-Ayats, P. Hartmann, T. Brezesinski, J. Janek, *Angew. Chem. Int. Ed.* **2019**, *58*, 10434, DOI: 10.1002/anie.201812472.
[81] C. Delmas, D. Carlier, M. Guignard, *Adv. Energy Mater.* **2021**, *11*, 2001201, DOI: 10.1002/aenm.202001201.
[82] Z. Lu, D. D. MacNeil, J. R. Dahn, *Electrochem. Solid-State Lett.* **2001**, *4*, A200, DOI: 10.1149/1.1413182.
[83] T. Ohzuku, Y. Makimura, *Chem. Lett.* **2001**, *30*, 642, DOI: 10.1246/cl.2001.642.
[84] T. Ohzuku, Y. Makimura, *Chem. Lett.* **2001**, *30*, 744, DOI: 10.1246/cl.2001.744.
[85] S. Madhavi, G. Subba Rao, B. Chowdari, S. Li, *J. Power Sources* **2001**, *93*, 156, DOI: 10.1016/S0378-7753(00)00559-0.
[86] M. Broussely, P. Blanchard, P. Biensan, J. Planchat, K. Nechev, R. Staniewicz, *J. Power Sources* **2003**, *119-121*, 859, DOI: 10.1016/S0378-7753(03)00188-5.
[87] T. Nonaka, C. Okuda, Y. Seno, H. Nakano, K. Koumoto, Y. Ukyo, *J. Power Sources* **2006**, *162*, 1329, DOI: 10.1016/j.jpowsour.2006.09.003.
[88] T. Sasaki, T. Nonaka, H. Oka, C. Okuda, Y. Itou, Y. Kondo, Y. Takeuchi, Y. Ukyo, K. Tatsumi, S. Muto, *J. Electrochem. Soc.* **2009**, *156*, A289, DOI: 10.1149/1.3076136.
[89] H.-J. Noh, S. Youn, C. S. Yoon, Y.-K. Sun, *J. Power Sources* **2013**, *233*, 121, DOI: 10.1016/j.jpowsour.2013.01.063.
[90] N. Voronina, Y.-K. Sun, S.-T. Myung, *ACS Energy Lett.* **2020**, *5*, 1814, DOI: 10.1021/acsenergylett.0c00742.
[91] Y. Makimura, T. Ohzuku, *J. Power Sources* **2003**, *119-121*, 156, DOI: 10.1016/S0378-7753(03)00170-8.
[92] M. E. Spahr, P. Novák, B. Schnyder, O. Haas, R. Nesper, *J. Electrochem. Soc.* **1998**, *145*, 1113, DOI: 10.1149/1.1838425.
[93] D. Caurant, N. Baffler, V. Bianchi, G. Grégoire, S. Bach, *J. Mater. Chem.* **1996**, *6*, 1149, DOI: 10.1039/JM9960601149.
[94] W.-S. Yoon, Y. Paik, X.-Q. Yang, M. Balasubramanian, J. McBreen, C. P. Grey, *Electrochem. Solid-State Lett.* **2002**, *5*, A263, DOI: 10.1149/1.1513001.
[95] J. Reed, G. Ceder, *Electrochem. Solid-State Lett.* **2002**, *5*, A145, DOI: 10.1149/1.1480135.
[96] B. Ammundsen, J. Paulsen, *Adv. Mater.* **2001**, *13*, 943, DOI: 10.1002/1521-4095(200107)13:12/13<943::AID-ADMA943>3.0.CO;2-J.
[97] Y. S. Meng, G. Ceder, C. P. Grey, W.-S. Yoon, Y. Shao-Horn, *Electrochem. Solid-State Lett.* **2004**, *7*, A155-A158, DOI: 10.1149/1.1718211.
[98] R. D. Shannon, *Acta Cryst. A* **1976**, *32*, 751, DOI: 10.1107/S0567739476001551.
[99] A. van der Ven, G. Ceder, *Electrochem. Commun.* **2004**, *6*, 1045, DOI: 10.1016/j.elecom.2004.07.018.
[100] Z. Hu, J. Zheng, C. Xin, G. Teng, Y. Zuo, F. Pan, *J. Phys. Chem. C* **2018**, *122*, 4125, DOI: 10.1021/acs.jpcc.7b10968.
[101] W.-S. Yoon, S. Iannopollo, C. P. Grey, D. Carlier, J. Gorman, J. Reed, G. Ceder, *Electrochem. Solid-State Lett.* **2004**, *7*, A167, DOI: 10.1149/1.1737711.
[102] J. Bréger, N. Dupré, P. J. Chupas, P. L. Lee, T. Proffen, J. B. Parise, C. P. Grey, *J. Am. Chem. Soc.* **2005**, *127*, 7529, DOI: 10.1021/ja050697u.
[103] J. Bréger, M. Jiang, N. Dupré, Y. S. Meng, Y. Shao-Horn, G. Ceder, C. P. Grey, *J. Solid State Chem.* **2005**, *178*, 2575, DOI: 10.1016/j.jssc.2005.05.027.
[104] Z. Lu, L. Y. Beaulieu, R. A. Donaberger, C. L. Thomas, J. R. Dahn, *J. Electrochem. Soc.* **2002**, *149*, A778, DOI: 10.1149/1.1471541.
[105] K. Kang, Y. S. Meng, J. Bréger, C. P. Grey, G. Ceder, *Science* **2006**, *311*, 977, DOI: 10.1126/science.1122152.
[106] H. Kobayashi, Y. Arachi, H. Kageyama, H. Sakaebe, K. Tatsumi, D. Mori, R. Kanno, T. Kamiyama, *Solid State Ion.* **2004**, *175*, 221, DOI: 10.1016/j.ssi.2003.12.027.
[107] A. Rougier, P. Gravereau, C. Delmas, *J. Electrochem. Soc.* **1996**, *143*, 1168, DOI: 10.1149/1.1836614.
[108] S.-T. Myung, S. Komaba, N. Hirosaki, K. Hosoya, N. Kumagai, *J. Power Sources* **2005**, *146*, 645, DOI: 10.1016/j.jpowsour.2005.03.083.
[109] K. A. Kurilenko, O. A. Shlyakhtin, O. A. Brylev, O. A. Drozhzhin, *Electrochim. Acta* **2015**, *152*, 255, DOI: 10.1016/j.electacta.2014.11.045.
[110] N. Yabuuchi, Y.-C. Lu, A. N. Mansour, T. Kawaguchi, Y. Shao-Horn, *Electrochem. Solid-State Lett.* **2010**, *13*, A158, DOI: 10.1149/1.3479664.
[111] E. McCalla, J. Li, A. W. Rowe, J. R. Dahn, *J. Electrochem. Soc.* **2014**, *161*, A606, DOI: 10.1149/2.083404jes.
[112] N. Dupré, J.-F. Martin, J. Oliveri, P. Soudan, A. Yamada, R. Kanno, D. Guyomard, *J. Power Sources* **2011**, *196*, 4791, DOI: 10.1016/j.jpowsour.2010.07.049.
[113] N. Yabuuchi, Y.-C. Lu, A. N. Mansour, S. Chen, Y. Shao-Horn, *J. Electrochem. Soc.* **2010**, *158*, A192, DOI: 10.1149/1.3526309.
[114] Y. Hinuma, Y. S. Meng, K. Kang, G. Ceder, *Chem. Mater.* **2007**, *19*, 1790, DOI: 10.1021/cm062903i.

[115] T. Gao, G. Yang, B. Yang, Y. Dai, *J. Alloys Compd.* **2016**, *680*, 694, DOI: 10.1016/j.jallcom.2016.04.187.
[116] N. Phattharasupakun, M. M. E. Cormier, Y. Liu, C. Geng, E. Zsoldos, I. Hamam, A. Liu, M. B. Johnson, M. Sawangphruk, J. R. Dahn, *J. Electrochem. Soc.* **2021**, *168*, 110502, DOI: 10.1149/1945-7111/ac3157.
[117] X. Bian, R. Zhang, X. Yang, *Inorg. Chem.* **2020**, *59*, 17535, DOI: 10.1021/acs.inorgchem.0c02766.
[118] L. Guo, X. Tan, D. Mao, T. Zhao, L. Song, Y. Liu, X. Kang, H. Wang, L. Sun, W. Chu, *Electrochim. Acta* **2021**, *370*, 137808, DOI: 10.1016/j.electacta.2021.137808.
[119] T. Ohzuku, M. Nagayama, K. Tsuji, K. Ariyoshi, *J. Mater. Chem.* **2011**, *21*, 10179, DOI: 10.1039/c0jm04325g.
[120] S.-T. Myung, S. Komaba, K. Kurihara, K. Hosoya, N. Kumagai, Y.-K. Sun, I. Nakai, M. Yonemura, T. Kamiyama, *Chem. Mater.* **2006**, *18*, 1658, DOI: 10.1021/cm052704j.
[121] H. Zhuo, Y. Zhang, D. Wang, C. He, C. Zhu, Q. Zhang, C. Li, L. Sun, J. Liu, S. Chen, *Electrochim. Acta* **2014**, *149*, 42, DOI: 10.1016/j.electacta.2014.10.078.
[122] O. A. Shlyakhtin, S.-H. Choi, Y. S. Yoon, Y.-J. Oh, *J. Power Sources* **2005**, *141*, 122, DOI: 10.1016/j.jpowsour.2004.08.052.
[123] B. Qiu, M. Zhang, L. Wu, J. Wang, Y. Xia, D. Qian, H. Liu, S. Hy, Y. Chen, K. An, Y. Zhu, Z. Liu, Y. S. Meng, *Nat. Commun.* **2016**, *7*, 12108, DOI: 10.1038/ncomms12108.
[124] W. Zuo, M. Luo, X. Liu, J. Wu, H. Liu, J. Li, M. Winter, R. Fu, W. Yang, Y. Yang, *Energy Environ. Sci.* **2020**, *13*, 4450, DOI: 10.1039/D0EE01694B.
[125] J. R. Rumble (Ed.) *CRC handbook of chemistry and physics*, CRC Press, Boca Raton, London, New York, **2022**.
[126] Z. Lu, Z. Chen, J. R. Dahn, *Chem. Mater.* **2003**, *15*, 3214, DOI: 10.1021/cm030194s.
[127] Z. Lu, D. D. MacNeil, J. R. Dahn, *Electrochem. Solid-State Lett.* **2001**, *4*, A191, DOI: 10.1149/1.1407994.
[128] J. Zheng, P. Xu, M. Gu, J. Xiao, N. D. Browning, P. Yan, C. Wang, J.-G. Zhang, *Chem. Mater.* **2015**, *27*, 1381, DOI: 10.1021/cm5045978.
[129] M. M. Thackeray, C. S. Johnson, J. T. Vaughey, N. Li, S. A. Hackney, *J. Mater. Chem.* **2005**, *15*, 2257, DOI: 10.1039/b417616m.
[130] H. Koga, L. Croguennec, P. Mannessiez, M. Ménétrier, F. Weill, L. Bourgeois, M. Duttine, E. Suard, C. Delmas, *J. Phys. Chem. C* **2012**, *116*, 13497, DOI: 10.1021/jp301879x.
[131] J.-S. Kim, C. S. Johnson, J. T. Vaughey, M. M. Thackeray, S. A. Hackney, W. Yoon, C. P. Grey, *Chem. Mater.* **2004**, *16*, 1996, DOI: 10.1021/cm0306461.
[132] Y. S. Meng, G. Ceder, C. P. Grey, W.-S. Yoon, M. Jiang, J. Bréger, Y. Shao-Horn, *Chem. Mater.* **2005**, *17*, 2386, DOI: 10.1021/cm047779m.
[133] A. Boulineau, L. Croguennec, C. Delmas, F. Weill, *Chem. Mater.* **2009**, *21*, 4216, DOI: 10.1021/cm900998n.
[134] R. A. House, G. J. Rees, M. A. Pérez-Osorio, J.-J. Marie, E. Boivin, A. W. Robertson, A. Nag, M. Garcia-Fernandez, K.-J. Zhou, P. G. Bruce, *Nat. Energy* **2020**, *5*, 777, DOI: 10.1038/s41560-020-00697-2.
[135] A. S. Menon, S. Khalil, D. O. Ojwang, K. Edström, C. P. Gomez, W. R. Brant, *Dalton Trans.* **2022**, *51*, 4435, DOI: 10.1039/d2dt00104g.
[136] D.-H. Seo, J. Lee, A. Urban, R. Malik, S. Kang, G. Ceder, *Nat. Chem.* **2016**, *8*, 692, DOI: 10.1038/nchem.2524.
[137] F. Schipper, P. K. Nayak, E. M. Erickson, F. Amalraj, O. Srur-Lavi, T. R. Penki, M. Talianker, J. Grinblat, H. Sclar, O. Breuer, C. M. Julien, N. Munichandraiah, D. Kovacheva, M. Dixit, D. T. Major, B. Markovsky, D. Aurbach, *Inorganics* **2017**, *5*, 32, DOI: 10.3390/inorganics5020032.
[138] A. R. Armstrong, M. Holzapfel, P. Novák, C. S. Johnson, S.-H. Kang, M. M. Thackeray, P. G. Bruce, *J. Am. Chem. Soc.* **2006**, *128*, 8694, DOI: 10.1021/ja062027.
[139] A. D. Robertson, P. G. Bruce, *Chem. Commun.* **2002**, 2790, DOI: 10.1039/b207945c.
[140] A. D. Robertson, P. G. Bruce, *Chem. Mater.* **2003**, *15*, 1984, DOI: 10.1021/cm030047u.
[141] A. D. Robertson, P. G. Bruce, *Electrochem. Solid-State Lett.* **2004**, *7*, A294, DOI: 10.1149/1.1783114.
[142] N. Tran, L. Croguennec, M. Ménétrier, F. Weill, P. Biensan, C. Jordy, C. Delmas, *Chem. Mater.* **2008**, *20*, 4815, DOI: 10.1021/cm070435m.
[143] Z. Lu, J. R. Dahn, *J. Electrochem. Soc.* **2002**, *149*, A815, DOI: 10.1149/1.1480014.
[144] G. Assat, J.-M. Tarascon, *Nat. Energy* **2018**, *3*, 373, DOI: 10.1038/s41560-018-0097-0.
[145] P. Kalyani, S. Chitra, T. Mohan, S. Gopukumar, *J. Power Sources* **1999**, *80*, 103, DOI: 10.1016/S0378-7753(99)00066-X.
[146] H. Koga, L. Croguennec, M. Ménétrier, P. Mannessiez, F. Weill, C. Delmas, *J. Power Sources* **2013**, *236*, 250, DOI: 10.1016/j.jpowsour.2013.02.075.
[147] G. Assat, D. Foix, C. Delacourt, A. Iadecola, R. Dedryvère, J.-M. Tarascon, *Nat. Commun.* **2017**, *8*, 2219, DOI: 10.1038/s41467-017-02291-9.
[148] M. Okubo, A. Yamada, *ACS Appl. Mater. Interfaces* **2017**, *9*, 36463, DOI: 10.1021/acsami.7b09835.
[149] J. Chen, W. Deng, X. Gao, S. Yin, L. Yang, H. Liu, G. Zou, H. Hou, X. Ji, *ACS nano* **2021**, *15*, 6061, DOI: 10.1021/acsnano.1c00304.

[150] Z. Q. Deng, A. Manthiram, *J. Phys. Chem. C* **2011**, *115*, 7097, DOI: 10.1021/jp200375d.
[151] M. Saubanère, E. McCalla, J.-M. Tarascon, M.-L. Doublet, *Energy Environ. Sci.* **2016**, *9*, 984, DOI: 10.1039/C5EE03048J.
[152] M. Sathiya, K. Ramesha, G. Rousse, D. Foix, D. Gonbeau, A. S. Prakash, M. L. Doublet, K. Hemalatha, J.-M. Tarascon, *Chem. Mater.* **2013**, *25*, 1121, DOI: 10.1021/cm400193m.
[153] M. Sathiya, G. Rousse, K. Ramesha, C. P. Laisa, H. Vezin, M. T. Sougrati, M.-L. Doublet, D. Foix, D. Gonbeau, W. Walker, A. S. Prakash, M. Ben Hassine, L. Dupont, J.-M. Tarascon, *Nat. Mater.* **2013**, *12*, 827, DOI: 10.1038/nmat3699.
[154] E. McCalla, A. M. Abakumov, M. Saubanère, D. Foix, E. J. Berg, G. Rousse, M.-L. Doublet, D. Gonbeau, P. Novák, G. van Tendeloo, R. Dominko, J.-M. Tarascon, *Science* **2015**, *350*, 1516, DOI: 10.1126/science.aac8260.
[155] K. Luo, M. R. Roberts, N. Guerrini, N. Tapia-Ruiz, R. Hao, F. Massel, D. M. Pickup, S. Ramos, Y.-S. Liu, J. Guo, A. V. Chadwick, L. C. Duda, P. G. Bruce, *J. Am. Chem. Soc.* **2016**, *138*, 11211, DOI: 10.1021/jacs.6b05111.
[156] T. Teufl, B. Strehle, P. Müller, H. A. Gasteiger, M. A. Mendez, *J. Electrochem. Soc.* **2018**, *165*, A2718, DOI: 10.1149/2.0691811jes.
[157] A. T. S. Freiberg, M. K. Roos, J. Wandt, R. de Vivie-Riedle, H. A. Gasteiger, *J. Phys. Chem. A* **2018**, *122*, 8828, DOI: 10.1021/acs.jpca.8b08079.
[158] C. Genevois, H. Koga, L. Croguennec, M. Ménétrier, C. Delmas, F. Weill, *J. Phys. Chem. C* **2015**, *119*, 75, DOI: 10.1021/jp509388j.
[159] M. M. Rahman, F. Lin, *Matter* **2021**, *4*, 490, DOI: 10.1016/j.matt.2020.12.004.
[160] P. K. Nayak, E. M. Erickson, F. Schipper, T. R. Penki, N. Munichandraiah, P. Adelhelm, H. Sclar, F. Amalraj, B. Markovsky, D. Aurbach, *Adv. Energy Mater.* **2018**, *8*, 1702397, DOI: 10.1002/aenm.201702397.
[161] W. Hua, S. Wang, M. Knapp, S. J. Leake, A. Senyshyn, C. Richter, M. Yavuz, J. R. Binder, C. P. Grey, H. Ehrenberg, S. Indris, B. Schwarz, *Nat. Commun.* **2019**, *10*, 5365, DOI: 10.1038/s41467-019-13240-z.
[162] E. Hu, X. Yu, R. Lin, X. Bi, J. Lu, S. Bak, K.-W. Nam, H. L. Xin, C. Jaye, D. A. Fischer, K. Amine, X.-Q. Yang, *Nat. Energy* **2018**, *3*, 690, DOI: 10.1038/s41560-018-0207-z.
[163] F. Wu, A. R. Schür, G.-T. Kim, X. Dong, M. Künzel, T. Diemant, G. D'Orsi, E. Simonetti, M. de Francesco, M. Bellusci, G. B. Appetecchi, S. Passerini, *Energy Storage Mater.* **2021**, *42*, 826, DOI: 10.1016/j.ensm.2021.08.030.
[164] F. Wu, G.-T. Kim, T. Diemant, M. Künzel, A. R. Schür, X. Gao, B. Qin, D. Alwast, Z. Jusys, R. J. Behm, D. Geiger, U. Kaiser, S. Passerini, *Adv. Energy Mater.* **2020**, *10*, 2001830, DOI: 10.1002/aenm.202001830.
[165] J. Zhao, X. Zhang, Y. Liang, Z. Han, S. Liu, W. Chu, H. Yu, *ACS Energy Lett.* **2021**, *6*, 2552, DOI: 10.1021/acsenergylett.1c00750.
[166] F. Wu, G.-T. Kim, M. Künzel, H. Zhang, J. Asenbauer, D. Geiger, U. Kaiser, S. Passerini, *Adv. Energy Mater.* **2019**, *9*, 1902445, DOI: 10.1002/aenm.201902445.
[167] P. K. Nayak, J. Grinblat, M. Levi, E. Levi, S. Kim, J. W. Choi, D. Aurbach, *Adv. Energy Mater.* **2016**, *6*, 1502398, DOI: 10.1002/aenm.201502398.
[168] Y. Lee, H. Park, M. Cho, J. Ahn, W. Ko, J. Kang, Y. J. Choi, H. Kim, I. Park, W.-H. Ryu, J. Hong, J. Kim, *Adv. Funct. Mater.* **2022**, *32*, 2204354, DOI: 10.1002/adfm.202204354.
[169] J. Zheng, S. Myeong, W. Cho, P. Yan, J. Xiao, C. Wang, J. Cho, J.-G. Zhang, *Adv. Energy Mater.* **2017**, *7*, 1601284, DOI: 10.1002/aenm.201601284.
[170] S. Hy, H. Liu, M. Zhang, D. Qian, B.-J. Hwang, Y. S. Meng, *Energy Environ. Sci.* **2016**, *9*, 1931, DOI: 10.1039/C5EE03573B.
[171] N. Leifer, T. Penki, R. Nanda, J. Grinblat, S. Luski, D. Aurbach, G. Goobes, *Phys. Chem. Chem. Phys.* **2020**, *22*, 9098, DOI: 10.1039/d0cp00400f.
[172] A. S. Menon, S. Ulusoy, D. O. Ojwang, L. Riekehr, C. Didier, V. K. Peterson, G. Salazar-Alvarez, P. Svedlindh, K. Edström, C. P. Gomez, W. R. Brant, *ACS Appl. Energy Mater.* **2021**, *4*, 1924, DOI: 10.1021/acsaem.0c03027.
[173] J. M. Zheng, X. B. Wu, Y. Yang, *Electrochim. Acta* **2011**, *56*, 3071, DOI: 10.1016/j.electacta.2010.12.049.
[174] J. Zheng, M. Gu, A. Genc, J. Xiao, P. Xu, X. Chen, Z. Zhu, W. Zhao, L. Pullan, C. Wang, J.-G. Zhang, *Nano Lett.* **2014**, *14*, 2628, DOI: 10.1021/nl500486y.
[175] C. Janiak, E. Riedel, *Riedel, moderne anorganische Chemie*, De Gruyter, Berlin, Boston, **2012**.
[176] H. Dong, G. M. Koenig, *CrystEngComm* **2020**, *22*, 1514, DOI: 10.1039/C9CE00679F.
[177] T. Pan, J. Alvarado, J. Zhu, Y. Yue, H. L. Xin, D. Nordlund, F. Lin, M. M. Doeff, *J. Electrochem. Soc.* **2019**, *166*, A1964-A1971, DOI: 10.1149/2.0091910jes.
[178] M. Keppeler, H.-Y. Tran, W. Braunwarth, *Energy Technol.* **2021**, *9*, 2100132, DOI: 10.1002/ente.202100132.
[179] R. Schmuch, R. Wagner, G. Hörpel, T. Placke, M. Winter, *Nat. Energy* **2018**, *3*, 267, DOI: 10.1038/s41560-018-0107-2.
[180] S. Ahmed, P. A. Nelson, K. G. Gallagher, N. Susarla, D. W. Dees, *J. Power Sources* **2017**, *342*, 733, DOI: 10.1016/j.jpowsour.2016.12.069.
[181] J. Lamb, A. Manthiram, *Chem. Mater.* **2020**, *32*, 8431, DOI: 10.1021/acs.chemmater.0c02435.
[182] P. Barai, Z. Feng, H. Kondo, V. Srinivasan, *J. Phys. Chem. B* **2019**, *123*, 3291, DOI: 10.1021/acs.jpcb.8b12004.

[183] D. Wang, I. Belharouak, G. M. Koenig, G. Zhou, K. Amine, *J. Mater. Chem.* **2011**, *21*, 9290, DOI: 10.1039/C1JM11077B.
[184] F. Wang, P. Barai, O. Kahvecioglu, K. Z. Pupek, J. Bai, V. Srinivasan, *J. Mater. Res.* **2022**, *37*, 3197, DOI: 10.1557/s43578-022-00678-z.
[185] Tobias Teufl, Benjamin Bergner, Patent WO2021156124A1, **2021**.
[186] Z. D. Hao, X. Xu, H. Wang, J. Liu, H. Yan, *Nano* **2018**, *13*, 1830007, DOI: 10.1142/S1793292018300074.
[187] X. Zhang, R. Yu, Y. Huang, X. Wang, Y. Wang, B. Wu, Z. Liu, J. Chen, *ACS Sustain. Chem. Eng.* **2018**, *6*, 12969, DOI: 10.1021/acssuschemeng.8b02436.
[188] M. Gu, A. Genc, I. Belharouak, D. Wang, K. Amine, S. Thevuthasan, D. R. Baer, J.-G. Zhang, N. D. Browning, J. Liu, C. Wang, *Chem. Mater.* **2013**, *25*, 2319, DOI: 10.1021/cm4009392.
[189] Z. Fang, W. Li, B. Zhao, J. Bai, K. Li, H. Ma, X. Zhu, Y. Sun, *ACS Appl. Energy Mater.* **2021**, *4*, 10986, DOI: 10.1021/acsaem.1c01941.
[190] J. Liu, H. Chen, J. Xie, Z. Sun, N. Wu, B. Wu, *J. Power Sources* **2014**, *251*, 208, DOI: 10.1016/j.jpowsour.2013.11.055.
[191] H.-H. Ryu, N.-Y. Park, D. R. Yoon, U.-H. Kim, C. S. Yoon, Y.-K. Sun, *Adv. Energy Mater.* **2020**, *10*, 2000495, DOI: 10.1002/aenm.202000495.
[192] J. Helbig, T. Beuse, V. Siozios, T. Placke, M. Winter, R. Schmuch, *Electrochim. Acta* **2021**, *366*, 137413, DOI: 10.1016/j.electacta.2020.137413.
[193] J. Helbig, T. Beuse, V. Siozios, T. Placke, M. Winter, R. Schmuch, *J. Electrochem. Soc.* **2020**, *167*, 60519, DOI: 10.1149/1945-7111/ab8405.
[194] B. Strehle, J. Yoon, F. Friedrich, H. A. Gasteiger, *J. Electrochem. Soc.* **2022**, *169*, 60521, DOI: 10.1149/1945-7111/ac766c.
[195] S. Jo, J. Han, S. Seo, O.-S. Kwon, S. Choi, J. Zhang, H. Hyun, J. Oh, J. Kim, J. Chung, H. Kim, J. Wang, J. Bae, J. Moon, Y.-C. Park, M.-H. Hong, M. Kim, Y. Liu, I. Sohn, K. Jung, J. Lim, *Adv. Mater.* **2022**, e2207076, DOI: 10.1002/adma.202207076.
[196] X. Gou, Z. Hao, Z. Hao, G. Yang, Z. Yang, X. Zhang, Z. Yan, Q. Zhao, J. Chen, *Adv. Funct. Mater.* **2022**, *32*, 2112088, DOI: 10.1002/adfm.202112088.
[197] E. Boivin, N. Guerrini, R. A. House, J. G. Lozano, L. Jin, G. J. Rees, J. W. Somerville, C. Kuss, M. R. Roberts, P. G. Bruce, *Adv. Funct. Mater.* **2021**, *31*, 2003660, DOI: 10.1002/adfm.202003660.
[198] X. Ding, D. Luo, J. Cui, H. Xie, Q. Ren, Z. Lin, *Angew. Chem. Int. Ed.* **2020**, *59*, 7778, DOI: 10.1002/anie.202000628.
[199] Y. Zheng, L. Chen, Y. Su, J. Tan, L. Bao, Y. Lu, J. Wang, R. Chen, S. Chen, F. Wu, *J. Mater. Chem. A* **2017**, *5*, 24292, DOI: 10.1039/C7TA08735G.
[200] S. Han, B. Qiu, Z. Wei, Y. Xia, Z. Liu, *J. Power Sources* **2014**, *268*, 683, DOI: 10.1016/j.jpowsour.2014.06.106.
[201] H. Sclar, J. Sicklinger, E. M. Erickson, S. Maiti, J. Grinblat, M. Talianker, F. Amalraj Susai, L. Burstein, H. Beyer, L. Hartmann, G. Avruschenko, H. A. Gasteiger, B. Markovsky, D. Aurbach, *J. Electrochem. Soc.* **2020**, *167*, 110563, DOI: 10.1149/1945-7111/aba6cb.
[202] J. Zhang, Z. Lei, J. Wang, Y. NuLi, J. Yang, *ACS Appl. Mater. Interfaces* **2015**, *7*, 15821, DOI: 10.1021/acsami.5b02937.
[203] P. Oh, S. Myeong, W. Cho, M.-J. Lee, M. Ko, H. Y. Jeong, J. Cho, *Nano Lett.* **2014**, *14*, 5965, DOI: 10.1021/nl502980k.
[204] S.-H. Kang, C. S. Johnson, J. T. Vaughey, K. Amine, M. M. Thackeray, *J. Electrochem. Soc.* **2006**, *153*, A1186, DOI: 10.1149/1.2194764.
[205] S. Ramakrishnan, B. Park, J. Wu, W. Yang, B. D. McCloskey, *J. Am. Chem. Soc.* **2020**, *142*, 8522, DOI: 10.1021/jacs.0c02859.
[206] D. Y. Yu, K. Yanagida, *J. Electrochem. Soc.* **2011**, *158*, A1015, DOI: 10.1149/1.3609849.
[207] J. Sicklinger, H. Beyer, L. Hartmann, F. Riewald, C. Sedlmeier, H. A. Gasteiger, *J. Electrochem. Soc.* **2020**, *167*, 130507, DOI: 10.1149/1945-7111/abb6cb.
[208] K. Xu, S. Pang, Y. Wang, X. Shen, H. Wen, W. Wang, Y. Su, X. Xi, *J. Electrochem. Soc.* **2017**, *164*, A2348-A2354, DOI: 10.1149/2.0731712jes.
[209] B. Liu, *Int. J. Electrochem. Sci.* **2018**, 7578, DOI: 10.20964/2018.08.50.
[210] S. Pang, M. Zhu, K. Xu, X. Shen, H. Wen, Y. Su, G. Yang, X. Wu, S. Li, W. Wang, X. Xi, H. Wang, *J. Electrochem. Soc.* **2018**, *165*, A1897-A1902, DOI: 10.1149/2.1481809jes.
[211] L. Hartmann, C. H. Ching, T. Kipfer, M. Koch, H. A. Gasteiger, *J. Electrochem. Soc.* **2022**, *169*, 70516, DOI: 10.1149/1945-7111/ac7ef0.
[212] Z. Yang, H. Zhou, Z. Bao, J. Li, C. Yin, *J. Mater. Sci.: Mater. Electron.* **2019**, *30*, 19493, DOI: 10.1007/s10854-019-02315-8.
[213] M.-J. Wang, A.-F. Shao, F.-D. Yu, G. Sun, D.-M. Gu, Z.-B. Wang, *ACS Sustain. Chem. Eng.* **2019**, *7*, 12825, DOI: 10.1021/acssuschemeng.9b01719.

[214] E. M. Erickson, H. Sclar, F. Schipper, J. Liu, R. Tian, C. Ghanty, L. Burstein, N. Leifer, J. Grinblat, M. Talianker, J.-Y. Shin, J. K. Lampert, B. Markovsky, A. I. Frenkel, D. Aurbach, *Adv. Energy Mater.* **2017**, *7*, 1700708, DOI: 10.1002/aenm.201700708.
[215] T. Nakamura, H. Gao, K. Ohta, Y. Kimura, Y. Tamenori, K. Nitta, T. Ina, M. Oishi, K. Amezawa, *J. Mater. Chem. A* **2019**, *7*, 5009, DOI: 10.1039/C8TA12484A.
[216] S.-L. Cui, X. Zhang, X.-W. Wu, S. Liu, Z. Zhou, G.-R. Li, X.-P. Gao, *ACS Appl. Mater. Interfaces* **2020**, *12*, 47655, DOI: 10.1021/acsami.0c14979.
[217] Z. Ye, B. Zhang, T. Chen, Z. Wu, D. Wang, W. Xiang, Y. Sun, Y. Liu, Y. Liu, J. Zhang, Y. Song, X. Guo, *Angew. Chem. Int. Ed.* **2021**, *60*, 23248, DOI: 10.1002/anie.202107955.
[218] Z. Huang, T. Xiong, X. Lin, M. Tian, W. Zeng, J. He, M. Shi, J. Li, G. Zhang, L. Mai, S. Mu, *J. Power Sources* **2019**, *432*, 8, DOI: 10.1016/j.jpowsour.2019.05.069.
[219] H. Lee, S. B. Lim, J. Y. Kim, M. Jeong, Y. J. Park, W.-S. Yoon, *ACS Appl. Mater. Interfaces* **2018**, *10*, 10804, DOI: 10.1021/acsami.7b12722.
[220] J. Liao, Z. Zhang, W. Fan, Q. Wang, D. Liao, *Electrochim. Acta* **2022**, *405*, 139798, DOI: 10.1016/j.electacta.2021.139798.
[221] Z. Li, Q. Li, A. Zhang, W. Wen, L. Wang, Z. Wang, J. Wang, S. Lu, X. Li, Z. Wang, *New J. Chem.* **2019**, *43*, 18943, DOI: 10.1039/C9NJ04531G.
[222] Y. Lee, J. Lee, K. Y. Lee, J. Mun, J. K. Lee, W. Choi, *J. Power Sources* **2016**, *315*, 284, DOI: 10.1016/j.jpowsour.2016.03.024.
[223] D. Chen, F. Zheng, L. Li, M. Chen, X. Zhong, W. Li, L. Lu, *J. Power Sources* **2017**, *341*, 147, DOI: 10.1016/j.jpowsour.2016.11.020.
[224] C.-H. Jo, D.-H. Cho, H.-J. Noh, H. Yashiro, Y.-K. Sun, S. T. Myung, *Nano Res.* **2015**, *8*, 1464, DOI: 10.1007/s12274-014-0631-8.
[225] G. Sun, C. Zhao, F.-D. Yu, R. Yu, J. Wang, J. Zhou, G. Shao, X. Sun, Z.-B. Wang, *Nano Energy* **2021**, *79*, 105459, DOI: 10.1016/j.nanoen.2020.105459.
[226] M. Xu, Z. Chen, L. Li, H. Zhu, Q. Zhao, L. Xu, N. Peng, L. Gong, *J. Power Sources* **2015**, *281*, 444, DOI: 10.1016/j.jpowsour.2015.02.019.
[227] Y. Wu, J. Ming, L. Zhuo, Y. Yu, F. Zhao, *Electrochim. Acta* **2013**, *113*, 54, DOI: 10.1016/j.electacta.2013.09.042.
[228] C. Zhou, P. Wang, B. Zhang, J. Zheng, Y. Zhou, C. Huang, X. Xi, *J. Electrochem. Soc.* **2018**, *165*, A1648-A1655, DOI: 10.1149/2.0441809jes.
[229] U. Breddemann, E. M. Erickson, V. Davis, F. Schipper, M. Ellwanger, M. Daub, A. Hoffmann, C. Erk, B. Markovsky, D. Aurbach, I. Krossing, *ChemElectroChem* **2019**, *6*, 3337, DOI: 10.1002/celc.201900733.
[230] H.-S. Kim, M. Kong, K. Kim, I.-J. Kim, H.-B. Gu, *J. Power Sources* **2007**, *171*, 917, DOI: 10.1016/j.jpowsour.2007.06.028.
[231] Q. Xia, X. Zhao, M. Xu, Z. Ding, J. Liu, L. Chen, D. G. Ivey, W. Wei, *J. Mater. Chem. A* **2015**, *3*, 3995, DOI: 10.1039/C4TA05848H.
[232] Z. Zhao, M. Sun, T. Wu, J. Zhang, P. Wang, L. Zhang, C. Yang, C. Peng, H. Lu, *Nano-Micro Lett.* **2021**, *13*, 118, DOI: 10.1007/s40820-021-00643-1.
[233] S. Pang, K. Xu, Y. Wang, X. Shen, W. Wang, Y. Su, M. Zhu, X. Xi, *J. Power Sources* **2017**, *365*, 68, DOI: 10.1016/j.jpowsour.2017.08.077.
[234] B. Song, C. Zhou, Y. Chen, Z. Liu, M. O. Lai, J. Xue, L. Lu, *RSC Adv.* **2014**, *4*, 44244, DOI: 10.1039/C4RA04976D.
[235] T. Lin, T. U. Schulli, Y. Hu, X. Zhu, Q. Gu, B. Luo, B. Cowie, L. Wang, *Adv. Funct. Mater.* **2020**, *30*, 1909192, DOI: 10.1002/adfm.201909192.
[236] A. R. Kathribail, A. Rezqita, D. Lager, R. Hamid, Y. Surace, M. Berecibar, J. van Mierlo, A. Hubin, M. Jahn, J. Kahr, *Batteries* **2021**, *7*, 69, DOI: 10.3390/batteries7040069.
[237] J. Wu, H. Li, Y. Liu, Y. Ye, Y. Yang, *ACS Sustain. Chem. Eng.* **2022**, *10*, 6165, DOI: 10.1021/acssuschemeng.1c07221.
[238] J. Paulsen, H. Hong, J. Oh, Patent US10411258B2, **2019**.
[239] Z. Xin-wen, Z. Dan, W. Li-na, L. Qiao-yun, Z. Hong-xing, Z. Ke-li, *Wuhan Univ. J. Nat. Sci.* **2005**, *10*, 909, DOI: 10.1007/BF02832437.
[240] V. Sharova, A. Moretti, G. Giffin, D. Carvalho, S. Passerini, *C* **2017**, *3*, 22, DOI: 10.3390/c3030022.
[241] B. Lin, Z. Wen, X. Wang, Y. Liu, *J. Solid State Electrochem.* **2010**, *14*, 1807, DOI: 10.1007/s10008-010-1115-8.
[242] H. Li, H. Zhou, *Chem. Commun.* **2012**, *48*, 1201, DOI: 10.1039/C1CC14764A.
[243] W. Guo, C. Zhang, Y. Zhang, L. Lin, W. He, Q. Xie, B. Sa, L. Wang, D.-L. Peng, *Adv. Mater.* **2021**, *33*, e2103173, DOI: 10.1002/adma.202103173.
[244] T. Sata, *Ceram. Int.* **1998**, *24*, 53, DOI: 10.1016/S0272-8842(96)00077-6.
[245] E. McCalla, G. H. Carey, J. R. Dahn, *Solid State Ion.* **2012**, *219*, 11, DOI: 10.1016/j.ssi.2012.05.007.

[246] T. Zhao, S. Chen, R. Chen, L. Li, X. Zhang, M. Xie, F. Wu, *ACS Appl. Mater. Interfaces* **2014**, *6*, 21711, DOI: 10.1021/am506934j.
[247] C. M. Julien, M. Massot, *Mater. Sci. Eng. B* **2003**, *100*, 69, DOI: 10.1016/S0921-5107(03)00077-1.
[248] P. Lanz, C. Villevieille, P. Novák, *Electrochim. Acta* **2013**, *109*, 426, DOI: 10.1016/j.electacta.2013.07.130.
[249] M. C. Militello, S. W. Gaarenstroom, *Surf. Sci. Spectra* **2001**, *8*, 207, DOI: 10.1116/11.20020402.
[250] M. H. Rossouw, M. M. Thackeray, *Mater. Res. Bull.* **1991**, *26*, 463, DOI: 10.1016/0025-5408(91)90186-P.
[251] P. Strobel, B. Lambert-Andron, *J. Solid State Chem.* **1988**, *75*, 90, DOI: 10.1016/0022-4596(88)90305-2.
[252] C. R. Fell, D. Qian, K. J. Carroll, M. Chi, J. L. Jones, Y. S. Meng, *Chem. Mater.* **2013**, *25*, 1621, DOI: 10.1021/cm4000119.

7. Appendix

7.1. Acknowledgements

Removed due to data privacy.

7.2. Publications and Conference Contributions

7.2.1. Conference Contributions

1) 242nd Electrochemical Society Meeting, Atlanta (Georgia, USA), 09 – 13 October 2022

Oral Presentation: **Surface Modification as a Key Factor for Spherical, Co-Free, High Capacity Li-Mn-Rich Layered Materials - from Small into the kg Scale**

F. Klein, C. Pfeifer, M. Lindén, M. Wohlfahrt-Mehrens, P. Axmann, *Meet. Abstr.* **2022**, *MA2022-02*, 283, DOI: 10.1149/MA2022-023283mtgabs.

2) Ulm ElectroChemical Talks (UECT), Ulm (Germany), 22 – 23 November 2021

Poster: **The Influence of Phosphate Coating on Co-free $Li_{1.2}Mn_{0.6}Ni_{0.2}O_2$ Particles Using Different Phosphate Precursors**

F. Klein, P. Axmann, C. Pfeifer, M. Wohlfahrt-Mehrens

3) Kraftwerk Battery – Advanced Battery Power, online, 28 – 29 April 2021

Poster: **Morphological study of cobalt free cathode materials from co-precipitated spherical $Mn_xNi_{1-x}(OH)_2$ precursors**

F. Klein, P. Axmann, M. Wohlfahrt-Mehrens

4) Advanced Lithium Batteries for Automobile Applications ABBA 12, Ulm (Germany), 6 – 9 October 2019

Participation only

7.2.2. List of Publications

1) **Enhanced electrochemical capacity of spherical Co-free $Li_{1.2}Mn_{0.6}Ni_{0.2}O_2$ particles after a water and acid treatment and its influence on the initial gas evolution behavior**

F. Klein, J. Bansmann, Z. Jusys, C. Pfeifer, P. Scheitenberger, M. Mundszinger, D. Geiger, J. Biskupek, U. Kaiser, R. J. Behm, M. Lindén, M. Wohlfahrt-Mehrens, P. Axmann, *ChemSusChem* **2022**, *15*, e202201061, DOI: 10.1002/cssc.202201061

2) **Three-in-One Surface Modification of Spherical, Co-Free Li-Rich Cathode Material for Li-Ion Batteries ($Li_{1.2}Mn_{0.6}Ni_{0.2}O_2$) with Citric Acid**

F. Klein, C. Pfeifer, J. Bansmann, Z. Jusys, R. J. Behm, M. Wohlfahrt-Mehrens, M. Lindén, P. Axmann, *J. Electrochem. Soc.* **2022***, 169,* 120533, DOI: 10.1149/1945-7111/acaa5c.

3) **In-depth structural characterization of the influence of Li^+ excess on spherical, Co-free layered $LiMn_{0.5}Ni_{0.5}O_2$ cathode material using correlative Raman-SEM microscopy**

F. Klein, C. Pfeifer, P. Scheitenberger, L. F. Pfeiffer, D. Zimmer, M. Wohlfahrt-Mehrens, M. Lindén, P. Axmann, *J. Mater. Chem. A* **2023***, 11,* 5135, DOI: 10.1039/D2TA05957F.

7.3. Curriculum Vitae

Removed due to data privacy.

7.4. Declaration of Authorship

Hiermit erkläre ich, Florian Dominik Klein, dass ich die vorliegende Arbeit selbstständig verfasst, keine andere als die angegebenen Quellen benutzt, und die den benutzten Quellen wörtlich und inhaltlich entnommenen Stellen als solche kenntlich gemacht habe. Außerdem erkläre ich, dass ich die in der Satzung der Universität Ulm zur Sicherung guter wissenschaftlicher Praxis in der jeweils gültigen Fassung festgelegten Grundsätze eingehalten habe. Ich erkläre weiterhin, dass diese Arbeit noch nicht an einer anderen Stelle zur Prüfung vorgelegt wurde.

_____ _____

Ort, Datum Florian Klein

7.5. Reprints of Publications

Enhanced electrochemical capacity of spherical Co-free $Li_{1.2}Mn_{0.6}Ni_{0.2}O_2$ particles after a water and acid treatment and its influence on the initial gas evolution behavior

Reprinted with permission from:

F. Klein, J. Bansmann, Z. Jusys, C. Pfeifer, P. Scheitenberger, M. Mundszinger, D. Geiger, J. Biskupek, U. Kaiser, R. J. Behm, M. Lindén, M. Wohlfahrt-Mehrens, P. Axmann, *ChemSusChem* **2022**, *15*, e202201061, DOI: 10.1002/cssc.202201061.

© 2022 The Authors. ChemSusChem published by Wiley-VCH GmbH

This open access article is reprinted under the terms of the Creative Commons Attribution License CC BY 4.0 (https://creativecommons.org/licenses/by/4.0/).

ChemSusChem

Research Article
doi.org/10.1002/cssc.202201061

Chemistry Europe
European Chemical Societies Publishing

www.chemsuschem.org

Enhanced Electrochemical Capacity of Spherical Co-Free $Li_{1.2}Mn_{0.6}Ni_{0.2}O_2$ Particles after a Water and Acid Treatment and its Influence on the Initial Gas Evolution Behavior

Florian Klein,[a] Joachim Bansmann,[b] Zenonas Jusys,[c] Claudia Pfeifer,[a] Philipp Scheitenberger,[d] Manuel Mundszinger,[e] Dorin Geiger,[e] Johannes Biskupek,[e] Ute Kaiser,[e] R. Jürgen Behm,[c, f] Mika Lindén,[d] Margret Wohlfahrt-Mehrens,[a, f] and Peter Axmann*[a]

Li-rich layered oxides (LRLO) with specific energies beyond 900 $Wh\,kg^{-1}$ are one promising class of high-energy cathode materials. Their high Mn-content allows reducing both costs and the environmental footprint. In this work, Co-free $Li_{1.2}Mn_{0.6}Ni_{0.2}O_2$ was investigated. A simple water and acid treatment step followed by a thermal treatment was applied to the LRLO to reduce surface impurities and to establish an artificial cathode electrolyte interface. Samples treated at 300 °C show an improved cycling behavior with specific first cycle capacities of up to 272 $mAh\,g^{-1}$, whereas powders treated at 900 °C were electrochemically deactivated due to major structural changes of the active compounds. Surface sensitive analytical methods were used to characterize the structural and chemical changes compared to the bulk material. Online DEMS measurements were conducted to get a deeper understanding of the effect of the treatment strategy on O_2 and CO_2 evolution during electrochemical cycling.

Introduction

Driven by the climate change, the importance of energy storage increased in the last years due to the expansion of renewable energies and the need for balancing their power fluctuations.[1] Additionally, different sectors, for example, the automotive industry, undergo a deep structural change from combustion engines to electric drive. To fulfill the requirements of the different sectors, lithium ion batteries (LIBs) are one of the most promising candidates in various applications due to their long cycling life, high energy density and strongly decreasing costs over the last years.[2] A further increase of the energy density can be achieved, for example, with the development of new cathode materials like Li-rich layered oxides (LRLO), which may increase the discharge capacity and the voltage window compared to commercially available cathode materials like $LiCoO_2$ (LCO) or $LiNi_{0.8}Mn_{0.1}Co_{0.1}O_2$ (NCM811). Simultaneously, the amount of critical raw materials like Co or in the future Ni can be reduced to lower both raw material costs and the environmental footprint.

In general, LRLOs with the chemical formula of $x\,Li_2MnO_3 \cdot (1-x)\,LiMn_{1-y-z}Ni_yCo_zO_2$ have to be taken into consideration as next generation cathode materials. Their high discharge capacity (over 250 $mAh\,g^{-1}$) with an average discharge potential of >3.5 V vs. Li/Li^+ is attributed to the combination of cationic and anionic redox reactions.[3,4] The detailed mechanism of the anionic redox reaction and the involved active species of oxygen is still under debate.[5,6] Furthermore, the structure of LRLOs is also under discussion. In 2005 Thackeray et al. suggested that the LRLO is a two component nanocomposite material consisting of monoclinic Li_2MnO_3 and a rhombohedral $LiTMO_2$.[7] Due to the structural relationship of the two phases, the monoclinic lattice can be described as a rhombohedral one (phase prototype: α-$NaFeO_2$) with a honeycomb superstructure. As a consequence, the material can be additionally classified as a solid solution with the general formula of $Li_{1.2}Mn_{0.8-y-z}Ni_yCo_zO_2$.[8,9]

However, the structure of the material strongly influences the redox-mechanism. Most reported materials show a large

[a] F. Klein, C. Pfeifer, Dr. M. Wohlfahrt-Mehrens, Dr. P. Axmann
Zentrum für Sonnenenergie- und Wasserstoffforschung Baden-Württemberg (ZSW)
Helmholtzstrasse 8, D-89081 Ulm (Germany)
E-mail: peter.axmann@zsw-bw.de
[b] Dr. J. Bansmann
Institute of Surface Chemistry and Catalysis
Ulm University
Albert-Einstein-Allee 47, D-89081 Ulm (Germany)
[c] Dr. Z. Jusys, Prof. Dr. R. J. Behm
Institute of Theoretical Chemistry
Ulm University
Albert-Einstein-Allee 11, D-89081 Ulm (Germany)
[d] Dr. P. Scheitenberger, Prof. Dr. M. Lindén
Institute for Inorganic Chemistry II
Ulm University
Albert-Einstein-Allee 11, D-89081 Ulm (Germany)
[e] M. Mundszinger, Dr. D. Geiger, Dr. J. Biskupek, Prof. Dr. U. Kaiser
Electron Microscopy Group of Materials Science
Ulm University
Albert-Einstein-Allee 11, D-89081 Ulm (Germany)
[f] Prof. Dr. R. J. Behm, Dr. M. Wohlfahrt-Mehrens
Helmholtz Institute Ulm Electrochemical Energy Storage (HIU)
Helmholtzstraße 11, D-89081 Ulm (Germany)

Supporting information for this article is available on the WWW under https://doi.org/10.1002/cssc.202201061

© 2022 The Authors. ChemSusChem published by Wiley-VCH GmbH. This is an open access article under the terms of the Creative Commons Attribution License, which permits use, distribution and reproduction in any medium, provided the original work is properly cited.

© 2022 The Authors. ChemSusChem published by Wiley-VCH GmbH

irreversible capacity loss during the first cycle, a poor rate capability, a large hysteresis due to the anionic redox system and voltage fading over the cycle life.[5] During the first delithiation, the Li_2MnO_3 part is electrochemically activated and the structure of the material changes into the electrochemically active Li_xMnO_2 phase. This goes along with the release of some lattice and surface oxygen.[6] The release of surface oxygen leading to surface rearrangement from layered over spinel to the inactive rock-salt structure (LS transition) has been suggested as the most likely reason for the observed voltage fading during cycling.[5,10] To mitigate these problems, different approaches have been tested, such as doping, coating and different surface treatments. Doping is used mainly to stabilize the host framework (e.g., Al, Fe),[11] or expand the Li layer spacing (e.g., Mg, Ca),[12] whereas coatings protect the surface from the direct interaction with the electrolyte and thus suppress side reactions.[13] Commonly used coatings are, for example, oxides,[14] phosphates[13–16] or fluorides.[15,17] Another approach involves a surface modification during the synthesis route, in order to generate a thin spinel layer on the surface. The spinel phase increases the electrochemical performance due to a higher Li^+ ion diffusion coefficient and the better electrical conductivity.[18,19] Typical synthesis procedures include a chemical Li^+ extraction, followed by a structural rearrangement step in the furnace, using different reactants: oxidizing or reducing agents like $Na_2S_2O_8$,[20] SO_2,[21] or N_2H_4[22] as well as acids like HNO_3,[23] H_2SO_4,[24,25] SO_3,[26] and organic acids,[19,27,28] or a simple water treatment.[29]

In this work, defined spherical precursor particles were synthesized in a continuous coprecipitation reaction, followed by an annealing step in the presence of Li^+ (Figure 1). Inspired by the literature, the as synthesized Co-free $Li_{1.2}Mn_{0.6}Ni_{0.2}O_2$ material was treated in a two-in-one procedure with water or HNO_3, followed by a thermal treatment at 300 °C or 900 °C to largely remove surface impurities from the calcination step, and to simultaneously activate the material chemically. All process steps from precursor coprecipitation to the post-treatment were selected with regard to the possibility of upscaling into the kg scale. The main objectives of this work are to map out and understand the relationship between the treatment procedure, in which the annealing temperature acts as a critical parameter, and the electrochemical cycling stability, the structural changes with respect to the primary and secondary particle architecture as well as the resulting gas evolution during the first cycles.

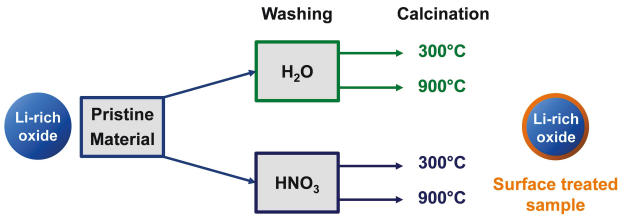

Figure 1. Schematic overview over the post treatment steps.

Results and Discussion

The as-prepared spherical, Co-free material (labelled as LRLO) with the general formula of $Li_{1.2}Mn_{0.6}Ni_{0.2}O_2$ was used as a reference material. The treated samples were named according to their treatment steps and calcination temperatures. Samples denoted W300 and W900 were washed with water, whereas A300 and A900 were treated with acid, respectively. Adding the LRLO powder into water instantaneously led to the formation of an alkaline suspension with a pH ≈ 11.6, reflecting the dissolution of Li^+ and other surface species into the washing solution (Figure S1). The addition of HNO_3 to the aqueous suspension led to an enduring decrease of the pH ≈ 6–7, accompanied by the formation of small gas bubbles, due to the formation of CO_2 from CO_3^{2-} species. A pH curve measured during the addition of the powder to an acidic solution with the same amount of HNO_3, added slowly during the post-treatment step, is presented in the Supporting Information (Figure S1). Possible Li^+ sources are water-soluble surface impurities and the exchange of Li^+ ions with H^+ in the crystal structure of LRLO. Surface impurities like hydroxides and carbonates were quantified by acid-base titration (Figure S2). The results verify that both washing procedures led to a pronounced decrease in the amount of carbonate and hydroxide species.

To quantify the metal leaching during the washing steps, inductively coupled plasma optical emission spectroscopy (ICP-OES) was used (Table 1). The amount of extracted Li^+ ions per formula unit increases with increasing acidity of the washing media, whereas the loss of Li^+ is very low using water. Water washing probably dissolves mainly surface species, while the acidic treatment extracts significantly more Li^+ out of the crystal lattice. Additionally, the Ni/Mn ratio is also decreasing for the acid treated samples. This leads to the assumption that

Table 1.
Results of elemental analysis by ICP-OES given as molar ratios (Li + Mn + Ni = 2), mean oxidation states (OS) of the transition metals (TM = Ni + Mn), the calculated oxygen stoichiometry and the experimental lattice parameters of the powders.

	Li	Mn	Ni	Na/TM	Ni/TM	Mean OS	$Li_xTM_{2-x}O_y$ y	Lattice parameter a [Å]	c [Å]
LRLO	1.22	0.59	0.19	0.08	0.246	3.59	2.01	2.858	14.257
W300	1.21	0.60	0.19	0.00	0.245	3.55	2.00	2.859	14.258
W900	1.21	0.60	0.19	0.00	0.246	3.53	2.00	2.860	14.262
A300	1.17	0.63	0.20	0.00	0.239	3.55	2.06	2.863	14.274
A900	1.16	0.64	0.20	0.00	0.240	3.50	2.05	2.849	14.264

© 2022 The Authors. ChemSusChem published by Wiley-VCH GmbH

the acid leaches not only Li^+ ions out of the structure, but also attacks the lattice of the host framework, which is implied by the significantly increased Ni^{2+} content in the washing solution (Table 2). Interestingly, the Mn ion leaching is negligible. The observed pH-dependent dissolution behavior is comparable to the results reported by Dahn's group for Ni-rich Li-TM-layered oxide materials, where a significant TM leaching was observed below a pH of about 8, and where the leaching increased with decreasing pH.[30] Besides the main elements Li^+, Ni and Mn ions, small amounts of Na^+ impurities were found in the pristine material, which are residues of the coprecipitation process. The Na^+ ions were likely incorporated into the grain structure of the carbonate precursor and cannot be removed even upon extensive washing. However, after lithiation and calcination the Na^+ ions can be quantitatively washed out easily with the used post-treatment steps. This suggests that most of the Na^+ impurities had segregated out of the particle architecture and deposited on the surface during the synthesis process of LRLO.

The second part of the post-treatment, the calcination procedure after the washing step, was investigated using thermogravimetric analysis coupled with a mass spectrometer (TGA-MS, Figure 2). The TGA curve of the pristine LRLO material (Figure 2a) is dominated by an initial mass loss of 0.5% with a subsequent slight decrease in mass up to 400–500 °C, followed by a plateau. An additional mass loss was observed at temperatures exceeding 700 °C. The low-temperature mass loss corresponds to the loss of crystal water from the Na_2CO_3 monohydrate, as illustrated by the increase of the H_2O signal in the MS and the small endothermic peak in the differential scanning calorimetry (DSC) curve.[31] Above 700 °C, decomposition of Li_2CO_3 followed by Na_2CO_3 occurs, as seen in the increasing CO_2 signal.[32] The broad CO_2 peak in the temperature range of 300 to 500 °C, accompanied by a slow decrease of the H_2O signal probably corresponds to the decomposition of basic Ni carbonate traces on the surface.[33–35] The O_2 signal is dominated by the background signal of the air atmosphere. The monotone increase correlates with the increase of the N_2 signal ($m/z = 28$, Figure S3) and corresponds to a measurement artefact of the TGA-MS setup. Unfortunately, the expected loss of O_2 during the TGA experiment caused by the decomposition of possible protonated species cannot be observed nor excluded due to the already high MS signal from the oxygen containing air. Both washing treatments led to a pronounced change in the mass loss curve. The mass loss related to carbonate decomposition is mainly absent, which confirms the virtually quantitative elimination of Na_2CO_3 and Li_2CO_3. Only a very small amount of surface carbonates is still observed, indicated by the increasing CO_2 signal above 700 °C. Possible sources are minor residues from an incomplete washing

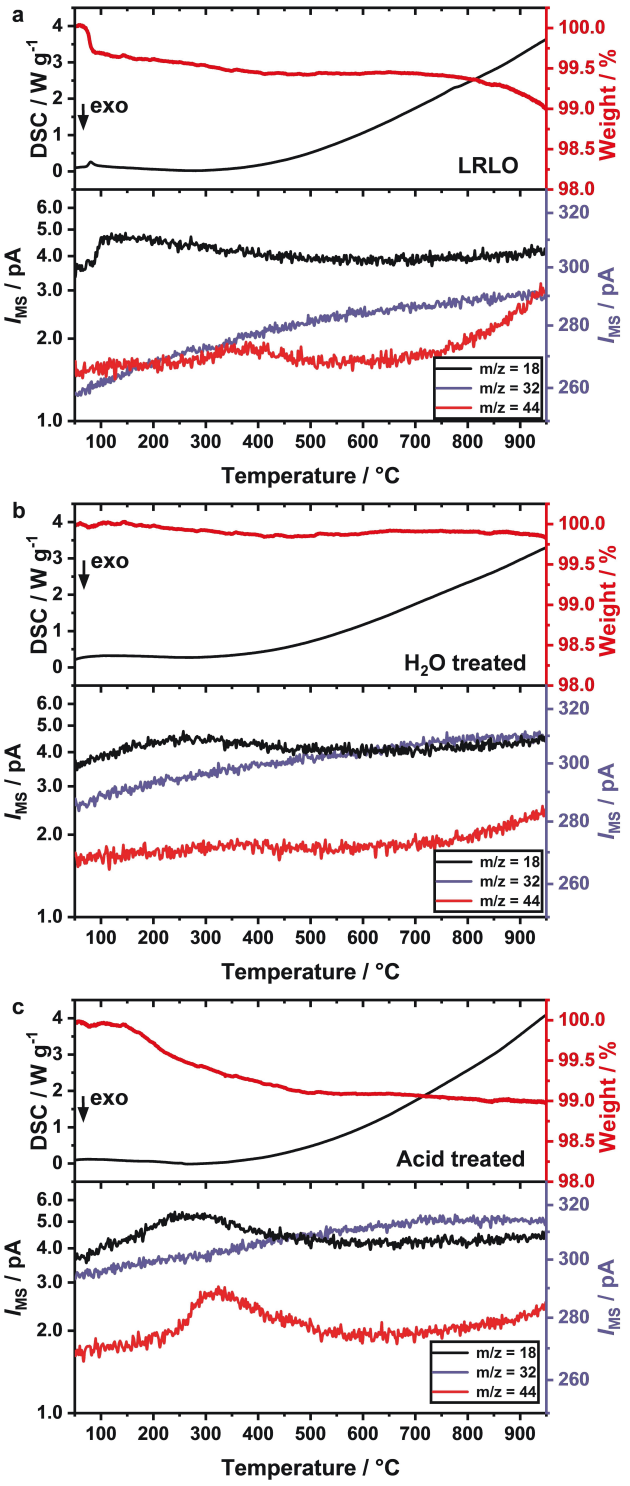

Figure 2. TGA-DSC-MS measured with a heating rate of 10 K min^{-1} under air for as-synthesized LRLO (a), LRLO after aqueous washing (b) and LRLO after acidic treatment (c). The relative mass loss curves are shown in red and the DSC curves in black. The corresponding ion currents of the mass spectrometer are shown for m/z = 18 (H_2O, black), m/z = 32 (O_2, purple) and m/z = 44 (CO_2, red).

Table 2. Quantitative ICP analysis of the washing solutions after the aqueous or acidic treatment of LRLO. The results were normalized to the dry mass of the washed powders.

	Li [‰]	Na [‰]	Ni [‰]	Mn [‰]
Aqueous treatment	0.91	13.7	< 0.00008	0.00374
Acidic treatment	3.70	13.8	0.429	0.00050

© 2022 The Authors. ChemSusChem published by Wiley-VCH GmbH

procedure or the formation of new carbonates upon contact with air.

The water washed material shows only a very small mass loss over the whole temperature range (Figure 2b). This we assign to the decomposition of $Li_{1.2-x}H_xMn_{0.6}Ni_{0.2}O_2$ species, indicating some Li^+/H^+ exchange during the washing procedure.[30]

For the acid treated sample (Figure 2c), the corresponding mass loss is more pronounced (150–500 °C, ≈0.85 %). In combination with the increased H_2O and CO_2 signals, the decomposition of basic Ni carbonates to NiO is very likely.[33–35] With respect to the ICP results, this might be an indication that the acid treatment strongly attacks the LRLO lattice. Mainly Li^+ and Ni^{2+} ions were dissolved, but most of the Ni^{2+} ions were likely deposited outside the LRLO crystal lattice as (oxo-)hydroxides or form similar surface groups, which further react with air to basic Ni carbonates. Based on the TGA-MS results and the corresponding literature,[33–36] we suggest that the Ni surface species are fully decomposed at the calcination temperature of 900 °C to a rock-salt like structure, whereas at 300 °C the surface species are only partially decomposed.

Therefore, the structural and morphological changes after both treatment steps were further investigated, using scanning electron microscopy (SEM), powder X-ray diffraction (XRD) and cerimetry (Figure 3). The SEM images (Figure 3a,b) of the pristine particles show a spherical morphology, derived from the spherical shape of the precursor. The secondary particles are agglomerates of primary particles with a few hundred-nanometer size. Regarding the post-treatment steps, there is no significant morphological difference (see Supporting Information Figure S4). The XRD diffraction patterns of all studied materials apart from the A900 material were similar, which is why they are discussed together in the following. All reflections can be assigned to the hexagonal crystal structure of the α-$NaFeO_2$ type with the space group *R-3m* and the monoclinic Li_2MnO_3 type (*C/2m*) with indications for the presence of a Li_2MnO_3 type super-structure, indicated by additional reflections in the 2θ range of 20–25° (Figure 3c).[37] The layered structure is well defined, indicated by the splitting of (006) and (102) as well as (108) and (110) reflections.[38,39] The (003), (101) and (104) reflections do not show shoulders or additional signals in their neighborhood indicating that the spinel phase content must be low (Figure 3d).[38,40] TOPAS V6 was used for Rietveld refinement of the XRD data, using the $Li_{1.2}Mn_{0.6}Ni_{0.2}O_2$ structural model of Fell et al.[41] Detailed results of the refinement and the corresponding plots are presented in the Supporting Information (Table S1, Figure S5). The lattice parameters *a* are in a comparable range $a = 2.858–2.863$ Å with the exception of

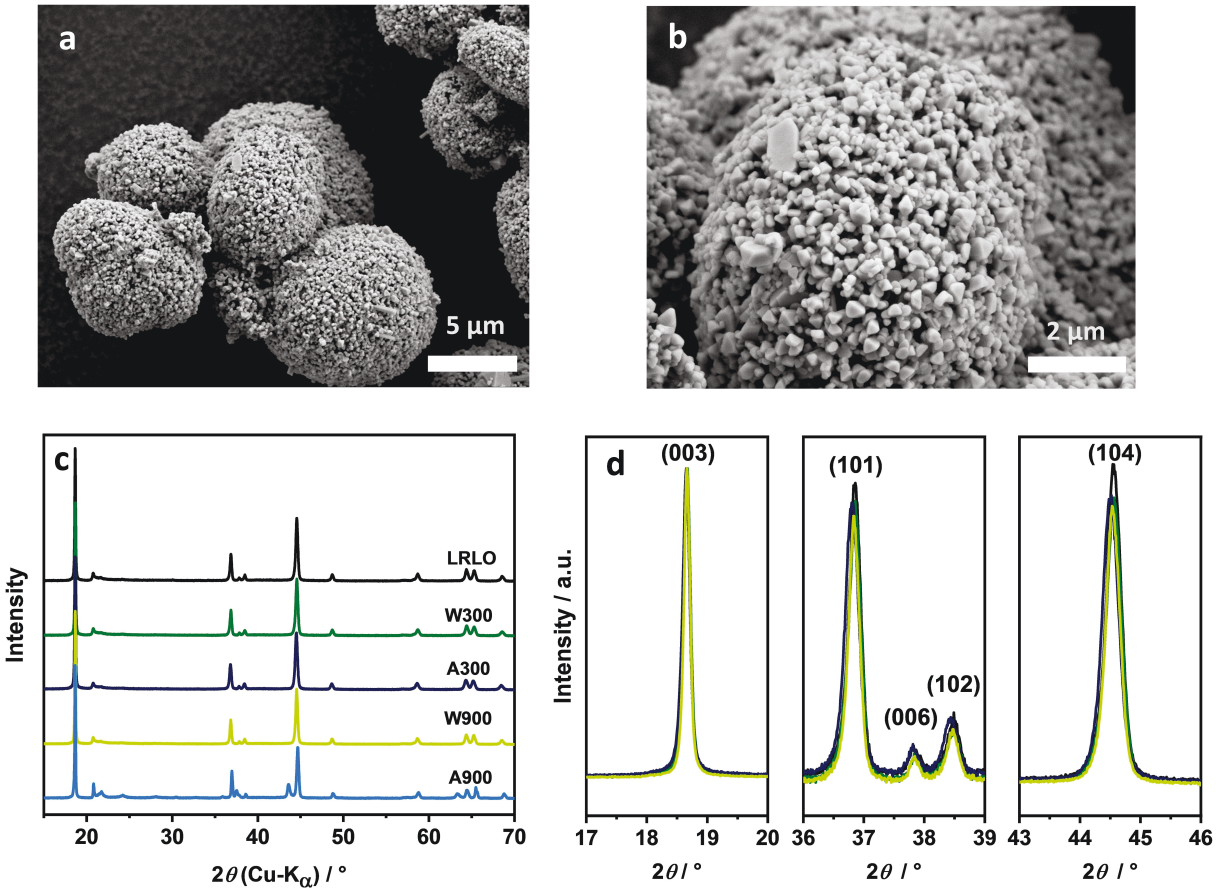

Figure 3. SEM images of LRLO (a, b). Powder XRD pattern of all the samples (c). XRD diffraction detail plots (d) of LRLO (black), W300 (green), A300 (dark blue) and W900 (light green).

© 2022 The Authors. ChemSusChem published by Wiley-VCH GmbH

A900 ($a = 2.849$ Å), being significantly lower (Table 1). In contrast, the value of the *c* parameter is strongly dependent on the washing conditions. The largest difference is observed between A300 ($c = 14.274$ Å), LRLO ($c = 14.257$ Å) and W300 ($c = 14.258$ Å). A possible explanation or the slight increase in the *a* parameter values after the treatments can be the adjustment to a new oxygen-TM stoichiometry during calcination, due to the release of thermodynamically unstable oxygen from the crystal lattice to compensate a local loss of Li^+ during washing, for example due to reduction of Mn^{IV} to Mn^{III}. The general phenomenon is called reduction expansion.[42,43] As a consequence, the cell volume increases and the activation energy for Li^+ ion transport is likely decreased.[44] However, the changes in the structure have to be very local, for example, on the surface of the primary particles, because the XRD patterns (bulk method) show that the hexagonal structure remains intact without visible structural changes.

The diffraction pattern of A900 differs strongly from that of the other powders. Additional reflections appear, which can be assigned to the rock salt structure of the type Mg_6MnO_8 (225) with a chemical composition of most probably Ni_6MnO_8.[45,46] Additionally, the reflections originating from a Li_2MnO_3-type super-structure between 20 and 25° 2θ are well defined and have a higher intensity as compared to the other materials studied. Compared to A300, both lattice parameters decrease dramatically. In combination, this implies that some phase transition or phase separation, respectively, occurred during the high-temperature calcination step. A more detailed discussion about A900 will follow in a separate section.

To verify the reduction expansion of the lattice parameters, TM mean oxidation states (OS) were investigated by cerimetric redox back titration. Generally, the TM mean OS decreases with the treatment steps compared to LRLO (Table 1). For an easier comparison of the results, the values were converted into the ratio of oxygen vs. metal with respect to the formula unit of the layered oxide $Li_{2-x}TM_xO_y$ ($y = 2.00$), using the Li/TM ratio obtained from ICP. Additionally, theoretical values for $LiTM_2O_4$ ($y = 2.67$) and Ni_6MnO_8 ($y = 2.29$) were calculated. The value of LRLO $y = 2.01$ corresponds to the theoretical one of $y = 2.00$, which fits well to the expectations. None of the water-treated samples show stoichiometric differences as compared to pristine LRLO. In contrast, the calculated amount of oxygen per formula unit of the acid treated samples A300 and A900 increased slightly. This indicates the presence of an O-richer crystallographic phase, like spinel-type (A300) or Ni_6MnO_8 (A900), in addition to the layered phase, which is in good agreement with the XRD results.

Deeper insight can be gained by more surface sensitive and high-resolution methods like X-ray photoelectron spectroscopy (XPS) as well as Raman and transmission electron microscopy (TEM). In contrast to XRD, Raman microscopy is sensitive to short range order and allows to differentiate between different coordination geometries and oxidation states.[47] If the LRLO structure is a nanocomposite of $LiTMO_2$ and Li_2MnO_3, the Raman spectrum should show lattice vibrations of both structures. The $LiTMO_2$ compound with the space group *R-3m* has two vibrational modes: the in-plane O–M–O bend vibrations E_g, where the oxygen ions vibrate in parallel to the Li/TM layers and the out-of-plane O–M stretching vibration mode A_{1g}, where the oxygen ions vibrate in opposite directions along the *c*-axis.[47,48] In case of a solid solution of different metals, for example $LiNi_{1-x}Mn_xO_2$, each type of TM ion bond has separate E_g and A_{1g} vibrations. Typical values for NCMs are around 500 cm^{-1} (E_g) and 600 cm^{-1} (A_{1g}), depending on the ratio of the TMs.[49] The symmetry of Li_2MnO_3 is lower and therefore more vibration bands can be excited at 612 (A_g), 568, 493, 438, 413, 369, 332, 308 and 248 cm^{-1}.[50] The measured spectrum of pristine LRLO shows a superposition of all modes (Figure 4), which is therefore in accordance with the literature. It is important to note that the vibration bands of Li_2MnO_3 between 200 and 440 cm^{-1} are less pronounced in LRLOs compared to the phase pure compound due to local structural differences like the exchange of Mn with Ni or Li/Ni disordering. Furthermore, this is a possible reason for band broadening and a shift to lower wavenumbers (red-shift).[9] Figure 4 shows a selected spectral range to focus on the important M–O vibrations. Additional vibrations beyond 800 cm^{-1} are detected only for LRLO at approximately 1080 cm^{-1} (compare Figure S6). This high wavenumber band can be attributed to the symmetrical stretching vibrations of the carbonate ions in Na_2CO_3.[51] It suggests that remaining sodium from the precipitation process is present as a separate, water-soluble phase and therefore can be removed completely during the post treatment steps, which confirms the ICP-OES results. The M–O vibrations supports the different observations of the bulk characterization. The spectra of LRLO, W300 and W900 show no significant differences between each other. In the spectrum of A300, an additional shoulder at ≈650 cm^{-1}, marked with a black arrow, can be observed. It shows the presence of some shorter Mn-O or Ni-O bonds in the structure, most likely due to the formation of some spinel domains in the crystal lattice during the Li^+ leaching and the low temperature treatment step.[9,50,52] Further vibration bands assignable to spinel structures are not visible, because they

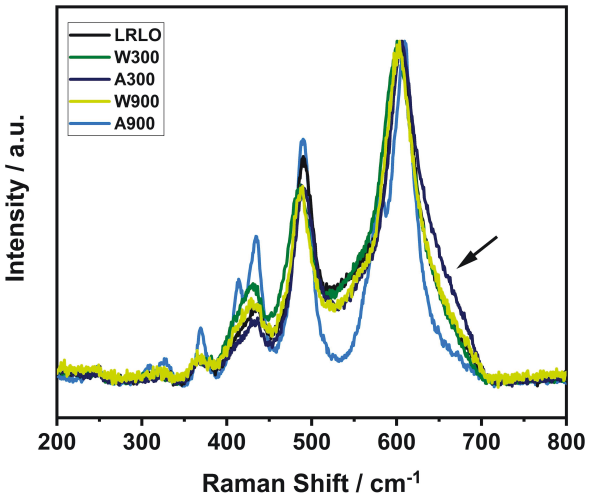

Figure 4. Raman spectra of the investigated powders ($\lambda = 532$ nm, $P = 1.5$ mW). The spectra were normalized to the vibrational band at approximately 600 cm^{-1}.

© 2022 The Authors. ChemSusChem published by Wiley-VCH GmbH

have lower intensity and are hidden under the signals of the main phase.[50]

Fundamentally different is the Raman spectrum of A900. The vibration bands are sharper and well-defined, especially in the range of 300–450 cm^{-1}. The most intense band is slightly shifted to higher wavenumbers compared to the other samples. Furthermore, an additional signal at 582 cm^{-1} can be observed. A cross-section of the material was prepared and studied by a combination of SEM and Raman microscopy (Figure 5a–c), correlating structural information (Raman) with higher resolution images (SEM). Similar Raman spectra were clustered into groups and presented in the mapping as areas with the same color (Figure 5b). The corresponding average Raman spectra (Figure 5c) show strong local differences in the signal intensity ratio between the vibration band centered at ≈582 cm^{-1} and the band at 612 cm^{-1}, while the intensity ratios of the vibrational bands at 612, 496, 435, 414, 370, 333, 309 and 249 cm^{-1} are approximately constant. This strongly indicates a mixture of two phases. The latter vibration bands can be assigned to the Li_2MnO_3 structure.[50] Therefore, a single vibration mode for the second phase at ≈582 cm^{-1} remains. This is in good agreement with the literature values for Ni_6MnO_8, showing a single vibration mode between 580 and 585 cm^{-1}.[53] With the additional reflections in the XRD (Figure 5f) and the strong decrease of the lattice parameters from A300 to A900, a phase separation into Ni_6MnO_8 and a Ni-poor LRLO with a high Li_2MnO_3 content for A900 is very likely. The TM separation is already visible in the contrast of the SEM image as well as in the high-angle annular dark field (HAADF) scanning (S)TEM images (Figure 5a,d). The Ni-rich regions are brighter due to the higher atomic number *Z*, scattering more electrons.[54] The Ni-rich particles can be found on the surface of the primary particles and at the grain boundaries, which is clearly indicated additionally by the Raman mapping (high intensity of the vibration band at ≈582 cm^{-1} in the bright areas of the SEM images). Energy dispersive X-ray (EDX) mapping of

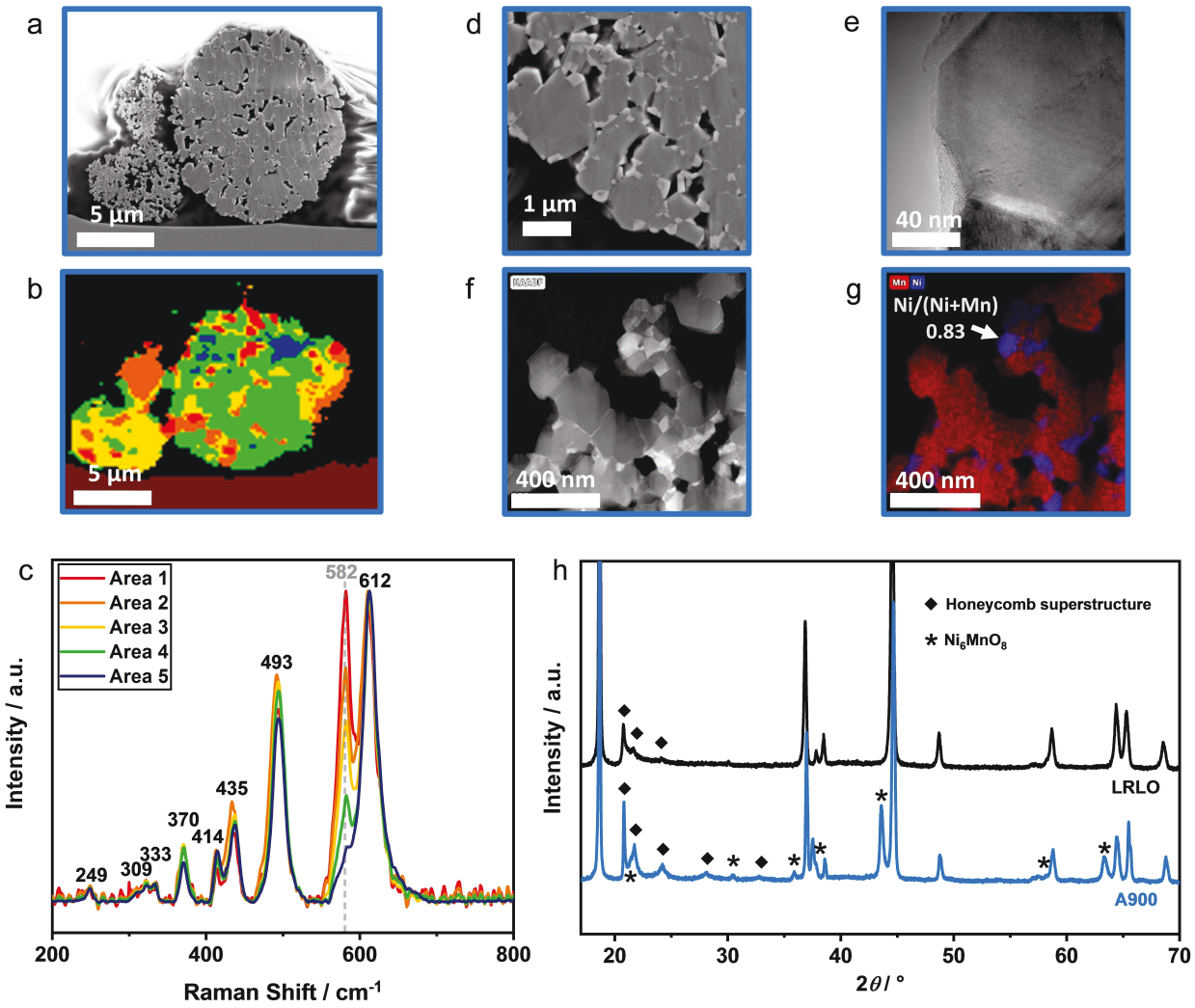

Figure 5. Detailed investigation of A900: SEM image of particle cross-section (a), Raman mapping of the same particle cross-section, clustering areas with similar spectra (b) and corresponding Raman spectra (c), SEM image (d) with higher magnification of (a), HRTEM image of a crystallite (e), HAADF STEM image (f) with corresponding elemental distribution of Mn and Ni determined with EDX (g), detailed XRD analysis (h) with phase identification of Ni_6MnO_8 (marked with *, reference: Taguchi et al.[46]).

© 2022 The Authors. ChemSusChem published by Wiley-VCH GmbH

the same TEM lamella supports these observations (Figure 5e). There are some local Ni enrichments, for example, with a Ni/TM ratio = 0.83 and the predominant part of dark particles with Ni/TM ≈0.07. Taken the results together, A900 indicates that the material was strongly attacked by the acid, and that the leaching process destabilized the structure in a manner that the subsequently high-temperature treatment, where especially the TM ions have a high mobility and move to the thermodynamically most stable lattice site, leads to phase separation. For W900, a similar reaction behavior is assumed to take place, but to a lower extent.

This behavior helps to interpret the changes in the 300 °C treated samples, which will be discussed in the following part. The results of the TEM and XPS investigation of LRLO, W300 and A300 are presented in Figure 6. TEM lamellas were cut using a focused Ga-ion beam (FIB). Typical and representative particles with diameters of around 15 μm were selected. The cuts were set in a way that the surface and the first few micrometers deep into the particles could be analyzed. The HAADF STEM images (Figure 6a–c) show the differences between the samples directly. LRLO consists of defined crystallites in the range of approximately 100–200 nm with a homogeneous surface and brightness. In contrast, the crystallite surface of W300 shows a large number of cavities and is generally inhomogeneous. The cavities originate most likely from the leaching process during the post-treatment and the associated surface corrosion. A300 has a smoother surface, in which the single crystallites are difficult to identify. Additionally, the parts of the crystallites located directly adjacent to the surface or pores appear brighter compared to parts farther away. EDX results are consistent with these observations. After both acid and water treatment, a local Mn- and Ni-enrichment can be observed whereas the pristine LRLO material has a homogeneous Mn–Ni distribution. High resolution (HR) TEM images (Figure 6g–i) show that the sharp edges of the well-defined crystallites (LRLO) become smoother for W300 and A300. Furthermore, some of the surface layers of A300 are likely exfoliated or have pronounced stacking faults, which might be a reason for the increased Li^+ and Ni^{II} concentrations in the washing solution. In the exfoliated areas, the accessibility to the Li^+ ions is strongly increased, supporting washing out. The TM layers are most likely preserved by the hardly soluble Mn^{IV} ions. However, the in general higher mobility of the Ni^{II} ions probably leads to the depletion of Ni in the TM layer and facilitates the local Mn- and Ni-enrichment and densification of the surface. Consequently, the results of the material treatment are strongly dependent on the pH: the higher the proton concentration in the washing solution, the stronger the surface reconstruction after the heat treatment.

To underline the experimental results of Raman measurements and cerimetry, the formation of spinel domains during the post treatment steps was characterized by X-ray photoelectron spectroscopy (XPS) (Figure 6j–l). The surface sensitive method was chosen in addition to the bulk sensitive cerimetric titration with the idea to investigate the reconstruction of the surface after Li^+ leaching. The oxidation states of Mn were determined through deconvolution of the Mn 3p spectra, using the approach of Ilton et al.[55] with five single peaks for each Mn OS (III/IV). The latter peaks were fitted with defined parameters (e.g. peak shape, width, relative binding energy and intensity) adapted from the literature values.[55] All components of each OS are shown in one peak for each OS for an easier interpretation of the spectra. The overlapping Li 1s signal was fitted with a single peak. Obviously, the surface Mn^{III} content increases from LRLO (4%) over W300 (12%) to A300 (20%), while the Mn^{III} content decreases slightly from A300 to A900 (Figure S7a). The Li 1s peaks are positioned in a comparable range of the BE of 54.2 ± 0.2 eV, corresponding to Li–O-bonds in LRLOs.[56] Nevertheless, the peaks of Li 1s and Mn 3p in A300 are not well separated, like in W300, due to a broadening of the Li peak. This can be related to the lower BE in spinel type material, for example $LiMn_2O_4$ with a Li 1s BE = 53.7 eV.[57] Further spectra are presented in the Supporting Information (Figure S7). A behavior similar to that of the Mn 3p states is observed also for the Mn 2p spectra (Figure S7b). Furthermore, we also recorded Ni 2p spectra, which showed no significant differences between the different materials (Figure S7c). They are dominated by a Ni $2p_{3/2}$ peak at around 854.7 eV, which is characteristic for Ni^{II}.[58]

After the detailed structural and chemical analysis of the powders, the influence of the chemical treatments on their electrochemical behavior was studied (Figure 7). The active materials were cycled against Li metal in a potential range between 2.5 and 4.8 V with C/10 (1 C = 250 mA g^{-1}). Due to the slow electrochemical activation step at approx. 4.5 V, the first cycle was conducted at a lower C-rate of C/20. The specific discharge capacity of LRLO is 184 mAh g^{-1} in the second cycle (Figure 7a) and does not reach the values reported in the literature for this material class, for example 240 mAh g^{-1} (C/10, 2.0–4.8 V).[59] Additionally, there is an increase of the capacity upon cycling, which indicates an activation of the cathode material. With respect to their electrochemical behavior, the treated samples can be separated into two groups. The materials with a post-treatment calcination temperature of 300 °C (A300 and W300) reach higher values, whereas W900 and A900 were deactivated. Especially the deactivation of the latter material is very pronounced. From the antecedent characterization, this can be assigned to the structural reorganization during high-temperature treatment. The lower electrochemical activity might be due to the presence of Ni-rich rock-salt structures, like Ni_6MnO_8, in the grain boundaries and on the surface of the primary particles. This layer can probably block the lithium diffusion pathways and deactivate the material electrochemically. Most likely, the same happens for W900, but to a lesser extent. A300 shows a very high specific discharge capacity of 267 mAh g^{-1} in the 2nd cycle as compared to W300 (231 mAh g^{-1}), but the capacity decreases rapidly during further cycling. W300 has a stable cycling behavior as well as LRLO. This is highlighted in more detail in the rate capability test and subsequent cycling at 1 C (100 cycles, Figure S8). A closer look at the voltage profiles and d*Q*/d*V* plots of LRLO, W300 and A300 helps to understand the different behavior of these materials. According to general knowledge, during the first delithiation Ni ions are oxidized in the sloping area of the

© 2022 The Authors. ChemSusChem published by Wiley-VCH GmbH

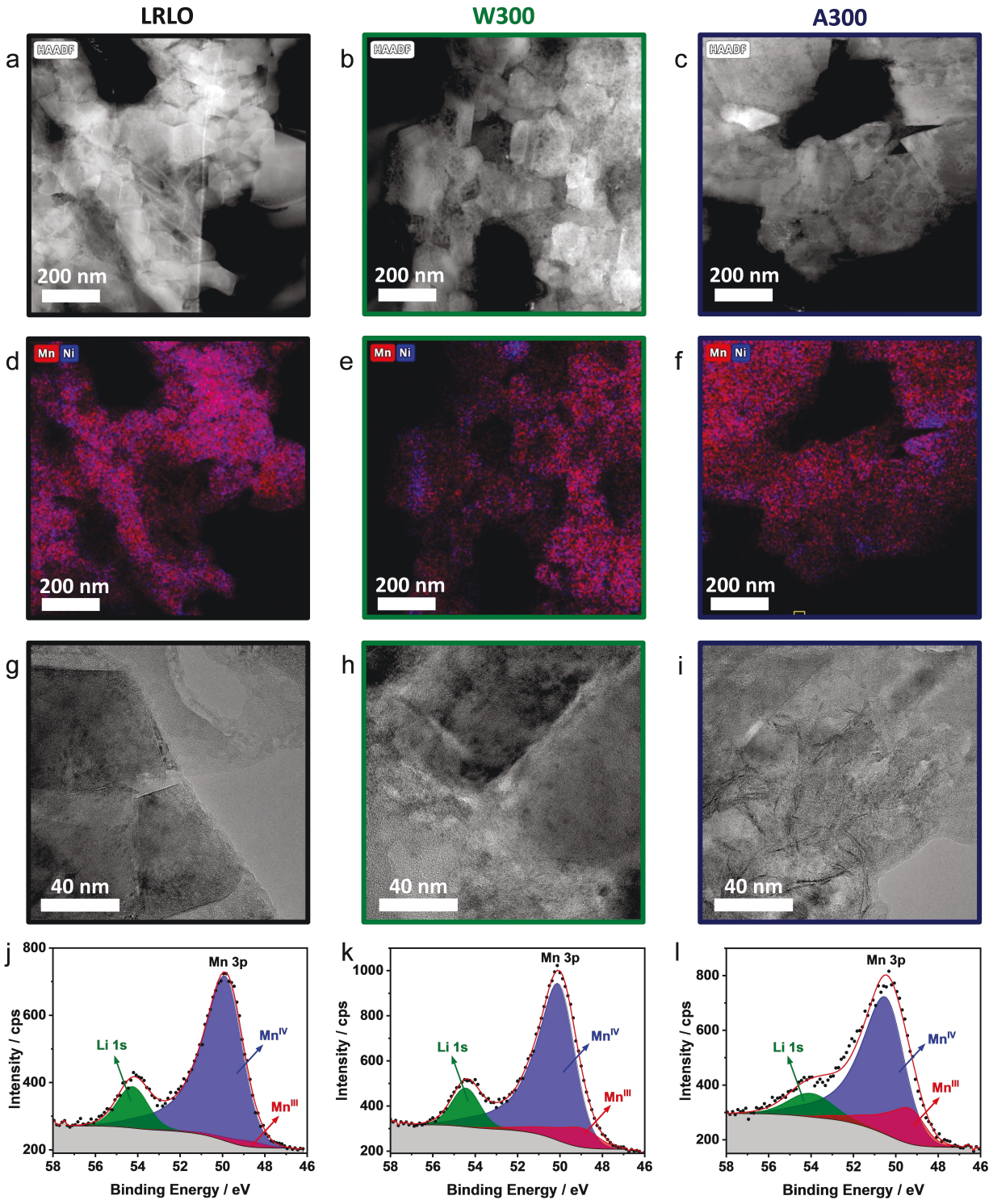

Figure 6. Detailed structural investigation of LRLO (black), W300 (green) and A300 (blue) with TEM (a–i) and XPS (j–l). HAADF STEM images (a–c), corresponding EDX elemental distribution of Mn and Ni (d–f), HRTEM images (g–i) and XPS spectra of Li 1s and Mn 3p (j–l).

voltage profile.[6] At approx. 4.5 V a plateau is reached, where the Li_2MnO_3 domains are activated. Lithium and oxygen species are extracted, which provides further capacity in addition to the TM redox system and the TM metals are rearranged.[60] During the subsequent re-lithiation process Li^+ mainly re-occupies positions in the Li^+ layer.[5,61] LRLO and W300 have the typical charge and discharge potential characteristic of the Li-rich material during the first cycle (Figure 7b). The voltage profiles only differ in length, but not fundamentally in the ratio of the sloping against the plateau region. If they were normalized on

© 2022 The Authors. ChemSusChem published by Wiley-VCH GmbH

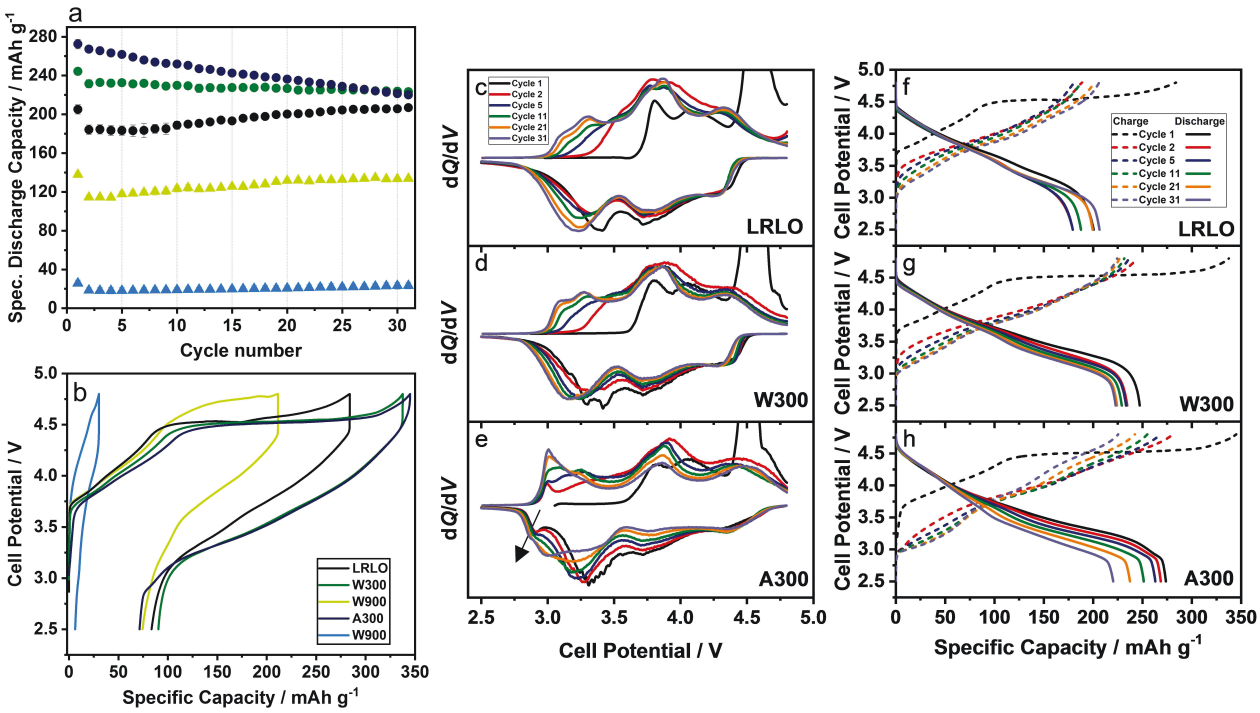

Figure 7. Specific discharge capacity (a) of C/10 cycling (first cycle C/20) and the galvanostatic potential curve (b) of the first cycle (C/20): LRLO (black), W300 (green), A300 (dark blue), W900 (light green) and A900 (blue). Corresponding dQ/dV plots (c–e) and potential curves of selected cycles (f–h): 1st (black), 2nd (red), 5th (blue), 11th (green), 21st (yellow) and 31st (grey).

their maximum specific charge capacity, the 1st cycle charging profile of LRLO is comparable to that of W300. This is in accordance with the d*Q*/d*V* plots of both materials (Figure 7c,d). A voltage shift towards higher or lower values cannot be observed there, but a closer look shows that the intensity of the oxidation peak beyond 4.2 V increases during the following cycles for LRLO, whereas for W300 it decreases. Secondly, the d*Q*/d*V* plot of LRLO shows an additional signal at the end of charge during the first few cycles. The combination of the slight capacity increase during cycling and the information from the d*Q*/d*V* plots indicates that only a part of LRLO material participates in the charge and discharge processes. Clogged diffusion paths in the secondary particle due to residues of the synthesis (e.g. Na_2CO_3 or Li^+ species) or in the primary particles may hinder electrochemical access to the other part of the material. During further cycling, some species can react (e.g., in the d*Q*/d*V* signal at the end of charge) and form additional diffusion pathways, which makes further active material accessible.

The first cycle potential curves of A300 are similar to those of the previous samples with one difference in the discharge profile, which has additional capacity in the region of $E \approx 2.7$–3.1 V and in the following cycles (Figure 7h). In the corresponding d*Q*/d*V* plot (Figure 7e), a peak in this potential range (black arrow) is observable, which increases in intensity during further cycling. During delithiation the peak between $E \approx 2.8$–3.2 V increases, too. Both are assigned in the literature to the Mn^{III}/Mn^{IV} redox couple of a spinel-like phase,[27,62,63] which confirms the results already presented like, for example, a higher Mn^{III} content in the XPS spectra or the additional shoulder in the Raman signal. Furthermore, most of the other d*Q*/d*V* peaks differ as well. The oxidation peak at $E \approx 4.5$ V is slightly shifted to higher potential and the beginning of discharge starts earlier and smoother. Especially in the Ni redox active region above $E \approx 3.2$ V,[63] the discharge peak intensity decreases strongly over cycling. The potential curves and the d*Q*/d*V* plots of the long-term cycling experiments, which show a strongly increased capacity for A300 in the potential range between $E \approx 2.8$–3.2 V after 145 cycles (Figure S8c,d), underline this hypothesis. This can be interpreted as a faster aging process due to the rapid transformation from a layered into spinel-like and rock-salt structure. One reason for this phase transformation might be the local enrichment of Ni in the surface-near areas, shown in the TEM analysis, and the Mn-enrichment of the bulk with a higher amount of Li_2MnO_3 domains. The increase of Li_2MnO_3 domains is in accordance with the reported characteristics of the d*Q*/d*V* data of Zhang et al., varying the ratio between (x) Li_2MnO_3 and ($1-x$) $LiMn_{0.5}Ni_{0.5}O_2$ ($0.3 \leq x \leq 0.6$).[60,64] A second possibility is the structural instability of the surface-near region after the acid treatment, which is indicated by the phase separation at 900 °C into rock-salt and Li–Mn-rich layered structures (A900). At 300 °C, a complete structural rearrangement is unlikely, but during subsequent cycling electrochemically induced oxygen release and repeated (de-)lithiation are likely to further destabilize the structure, which leads to a strong surface densification and a decrease of the bulk accessibility.

© 2022 The Authors. ChemSusChem published by Wiley-VCH GmbH

More information about possible gas evolution in the electrochemical activation of these materials and the influence of the different treatment steps thereon was obtained by DEMS measurements (Figure 8). They were performed under galvanostatic conditions ($I \approx$C/10), to be comparable with the electrochemical measurements in coin-cells (for details see Experimental section). Most important, they were conducted under truly differential conditions, as the working electrode was directly deposited on the membrane inlet to the mass spectrometer chamber, which allows a fast transfer of the gaseous products to the mass spectrometer (time resolution of ~2 s).[65] Therefore, the signals can be directly correlated with the formation rates of the respective gases. To the best to our knowledge, such DEMS measurements are applied here for the first time. They differ by their much higher time resolution from the commonly used carrier gas assisted online mass spectrometry (OEMS) approach.[4,61,66–68]

The potential curves in the upper panel (Figure 8, red lines) are comparable to the electrochemical data obtained from coin cells that were shown before (Figure 7). The transients of selected ion currents presented in the other panels, which were acquired simultaneously, are plotted in the lower panels. They provide information on the gas formation rates from the active materials. Qualitatively, they clearly indicate the formation of O_2 ($m/z=32$, with a fragment at $m/z=16$) and CO_2 ($m/z=44$, with fragments at $m/z=28$ and $m/z=16$) in the range of high potentials.[69] For none of the three powders we observed an O_2 signal in the second cycle. The peak shapes and intensities differ, however, significantly for the different electrodes, with the amount of released O_2 increasing in the order LRLO < W300 < A300. CO_2 formation is also most pronounced in the first cycle, but occurs to a lower extent also in the second cycle. Comparable results had been reported by Streich et al. for Co-containing LRLO/SFG6 full cells.[70] In contrast to the O_2 signal, the amount of CO_2 formation is highest for the pristine LRLO, and much lower for the treated samples.

The much higher amount of O_2 formation after pre-treatment as compared to pristine LRLO seems to be in contrast to findings reported in the literature. Ramakrishnan et al. reported that acid washing and subsequent drying ($T_{max}=135\,^{\circ}C$) results in complete suppression of O_2 evolution during charging of Co-containing LRLO material and an almost complete suppression of CO_2 evolution.[24] They explained the latter by a combination of partial removal of Li_2CO_3 (surface) impurities and surface passivation against electrolyte decomposition.[24] Qiu et al. reported a strongly reduced O_2 and CO_2 evolution from a post-treated Co-containing LRLO material during charging, too.[4] In their case, the electrode material reacted with CO_2 to create O-vacancies, followed by washing and drying to remove the Li_2CO_3 surface layer partly formed during this treatment. They attributed the suppression of gas evolution to the formation of O-vacancies in the surface-near region, which inhibit O_2 evolution. This should also cause the inhibition of CO_2 evolution, which according to these authors results from reaction between oxygen radicals and electrolyte.[4] Because the results of the redox titration indicates the absence of O-vacancies in the series of powders investigated here, it is assumed that during the thermal treatment under air at 300 °C and 900 °C, respectively, possible vacancies are removed and/or more thermodynamically favored phases are formed, for example, a spinel-like phase. Consequently, the results of the DEMS measurements of LRLO, W300 and A300 are hardly comparable with the above studies.

The present result of a lower O_2 evolution from the pristine LRLO sample as compared to the post-treated W300 and A300 electrodes can be explained by a combination of less electrochemical oxygen removal and a higher conversion of the evolving reactive oxygen into several products. The first effect is supported by the observation of a lower capacity for the

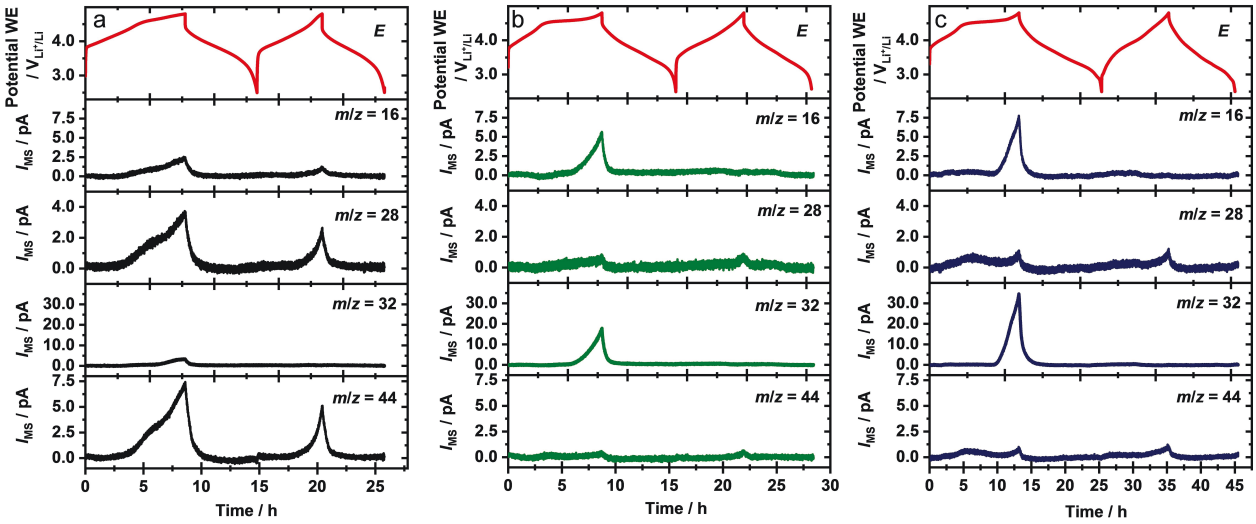

Figure 8. DEMS measurements of LRLO (a), W300 (b) and A300 (c) in half cell configuration (C/10) during the first two full cycles using a membrane inlet to transfer the gaseous products to the mass spectrometer: Cathode potential curve (upper panel) as well as mass spectrometer signals (remaining panels) for m/z = 16, 28, 32 and 44 vs. time.

© 2022 The Authors. ChemSusChem published by Wiley-VCH GmbH

pristine sample, which we mainly attribute to a lower electrochemical accessibility of the surface regions due to the Na_2CO_3 deposits and a possible lower particle surface. The second contribution can result from a partial trapping of reactive oxygen species below or in the Na_2CO_3 impurities, provided that these species have a sufficiently long lifetime. This will not only reduce the measured O_2 signal, but also allow a more efficient reaction between the evolved reactive oxygen and the electrolyte, in good agreement with the significantly more pronounced CO_2 evolution on this sample as compared to the treated samples. The absence of measurable O_2 evolution in the second cycle in all three samples tested here corresponds to previous findings for comparable systems,[61,67,70] where this was related to complete depletion of removable oxygen during activation. However, it cannot be excluded that there is some further oxygen release during subsequent cycling, which directly reacts with the electrolyte. Comparing with the d*Q*/dV signals of the electrochemical cycling above 4.5 V, this effect is likely more pronounced for LRLO and A300.

The increase of the O_2 signal from W300 to A300 can be explained by the structural instability of the material before the calcination step. Nakamura et al.[42] investigated the influence of vacancies on the stability of $Li_{1.2}Mn_{0.6}Ni_{0.2}O_{2-\delta}$ and reported a phase separation for $\delta > 0.042$ into Ni_6MnO_8 and a layered Ni-deficient Li–Mn enriched $Li(Li,Mn,Ni)O_{2-\delta}$ phase after calcination above 400 °C under atmosphere with reduced oxygen partial pressure. In A900, a similar phase segregation was observed, leading to the assumption that the acid treatment leads probably to the formation of O vacancies. After the calcination step at 300 °C, A300 is most probably in a metastable state. During electrochemical cycling a phase transformation into a thermodynamically more favored equilibrium is supposed, which is accompanied by a strong oxygen loss in the structure. Furthermore, the TEM investigation of A300 has shown a formation of Ni-enriched and Mn-enriched domains, which leads to the assumption that the content of oxygen releasing Li_2MnO_3 domains is increased. Both explanations are in accordance with the faster electrochemical aging behavior of A300.

The significantly lower amount of CO_2 evolution on the post-treated samples as compared to pristine LRLO is explained by the essentially complete removal of Na_2CO_3 after washing. In that case, CO_2 formation is only possible by reaction with the electrolyte, whereas for the pristine LRLO electrode CO_2 formation is also possible by decomposition of Na_2CO_3, for example, by chemical reaction with H^+ species.[66] A more detailed analysis of the CO_2 peak shapes and potential ranges is given below.

More detailed information on the potential dependence of the gas evolution is obtained from Figure 9, where the main mass spectrometric signals ($m/z = 32$ and $m/z = 44$) are plotted as a function of the potential. For all three electrodes, O_2 release starts at approximately ≈4.6 V, followed by a steep increase of the signal up to the upper potential limit of 4.8 V. Based on previous reports for similar materials,[61,68,71] it is assigned to the electrochemical activation of the Li_2MnO_3 domains present in the materials. Interestingly, the increase of the $m/z = 32$ ion current vs. potential differs from the exponential behavior expected from the common Butler-Volmer kinetics in a potentiodynamic scan at constant potential scan rate. The increase of the signal starts rapid upon 4.6 V, with a slight decrease of the slope at the end of charge. This is more pronounced for the treated samples. Switching from the end of charge to the beginning of discharge, the potential very rapidly (within few seconds) shifts to approximately 4.4 V at a nearly constant O_2 formation rate for the LRLO sample. For the W300 and A300 electrodes, the potential shift is less pronounced, reaching approximately 4.5 and 4.7 V, respectively. The following strong signal decay deviates for all samples from an exponential decay with decreasing potential, changing to a more sigmoidal shape. The background level is reached at approximately 4.0 V. In the second cycle, the $m/z = 32$ signal

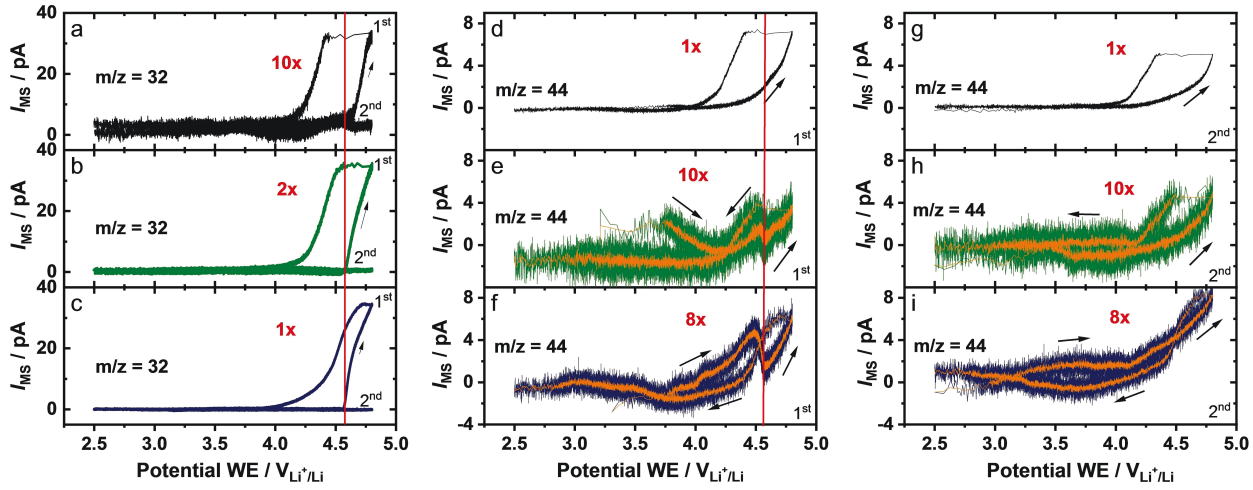

Figure 9. Mass spectrometric signals for m/z = 32 and m/z = 44 from Figure 7, replotted as a function of the potential for m/z = 32 (a–c, 1st and 2nd cycle), m/z = 44 (d–f, 1st cycle) and m/z = 44 (g–i, 2nd cycle). The same material is arranged horizontally in the same line and in the corresponding color: LRLO (black, topmost panel), W300 (green, middle panel) and A300 (blue, bottom panel). Averaged curves (10 points average) have been added for better clarity over the signal course of some graphs in orange. The enlargement factors are given in red for better comparability.

© 2022 The Authors. ChemSusChem published by Wiley-VCH GmbH

remains at the background level, irrespective of the applied potential. As it has been derived from a mass spectrometry study using ^{18}O labeled layered $Li[Li_{0.2}Ni_{0.2}Mn_{0.6}]O_2$ material,[72] it is assumed that the O_2 originates mainly from the active electrode material rather than from the organic carbonate based electrolyte.

The differences in shape of the O_2 evolution curves of LRLO, W300 and A300 are predominantly caused by differences in their potential curves and the corresponding potential variation rates. As evident from the potential curves (Figure 8), these differences are more pronounced for the W300 and A300 electrodes, in particular for the latter one. The strong increase of the O_2 evolution starts in the flat potential plateau region with a low potential variation rate and ends up with a high potential variation rate at the end of charge, which explains the decreased slope of the O_2 signal (Figure 9a–c). The differences in the potential drop at the beginning of discharge and in the subsequent signal decay of the oxygen can be explained by the comparison with the d*Q*/d*V* data (Figure 7c–e), since in contrast to LRLO, A300 shows a lower overpotential and smoother change potential variation rate.

Moving on to the CO_2 signal, a pronounced signal for the LRLO electrode with an onset at approximately 4.1 V, well below the onset of O_2 evolution (Figure 9d), is found in the first cycle. This is followed by an almost exponential increase above about 4.6 V. In contrast, the CO_2 signal of A300 is significantly lower and clearly shows a first increase up to 4.4 V and a second one above 4.6 V, with a local minimum in between (Figure 9f). A similar, but less pronounced characteristic curve is observed for W300 (Figure 9e). It can be assumed that both maxima of W300 and A300 reflect contributions from different processes, as it had been proposed in previous studies.[61,68] In those studies the authors suggested that the CO_2 evolution at lower potentials is either caused by the oxidation/decomposition of (surface) impurities[68,73–76] or by oxidation of the electrolyte by high-valence Ni ions.[61] The results of an operando mass spectrometry study by Luo et al.,[72] using ^{18}O labeled layered $Li_{1.2}Ni_{0.2}Mn_{0.6}O_2$ material with Li_2CO_3 impurities, showed that the CO_2 evolution observed for this material includes significant amounts of labelled $C^{18}O^{16}O$. They assumed that this originated from the oxidation of electrolyte with released lattice oxygen species, over the entire range of CO_2 evolution, from 4.2 to 4.8 V. However, it should be noted that the ^{18}O exchange treatment used by these authors results in partial ^{18}O exchange both in the oxide and in the Li_2CO_3 impurity.[68] Therefore, we favor the assignment for the low potential peak put forward by Yabuuchi et al. and by the Gasteiger group,[66,68,73–76] who proposed that this peak results from a proton induced decomposition of Li_2CO_3, according to Equation (1).

$$2\ H^+ + Li_2CO_3 \rightarrow CO_2 + H_2O + 2\ Li^+. \quad (1)$$

The protons are likely formed by oxidation of trace impurities in the electrolyte or of the electrolyte itself.[66]

The high-potential CO_2 peak, which appears at potentials above $E \approx 4.6$ V and essentially corresponds to the O_2 evolution peak, is attributed to oxidation of the electrolyte by reaction with reactive (singlet) oxygen, which is released from the electrode upon activation of the Li_2MnO_3 domains.[61,66–68,70,72,77]

Plotting the MS signal against the potential highlights the strength of this DEMS setup. Here, the decrease of the signal at 4.5 V after the first maximum is clearly visible for W300 and A300, compared to the time dependent plot (Figure 7) and data given in the related, above-discussed literature. Strehle et al. explained the decrease of the CO_2 evolution rate with a limited quantity of possible reactants (impurities) for the reaction, being responsible for the first peak.[68] However, from the location of the signal drop, it cannot be excluded that the decrease of the signal is only related to the constant potential at the flat plateau. Under the hypothesis that the CO_2 evolving side reaction is related to the surface potential, the reaction has to reach a chemical equilibrium, which leads to a decrease of the gas evolution during the occurring phase transformation of the material at the plateau.

The remaining CO_2 signal in the second cycle can be mainly attributed to different Li species, like Li_2O_2 or Li_2CO_3, which can be formed at the end of the discharge and to the reaction of further released oxygen at potentials >4.6 V with the electrolyte.[73] This also means that in the second cycle sizable amounts of reactive oxygen are released, which, however, are fully consumed for reaction with the electrolyte. This is in accordance with the absence of the O_2 signal. Consequently, the higher CO_2 signal for A300 compared to W300 supports the observation of a faster capacity decrease of A300 due to a higher oxygen release.

For LRLO, the situation differs significantly from the W300 and A300 materials by the high amounts of Na_2CO_3 in the powder. There is the pronounced shoulder at ~4.6–4.7 V, which is clearly visible in the plots vs. time (Figure 8a), but hardly resolved in the plot vs. potential (Figure 9d). This discrepancy is caused by the location of the shoulder in the range of the potential plateau region, with fast changes of the potential curve slope at the beginning and at the end of the plateau. However, the high CO_2 evolution rate and the missing characteristic signal drop at 4.5 V in Figure 9d compared to A300 and W300 indicate that the CO_2 evolution in LRLO is dominated by the Na_2CO_3 decomposition, analogous to Equation (1). A competing electrochemical oxidation of Na_2CO_3, which cannot be fully excluded from the present data, would not affect the signal shape in Figure 9d. Furthermore, the possible presence of a Na_2CO_3 cover layer can increase the reaction efficiency between the electrolyte and reactive oxygen species due to the slower off-transport of the oxygen species and the related reaction products, like protons. This mechanism explains the much smaller O_2 peak (first cycle) observed for LRLO compared to the treated W300 and A300 electrodes.

The CO_2 signal of LRLO in the second cycle is lower compared to the first cycle, but still high relatively to the other electrodes. Most likely, the Na_2CO_3 impurities are not fully removed in the first cycle, further decomposition can occur in the second cycle and presumably also in the following ones. Additionally, it is possible that the amount of reactive oxygen evolved on the LRLO electrode in the second cycle is also significantly higher than on the other samples. This can be

© 2022 The Authors. ChemSusChem published by Wiley-VCH GmbH

understood when considering that part of the surface was not accessible in the first cycle due to the Na_2CO_3 impurities, resulting in a successive activation of the material, which was already suggested during the electrochemical cycling.

Summarizing the DEMS results, the more pronounced O_2 formation for the treated samples and the opposite trend for the CO_2 formation clearly indicate that the Na_2CO_3 impurities were removed during the treatment and that the chemical activation of the material was successful. Additionally, the high CO_2 formation of LRLO supports the assumption that during subsequent cycling the active material becomes more accessible and that the Na_2CO_3 impurities are not fully decomposed even after the first two cycles. Finally, the high O_2 signal in the first and the increased CO_2 signal in the second cycle of A300 underlines in combination with the decreasing discharge capacity during electrochemical cycling the hypothesis that the acidic treatment was too aggressive and therefore A300 undergoes a faster surface densification into a structure similar to A900.

Conclusion

Spherical, Co-free $Li_{1.2}Mn_{0.6}Ni_{0.2}O_2$ was synthesized using a scalable process. Post-treatment of the as-synthesized material with water or diluted HNO_3, followed by calcination at 300 °C and 900 °C, respectively, had a strong effect on the electrochemical performance. Chemical impurities from the synthesis process were eliminated independently from the applied washing procedure. The effect of the post-treatment steps could be classified into two groups. While the 300 °C treated samples were electrochemically activated (up to 270 mAh g^{-1}), heat treatment at 900 °C lead to deactivation of the materials. The effect of the post-treatment increased with higher acidity of the washing media, leaching more metal ions out of the materials, and thus leading to local Mn- and Ni-enrichments. The activation could be explained by the formation of a thin spinel phase on top of the surface of the primary crystallites. This was indicated by the increasing fraction of Mn^{III} ions detected by XPS analysis, and supported by XRD and Raman spectroscopy. DEMS measurements showed an increased O_2 release during the first delithiation with a simultaneously reduced CO_2 formation, which underlined the complete removal of Na_2CO_3. It was clearly shown that the deactivation of the materials calcinated at 900 °C was caused by the phase separation of the powders into Mn-enriched LRLO particles and Ni-rich rock-salt structures, such as Ni_6MnO_8. The latter was located predominantly at the grain boundaries and the surface regions of the crystallites and it was assumed to block Li^+ diffusion pathways. Overall, this work showed that simple post-treatment steps could have significant positive impact on the electrochemical performance of Co-free LRLO material. Critical parameters, like the pH of the applied solution or the temperature of the subsequent heat treatment, have a strong influence on the electrochemical behavior and need to be adjusted carefully.

Experimental Section

Synthesis of the pristine material and post treatment steps

The pristine powder $Li_{1.2}Mn_{0.6}Ni_{0.2}O_2$ (LRLO) was synthesized by coprecipitation route. In a continuous stirred tank reactor (CSTR, $V = 1$ L) a solution of manganese and nickel nitrate (Roth) was mixed under vigorous stirring with a NH_4OH (Roth), a Na_2CO_3 (Roth) and a small amount of NaOH (Roth, to adjust the pH) solution. The excess suspension was filtrated continuously. The resulting spherical precursor material (Mn/Ni = 3:1) was washed extensively with deionized water, dried and a small amount was mixed with stoichiometric amount of LiOH x H_2O (Roth, Li/M = 1.50). The final calcination step was conducted at 900 °C under air.

The different post treatment steps were done in a similar way, using ultrapure H_2O ($\sigma < 0.55$ µS cm^{-1}). For the water treatment, pristine LRLO (5.5 g) was mixed with hot H_2O (20 mL), stirred for 20 min and finally the water was decanted. This procedure was repeated three times and after the last residence time the suspension was filtrated and the powder was dried (120 °C, overnight). For acidic treatment HNO_3 (65 %, Merck) was used. LRLO (5.5 g) was mixed with H_2O (RT, 20 mL), acid was carefully added until the pH of the solution reached a value of pH = 7, the suspension was stirred for 20 min and afterwards the solution was decanted, too. In the second and third repetition, only H_2O without additional acid was used. As a last step, the mixture was filtrated and the solid residue was dried (120 °C, overnight). Both water and acid treated powders were divided in two equal portions. They were calcinated at 300 °C (W300 and A300) as well as at 900 °C (W900 and A900).

Investigation of the post-treatment procedure

Both types of washing solutions were collected, filtrated, acidified with HNO_3 (conc., p.a.), diluted to a defined volume and analyzed by ICP-OES (Spectro Arcos SOP). For further understanding of the heat treatment step after washing, the freshly washed powders were dried overnight under vacuum (80 °C) and subsequently TGA-DSC-MS measurements (heating rate: 10 K min^{-1}) were conducted in Al_2O_3 crucibles under air, using a TGA-DSC device (Netzsch STA 449 C) coupled with a mass spectrometer (Netzsch QMS 403). DSC measurements were corrected with a blank measurement under the same conditions. The same powders were used without further heat treatment for the quantification of surface carbonates and hydroxides through acid-base titration measurements. 0.20 g of powder was stirred in degassed ultrapure H_2O ($\sigma < 0.55$ µS cm^{-1}, 30 mL, 7 min) under a N_2 gas flow to avoid further carbonate contamination. The suspension was filtrated and the filtrate was instantaneously titrated with hydrochloric acid (0.01 M, OMNIS titrator, Metrohm) under N_2 gas flow. The equivalence points (EPs) were determined using potentiometric endpoint detection with a pH electrode. The amount of carbonate and hydroxide ions were calculated from the EPs based on the method of Warder.[78] The evolution of the pH after adding the LRLO powder (2.0 g) into water or acid containing solution (12 mL), respectively, was measured with a calibrated pH electrode and recorded by the OMNIS titration system at room temperature.

Structural and chemical characterization

The chemical characterization of the powders was done by ICP-OES measurements of a diluted aqua regia digestion (Spectro Arcos SOP) and cerimetric redox titration. For the latter, the amount of transition metal in the powders was determined through complexometric back titration of Na-EDTA with a Cu^{II} solution, buffering

© 2022 The Authors. ChemSusChem published by Wiley-VCH GmbH

the pH with NH_4^+/NH_3 buffer. In a second titration step the powder was digested in an acidic $(NH_4)_2Fe(SO_4)_2$ solution under nitrogen and the remaining Fe^{II} was back titrated with Ce^{IV} solution. All titration experiments were conducted with an OMNIS titrator (Metrohm). The oxygen stoichiometry was calculated by the combination of the ICP and cerimetry results. XRD measurements were performed using a D8 Advance diffractometer (Bruker AXS, Bragg-Brentano geometry in reflection mode, Cu-K_α radiation, LYNXEYE XE detector). TOPAS V6 was used for Rietveld refinement of the diffraction data, using a $Li_{1.2}Mn_{0.6}Ni_{0.2}O_2$ structural model of Fell et al.[41] For A900 an additional Ni_6MnO_8 structural model was applied.[46] SEM images were obtained by using a Leo 1530 VP (Zeiss) scanning electron microscope with an acceleration voltage of 5 kV and an Everhart-Thornley-detector. The cross-section of the particles was prepared by mixing the powder with an epoxy resin, applying the mixture on a support substrate and polishing the surface with a broad Ar^+ ion beam (IM4000Plus, Hitachi). The Raman investigations of the powders and the cross section were carried out with an alpha300 R (WITec) confocal Raman microscope over a spectral range between −70 and 1108 rel. cm^{-1}. The system consists of a spectrometer with a grating of 1800 l mm^{-1} and a CCD-camera (1600×200 pixels) as well as a Nd:YAG laser with an excitation wavelength of 532 nm. The laser power was adjusted to 1.5 mW after microscope transit. The powders were measured using a 10x objective and for the cross sections a 100x objective was used (both Zeiss).

Electron transparent TEM samples were prepared using a focused Ga-ion beam (FIB) system (Zeiss, type NVision 40). The surface of a typical sample particle of about 15 μm in diameter was protected using carbon deposition and applying the in situ gas injection (GIS) system integrated into the FIB. A slab of material of about 10 μm by 4 μm by 10 μm (length, width, depth) was etched out of the particle using a 30 kV Ga-ion beam. This slab was lifted out and welded to a TEM lift out grid (Pelco company) using a piezo micromanipulator. The sample was subsequently thinned down to a final thickness of about 50 to 80 nm. The Ga-ion beam current was reduced and the voltage was lowered to 5 kV to minimize amorphization damage.

The TEM investigations were carried out using a Talos 200X STEM (Thermofisher) operated at 200 kV. The system was equipped with an energy dispersive X-ray (EDX) detector (type Thermofisher SuperX). TEM images were acquired using a CMOS camera (16 M pixels, type Thermofisher CETA). HAADF images together with EDX mappings were acquired to determine the local elemental composition. HRTEM images and diffraction pattern were used to determine the crystal structure.

For the XPS measurements, a commercial XPS machine from Physical Electronics (PHI 5800 ESCA) equipped with a hemispherical electron analyzer, a monochromatic Al K_α X-ray source (1486.6 eV) and a flood gun to avoid charging of the sample was used. Survey spectra were recorded using a pass energy of 93.9 eV, detail spectra with 29.35 eV. Both angles (angle of photon incidence on the sample and angle of emitted photoelectrons) are 45° with respect to the surface normal (sample holder, respectively). The binding energies (BEs) of all spectra were calibrated with respect to the C 1s peak of ubiquitous carbon, which was fixed at a binding energy (BE) of 284.8 eV. The data were evaluated (deconvolution of spectra) by using the commercial software package CasaXPS (Casa Software Ltd., version 2.3.23PR1.0). The fitting of the Mn 2p spectra was performed according to data by Biesinger et al.[79] for the Mn 2p, Mn 3s, and Mn 3p spectra, we additionally refer to the publication by Ilton et al.[55]

Electrochemical characterization

A homogeneous slurry of each active material, polyvinylidene difluoride (PVDF, Solef 5130, Solvay) and conductive carbon Super C45 (Timcal) (dry ratio of 85:5:10) dispersed in an adequate amount of *N*-methyl-2-pyrrolidinone (NMP, Sigma Aldrich) was coated on an aluminum foil using the doctor blade technique. After drying, disk electrodes with a diameter of 12 mm were punched out, pressed with a hydraulic press (8 t cm^{-2} for 60 s), dried overnight under vacuum (120 °C) and transferred directly without contact to air into an argon-filled glovebox (MBraun, O_2 and H_2O < 0.1 ppm). Subsequently, the CR2032 coin cells (Hohsen) were assembled with one disk electrode, a lithium metal foil (450 μm, 12 mm diameter), two glass fiber coins (16 mm diameter, Whatman) as a separator and electrolyte (150 μL, 1 M $LiPF_6$ in EC/DMC = 1:1 by wt.). The typical active material loading of the electrodes was between 3 and 4 mg. The cells were cycled between 2.5 and 4.8 V using a BaSyTec galvanostat at room temperature. The applied currents are presented in the corresponding figures (1 C = 250 mA g^{-1}). The presented capacities of the electrochemical measurements are mean values of at least three cells.

The design of the DEMS cell used was similar to that already reported.[65] Differently from the previous design, for contacting the working electrode an Al O-ring and Al wire were used. The steel frit underneath the membrane was exchanged by perforated polyether-ether-ketone (PEEK) plate to avoid side reactions. The electrode preparation was done similarly to the electrodes for electrochemical testing but on an Al coated (ALD) FEP membrane (50 μm thickness, Bohlender, Bola) instead of Al foil. The electrodes of 12 mm in diameter were punched from the membrane, dried at 100 °C under vacuum in a glovebox under argon atmosphere (LabMaster, MBraun, water and oxygen content < 0.5 ppm) before use. Li metal stripes were used as counter and reference electrodes, respectively. They were cut from lithium foil (purity 99.9 %, Alfa Aesar) and separated in the cell by a Teflon plate. The bottom part was connected to the ultrahigh vacuum (UHV) chamber inlet of the mass spectrometer (Pfeiffer Vacuum QMA 410) to monitor the gas evolution upon cycling differentially without using any carrier gas. LP30 electrolyte (1 M $LiPF_6$ in EC/DMC = 1:1 by wt, Solvionic, purity > 99.9 %, water content < 20 ppm) was filled into the DEMS cell (0.7 mL). The assembly of the cell and all measurements were performed in an Ar filled glovebox (LabMaster Pro, MBraun, oxygen content < 0.1 ppm, water content < 0.5 ppm). Prior to the measurements the electrodes were resting in the electrolyte-filled cell for at least two hours, to achieve stable OCP values (typically, around 3.0 V vs. Li^+/Li) and stable background signals of the selected ion currents. A Princeton Research Instruments (PAR) 263 A potentiostat was used to conduct the galvanostatic experiments with a current of 0.1 mA, which corresponds to the C/10 rate at the applied loading of the active material, at cut-off potentials 2.5 and 4.8 V (vs. Li^+/Li), simultaneously measuring the intensity of selected ion currents.

Acknowledgements

This work received funding by the European Union within the Si-DRIVE project as a part of the European Union's Horizon 2020 research and innovation programme under grant agreement No. 814464 and by the German Federal Ministry of Education and Research (BMBF) in the cluster project ExcellBattMat (grant numbers 03XP0257 A and 03XP0257 C). The authors thank Wolfgang Weirather and Dagmar Weirather-Köstner (both ZSW) for their support during the synthesis process and the electrochemical

© 2022 The Authors. ChemSusChem published by Wiley-VCH GmbH

characterization of the materials as well as Gisela Arnold (ZSW) for the ICP-OES and Peter Sichler (ZSW) for the TGA-MS measurements. The work contributes to the research performed at CELEST (Center for Electrochemical Energy Storage Ulm-Karlsruhe).

Conflict of Interest

The authors declare no conflict of interest.

Data Availability Statement

The data that support the findings of this study are available from the corresponding author upon reasonable request.

Keywords: acid treatment · DEMS measurements · Li-rich cathode materials · lithium-ion batteries · surface modification

[1] M. Child, D. Bogdanov, C. Breyer, *Energy Procedia* **2018**, *155*, 44.
[2] a) B. Nykvist, M. Nilsson, *Nat. Clim. Change* **2015**, *5*, 329; b) M. Marinaro, D. Bresser, E. Beyer, P. Faguy, K. Hosoi, H. Li, J. Sakovica, K. Amine, M. Wohlfahrt-Mehrens, S. Passerini, *J. Power Sources* **2020**, *459*, 228073.
[3] A. Manthiram, J. C. Knight, S.-T. Myung, S.-M. Oh, Y.-K. Sun, *Adv. Energy Mater.* **2016**, *6*, 1501010.
[4] B. Qiu, M. Zhang, L. Wu, J. Wang, Y. Xia, D. Qian, H. Liu, S. Hy, Y. Chen, K. An, Y. Zhu, Z. Liu, Y. S. Meng, *Nat. Commun.* **2016**, *7*, 12108.
[5] W. Zuo, M. Luo, X. Liu, J. Wu, H. Liu, J. Li, M. Winter, R. Fu, W. Yang, Y. Yang, *Energy Environ. Sci.* **2020**, *13*, 4450.
[6] R. A. House, G. J. Rees, M. A. Pérez-Osorio, J.-J. Marie, E. Boivin, A. W. Robertson, A. Nag, M. Garcia-Fernandez, K.-J. Zhou, P. G. Bruce, *Nat. Energy* **2020**, *5*, 777.
[7] M. M. Thackeray, C. S. Johnson, J. T. Vaughey, N. Li, S. A. Hackney, *J. Mater. Chem.* **2005**, *15*, 2257.
[8] Z. Lu, Z. Chen, J. R. Dahn, *Chem. Mater.* **2003**, *15*, 3214.
[9] H. Koga, L. Croguennec, P. Mannessiez, M. Ménétrier, F. Weill, L. Bourgeois, M. Duttine, E. Suard, C. Delmas, *J. Phys. Chem. C* **2012**, *116*, 13497.
[10] a) W. Hua, S. Wang, M. Knapp, S. J. Leake, A. Senyshyn, C. Richter, M. Yavuz, J. R. Binder, C. P. Grey, H. Ehrenberg, S. Indris, B. Schwarz, *Nat. Commun.* **2019**, *10*, 5365; b) F. Wu, G.-T. Kim, T. Diemant, M. Kuenzel, A. R. Schür, X. Gao, B. Qin, D. Alwast, Z. Jusys, R. J. Behm, D. Geiger, U. Kaiser, S. Passerini, *Adv. Energy Mater.* **2020**, *10*, 2001830; c) Y. Li, M. J. Zuba, S. Bai, Z. W. Lebens-Higgins, B. Qiu, S. Park, Z. Liu, M. Zhang, L. F. Piper, Y. S. Meng, *Energy Storage Mater.* **2021**, *35*, 99.
[11] a) P. K. Nayak, J. Grinblat, M. Levi, E. Levi, S. Kim, J. W. Choi, D. Aurbach, *Adv. Energy Mater.* **2016**, *6*, 1502398; b) F. Wu, G.-T. Kim, M. Kuenzel, H. Zhang, J. Asenbauer, D. Geiger, U. Kaiser, S. Passerini, *Adv. Energy Mater.* **2019**, *9*, 1902445; c) G. Chen, J. An, Y. Meng, C. Yuan, B. Matthews, F. Dou, L. Shi, Y. Zhou, P. Song, G. Wu, D. Zhang, *Nano Energy* **2019**, *57*, 157; d) J. An, L. Shi, G. Chen, M. Li, H. Liu, S. Yuan, S. Chen, D. Zhang, *J. Mater. Chem. A* **2017**, *5*, 19738.
[12] a) C. P. Laisa, R. N. Ramesha, K. Ramesha, *Electrochim. Acta* **2017**, *256*, 10; b) X. Jin, Q. Xu, H. Liu, X. Yuan, Y. Xia, *Electrochim. Acta* **2014**, *136*, 19; c) H. Xu, S. Deng, G. Chen, *J. Mater. Chem. A* **2014**, *2*, 15015.
[13] D. Chen, F. Zheng, L. Li, M. Chen, X. Zhong, W. Li, L. Lu, *J. Power Sources* **2017**, *341*, 147.
[14] a) Y. Wu, J. Ming, L. Zhuo, Y. Yu, F. Zhao, *Electrochim. Acta* **2013**, *113*, 54; b) M. Xu, Z. Chen, L. Li, H. Zhu, Q. Zhao, L. Xu, N. Peng, L. Gong, *J. Power Sources* **2015**, *281*, 444; c) C. Zhou, P. Wang, B. Zhang, J. Zheng, Y. Zhou, C. Huang, X. Xi, *J. Electrochem. Soc.* **2018**, *165*, A1648-A1655.
[15] X. Zhang, R. Yu, Y. Huang, X. Wang, Y. Wang, B. Wu, Z. Liu, J. Chen, *ACS Sustainable Chem. Eng.* **2018**, *6*, 12969.
[16] Y. Lee, J. Lee, K. Y. Lee, J. Mun, J. K. Lee, W. Choi, *J. Power Sources* **2016**, *315*, 284.
[17] U. Breddemann, E. M. Erickson, V. Davis, F. Schipper, M. Ellwanger, M. Daub, A. Hoffmann, C. Erk, B. Markovsky, D. Aurbach, I. Krossing, *ChemElectroChem* **2019**, *6*, 3337.
[18] X. Ding, D. Luo, J. Cui, H. Xie, Q. Ren, Z. Lin, *Angew. Chem. Int. Ed.* **2020**, *59*, 7778.
[19] W. Guo, C. Zhang, Y. Zhang, L. Lin, W. He, Q. Xie, B. Sa, L. Wang, D.-L. Peng, *Adv. Mater.* **2021**, *33*, e2103173.
[20] S. Han, B. Qiu, Z. Wei, Y. Xia, Z. Liu, *J. Power Sources* **2014**, *268*, 683.
[21] H. Sclar, J. Sicklinger, E. M. Erickson, S. Maiti, J. Grinblat, M. Talianker, F. Amalraj Susai, L. Burstein, H. Beyer, L. Hartmann, G. Avruschenko, H. A. Gasteiger, B. Markovsky, D. Aurbach, *J. Electrochem. Soc.* **2020**, *167*, 110563.
[22] a) J. Zhang, Z. Lei, J. Wang, Y. NuLi, J. Yang, *ACS Appl. Mater. Interfaces* **2015**, *7*, 15821; b) P. Oh, S. Myeong, W. Cho, M.-J. Lee, M. Ko, H. Y. Jeong, J. Cho, *Nano Lett.* **2014**, *14*, 5965.
[23] S.-H. Kang, C. S. Johnson, J. T. Vaughey, K. Amine, M. M. Thackeray, *J. Electrochem. Soc.* **2006**, *153*, A1186.
[24] S. Ramakrishnan, B. Park, J. Wu, W. Yang, B. D. McCloskey, *J. Am. Chem. Soc.* **2020**, *142*, 8522.
[25] D. Y. Yu, K. Yanagida, *J. Electrochem. Soc.* **2011**, *158*, A1015.
[26] a) M. Metzger, H. Beyer, J. Sicklinger, D. Pritzl, B. Strehle, H. A. Gasteiger, H. Sclar, E. M. Erickson, F. Amalraj, J. Grinblat, D. Aurbach, WO2019/002116 A1, **2019**; b) J. Sicklinger, H. Beyer, L. Hartmann, F. Riewald, C. Sedlmeier, H. A. Gasteiger, *J. Electrochem. Soc.* **2020**, *167*, 130507.
[27] K. Xu, S. Pang, Y. Wang, X. Shen, H. Wen, W. Wang, Y. Su, X. Xi, *J. Electrochem. Soc.* **2017**, *164*, A2348-A2354.
[28] a) S. Pang, M. Zhu, K. Xu, X. Shen, H. Wen, Y. Su, G. Yang, X. Wu, S. Li, W. Wang, X. Xi, H. Wang, *J. Electrochem. Soc.* **2018**, *165*, A1897-A1902; b) B. Liu, *Int. J. Electrochem. Sci.* **2018**, 7578.
[29] M.-J. Wang, A.-F. Shao, F.-D. Yu, G. Sun, D.-M. Gu, Z.-B. Wang, *ACS Sustainable Chem. Eng.* **2019**, *7*, 12825.
[30] I. Hamam, N. Zhang, A. Liu, M. B. Johnson, J. R. Dahn, *J. Electrochem. Soc.* **2020**, *167*, 130521.
[31] M. Hartman, O. Trnka, V. Veselý, K. Svoboda, *Chem. Eng. Commun.* **2001**, *185*, 1.
[32] J.-W. Kim, H.-G. Lee, *Metall. Mater. Trans. B* **2001**, *32*, 17.
[33] I. A. Reyes, M. Flores, E. G. Palacios, H. Islas, J. C. Juárez, M. Reyes, A. M. Teja, C. A. Pérez, *Minerals* **2021**, *11*, 34.
[34] M. A. Rhamdhani, E. Jak, P. C. Hayes, *Metall. Mater. Trans. B* **2008**, *39*, 218.
[35] H. Henmi, M. Mori, T. Hirayama, N. Mizutani, M. Kato, *Thermochim. Acta* **1986**, *104*, 101.
[36] a) J. Pan, Y. Sun, P. Wan, Z. Wang, X. Liu, *Electrochem. Commun.* **2005**, *7*, 857; b) D. Pritzl, T. Teufl, A. T. S. Freiberg, B. Strehle, J. Sicklinger, H. Sommer, P. Hartmann, H. A. Gasteiger, *J. Electrochem. Soc.* **2019**, *166*, A4056-A4066.
[37] a) P. Strobel, B. Lambert-Andron, *J. Solid State Chem.* **1988**, *75*, 90; b) M. H. Rossouw, M. M. Thackeray, *Mater. Res. Bull.* **1991**, *26*, 463.
[38] T. Zhao, S. Chen, R. Chen, L. Li, X. Zhang, M. Xie, F. Wu, *ACS Appl. Mater. Interfaces* **2014**, *6*, 21711.
[39] A. Rougier, P. Gravereau, C. Delmas, *J. Electrochem. Soc.* **1996**, *143*, 1168.
[40] a) Z. Yang, H. Zhou, Z. Bao, J. Li, C. Yin, *J. Mater. Sci. Mater. Electron.* **2019**, *30*, 19493; b) K. Xu, S. Pang, Y. Wang, X. Shen, H. Wen, W. Wang, Y. Su, X. Xi, *J. Electrochem. Soc.* **2017**, *164*, A2348-A2354.
[41] C. R. Fell, D. Qian, K. J. Carroll, M. Chi, J. L. Jones, Y. S. Meng, *Chem. Mater.* **2013**, *25*, 1621.
[42] T. Nakamura, H. Gao, K. Ohta, Y. Kimura, Y. Tamenori, K. Nitta, T. Ina, M. Oishi, K. Amezawa, *J. Mater. Chem. A* **2019**, *7*, 5009.
[43] D. Marrocchelli, S. R. Bishop, H. L. Tuller, B. Yildiz, *Adv. Funct. Mater.* **2012**, *22*, 1958.
[44] W. Lee, D. Lee, Y. Kim, W. Choi, W.-S. Yoon, *J. Mater. Chem. A* **2020**, *8*, 10206.
[45] H. Taguchi, S. Omori, M. Nagao, H. Kido, M. Shimada, *J. Solid State Chem.* **1995**, *118*, 112.
[46] H. Taguchi, A. Ohta, M. Nagao, H. Kido, *J. Solid State Chem.* **1998**, *135*, 322.
[47] C. Julien, *Solid State Ionics* **2000**, *136–137*, 887.
[48] R. E. Ruther, A. F. Callender, H. Zhou, S. K. Martha, J. Nanda, *J. Electrochem. Soc.* **2014**, *162*, A98.
[49] K. Ben-Kamel, N. Amdouni, A. Mauger, C. M. Julien, *J. Alloys Compd.* **2012**, *528*, 91.
[50] C. M. Julien, M. Massot, *Mater. Sci. Eng. B* **2003**, *100*, 69.
[51] M. H. Brooker, J. B. Bates, *J. Chem. Phys.* **1971**, *54*, 4788.
[52] P. Lanz, C. Villevieille, P. Novák, *Electrochim. Acta* **2013**, *109*, 426.

© 2022 The Authors. ChemSusChem published by Wiley-VCH GmbH

[53] J. Zhang, R. Hu, P. Dai, Z. Bai, X. Yu, M. Wu, G. Li, *J. Mater. Sci. Mater. Electron.* **2018**, *29*, 7510.
[54] G. E. Lloyd, *Mineral. Mag.* **1987**, *51*, 3.
[55] E. S. Ilton, J. E. Post, P. J. Heaney, F. T. Ling, S. N. Kerisit, *Appl. Surf. Sci.* **2016**, *366*, 475.
[56] a) R. T. Haasch, D. P. Abraham, *Surf. Sci. Spectra* **2019**, *26*, 14010; b) M. Sathiya, K. Ramesha, G. Rousse, D. Foix, D. Gonbeau, A. S. Prakash, M. L. Doublet, K. Hemalatha, J.-M. Tarascon, *Chem. Mater.* **2013**, *25*, 1121.
[57] M. C. Militello, S. W. Gaarenstroom, *Surf. Sci. Spectra* **2001**, *8*, 207.
[58] H. Liu, Y. Yang, J. Zhang, *J. Power Sources* **2007**, *173*, 556.
[59] J. Zheng, P. Xu, M. Gu, J. Xiao, N. D. Browning, P. Yan, C. Wang, J.-G. Zhang, *Chem. Mater.* **2015**, *27*, 1381.
[60] X. Zhang, M. Lengyel, R. L. Axelbaum, *AIChE J.* **2014**, *60*, 443.
[61] S. Shen, Y. Hong, F. Zhu, Z. Cao, Y. Li, F. Ke, J. Fan, L. Zhou, L. Wu, P. Dai, M. Cai, L. Huang, Z. Zhou, J. Li, Q. Wu, S. Sun, *ACS Appl. Mater. Interfaces* **2018**, *10*, 12666.
[62] a) J. Zhang, R. Gao, L. Sun, Z. Li, H. Zhang, Z. Hu, X. Liu, *Phys. Chem. Chem. Phys.* **2016**, *18*, 25711; b) Y. Zheng, L. Chen, Y. Su, J. Tan, L. Bao, Y. Lu, J. Wang, R. Chen, S. Chen, F. Wu, *J. Mater. Chem. A* **2017**, *5*, 24292.
[63] G. Assat, D. Foix, C. Delacourt, A. Iadecola, R. Dedryvère, J.-M. Tarascon, *Nat. Commun.* **2017**, *8*, 2219.
[64] S. Gao, Y. Zhang, H. Zhang, D. Song, X. Shi, L. Zhang, *New J. Chem.* **2017**, *41*, 10048.
[65] Z. Jusys, M. Binder, J. Schnaidt, R. J. Behm, *Electrochim. Acta* **2019**, *314*, 188.
[66] A. T. Freiberg, J. Sicklinger, S. Solchenbach, H. A. Gasteiger, *Electrochim. Acta* **2020**, *346*, 136271.
[67] T. Teufl, B. Strehle, P. Müller, H. A. Gasteiger, M. A. Mendez, *J. Electrochem. Soc.* **2018**, *165*, A2718.
[68] B. Strehle, K. Kleiner, R. Jung, F. Chesneau, M. Mendez, H. A. Gasteiger, M. Piana, *J. Electrochem. Soc.* **2017**, *164*, A400-A406.
[69] P. Linstrom, W. G. Mallard, *"Mass Spectra" in NIST Chemistry WebBook; National Institute of Standards and Technology: Gaithersburg, MD 20899*, **2010**.
[70] D. Streich, A. Guéguen, M. Mendez, F. Chesneau, P. Novák, E. J. Berg, *J. Electrochem. Soc.* **2016**, *163*, A964-A970.
[71] N. Guerrini, L. Jin, J. G. Lozano, K. Luo, A. Sobkowiak, K. Tsuruta, F. Massel, L.-C. Duda, M. R. Roberts, P. G. Bruce, *Chem. Mater.* **2020**, *32*, 3733.
[72] K. Luo, M. R. Roberts, N. Guerrini, N. Tapia-Ruiz, R. Hao, F. Massel, D. M. Pickup, S. Ramos, Y.-S. Liu, J. Guo, A. V. Chadwick, L. C. Duda, P. G. Bruce, *J. Am. Chem. Soc.* **2016**, *138*, 11211.
[73] N. Yabuuchi, K. Yoshii, S.-T. Myung, I. Nakai, S. Komaba, *J. Am. Chem. Soc.* **2011**, *133*, 4404.
[74] M. Metzger, B. Strehle, S. Solchenbach, H. A. Gasteiger, *J. Electrochem. Soc.* **2016**, *163*, A1219-A1225.
[75] S. Meini, N. Tsiouvaras, K. U. Schwenke, M. Piana, H. Beyer, L. Lange, H. A. Gasteiger, *Phys. Chem. Chem. Phys.* **2013**, *15*, 11478.
[76] R. Jung, M. Metzger, F. Maglia, C. Stinner, H. A. Gasteiger, *J. Electrochem. Soc.* **2017**, *164*, A1361-A1377.
[77] a) A. T. S. Freiberg, M. K. Roos, J. Wandt, R. de Vivie-Riedle, H. A. Gasteiger, *J. Phys. Chem. A* **2018**, *122*, 8828; b) N. Mahne, S. E. Renfrew, B. D. McCloskey, S. A. Freunberger, *Angew. Chem. Int. Ed.* **2018**, *57*, 5529.
[78] a) A. A. Benedetti-Pichler, M. Cefola, *Ind. Eng. Chem. Anal. Ed.* **1939**, *11*, 327; b) R. B. Warder, *Chem. News* **1881**, *43*, 228.
[79] M. C. Biesinger, B. P. Payne, A. P. Grosvenor, L. W. Lau, A. R. Gerson, R. S. Smart, *Appl. Surf. Sci.* **2011**, *257*, 2717.

Manuscript received: June 3, 2022
Revised manuscript received: July 25, 2022
Accepted manuscript online: July 26, 2022
Version of record online: September 8, 2022

© 2022 The Authors. ChemSusChem published by Wiley-VCH GmbH

ChemSusChem

Supporting Information

Enhanced Electrochemical Capacity of Spherical Co-Free $Li_{1.2}Mn_{0.6}Ni_{0.2}O_2$ Particles after a Water and Acid Treatment and its Influence on the Initial Gas Evolution Behavior

Florian Klein, Joachim Bansmann, Zenonas Jusys, Claudia Pfeifer, Philipp Scheitenberger, Manuel Mundszinger, Dorin Geiger, Johannes Biskupek, Ute Kaiser, R. Jürgen Behm, Mika Lindén, Margret Wohlfahrt-Mehrens, and Peter Axmann*© 2022 The Authors. ChemSusChem published by Wiley-VCH GmbH. This is an open access article under the terms of the Creative Commons Attribution License, which permits use, distribution and reproduction in any medium, provided the original work is properly cited.

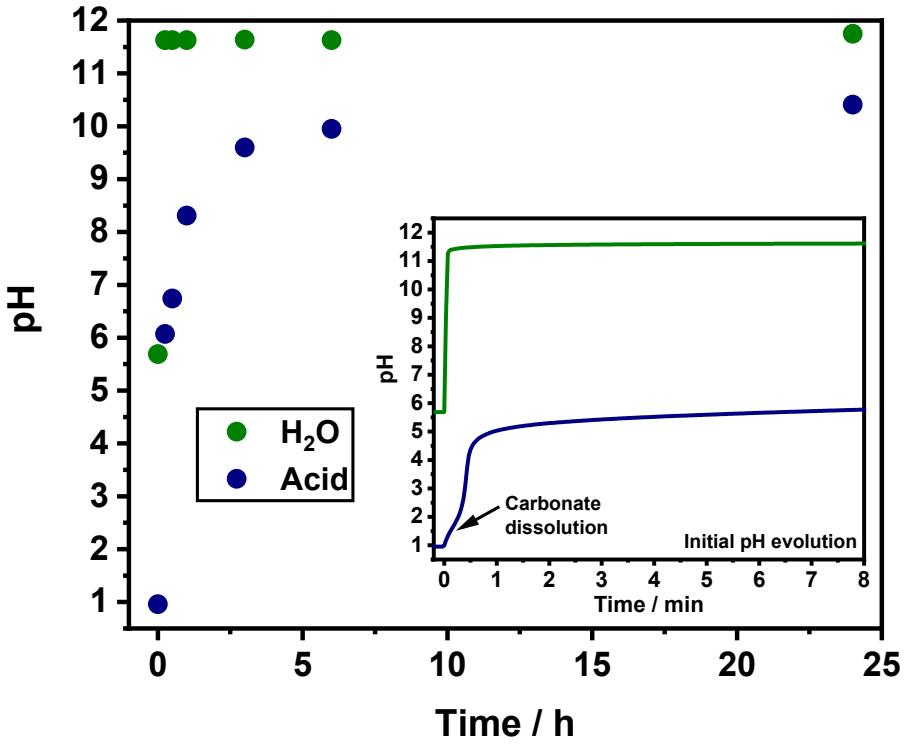

Figure S1. Evolution of the pH after adding LRLO powder into water (green) and into acidic solution (blue). Detailed initial evolution is presented in the inset.

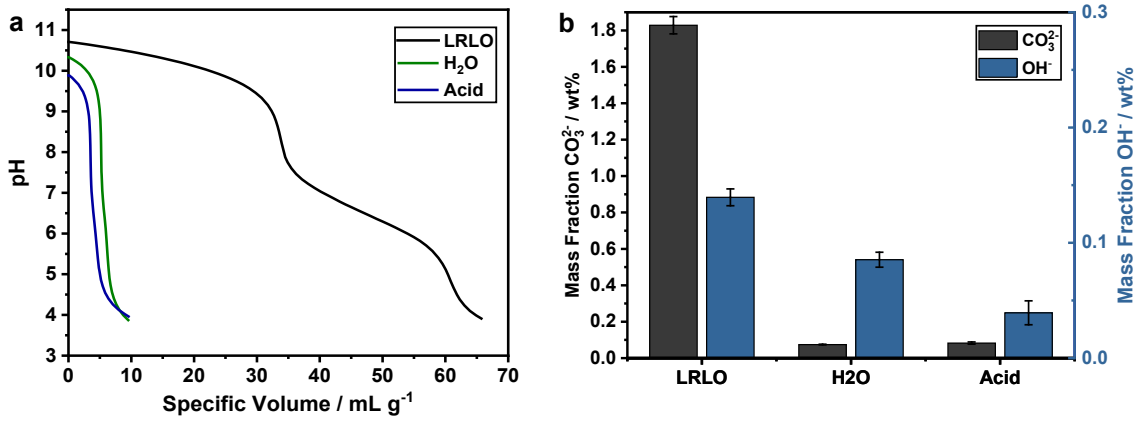

Figure S2. Investigation of the soluble surface species on the LRLO powder (black) after water (green) and acidic (blue) treatment without heat treatment: a) acid-base-titration curve with 0.01 M hydrochloric acid and b) quantitative analysis of carbonate (dark grey) and hydroxide ions (blue).

Table S1. Detailed results of the Rietveld refinement based on the structural model for $Li_{1.2}Mn_{0.6}Ni_{0.2}O_2$ of Fell et al.[1]: space group, lattice parameters, Cell Volume *V*, cation occupancies, atom coordinate *z* of the oxide ions, the estimated crystallite size (integral breadth) and the *R* factor.

	LRLO	**W300**	**W900**	**A300**	**A900***
Spacegroup	*R-3m* (166)	*R-3m* (166)	*R-3m* (166)	*R-3m* (166)	*R-3m* (166)
***a* / Å**	2.858	2.859	2.860	2.863	2.849
***c* / Å**	14.257	14.258	14.262	14.274	14.264
V / Å³	100.9	100.9	101.1	101.3	100.2
Li_{Li} (3a: 0, 0, 0)	0.98	0.99	0.99	0.99	0.99
Ni_{Li} (3a: 0, 0, 0)	0.02	0.01	0.01	0.01	0.01
Li_{TM} (3b: 0, 0, 1/2)	0.23	0.22	0.18	0.18	0.18
Mn_{TM} (3b: 0, 0, 1/2)	0.59	0.60	0.60	0.63	0.64
Ni_{TM} (3b: 0, 0, 1/2)	0.18	0.18	0.18	0.19	0.18
***z* [O (6c: 0, 0, z)]**	0.240	0.240	0.240	0.240	0.240
Crystallite Size / nm	108	120	146	93	181
R_{wp} / %	9.6	10.0	9.6	8.4	11.7

* additional Ni_6MnO_8 phase was used for the refinement based on Taguchi et al.[2]

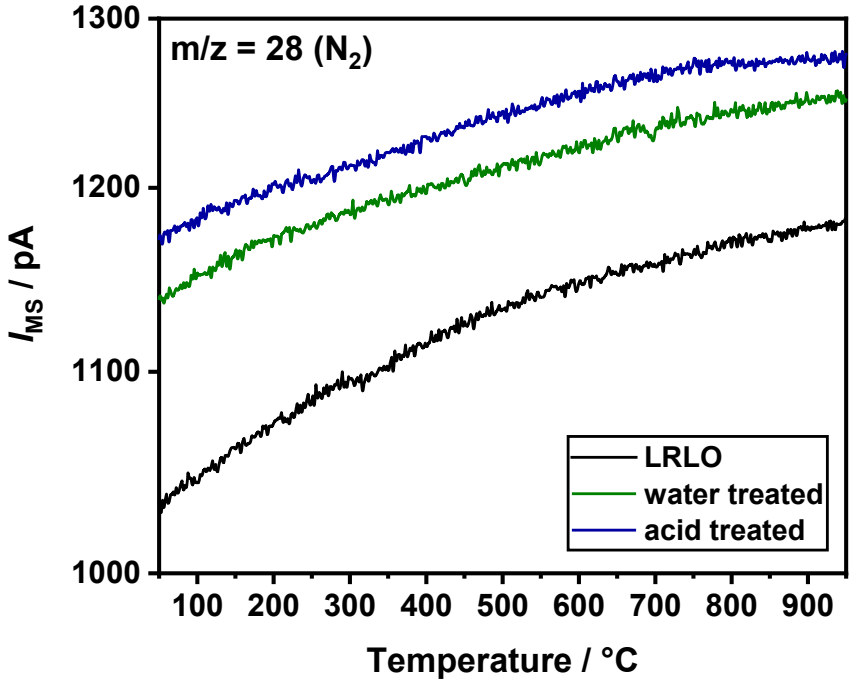

Figure S3. Corresponding MS curves to the TGA-DSC-MS experiments for m/z = 28 (N_2) measured with a heating rate of 10 K min^{-1} under air atmosphere for the as-synthesized LRLO powder (black), LRLO after aqueous washing (green) and LRLO after acidic treatment (blue).

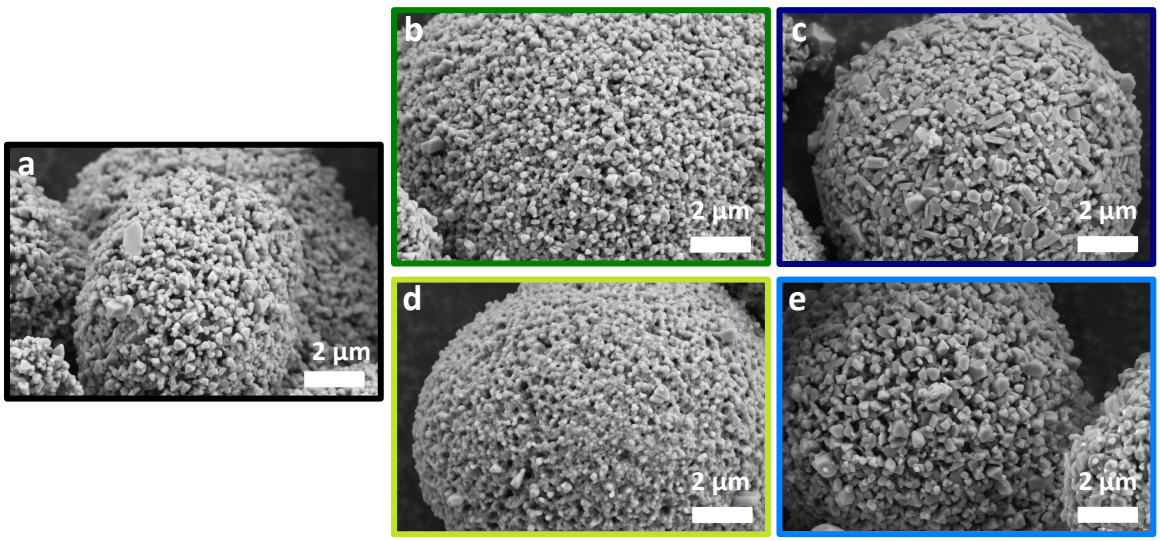

Figure S4. SEM images of the different synthesized materials: a) as-synthesized LRLO, b) W300, c) A300, d) W900 and e) A900.

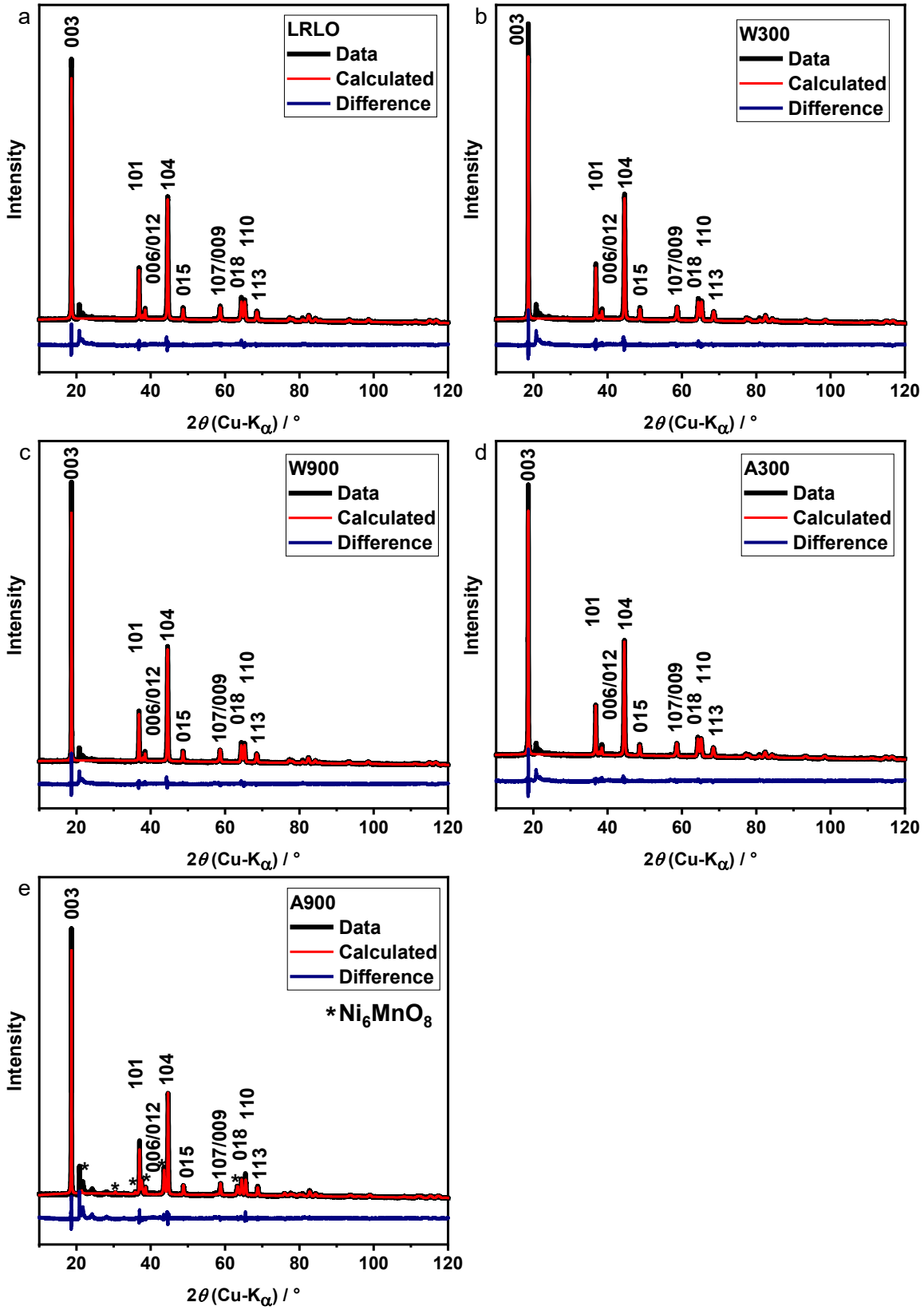

Figure S5. Comparison of the measured XRD pattern (black line) with the calculated pattern, using Rietveld refinement (red line) and their difference (blue line) of a) LRLO, b) W300, c) W900, d) A300 and e) A900.

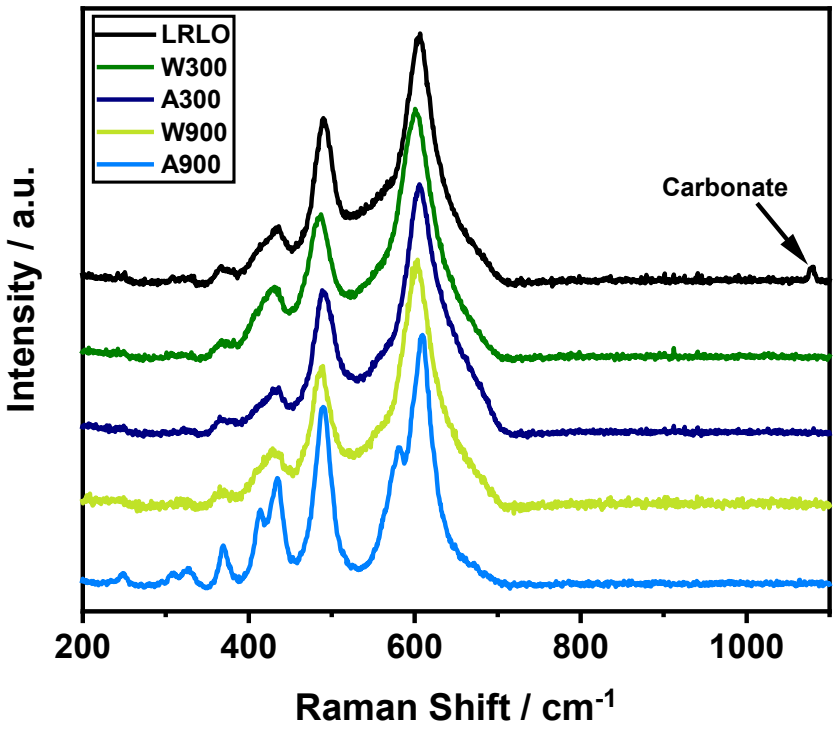

Figure S6. Raman overview spectra showing the non-existence of carbonates after the different treatments.

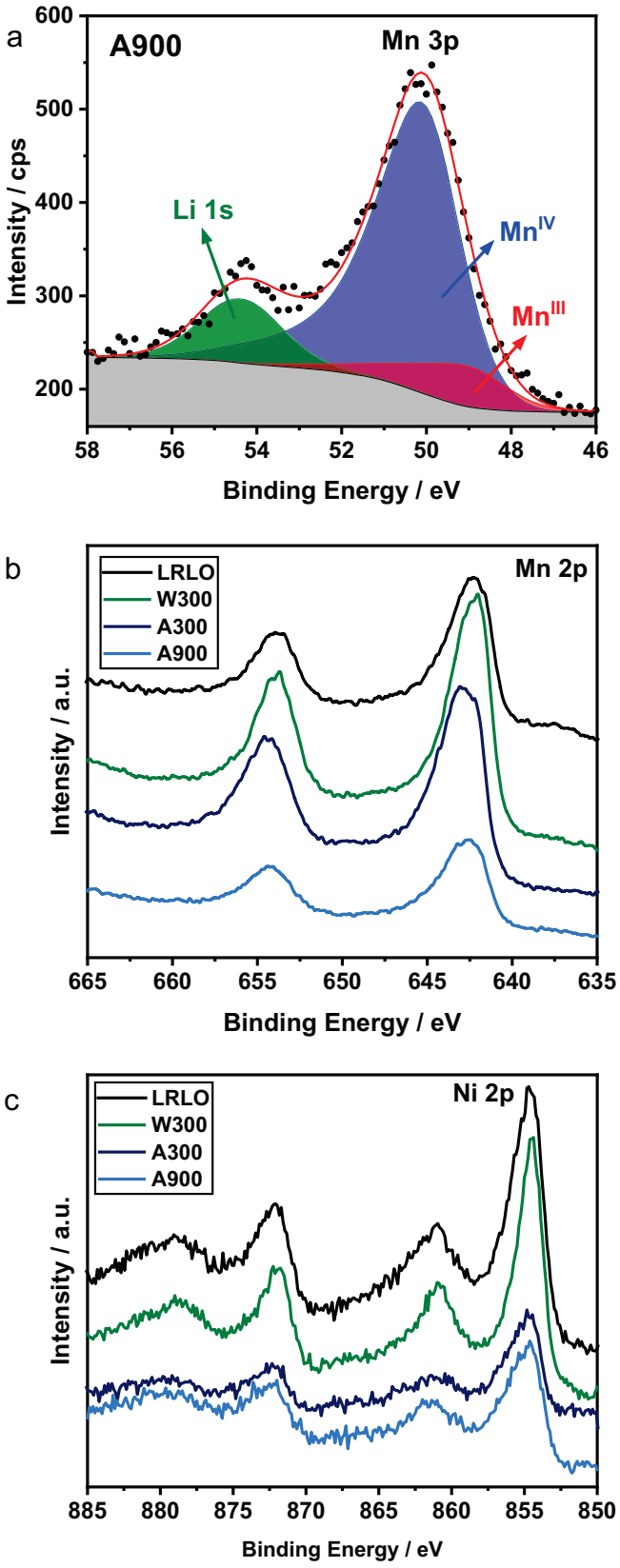

Figure S7. XPS spectra of a) A900 (Mn 3p and Li 1s) as well as LRLO, W300, A300 and A900: b) Mn 2p and c) Ni 2p

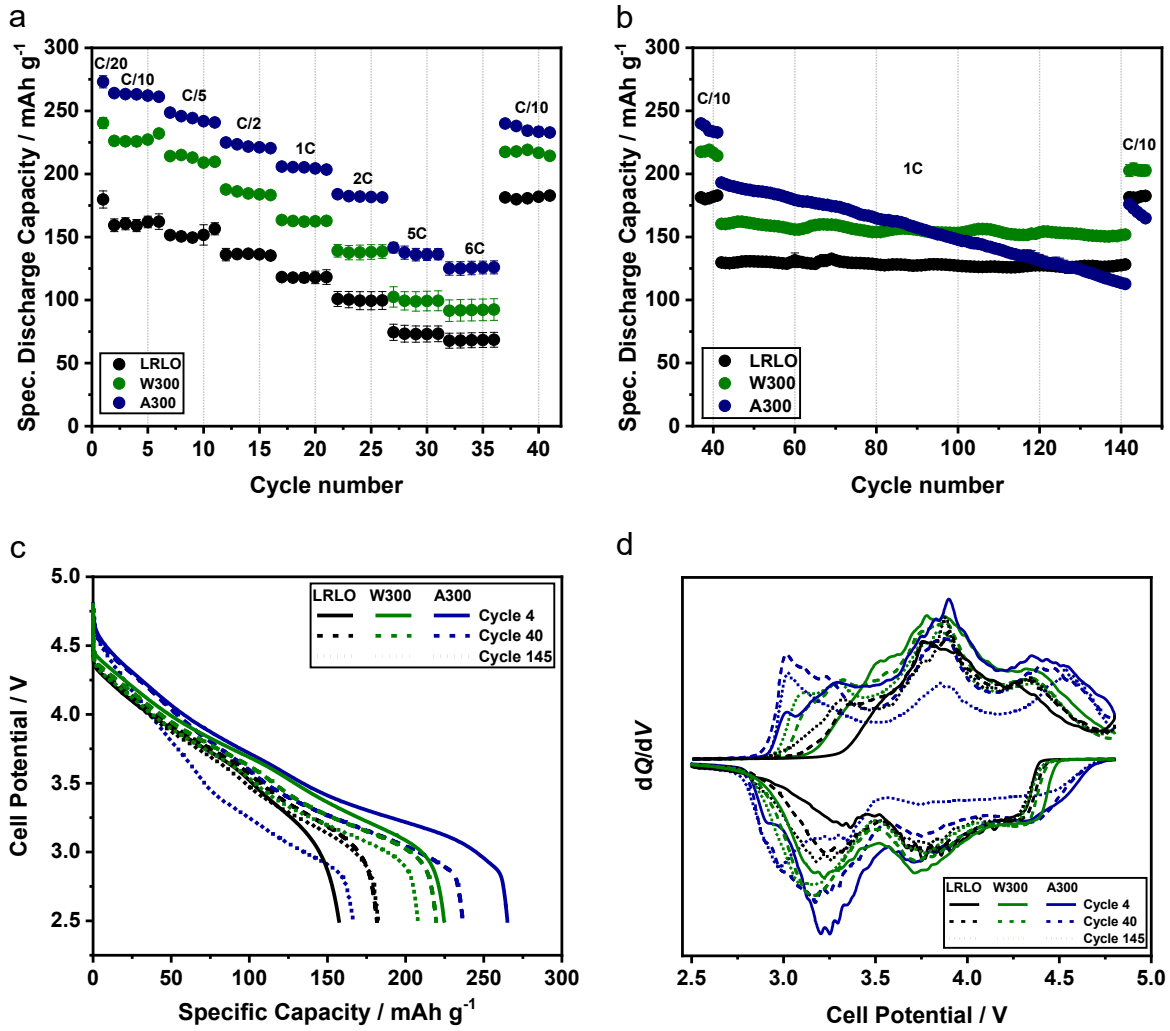

Figure S8. a) Rate capability test of LRLO, W300 and A300 with b) further cycling at 1C; c) Potential curves of LRLO, W300 and A300 of selected C/10 cycles during the long-term cycling and d) corresponding d*Q*/d*V* plots.

References

[1] C. R. Fell, D. Qian, K. J. Carroll, M. Chi, J. L. Jones, Y. S. Meng, *Chem. Mater.* **2013**, *25*, 1621.

[2] H. Taguchi, A. Ohta, M. Nagao, H. Kido, *J. Solid State Chem.* **1998**, *135*, 322.

Effect of Three-in-one Surface Modification of Spherical, Co-free Li-rich Cathode Material for Li-Ion Batteries ($Li_{1.2}Mn_{0.6}Ni_{0.2}O_2$) with Citric Acid

Reprinted with permission from:

F. Klein, C. Pfeifer, J. Bansmann, Z. Jusys, R. J. Behm, M. Wohlfahrt-Mehrens, M. Linden, P. Axmann, *J. Electrochem. Soc.* **2022***, 169,* 120533*,* DOI: 10.1149/1945-7111/acaa5c.

© 2022 The Authors. Published on behalf of The Electrochemical Society by IOP Publishing Limited. This open access article is reprinted under the terms of the Creative Commons Attribution 4.0 License (CC BY 4.0, https://creativecommons.org/licenses/by/4.0/).

Journal of The Electrochemical Society, 2022 **169** 120533

Effect of Three-in-One Surface Modification of Spherical, Co-Free Li-Rich Cathode Material for Li-Ion Batteries ($Li_{1.2}Mn_{0.6}Ni_{0.2}O_2$) with Citric Acid

Florian Klein,[1] Claudia Pfeifer,[1] Joachim Bansmann,[2] Zenonas Jusys,[3] R. Jürgen Behm,[3,4] Margret Wohlfahrt-Mehrens,[1,4] Mika Lindén,[5,z] and Peter Axmann[1,z]

[1]*Zentrum für Sonnenenergie- und Wasserstoffforschung Baden-Württemberg (ZSW), D-89081 Ulm, Germany*
[2]*Institute of Surface Chemistry and Catalysis, Ulm University, D-89081 Ulm, Germany*
[3]*Institute of Theoretical Chemistry, Ulm University, D-89081 Ulm, Germany*
[4]*Helmholtz Institute Ulm Electrochemical Energy Storage (HIU), D–89081 Ulm, Germany*
[5]*Institute for Inorganic Chemistry II, Ulm University, D-89081 Ulm, Germany*

The electrochemical activation of Li_2MnO_3 domains in Li- and Mn-rich layered oxides (LRLO) is highly important, and can be tuned by surface modification of the active materials to improve their cycling performance. In this study, citric acid was employed as a combined organic acid, reducing agent, and carbon precursor in order to remove surface residues from the calcination process, implement an oxygen deficient layer on the surface of the primary LRLO particles, and cover their surface with a carbon-containing coating after a final annealing step. A broad selection of bulk and surface sensitive characterization methods was used to characterize the post-treated spherical particles, providing the evidence for successful creation of an oxygen deficient near-surface region, covered by carbon-containing deposits. Post-treated materials show enhanced electrochemical discharge capacities after progressive Li_2MnO_3 activation, reaching maximum capacities of 247 mAh g^{-1}. Gassing measurements reveal the suppression of oxygen release during the first cycle, concomitant with an increased CO_2 formation for the carbon-coated materials. The voltage profile analysis in combination with post-mortem characterization after 300 cycles provide insights into the aging of the treated materials, which underlines the importance of the relationship between structural changes during scalable post-treatment and the electrochemical performance of the powders.
© 2022 The Author(s). Published on behalf of The Electrochemical Society by IOP Publishing Limited. This is an open access article distributed under the terms of the Creative Commons Attribution 4.0 License (CC BY, http://creativecommons.org/licenses/by/4.0/), which permits unrestricted reuse of the work in any medium, provided the original work is properly cited. [DOI: 10.1149/1945-7111/acaa5c]

Manuscript submitted September 30, 2022; revised manuscript received November 17, 2022. Published December 30, 2022.

Supplementary material for this article is available online

Li-ion batteries have become an important part of our high-tech everyday lives due to their long cycle lives and high energy densities. In addition to mobile applications in the IT sector, their application in the automotive sector is becoming more and more important.[1] Simultaneously, the demand of the battery field for natural resources is significantly increasing.[2] For this reason, it is important to reduce dramatically the content of critical raw materials, such as Co and Ni compared to Ni-rich layer oxides, e.g., NCM-811, and thus both the cost and environmental footprint.

Li- and Mn-rich layered oxides (LRLO) with the general formula of $x\ Li_2MnO_3 \cdot (1\text{-}x)\ LiMn_{1-y-z}Ni_yCo_zO_2$ have attracted a lot of recent interest in this respect. Depending on the stoichiometry, especially the value of x, the materials can provide specific energy energies beyond 900 Wh kg^{-1} with an average discharge potential of >3.5 V vs Li^+/Li.[3–5] The high discharge capacity is based on the combination of cationic (transition metals, TM) and anionic (oxygen species) redox reactions, where the detailed mechanism of the anionic redox is still under scientific debate.[6–9] Furthermore, there is a discussion about the structure of the material, both solid solution ($Li_{1.2}Mn_{0.8-y-z}Ni_yCo_zO_2$) and a nanocomposite consisting of monoclinic Li_2MnO_3 and rhombohedral $LiTMO_2$ domains have been suggested.[10–12] Despite their many attractive characteristics, LRLO materials are prone to several problems. The most important ones are a large voltage hysteresis, a high initial irreversible capacity loss, and voltage fading during cycling. These are related to the release of O_2 during the first delithiation beyond 4.5 V, when Li_2MnO_3 domains are electrochemically activated.[13,14] O_2 release during further cycling was considered as the main origin of the phase transformation from a layered into a spinel-like and an electrochemically inactive rock-salt structure, which significantly reduces the average discharge voltage.[6,15–17]

Commonly used mitigation strategies include, modification of the electrolyte,[18–20] doping,[21–25] surface treatments or introduction of a surface coating.[26] Doping mainly stabilizes the host framework and/or increases the Li layer spacing, with the latter leading to a faster Li^+ diffusion.[7] Most of the surface treatments generate a thin spinel-like surface layer, which improves the electrochemical performance and stabilizes the surface. A broad variety of chemicals have been applied for pretreating the electrode material in order to generate a more stable outer particle surface in contact with the electrolyte during cycling, e.g., oxidizing or reducing agents,[27–29] mineral and organic acids[30–38] or H_2O.[38,39] Coating of the particles is mostly used to stabilize the surface against side reactions with the electrolyte, to improve the conductivity of the surface layer, and reduce the oxygen release during cycling.[40,41] Besides the deposition of phosphate,[42–45] oxide,[40,46–48] and fluoride coatings,[43,49] different approaches to introduce carbon-containing coatings have been reported, using precursors like urea, C-polymorphs and different polymers.[50–56] A second low temperature treatment is typically employed to convert the carbon precursor into carbon, which partially reduces the TM in the near-surface region, resulting in a combination of surface coating and a modified spinel-like, oxygen-vacant surface region with improved electrochemical properties.[55,57]

Recently, we reported that washing the LRLO after calcination with diluted nitric acid or water to remove reaction residues from the calcination process and to activate the material chemically, leads to an improved cycling behavior.[38] Therefore, the aim of this work is to combine the washing procedure to remove the residues with the deposition of citric acid (CA) as a carbon precursor for subsequent carbothermal reduction under inert atmosphere to implement a restructured surface layer protected with a C-containing coating on as-synthesized, spherical, Co-free $Li_{1.2}Mn_{0.6}Ni_{0.2}O_2$ particles (Fig. 1). To the best of our knowledge, such a 3-in-1 procedure with CA has been applied here for the first time for LRLO material. The influences of the applied amount of CA on the bulk and surface

[z]E-mail: mlinden@uni-ulm.de; Peter.Axmann@zsw-bw.de

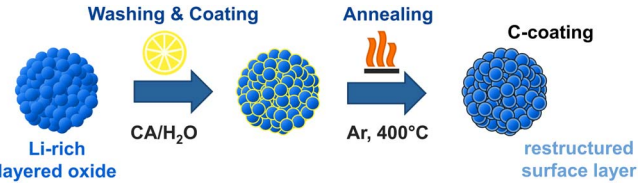

Figure 1. Schematic overview over the applied 3-in-1 post-treatment procedure.

structure, the electrochemical cycling stability and the gas evolution during the initial cycles were systematically investigated.

Experimental

Synthesis of the pristine material and coating procedure.—The pristine powder $Li_{1.2}Mn_{0.6}Ni_{0.2}O_2$ was synthesized via lithiation and calcination of a spherical, coprecipitated $TMCO_3$ (TM= Mn, Ni and Mn/Ni = 3:1) precursor. The precursor was mixed with a stoichiometric amount of LiOH x H_2O (Roth, Li/M = 1.53) and an adequate amount of water to obtain a highly viscous slurry. Subsequently, the mixture was dried at 120°C and the final calcination step was conducted at 900°C under air.

For the coating and washing procedure, the as-synthesized LRLO (7.00 g) was added to a warm solution of citric acid (CA) monohydrate (Riedel-de Haën) in ultrapure H_2O (14 ml, σ <0.55 μS cm^{-1}). The mixture was stirred in a rotary evaporator (20 min, T_{bath} = 80°C). Afterwards, the water was evaporated under vacuum and the resulting mixture was dried (80 °C, overnight). As a last step, the powder was calcined at 400°C (5 h) under Ar atmosphere. Different CA/LRLO ratios of 0.88 wt% (C1), 1.76 wt% (C2) and 2.95 wt% (C3) were employed. A reference sample without CA was synthesized in the same way, including the final calcination step (C0).

The post-treatment calcination process was investigated by thermogravimetric analysis (Netzsch STA 449 C) coupled with mass spectrometry (Netzsch QMS 403, TGA-DSC-MS). For the TGA-DSC-MS experiments, a heating rate of 10 K min^{-1} under Ar atmosphere was applied and corundum crucibles were used. The DSC measurements were background-corrected with a blank measurement under the same conditions.

Structural and chemical characterization.—The chemical composition was analyzed by ICP-OES measurements of a diluted aqua regia digestion (Spectro Arcos SOP). Combustion analysis under O_2 coupled with nondispersive infrared sensor was conducted to quantify the total carbon content in the samples (Analytik Jena, multi-EA-4000). The total inorganic carbon was determined in the same device, quantifying the evolved CO_2 from a suspension of the active material in phosphoric acid. The mean TM oxidation state was determined by two different titration techniques. At first, the TM content was quantified via complexometric back-titration with $CuSO_4$ solution of the digested powder (for sample preparation see ICP-OES measurements), diluted in a defined amount of EDTA solution and NH_4^+/NH_3 buffer solution (pH = 10). For the second titration, the powders were digested in a sulfuric $(NH_4)_2Fe(SO_4)_2$ solution. The mean TM oxidation state was finally determined via titration of the unreacted Fe^{2+} ions with acidic $Ce(SO_4)_2$ solution and the result of the complexometric titration method. All titration experiments were conducted at an OMNIS titration station (Metrohm) with potentiometric endpoint determination. A D8 Advance diffractometer (Bruker AXS, reflection mode, Bragg-Brentano geometry, Cu K_α radiation, LYNXEYE_XE detector) was used for XRD measurements of the powders. Rietveld analysis of the diffraction patterns was conducted with TOPAS V6 (Bruker AXS) and the structural model for $Li_{1.2}Mn_{0.6}Ni_{0.2}O_2$ of Fell et al.[58] Particle morphology was determined using a Leo 1530 VP (ZEISS) scanning electron microscope with an acceleration voltage of 5 kV and an Everhart-Thornley-detector. The surface of sample C3 was investigated with a Gemini SEM 460 (ZEISS) using an Inlens- and EsB-detector at a working distance of 2.1 mm to 2.2 mm and an acceleration voltage of 800 V. Images were acquired using either line integration or drift compensated frame integration. Raman measurements of the powders (C0 and C3) were conducted at an alpha300 R confocal Raman microscope (WITec) equipped with an Nd:YAG laser (532 nm excitation wavelength), 100x objective (Zeiss, NA = 0.9), grating with 300 lines mm^{-1} and a CCD-camera. Laser power was adjusted individually to maximize the signal without destruction of the samples. The data were evaluated with Project FIVE software (WITec). A commercial X-ray photoelectron spectroscopy (XPS) machine from Physical Electronics (PHI 5800 ESCA) equipped with a hemispherical electron analyzer, a monochromatic Al K_α X-ray source (1486.6 eV) and a flood gun to avoid charging of the sample was used for XPS measurements. Both angles (angle of photon incidence on the sample and angle of emitted photoelectrons are 45° with respect to the surface normal (sample holder, respectively)). Survey spectra were recorded using a pass energy of 93.9 eV, detail spectra with 29.35 eV. The binding energies (BEs) of all spectra were calibrated with respect to the C 1 s peak of ubiquitous carbon, which was fixed at a binding energy (BE) of 284.7 eV. The data were evaluated (deconvolution of spectra) by using the commercial software package CasaXPS (Casa Software Ltd, version 2.3.23PR1.0). The oxidation states of Mn were determined via deconvolution of the Mn 2p and 3p spectra, based on the approach of Ilton et al., who used five single peaks for the Mn 3p state and 8 peaks for the Mn 2p to identify the Mn OS (III/IV).[59] The latter peaks were fitted with defined parameters (e.g., peak shape, width, relative binding energy and intensity) adapted from the literature values.[59] For simplification, all components belonging to a single OS of Mn were summarized into a single peak. The Mn 3p photoemission peak overlaps with Li 1 s signal, which was fitted with one single peak. We additionally used the Mn 2p peaks to confirm the oxidation state derived by the deconvolution of the combined Mn 3p/Li 1 s states. In some cases, the results were quite different from those determined from the Mn 3p states. It turned out, that the intensity and the shape of the Mn $2p_{3/2}$ peaks were affected by an Ni Auger ($L_2M_{23}M_{45}$) feature.[60] After correcting for the Ni contribution, the data were in good agreement with those derived from the Mn 3p states.

Electrochemical characterization.—In order to study the electrochemical behavior of the samples, a homogeneous slurry of each active material with polyvinylidene difluoride (PVdF, Solef 5130, Solvay) and conductive carbon Super C65 (Timcal) (dry ratio of 85:5:10) dispersed in an adequate amount of *N*-methyl-2-pyrrolidinone (NMP, Sigma Aldrich) was coated on an aluminum foil using the doctor blade technique. After drying, the electrodes were calendered to a thickness of 47 μm (100°C). Disk electrodes (12 mm diameter) were punched out, were dried overnight under vacuum (120°C) and were transferred subsequently without contact to air into an argon-filled glovebox (MBraun, O_2 and H_2O <0.1 ppm). Typical active material loading of one disc electrode was in the range of 3 and 4 mg. Finally, CR2032 coin cells (Hohsen) were assembled in the same glovebox with one disk electrode (working electrode), two glass fiber coins (16 mm diameter, Whatman) as separator, a lithium metal foil (450 μm, 12 mm diameter) as counter electrode and electrolyte (150 μl, 1 M $LiPF_6$ in EC:DMC = 1:1 by wt, Solvionic). The cells were galvanostically charged and discharged in the voltage range of E = 2.5–4.8 V under constant current conditions using different C-rates (1 C = 250 mA g^{-1}).

The design of the DEMS cell and the preparation of the electrodes are reported elsewhere.[38,61] In short, the electrodes were prepared on an Al coated FEP membrane (50 μm thickness, Bohlender, Bola) instead of Al foil. The membrane was supported on a perforated poly-ether-ether-ketone (PEEK) plate, which was directly connected to the ultrahigh vacuum (UHV) chamber inlet of the mass spectrometer (Pfeiffer Vacuum QMA 410). This set-up allowed monitoring the gas evolution differentially upon cycling

without using any carrier gas. The measurements were conducted in a half-cell configuration with Li metal as counter electrode and reference electrode as well as LP30 electrolyte (1:1 wt. EC/DMC + 1 M $LiPF_6$, Solvionic, purity >99.9%, water content <20 ppm, 0.7 ml). The soaking time after filling the cell with electrolyte was at least two hours to achieve stable background signals of the selected ion currents and a stable OCV. Galvanostatic cycling with a current of 0.1 mA (corresponding to C/10) and cut-off potentials of 2.5 and 4.8 V (vs Li^+/Li) was applied (Princeton Research Instruments (PAR) 263 A), simultaneously recording the MS ion currents.

Post-mortem analysis of the electrodes.—After the last discharge, the cells were disconnected and disassembled in an argon-filled glovebox. Subsequently, the cathodes were washed two times in fresh DMC, dried and stored inside the glovebox. For XRD measurements, the coating was mechanically removed from the current collector, homogenized with a mortar and filled into a glass capillary without air contact. XRD measurements were conducted in a D8 Advance diffractometer (Bruker AXS, transmission mode, Bragg-Brentano geometry, Cu K_α radiation, LYNXEYE_XE_T detector). Electrode cross-sections (CS) perpendicular to the electrode surface were prepared with the help of a broad Ar^+ ion beam polishing device (IM4000Plus, Hitachi). SEM images of the CS were taken with the same parameters, which were used to characterize the particle morphology. After SEM characterization, the CS were transferred to an alpha300 R confocal Raman microscope (WITec, details see characterization of the powders). A grating with 1800 lines mm^{-1} was used. Evaluation of the Raman data as well as the correlation with the SEM images was performed with Project FIVE software (WITec).

Results and Discussion

Chemical and structural characterization.—The base material of this study is a scalable, Co-free, and spherical Li- and Mn-rich layered oxide ($Li_{1.2}Mn_{0.6}Ni_{0.2}O_2$), which was obtained after lithiation and calcination of the coprecipitated carbonate precursor in the hundred-gram scale. Subsequent post-treatment of smaller fractions with different amounts of CA in an aqueous solution, drying and calcination under inert atmosphere complete the synthesis procedure. For convenience, the names of the treated samples are abbreviated in ascending order according to the applied amount of CA. The reference sample treated similarly without CA is named as C0. SEM images of C0 are presented in the supporting information (Fig. S1). These spherical secondary particles, which agglomerated from sintered primary particles of sub-micrometer size, have a higher porosity compared to very dense spherical particles in, e.g., high-voltage spinel.[62]

The thermal treatment process was analyzed with TGA-DSC-MS measurements for CA/LRLO = 0 wt% (C0) and CA/LRLO ≈ 3.0 wt % (C3) after the washing step (Fig. 2). C0 showed a monotonic decrease of the sample mass over the entire temperature range by 0.9 wt% (Fig. 2a). The corresponding MS signals of $m/z = 18$ and $m/z = 44$ were assigned to H_2O and CO_2, respectively.[63] The broad water signal between 50°C and 300°C and the small CO_2 signal in the temperature range of 400 and 500°C, indicate the desorption of surface water molecules and the decomposition of traces of TM carbonates, respectively.[64] The carbonates were likely formed directly after the washing procedure with CO_2 present in air. Further reasons for the weight loss of the sample are the possible removal of oxygen during heating under the Ar atmosphere and the decomposition of Li_2CO_3, which is reflected by the small increase of the CO_2 signal beyond 700°C.[64–66] For the interpretation of the TGA results of the CA treated powder (C3, Fig. 2b), it has to be considered that the addition of CA into the alkaline LRLO suspension in water most probably leads to the formation of Li-, Ni- or Mn-containing citrates at latest during drying. Generally, the continuous mass loss in the analyzed temperature range of the CA-LRLO-mixture (C3) can be divided into three regions with different

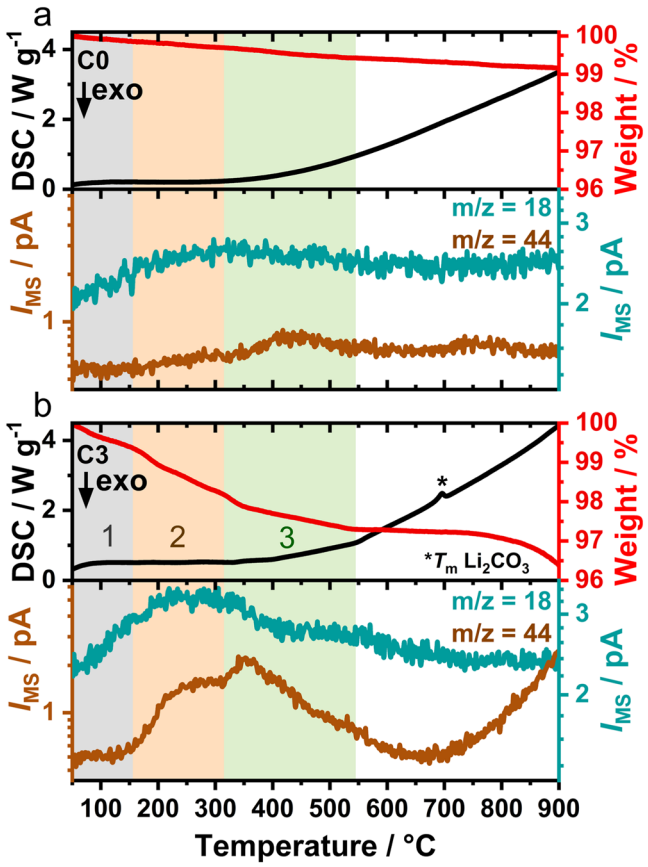

Figure 2. Evaluation of the post-treatment calcination step using TGA-DSC analysis (upper panel) coupled with MS (bottom panel) with a heating rate of 10 K min^{-1} under Ar atmosphere: a) ratio (CA/LRLO) = 0% (C0) and b) (CA/LRLO) = 3% (C3).

slopes, before a plateau is reached at approximately 540°C. Below 160°C, the sample loses around 0.5 % of weight, accompanied by a slight increase of the H_2O signal, which mainly indicates the release of crystallization water from metal citrates.[67] The regions 2 and 3 (approx. 160°C–540°C) are dominated by the decomposition of these citrate salts. This is indicated by the strongly increased signals of H_2O and CO_2 and the significant mass loss. When comparing these temperature ranges with those reported for metal citrate decomposition in literature, the mass loss observed in region 2 can be assigned to the decomposition of lithium citrate, Li_3(citrate) × 5 H_2O, into Li_2CO_3, while decomposition of nickel citrate is likely responsible for the mass loss observed in region 3.[67,68] Further indication for the decomposition of Ni citrate is the beginning of the plateau region at around 540°C, which indicates the completion of the decomposition reaction.[68] However, the influence of the carbothermal reaction with the LRLO on the CO_2 signal as well as the decomposition of citric acid or Li citrate monohydrate, Li(citrate) × H_2O, cannot be fully excluded due to the relatively small changes in the TGA and DSC curves.[68–70] At 700°C, the DSC curve shows an endothermal peak, attributed to the melting of Li_2CO_3.[66] Further increasing the temperature correlates with a slow increase of the mass loss and a strong increase of the CO_2 signal. Both are indicators of the decomposition of Li_2CO_3, which was formed as a main product of the carbothermal reaction of carbon species with LRLO and of the thermal decomposition of Li citrate.[66,68,71] Based on the TGA measurements, the calcination temperature for the post-treatment step was fixed to a value of 400°C as a reasonable compromise between an adequate progress of the CA decomposition and the protection of the active material from excessive reduction, which can lead to the formation of undesirable rock-salt structures.[65]

Structural, chemical and morphological bulk changes related to the post-treatment were analyzed in-depth (Fig. 3). The morphology of the slightly porous, spherical secondary particles of C3 (Fig. 3a) closely resembles that of C0, which also holds true for primary particle size (Fig. S1). Hence, the applied CA treatment had no influence on these parameters. The elemental composition was investigated via ICP-OES measurements. Based on the ICP-OES analysis, the CA treated materials exhibited a constant elemental ratio of Li:Mn:Ni = 1.20:0.59:0.21, which is similar to that of the as-synthesized material (Table S1). Slight deviations between the samples are within the error range of the ICP-OES measurement. XRD patterns of all powders can be assigned to the α-$NaFeO_2$ structure with the space group *R-3m* (Fig. 3c, Fig. S2).[72] Weak additional reflections in the 2θ range between 20 and 23° can be ascribed to the monoclinic Li_2MnO_3 superstructure (space group *C2/m*) due to Li/Mn clustering in the TM layer.[72] Both are typical structural attributes of LRLO materials.[14] The sharp reflections and the splitting of the (006)/(102) and (018)/(110) reflections suggest well-defined and highly ordered layered structures.[73] The presence of a crystalline spinel phases in the bulk in a larger quantity can be excluded based on the absence of shoulders next to the (003), (101) and (104) reflections.[52,74,75] Furthermore, very small reflections attributable to Li_2CO_3 are visible for the CA treated samples (Fig. S2b).[76]

The XRD patterns of the different powders are similar, but the position of the reflections slightly shifted to lower 2θ angles with increasing CA amount. Further analysis of these shifts were carried out via Rietveld refinement with TOPAS V6 applying the $Li_{1.2}Mn_{0.6}Ni_{0.2}O_2$ structural model of Fell et al.[58] Detailed results and the correlating plots are presented in Table S2 and Fig. S2. Depending on the sample, the lattice parameters are in the range of a = 2.862–2.865 Å and c = 14.260–14.270 Å, respectively. Increasing the applied amount of CA induces an expansion of the lattice parameters, which indicates partial TM reduction in the bulk of the materials during the post-treatment steps. This phenomena, so-called reduction expansion, is most probably caused by the larger ionic radii of Mn^{3+} compared to Mn^{4+} and the resulting elongation of the TM-O bonds.[65,77,78] Deeper investigation of the mean TM oxidation state (OS) was conducted by cerimetric titration. For an easier interpretation, the mean TM OS from titration were converted into an oxygen coefficient in the formula unit $Li_{1.2}Mn_{0.6}Ni_{0.2}O_y$, assuming a) full occupation of the TM and Li sites, and b) correction of the bulk Li^+ content (ICP-OES) under the consideration of Li^+ ions trapped outside the LRLO bulk structure in surface carbonates (Fig. 3b, blue squares). While C0 was stoichiometric in its oxygen content (y = 2.00), the formal oxygen deficiency slightly increases with the amount of applied reducing agent CA (y(C3) = 1.98). However, the stability limit of $Li_{1.2}Mn_{0.6}Ni_{0.2}O_2$ of y = 1.96, at which phase separation into a Ni_6MnO_8 rock salt structure is reported, was not reached.[65] The combination of XRD and cerimetry clearly indicates the formation of oxygen vacancies in the bulk structure of the primary particles, due to the carbothermal reaction of the citrates with the LRLO. Nakamura et al. reported comparable changes of the lattice parameters between $Li_{1.2}Mn_{0.6}Ni_{0.2}O_2$ and $Li_{1.2}Mn_{0.6}Ni_{0.2}O_{1.96}$ with oxygen vacancies, after applying an additional heat-treatment with different O_2 partial pressures.[65]

We expect Li_2CO_3 as main product of the carbothermal reduction reaction, which was already identified in the TGA and XRD

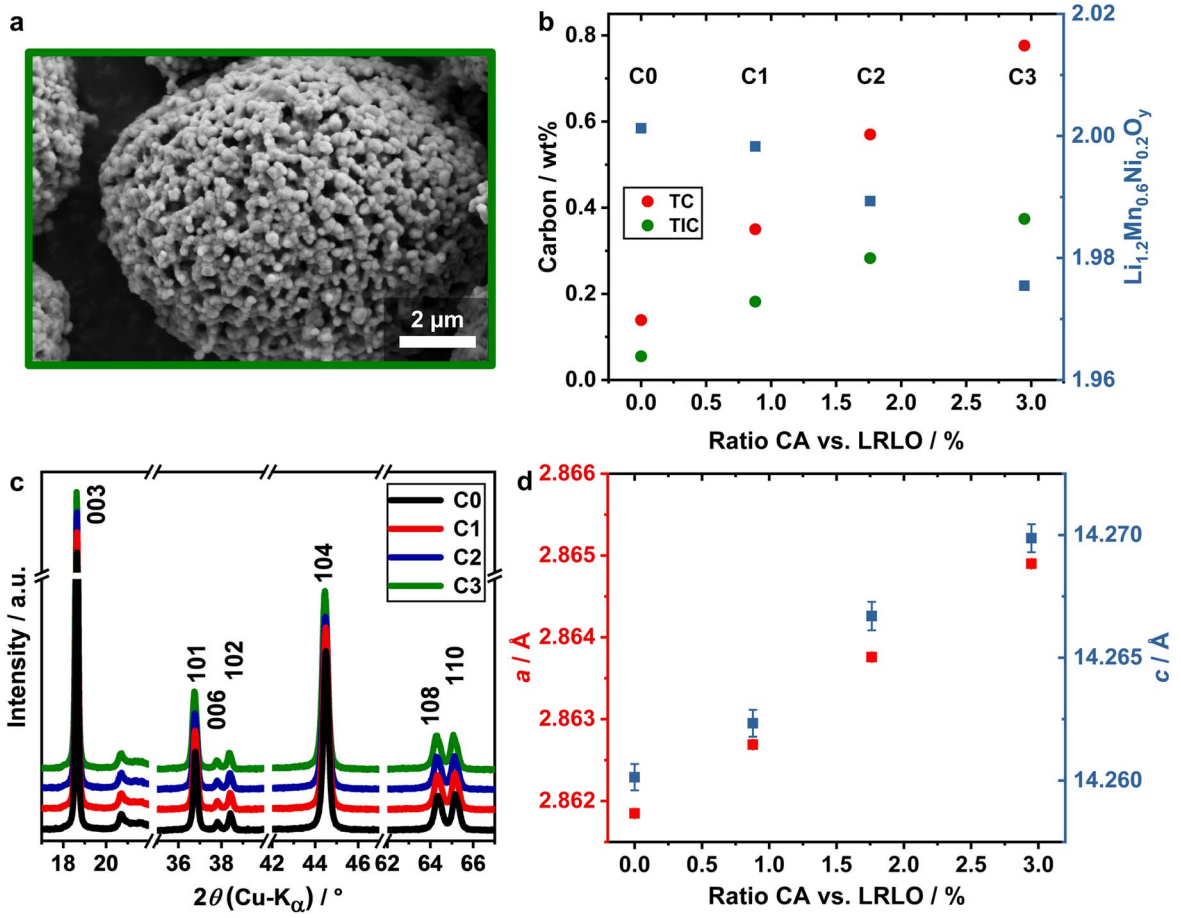

Figure 3. Morphology and bulk characterization of the investigated powders related to the applied amount of CA: (a) porous secondary particle architecture of C3 (SEM image with SE detector, 5 kV), (b) total carbon (red dots), total inorganic carbon (green dots) and calculated oxygen stoichiometry from cerimetric redox titration (blue squares), (c) detailed XRD pattern of C0 (black), C1 (red), C2 (blue) and C3 (green), and (d) calculated lattice parameters resulting from Rietveld refinement of the experimental patterns.

experiments. To quantify the amount of Li_2CO_3 and carbon-containing coating, the total inorganic carbon (TIC) and total carbon (TC) contents were determined (Fig. 3b). Both, the TC and TIC in the treated powders increase with increasing CA/LRLO ratio up to maximum values of 0.78 wt% and 0.37 wt%, respectively. Interestingly, the TC content is approximately linear with the applied amount of CA, whereas the slope of TIC decreases with higher CA/LRLO ratios. This observation indicates the formation of an inorganic carbon-containing layer on the primary particle surfaces, most probably consisting of Li_2CO_3. This layer may act as passivation layer, and stabilizes the organic carbon species against further decomposition, which lead to an increased TC/TIC ratio, and thus to an increase in the carbon/carbonate ratio at higher CA contents.

In order to prove this hypothesis, the samples were further analyzed by surface sensitive XPS measurements (Fig. 4a-c, Figs. S3–5). The contributions from different Mn OS were determined by deconvolution of the Mn 3p (Fig. 4a) and Mn $2p_{3/2}$ (Fig. S3) signals of the powders. For convenience, the defined peaks in the used deconvolution model of Ilton et al. were summarized into a single peak for each Mn OS.[59] As shown in Fig. 4a, C0 is dominated by Mn^{4+} ions. The amount of Mn^{3+} ions at the surface dramatically increased upon CA treatment (C3, Fig. 4a). A similar tendency is observed for C1 and C2 materials, but to a lesser extent (Fig. S4). The Ni 2p spectra of the samples remained unaffected by the CA treatment. Their Ni $2p_{3/2}$ peak maxima are in the range of 854.6–855.2 eV, which is typical for Ni^{2+} (Fig. S5).[79–81] The O 1s spectra can be deconvoluted into three peaks at approximately 529.6 eV (lattice oxygen ions O^{2-} of LRLO), 531.8 eV (M–OH, carbonates and other C-containing species) and 533 eV (most likely adsorbed water).[82–85]

Interestingly, the shape of the O 1s signal differs strongly between C0 and C3. While in the spectrum of C0 the peaks at 529.6 eV (brown) and 531.6 eV (dark green) are well separated and similar in height and area, for C3, the spectrum is dominated by the peak at 531.5 eV (dark green). Apparently, the signal of the LRLO lattice oxygen is broadened and appears attenuated in intensity compared to that in C0. The broadening (2.1 eV compared to 1.5 eV) may reflect structural disorder. A similar behavior of the lattice oxygen peak was reported previously upon different reductive treatments.[51,57] The Mn and O spectra provide clear evidence of a strong reduction of the Mn ions in the surface region, while based on the cerimetry data we would not expect a similar decrease of the OS in the bulk of the material. From the XRD measurements, the long-range ordering of the LRLO bulk structure seemed to be mostly unaffected by the treatment. However, the presence of oxygen deficiencies and slight changes causing the increase of the lattice parameters are possible and probable for the treated materials.

The lower intensity of the XPS O 1s lattice oxygen signal of C3, which correlates with the much lower Mn 2p intensity (only 45% in peak area intensity compared to C0) and a significantly reduced Ni 2p intensity (70% compared to C0) is most likely due to the formation of a cover layer. The latter is indicated also by the higher contents of carbonate species on the surface of the C3 particles as compared to the C0 particles. This is in good agreement with the conclusions drawn based on the thermogravimetric analysis as well as the TIC and TC results.

The C 1s spectra were deconvoluted by four peaks, reflecting C–C, C–H bonds at approximately 284.7 eV, C–O–C, C–OH species at around 286.5 eV, C=O and O–C=O species at about 289 eV, and carbonates at around 290 eV.[84,86] It is important to note that the peak of 284.7 eV originates both from the carbon pad supporting the

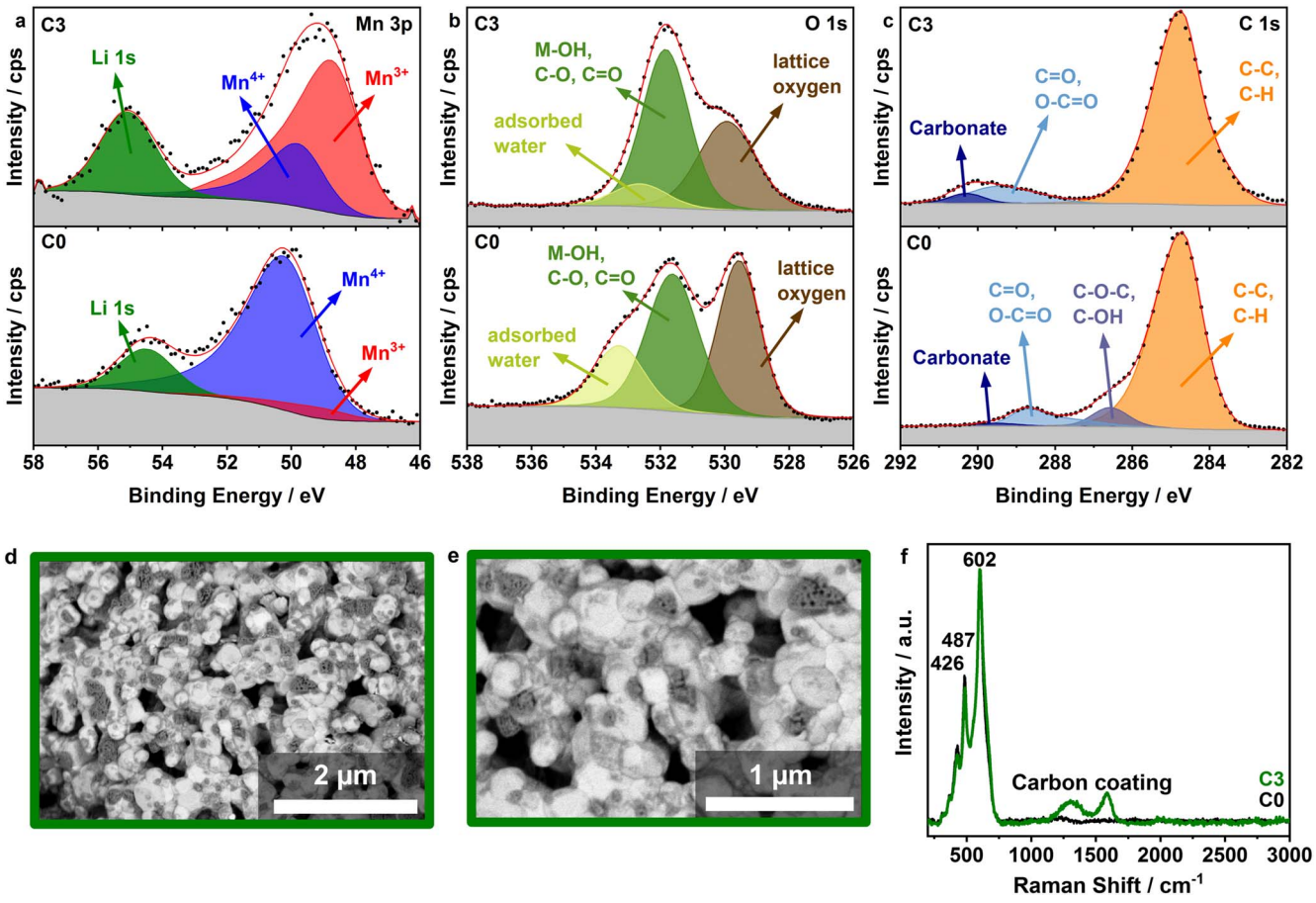

Figure 4. Characterization of the surface coating: (a-c) XPS spectra of C0 and C3, (d-e) SEM images of C3 taken with an EsB detector, and (f) Raman spectra of C0 and C3 powders.

powder sample and from the powders themselves. The spectra of the different powders show an increase of the carboxyl and carbonyl groups with higher CA/TM ratio, which might be attributed to functional groups of the carbon coating. Furthermore, we observed an increase of the carbonate signal from C0 to C3, which relates to Li_2CO_3 formed during the carbothermal reaction of the carbon-containing species with the LRLO during calcination (Figs. 4a, 4c). This fits also to the trend in the O 1s spectra, which showed a decreasing signal of the lattice oxygen with higher amount of applied CA and the TIC and TC results.

Further information is obtained from SEM imaging under more surface sensitive conditions, e.g., with very low accelerating voltage of 0.8 kV and an EsB detector (Figs. 4d–4e, Fig. S6). Figure 4e shows amorphous and porous structures, which partially cover the surface of the primary particles of C3. At higher magnification (Fig. S6d) very small grey dots are visible, which may reflect a thin carbon deposit on the surface. Additional confocal Raman microscopy was applied to characterize these carbon-containing structures and the short range ordering of the material in the surface near region. Generally, layered oxides with the space group *R-3m* have two TM–O vibration bands based on the factor group analysis: the in-plane bend vibrations in parallel to the metal layers (E_g) and the out-of-plane stretching vibrations along the *c*-axis of the crystal lattice (A_{1g}).[87] LRLO materials have lower symmetry (*C2/m*) due to the Li_2MnO_3 domains in the structure and therefore a higher number of vibration bands.[88,89] The Raman spectra of C0 (black) and C3 (green) show typical Raman shifts for $Li_{1.2}Mn_{0.6}Ni_{0.2}O_2$ materials (Fig. 4f).[88,90] The bands at 602 cm^{-1} (A_{1g}) and 487 cm^{-1} (E_g) are assigned to the $LiTMO_2$ compound, whereas the shoulder at around 560 cm^{-1} and the peaks below 430 cm^{-1} correspond to the Li_2MnO_3 domains.[88,90] Compared to the C0 reference, the spectrum measured for C3 shows a slightly increased intensity at 630 cm^{-1}, which fits to an elongation of the Mn–O bonds in the active material due to the higher Mn^{3+} content in the near-surface region (Fig. S7e). Several authors assigned such a shoulder to the formation of an oxygen deficient, spinel-like phase.[91,92] Furthermore, additional vibration bands at approximately 1300 and 1590 cm^{-1} are observed for C3. Both are allocated to the D- and G-bands of carbon species.[93] With respect to the broad D-band, a low degree of graphitization and a high amount of sp^2-sp^3-vibrations or polyene like structures are probable.[93] A spectral demixing of the Raman signals into the carbon and the LRLO spectrum (Figs. S7a-d) supports the SEM based conclusion of small carbon-containing agglomerates on the surface of the primary particles. Between the agglomerates, very low intense, locale carbon signals were detected (Fig. S7b), suggesting that carbon based deposits cover partially the LRLO surface.

Overall, the results of the comprehensive characterization demonstrate that the post-treatment procedure leads to the formation of a two-layer surface modification with a layered, oxygen deficient structure containing a fair portion of Mn in an OS of III at the particle surface, which is covered by Li_2CO_3 and organic carbon species. Furthermore, a slight reduction of the bulk material took place, increasing both lattice parameters, which likely results in a better Li^+ diffusivity.

Electrochemical performance.—The applied post-treatment strongly influences the electrochemical performance during the initial cycles (Fig. 5a). Whereas C0 has an initial discharge capacity of 237 mAh g^{-1} and a stable capacity retention, the initial discharge capacity decreases with increasing CA/LRLO ratio from 219 (C1) to 208 mAh g^{-1} (C3, C/20). During subsequent cycling, the capacities of C1, C2 and C3 increase again, cross the curve of C0 after around 5 cycles and become constant with up to 236 mAh g^{-1} (C/10) after approximately 20 cycles. Compared to the first cycle, the order of the materials regarding the obtained capacities is inversed, which indicates that the amount of the applied CA has a positive mid-term effect on the degree of utilization. The coulombic efficiency (CE) of the initial cycle is similar for all samples within the error bars (CE ≈ 75%). A slight decreasing tendency from C0 to C3 is possible, but highly speculative (Fig. S8). The rate capability test, performed after the first 20 cycles, shows that the rate-capability increases with capacity as well (Fig. S9). In order to understand the changes of the material further, the activation process was analyzed in more detail. The first cycle voltage curve of C0 shows typical characteristics of LRLO materials (Fig. 5c). The delithiation begins with a sloping voltage between 3.6 and 4.4 V, related to the extraction of Li^+ out of the $LiTMO_2$ phase and the oxidation of the Ni ions (Ni^{2+}/Ni^{4+}).[80] Beyond 4.4 V, the Li_2MnO_3 domains are electrochemically activated under further Li^+ extraction and participation of the anionic redox reaction of the lattice oxygen, indicated by the voltage plateau at approximately 4.5 V.[6] During relithiation a typical sloping voltage curve is observed.[94] The treated samples have similar voltage characteristics but vary in their overvoltage, which increases for the samples with higher CA/LRLO ratio. Consequently, this leads to lower degree of delithiation during the first charge to 4.8 V, which reflects a lower degree of Li_2MnO_3 activation and lower specific discharge capacities at the end of the first cycle. The increasing utilization can be explained by a progressive activation of remaining, but not yet activated Li_2MnO_3 domains.

The related change of the voltage profiles during the following 20 cycles, described by their d*Q*/d*V* plots (Fig. 5b) supports this hypothesis. The corresponding original voltage curves are presented in the supporting information (Fig. S10). All plots show three main peaks each during the delithiation and lithiation. They were assigned by Assat et al. to the $Mn^{3+/4+}$ (≈3.3 V), $Ni^{2+/4+}$ (≈3.8 V) and oxygen (>4.4 V) redox couples.[80] The lithiation peaks were reported at slightly lower voltages for the cationic redox reaction than during delithiation, whereas these differences are more pronounced for the anionic redox system, leading to a peak at ≈3.1 V.[80] Interestingly, this peak appears already as a distinct feature in the second cycle for C0, while for C1-C3 it is initially absent and forms during subsequent cycling. In combination with the additional peak at the end of the charge, which disappears after 10 cycles for all treated samples, it is likely that the Li_2MnO_3 domains were successively activated, leading to an enhanced discharge capacity.[54] Furthermore, a closer look on the edge at the beginning of lithiation (IR-drop in the voltage curves) indicates the suppression of a resistance increase at higher voltages by the coating, indicated by the very slow kinetics in this voltage range.[80] For C3, a slight shift to higher voltages at the beginning of lithiation might be explained by decomposition of an insulating surface Li_2CO_3 coating or a beginning structural rearrangement. The shoulder below 3.0 V is in accordance with the presence of spinel-like phases, which are typical products of the electrochemical transformation of the oxygen-deficient structures.[95]

DEMS measurements were conducted to investigate the impact of the post-treatment on the gassing behavior of the active materials and to check the stability of the coating (Fig. 6). Opposite to the commonly used carrier gas driven online mass spectrometry (OEMS), the gaseous products are directly transferred to the MS via a membrane inlet, which allows a higher time resolution.[61,96–99] The potential curves are similar to those measured in the coin cell setup (Fig. 6, topmost panel). Simultaneously recorded time-resolved ion currents (lower panels) provide qualitative information about the gas evolution rates at the different potentials. As above, the signals of $m/z = 32$ and $m/z = 44$, which are ascribed to O_2 and CO_2, respectively (Fig. 6, middle and bottom panel), differ strongly for the different samples. In the first cycle measured for C0, we find a pronounced O_2 peak starting at a potential of ≈4.6 V with its maximum at the upper cut-off potential of 4.8 V. It clearly demonstrates the O_2 release during electrochemical activation of the Li_2MnO_3 domains.[100] At the beginning of the lithiation, the O_2 evolution rate returns to the baseline, which is reached at approx. 4.0 V. Compared to C0, this O_2 signal is significantly lower for C1 and barely detected for C3. In the subsequent cycles, no O_2 evolution was observed for any of the samples. The decrease of the O_2 release with increasing carbon coating can be explained in different ways. One possible explanation is based on the oxygen deficiency in the surface near region of the primary particles, which decreases the

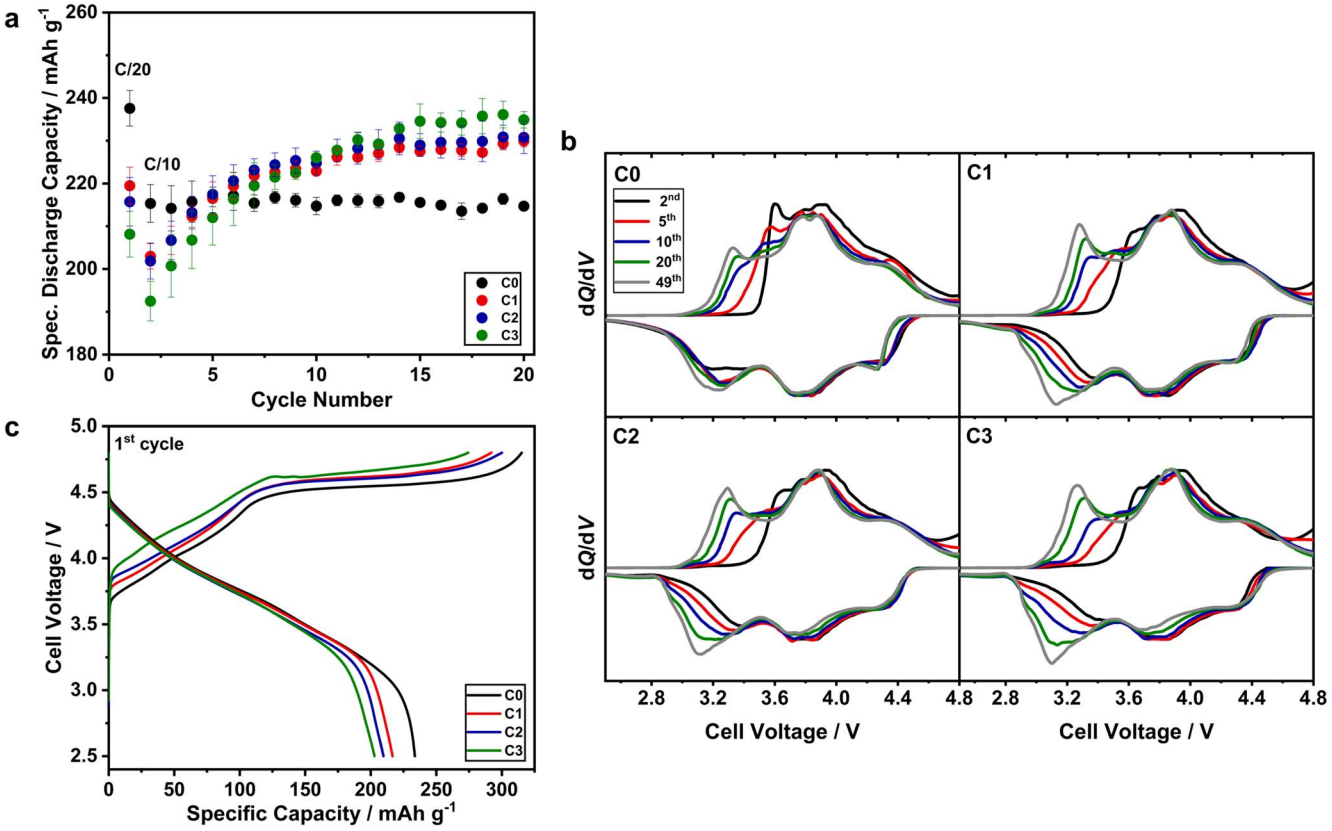

Figure 5. Electrochemical performance of the investigated powders: a) development of the specific discharge capacity during the initial cycles, b) dQ/dV curves of cycle 2 (black), 5 (red), 10 (blue), 20 (green) and 49 (grey), and c) 1st cycle voltage profiles. In a) and c) the samples were colored in black (C0), red (C1), blue (C2), and green (C3).

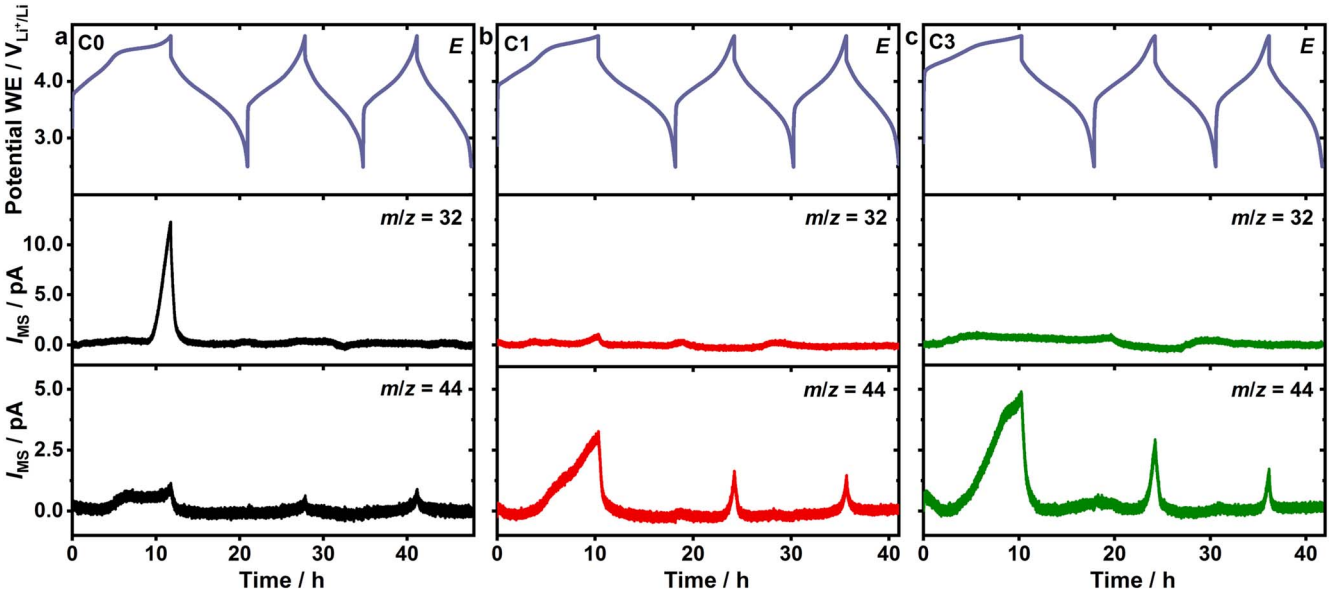

Figure 6. DEMS results of a) C0, b) C1, and c) C3 during the first three cycles. The potential curve of the half-cell configuration is presented in the topmost panel (I ≈ C/10). The MS signals for m/z = 32 and 44 of the gaseous products, directly transferred via membrane inlet, are presented in the middle and the bottom panel, respectively.

partial pressure of surface oxygen and thus reduces the O_2 release.[9] Secondly, the O_2 release may further be hindered, at least locally, by the carbon-containing deposits, which may inhibit O_2 release. O_2 trapped in the electrode could possibly be electrochemically reduced during the lithiation process, contributing to the overall increased capacity.

However, looking at the CO_2 signal, we assume that most of the released oxygen species directly reacts with the carbon coating under the formation of CO_2. This could explain the strong increase of the CO_2 signals in the order of C0 < C1 < C3. Generally, the CO_2 signals differ in their size and shape and arise only during charging of the LRLO materials. We have no indication that the evolved CO_2

will react with the electrolyte. Contributions from such reactions to the CEI formation at the working electrode are therefore unlikely.[101] In the first cycle, the CO_2 evolution begins at the end of the sloping potential region (≈4.4 V) and reaches the maximum evolution rate at the upper cut-off potential, similar to the O_2 evolution. In the subsequent cycles, peaks above a slightly increased potential (≈4.5 V) with higher symmetry, due to the missing plateau, and decreasing intensity are visible. The origin of the CO_2 signals at a potential of around 4.4 V has been discussed extensively in the literature with explanations including the decomposition/oxidation of (surface) impurities or the oxidation of the carbonate solvents in the electrolyte by high valence Ni ions.[96,98,102–104] As discussed in detail elsewhere,[38] we favor the suggestion of the Gasteiger group.[97] These authors proposed a proton-derived decomposition of Li_2CO_3, which is supported by the specific profiles of the CO_2 signals of C0 compared to C1 and C3. Whereas the CO_2 signal of C0 decreased slightly until a potential of ≈4.6 V, the signals of C1 and C3 increased monotonously. A possible explanation for the intermediate decrease is the limited amount of impurities, e.g., surface carbonates.[98] In contrast, the significantly higher carbonate content of C1 and C3 supports a continuous decomposition. The signals at potentials >4.6 V increased simultaneously with the O_2 signals and most probably originate from oxidation of the electrolyte with reactive oxygen species, which are released during the electrochemical activation reaction of Li_2MnO_3 domains.[98] Besides this, the following additional reactions are likely for C1 and C3: (a) electrochemical oxidation of the carbon coating (>4.75 V),[105] (b) chemical oxidation of the carbon species with reactive oxygen species from the LRLO lattice and (c) an increased amount of carbonate decomposition due to a higher proton concentration from the oxidation of functional groups of the carbon species. The proposed mechanisms are most probably the main reasons for the increased CO_2 signal with higher amount of carbon coating on the surface of LRLO. An OEMS study of ^{13}C labeled carbon coated phospho-olivine cathode material, which allowed to differentiate the anodic oxidation of the coating (^{13}C) from the oxidation of electrolyte, conductive carbon, and binder (all ^{12}C) in the EC based electrolyte, clearly demonstrated that the oxidation of the carbon coating is possible in the investigated cell chemistry.[105] The pronounced CO_2 signals in the second and third cycle of C3 indicate further decomposition of Li_2CO_3 and an ongoing oxidation of the carbon coating at high potentials by further released O_2. In combination with the electrochemical results of the coin cell testing, the DEMS data provide strong evidence that these reactions continue during subsequent cycles and might be the reason for the decrease of the overvoltage upon cycling.

Long-term cycling tests at RT and at 40°C were carried out to further investigate the cycling performance and the structural degradation of the materials (Fig. 7, Fig. S11). The initial cycles of all powders at RT are comparable to the former measurements in Fig. 5. The capacity of the reference C0 continuously decreased, beginning from the first cycle. This results in a capacity retention of 83% after 300 cycles. Compared to that, the coated samples reached capacities up to 247 mAh g^{-1} after 100 cycles depending on the amount of carbon-containing coating. The end of the activation process can be identified based on the mean discharge voltage, as the curves changes significantly their slope after 80 (C3) and 70 (C1 and C2) cycles, respectively. After the activation process, the treated samples behave similarly as C0 with respect to the capacity loss and the mean discharge voltage, which indicates the same aging mechanism for all cathodes studied. After 300 cycles, we found a specific discharge capacity of 221 mAh g^{-1} (C/10) for C3 compared to 200 mAh g^{-1} for C0, which is an improvement of 10%. Similar results are observed for the specific discharge energy (Fig. S11).

Contrary to the observations at RT, cycling at elevated temperature (40°C) changed the electrochemical performance of the treated materials significantly. Both C2 and C3 showed a higher specific discharge capacity than C0 already in the second cycle. One reason is likely the faster kinetics of the Li_2CO_3 decomposition compared to the cycling at RT and consequently easier accessibility of the LRLO. This might be the cause that both samples behave identically up to approx. 150 cycles with discharge capacities in the 100th cycle of up to 276 mAh g^{-1}. After 150 cycles, a strong capacity fade, which is not linked with a strong decrease of the mean discharge voltage, was observed for C2 and even more for C3. The voltage profiles (Fig. 7b) show that the main part of the voltage fade occurred in the lower voltage region during both, charge and discharge. This can be explained by the formation of oxygen vacancies and phase transformation from layered-to-spinel via a defect spinel-like LT-$LiCoO_2$ (*Fd-3m*) structure and finally into disordered rock-salt phase (*Fm-3m*).[95,106,107] Based on the voltage profiles at RT, the main phase transformation into spinel-like phase takes place for all samples during the first 100 cycles, indicated by the strong fade of the mean discharge voltage. The capacity fade during subsequent cycling is likely caused by the further densification of the materials. However, a coexistence of layered and spinel-like phases is probable even after 300 cycles, which is indicated by the typical voltage curve shape of a solid solution and the non-existence of a defined voltage plateau. At an elevated temperature of 40 °C, the aging was obvious for the post-treated materials, also shown in Fig. 7. After 300 cycles, they exhibited a distinct flat sloping region between approximately 2.8 and 3.5 V, which clearly indicates a strongly progressed layered-to-spinel transformation.[95,107] Furthermore, a defined high-voltage step can be resolved mainly for C2 and C3, which might be ascribed to redox active Ni ions in the LT-$LiCoO_2$ structure.[108] As a result, we suggest that the pronounced structural changes and the more intensive use of the material led to the strong capacity decrease of the coated materials starting after approximately 150 cycles.

Cycled electrode composites obtained after 300 cycles were characterized by XRD and by correlative SEM-Raman microscopy of the corresponding electrode cross-sections (Fig. 8). For an easier interpretation of the Raman mappings, similar spectra were clustered into groups. For both samples two clusters were considered adequate: the spectra indicated in blue are dominated by the vibrations of the layered oxide compound, whereas the spectra indicated in orange show mainly vibration bands assignable to the spinel-like structures (Fig. 8b).[56,88,89] The most intense typical spinel-like vibration bands are located, e.g., for the $LiMn_2O_4$ spinel (*Fd-3m*), at 625, 583, 483, and 432 cm^{-1}.[89] Further comparison of both orange spectra suggests that the fraction of the layered vibration bands is negligible in the orange colored spectrum of the electrode cycled at 40°C, whereas the orange spectrum of the RT-cycled electrode is a mixture of the layered and the spinel-type Raman bands. Additionally, the correlative SEM-Raman image of C3 at 40°C (Fig. 8a, bottom panel) shows larger orange areas compared to the electrode cycled at RT (Fig. 8a, topmost panel).

The higher fraction of spinel-type structures in the material after cycling at 40°C indicates that there is a substantially more pronounced layered-to-spinel transformation with increasing cycling temperature. This confirms the interpretation of the voltage profiles after long-term cycling experiments. Furthermore, the Raman mappings, especially the upper panel of Fig. 8a, indicate that the progressive layered-to-spinel transformation occurs inhomogeneously within the secondary particles forming contiguous regions, which are either dominated by spinel and layered structure. One possible mechanism might be an accelerated transformation of layered domains, which are adjacent to strongly aged ones, due to dislocations at the shared grain boundaries. A second possible reason for the inhomogeneous growth is likely based on the secondary particle architecture. Figure 8a indicates that the primary particles on the surface of the secondary particles aged faster compared to the bulk. However, in the bulk structure further aging was observed. Due to the local deviations in the particles architecture such as slight deviations in pore size and distribution, different accessibility of fresh electrolyte might lead to different concentrations of soluble electrolyte decomposition products (e.g., H_2O or HF) in the pores and by that on the surface of the primary particles. These can attack the active material and accelerate aging.

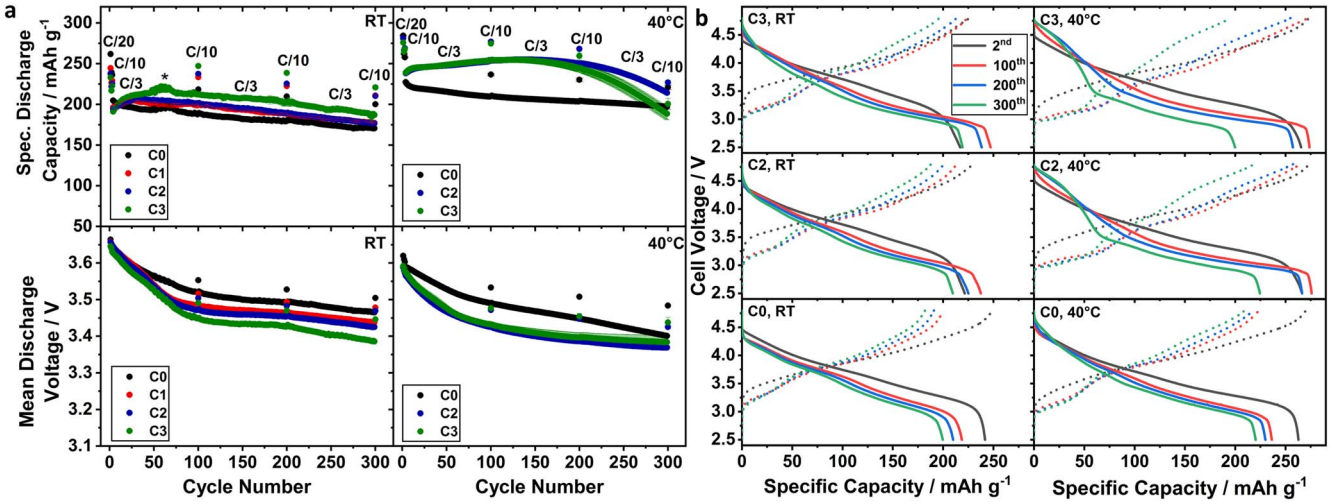

Figure 7. Long-term stability tests of C0 (black), C1 (red), C2 (blue), and C3 (green) at RT (left column) and of C0, C2, and C3 (same color code) at 40 °C (right column). a) Specific discharge capacities are presented in the topmost panels and mean discharge voltages in the bottom panels. The peaks marked with a star (*) of C3 and C0 are artefacts from temporarily slightly increased RT ($\Delta T \approx 3$ °C). b) Corresponding voltage profiles of C0, C2, and C3 at RT (left column) and 40 °C (right column) in the 2nd (black), 100th (red), 200th (blue), and 300th cycle (green).

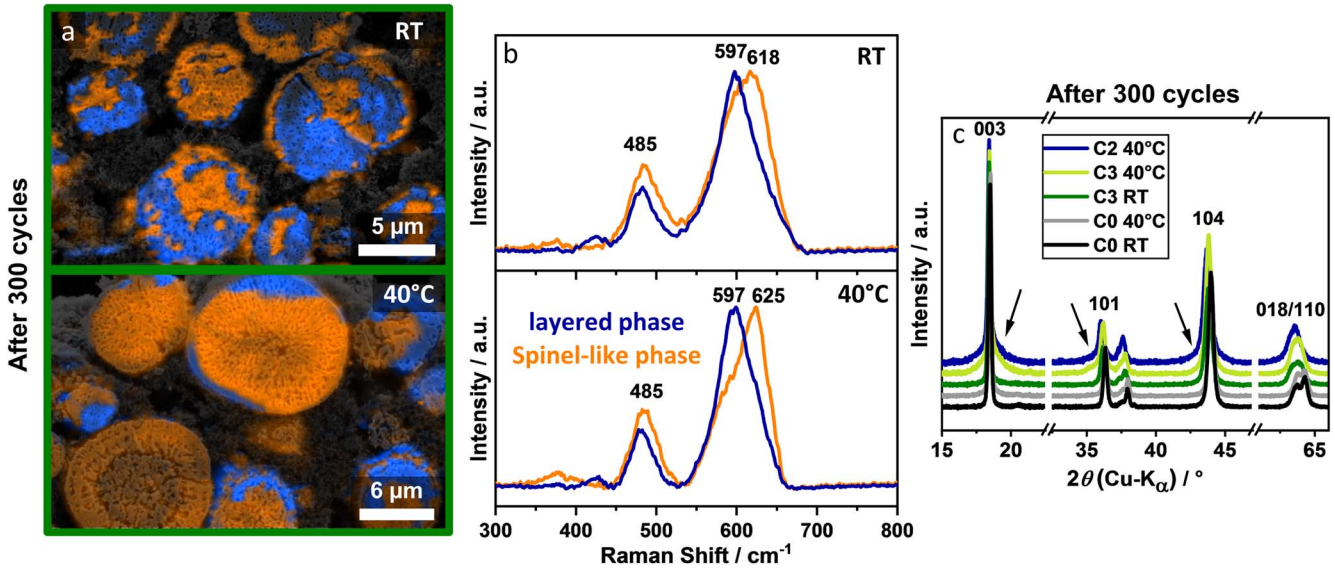

Figure 8. Structural characterization of cycled electrodes after 300 cycles in half-cell configuration: (a) correlative SEM-Raman microscopy of C3 cycled at RT and 40 °C with (b) the corresponding Raman spectra and (c) XRD diffraction pattern of C0 cycled at RT (black) and 40 °C (grey), C3 (green and light green, respectively) and C2 (dark blue, 40 °C).

Finally, the XRD pattern can be indexed to the *R-3m* space group, which shows that the general structure was maintained. However, compared to the as-synthesized materials (Fig. 3c), there is a slight shift towards smaller 2θ angels, indicative of the expansion of the lattice, some shoulders (Fig. 8c, marked with arrows), arising most probably from spinel-like phase, and the coalescence of the (018) with the (110) reflection upon cycling. All together, these results support the conclusion of a structural transformation and densification of the structure.[95]

As a result of the long-term cycling and the structural characterization of the cycled electrodes, we can conclude that the post-treatment step most probably builds an oxygen deficient layer on top of the primary particles, which helps to increase the specific energy of the material, but leads to a faster structural degradation. Furthermore, the oxygen vacancies in the strongly reduced surface region possibly pre-stress the treated materials and likely form regions with lower activation barrier for the layer-to-spinel transformation.

Conclusions

We have investigated in a comprehensive approach the impact of surface modification of LRLO materials by different amounts of citric acid (CA) and subsequent calcination under an inert-atmosphere at 400°C on the electrochemical performance, employing a wide variety of electrochemical, microscopic, and spectroscopic methods. TGA-MS analysis revealed decomposition of the different citrate species and the formation of Li_2CO_3 as a side-product of the carbothermal reaction. Structural characterization of the bulk indicates the preservation of the secondary particles architecture and of the layered structure with slightly increased lattice parameters for increasing amount of applied CA, due to a slight loss of oxygen. Additionally, increasing the CA/LRLO ratio leads to a higher amount of carbon-containing species and carbonates. Surface characterization, e.g., by XPS, Raman microscopy, and SEM imaging using an EsB detector, indicated that the post-treatment steps with CA lead to pronounced oxygen loss in the surface near-

region and the formation of an oxygen-deficient layer, which is covered by additional carbon-containing deposits. The post-treated materials showed, after an electrochemical activation, a higher electrochemical performance as compared to untreated material, with discharge capacities of up to 247 mAh g^{-1} at RT and 276 mAh g^{-1} at 40°C (both C/10) after 100 cycles. Analysis of the gas evolution during the first three cycles showed that the coating partially suppressed the release of O_2, but increased the CO_2 signal, which was attributed to the decomposition of Li_2CO_3 and reaction between evolving oxygen and C-containing species in the post-treated samples. Long-term cycling experiments indicated a slightly faster structural transformation from a layered to a spinel phase at RT for the coated materials, but enhanced aging at 40°C after 300 cycles, compared to reference sample C0. Subsequent post-mortem analysis of the cycled electrodes with correlative SEM-Raman-microscopy supports the conclusions from the electrochemical data. However, higher discharge capacities overcompensate the slightly higher voltage fade, which leads to higher specific energies for all treated materials under these conditions. Overall, the implementation of a 3-in-1 post-treatment procedure for as-synthesized, Co-free Li- and Mn-rich layered oxide particles, including washing, generation of a spinel-like phase in the near-surface region, and formation of a surface coating were successfully demonstrated in this work. We propose the long-term stability can be improved in the future based on the knowledge on the relationship of structural changes and the aging behavior of the material gained in this study.

Acknowledgments

This work received funding by the European Union within the Si-DRIVE project as a part of the European Union's Horizon 2020 research and innovation programme under grant agreement No. 814464 and by the German Federal Ministry of Education and Research (BMBF) in the project ExcellBattMat (03XP0257A and 03XP0257C). The authors thank Dr. M. Boehmler, Dr. J. Englert and Dr. U. Schmidt (WITec) for their scientific support and Raman measurements of the C3 powder. Furthermore, the authors thank Dr. M. Eder (Carl Zeiss Microscopy) for the EsB images of the C3 material as well as P. Drews, G. Arnold, W. Weirather and P. Sichler (all ZSW) for their support during synthesis and characterization of the materials.

ORCID

Florian Klein https://orcid.org/0000-0002-8768-0111
Joachim Bansmann https://orcid.org/0000-0003-3205-7450
Zenonas Jusys https://orcid.org/0000-0003-3970-5799
R. Jürgen Behm https://orcid.org/0000-0002-7565-0628
Mika Lindén https://orcid.org/0000-0003-1736-0638
Peter Axmann https://orcid.org/0000-0003-0274-1796

References

1. M. Marinaro, D. Bresser, E. Beyer, P. Faguy, K. Hosoi, H. Li, J. Sakovica, K. Amine, M. Wohlfahrt-Mehrens, and S. Passerini, *J. Power Sources*, **459**, 228073 (2020).
2. Y. Zhao, O. Pohl, A. I. Bhatt, G. E. Collis, P. J. Mahon, T. Rüther, and A. F. Hollenkamp, *Sustain. Chem.*, **2**, 167 (2021).
3. M. Armand et al., *J. Power Sources*, **479**, 228708 (2020).
4. J. Wang, X. He, E. Paillard, N. Laszczynski, J. Li, and S. Passerini, *Adv. Energy Mater.*, **6**, 1600906 (2016).
5. J. Zheng, S. Myeong, W. Cho, P. Yan, J. Xiao, C. Wang, J. Cho, and J.-G. Zhang, *Adv. Energy Mater.*, **7**, 1601284 (2017).
6. R. A. House, G. J. Rees, M. A. Pérez-Osorio, J.-J. Marie, E. Boivin, A. W. Robertson, A. Nag, M. Garcia-Fernandez, K.-J. Zhou, and P. G. Bruce, *Nat. Energy*, **5**, 777 (2020).
7. W. Zuo, M. Luo, X. Liu, J. Wu, H. Liu, J. Li, M. Winter, R. Fu, W. Yang, and Y. Yang, *Energy Environ. Sci.*, **13**, 4450 (2020).
8. A. Manthiram, J. C. Knight, S.-T. Myung, S.-M. Oh, and Y.-K. Sun, *Adv. Energy Mater.*, **6**, 1501010 (2016).
9. B. Qiu et al., *Nat. Commun.*, **7**, 12108 (2016).
10. M. M. Thackeray, C. S. Johnson, J. T. Vaughey, N. Li, and S. A. Hackney, *J. Mater. Chem.*, **15**, 2257 (2005).
11. Z. Lu, Z. Chen, and J. R. Dahn, *Chem. Mater.*, **15**, 3214 (2003).
12. H. Koga, L. Croguennec, P. Mannessiez, M. Ménétrier, F. Weill, L. Bourgeois, M. Duttine, E. Suard, and C. Delmas, *J. Phys. Chem. C*, **116**, 13497 (2012).
13. Z. Lu and J. R. Dahn, *J. Electrochem. Soc.*, **149**, A815 (2002).
14. E. M. Erickson, F. Schipper, T. R. Penki, J.-Y. Shin, C. Erk, F.-F. Chesneau, B. Markovsky, and D. Aurbach, *J. Electrochem. Soc.*, **164**, A6341 (2017).
15. B. Xu, C. R. Fell, M. Chi, and Y. S. Meng, *Energy Environ. Sci.*, **4**, 2223 (2011).
16. P. Yan, J. Zheng, J.-G. Zhang, and C. Wang, *Nano Lett.*, **17**, 3946 (2017).
17. M. Bianchini et al., *Chem. Mater.*, **32**, 9211 (2020).
18. F. Wu et al., *Energy Storage Mater.*, **42**, 826 (2021).
19. F. Wu et al., *Adv. Energy Mater.*, **10**, 2001830 (2020).
20. J. Zheng, D. Zhu, Y. Yang, and Y. Fung, *Electrochim. Acta*, **59**, 14 (2012).
21. C. P. Laisa, R. N. Ramesha, and K. Ramesha, *Electrochim. Acta*, **256**, 10 (2017).
22. X. Jin, Q. Xu, H. Liu, X. Yuan, and Y. Xia, *Electrochim. Acta*, **136**, 19 (2014).
23. H. Xu, S. Deng, and G. Chen, *J. Mater. Chem. A*, **2**, 15015 (2014).
24. P. K. Nayak, J. Grinblat, M. Levi, E. Levi, S. Kim, J. W. Choi, and D. Aurbach, *Adv. Energy Mater.*, **6**, 1502398 (2016).
25. F. Wu, G.-T. Kim, M. Kuenzel, H. Zhang, J. Asenbauer, D. Geiger, U. Kaiser, and S. Passerini, *Adv. Energy Mater.*, **9**, 1902445 (2019).
26. S. Sharifi-Asl, J. Lu, K. Amine, and R. Shahbazian-Yassar, *Adv. Energy Mater.*, **9**, 1900551 (2019).
27. S. Han, B. Qiu, Z. Wei, Y. Xia, and Z. Liu, *J. Power Sources*, **268**, 683 (2014).
28. J. Zhang, Z. Lei, J. Wang, Y. NuLi, and J. Yang, *ACS Appl. Mater. Interfaces*, **7**, 15821 (2015).
29. P. Oh, S. Myeong, W. Cho, M.-J. Lee, M. Ko, H. Y. Jeong, and J. Cho, *Nano Lett.*, **14**, 5965 (2014).
30. H. Sclar et al., *J. Electrochem. Soc.*, **167**, 110563 (2020).
31. J. Sicklinger, H. Beyer, L. Hartmann, F. Riewald, C. Sedlmeier, and H. A. Gasteiger, *J. Electrochem. Soc.*, **167**, 130507 (2020).
32. S.-H. Kang, C. S. Johnson, J. T. Vaughey, K. Amine, and M. M. Thackeray, *J. Electrochem. Soc.*, **153**, A1186 (2006).
33. S. Ramakrishnan, B. Park, J. Wu, W. Yang, and B. D. McCloskey, *J. Am. Chem. Soc.*, **142**, 8522 (2020).
34. D. Y. Yu and K. Yanagida, *J. Electrochem. Soc.*, **158**, A1015 (2011).
35. K. Xu, S. Pang, Y. Wang, X. Shen, H. Wen, W. Wang, Y. Su, and X. Xi, *J. Electrochem. Soc.*, **164**, A2348 (2017).
36. S. Pang et al., *J. Electrochem. Soc.*, **165**, A1897 (2018).
37. B. Liu, *Int. J. Electrochem. Sci.*, 7578 (2018).
38. F. Klein et al., *ChemSusChem*, **15**, e202201061 (2022).
39. M.-J. Wang, A.-F. Shao, F.-D. Yu, G. Sun, D.-M. Gu, and Z.-B. Wang, *ACS Sustain. Chem. Eng.*, **7**, 12825 (2019).
40. Y.-Q. Sun, W. Fu, Y.-X. Hu, J. Vaughan, and L.-Z. Wang, *Tungsten*, **3**, 245 (2021).
41. Z. Ye et al., *Angew. Chem. Int. Ed.*, **60**, 23248 (2021).
42. Y. Lee, J. Lee, K. Y. Lee, J. Mun, J. K. Lee, and W. Choi, *J. Power Sources*, **315**, 284 (2016).
43. X. Zhang, R. Yu, Y. Huang, X. Wang, Y. Wang, B. Wu, Z. Liu, and J. Chen, *ACS Sustain. Chem. Eng.*, **6**, 12969 (2018).
44. D. Chen, F. Zheng, L. Li, M. Chen, X. Zhong, W. Li, and L. Lu, *J. Power Sources*, **341**, 147 (2017).
45. C.-H. Jo, D.-H. Cho, H.-J. Noh, H. Yashiro, Y.-K. Sun, and S. T. Myung, *Nano Res.*, **8**, 1464 (2015).
46. Y. Wu, J. Ming, L. Zhuo, Y. Yu, and F. Zhao, *Electrochim. Acta*, **113**, 54 (2013).
47. M. Xu, Z. Chen, L. Li, H. Zhu, Q. Zhao, L. Xu, N. Peng, and L. Gong, *J. Power Sources*, **281**, 444 (2015).
48. C. Zhou, P. Wang, B. Zhang, J. Zheng, Y. Zhou, C. Huang, and X. Xi, *J. Electrochem. Soc.*, **165**, A1648 (2018).
49. U. Breddemann et al., *ChemElectroChem*, **6**, 3337 (2019).
50. X. Ding, D. Luo, J. Cui, H. Xie, Q. Ren, and Z. Lin, *Angew. Chem. Int. Ed.*, **59**, 7778 (2020).
51. T. Lin, T. U. Schulli, Y. Hu, X. Zhu, Q. Gu, B. Luo, B. Cowie, and L. Wang, *Adv. Funct. Mater.*, **30**, 1909192 (2020).
52. Q. Xia, X. Zhao, M. Xu, Z. Ding, J. Liu, L. Chen, D. G. Ivey, and W. Wei, *J. Mater. Chem. A*, **3**, 3995 (2015).
53. S. Pang, K. Xu, Y. Wang, X. Shen, W. Wang, Y. Su, M. Zhu, and X. Xi, *J. Power Sources*, **365**, 68 (2017).
54. B. Song, C. Zhou, Y. Chen, Z. Liu, M. O. Lai, J. Xue, and L. Lu, *RSC Adv.*, **4**, 44244 (2014).
55. Z. Li, Q. Li, A. Zhang, W. Wen, L. Wang, Z. Wang, J. Wang, S. Lu, X. Li, and Z. Wang, *New J. Chem.*, **43**, 18943 (2019).
56. W. Guo, C. Zhang, Y. Zhang, L. Lin, W. He, Q. Xie, B. Sa, L. Wang, and D.-L. Peng, *Adv. Mater.*, **33**, e2103173 (2021).
57. J. Liao, Z. Zhang, W. Fan, Q. Wang, and D. Liao, *Electrochim. Acta*, **405**, 139798 (2022).
58. C. R. Fell, D. Qian, K. J. Carroll, M. Chi, J. L. Jones, and Y. S. Meng, *Chem. Mater.*, **25**, 1621 (2013).
59. E. S. Ilton, J. E. Post, P. J. Heaney, F. T. Ling, and S. N. Kerisit, *Appl. Surf. Sci.*, **366**, 475 (2016).
60. J. F. Moulder and J. Chastain (ed.), *Handbook of X-ray Photoelectron Spectroscopy: A Reference Book of Standard Spectra for Identification and Interpretation of XPS Data* (Perkin-Elmer Corporation, Eden Prairie, Minn.) (1992).
61. Z. Jusys, M. Binder, J. Schnaidt, and R. J. Behm, *Electrochim. Acta*, **314**, 188 (2019).
62. M. Mancini, P. Axmann, G. Gabrielli, M. Kinyanjui, U. Kaiser, and M. Wohlfahrt-Mehrens, *ChemSusChem*, **9**, 1843 (2016).

63. P. Linstrom and W. G. Mallard, *'Mass Spectra' in NIST Chemistry WebBook* (National Institute of Standards and Technology, Gaithersburg, MD) (2010), 20899.
64. J. Sicklinger, M. Metzger, H. Beyer, D. Pritzl, and H. A. Gasteiger, *J. Electrochem. Soc.*, **166**, A2322 (2019).
65. T. Nakamura, H. Gao, K. Ohta, Y. Kimura, Y. Tamenori, K. Nitta, T. Ina, M. Oishi, and K. Amezawa, *J. Mater. Chem. A*, **7**, 5009 (2019).
66. J.-W. Kim and H.-G. Lee, *Metall. Mater. Trans. B*, **32**, 17 (2001).
67. G. E. Tobón-Zapata, E. G. Ferrer, S. B. Etcheverry, and E. J. Baran, *J. Therm. Anal. Calorim.*, **61**, 29 (2000).
68. B. M. Abu-Zied and A. M. Asiri, *Thermochim. Acta*, **649**, 54 (2017).
69. D. Wyrzykowski, E. Hebanowska, G. Nowak-Wiczk, M. Makowski, and L. Chmurzyński, *J. Therm. Anal. Calorim.*, **104**, 731 (2011).
70. M. M. Barbooti and D. A. Al-Sammerrai, *Thermochim. Acta*, **98**, 119 (1986).
71. G. Lombardo, B. Ebin, M. R. S. J. Foreman, B.-M. Steenari, and M. Petranikova, *ACS Sustain. Chem. Eng.*, **7**, 13668 (2019).
72. J. R. Croy, D. Kim, M. Balasubramanian, K. Gallagher, S.-H. Kang, and M. M. Thackeray, *J. Electrochem. Soc.*, **159**, A781 (2012).
73. T. Zhao, S. Chen, R. Chen, L. Li, X. Zhang, M. Xie, and F. Wu, *ACS Appl. Mater. Interfaces*, **6**, 21711 (2014).
74. Z. Yang, H. Zhou, Z. Bao, J. Li, and C. Yin, *J. Mater. Sci., Mater. Electron.*, **30**, 19493 (2019).
75. S. Maiti, H. Sclar, J. G. Rosy, M. Talianker, L. Burstein, M. Noked, B. Markovsky, and D. Aurbach, *ACS Appl. Mater. Interfaces*, **12**, 32698 (2020).
76. J. Zemann, *Acta Cryst.*, **10**, 664 (1957).
77. D. Marrocchelli, S. R. Bishop, H. L. Tuller, and B. Yildiz, *Adv. Funct. Mater.*, **22**, 1958 (2012).
78. R. D. Shannon, *Acta Cryst. A*, **32**, 751 (1976).
79. M. C. Biesinger, B. P. Payne, A. P. Grosvenor, L. W. Lau, A. R. Gerson, and R. S. Smart, *Appl. Surf. Sci.*, **257**, 2717 (2011).
80. G. Assat, D. Foix, C. Delacourt, A. Iadecola, R. Dedryvère, and J.-M. Tarascon, *Nat. Commun.*, **8**, 2219 (2017).
81. H. Liu, Y. Yang, and J. Zhang, *J. Power Sources*, **173**, 556 (2007).
82. J.-C. Dupin, D. Gonbeau, P. Vinatier, and A. Levasseur, *Phys. Chem. Chem. Phys.*, **2**, 1319 (2000).
83. B. Zhang, L. Wang, F. Bai, P. Xiao, B. Zhang, X. Chen, J. Sun, and W. Yang, *Dalton Trans.*, **48**, 3209 (2019).
84. Z. Zhao, M. Sun, T. Wu, J. Zhang, P. Wang, L. Zhang, C. Yang, C. Peng, and H. Lu, *Nano-Micro Lett.*, **13**, 118 (2021).
85. E. McCalla et al., *Science*, **350**, 1516 (2015).
86. K. N. Wood and G. Teeter, *ACS Appl. Energy Mater.*, **1**, 4493 (2018).
87. E. Flores, P. Novák, and E. J. Berg, *Front. Energy Res.*, **6**, 82 (2018).
88. P. Lanz, C. Villevieille, and P. Novák, *Electrochim. Acta*, **130**, 206 (2014).
89. C. M. Julien and M. Massot, *Mater. Sci. Eng. B*, **100**, 69 (2003).
90. A. Abdel-Ghany, A. M. Hashem, A. Mauger, and C. M. Julien, *Energies*, **13**, 3487 (2020).
91. S. Francis Amalraj et al., *Electrochim. Acta*, **78**, 32 (2012).
92. P. Lanz, C. Villevieille, and P. Novák, *Electrochim. Acta*, **109**, 426 (2013).
93. A. Sadezky, H. Muckenhuber, H. Grothe, R. Niessner, and U. Pöschl, *Carbon*, **43**, 1731 (2005).
94. E. Boivin, N. Guerrini, R. A. House, J. G. Lozano, L. Jin, G. J. Rees, J. W. Somerville, C. Kuss, M. R. Roberts, and P. G. Bruce, *Adv. Funct. Mater.*, **31**, 2003660 (2021).
95. W. Hua et al., *Nat. Commun.*, **10**, 5365 (2019).
96. S. Shen et al., *ACS Appl. Mater. Interfaces*, **10**, 12666 (2018).
97. A. T. Freiberg, J. Sicklinger, S. Solchenbach, and H. A. Gasteiger, *Electrochim. Acta*, **346**, 136271 (2020).
98. B. Strehle, K. Kleiner, R. Jung, F. Chesneau, M. Mendez, H. A. Gasteiger, and M. Piana, *J. Electrochem. Soc.*, **164**, A400 (2017).
99. T. Teufl, B. Strehle, P. Müller, H. A. Gasteiger, and M. A. Mendez, *J. Electrochem. Soc.*, **165**, A2718 (2018).
100. K. Luo et al., *J. Am. Chem. Soc.*, **138**, 11211 (2016).
101. S. Solchenbach, M. Wetjen, D. Pritzl, K. U. Schwenke, and H. A. Gasteiger, *J. Electrochem. Soc.*, **165**, A512 (2018).
102. N. Yabuuchi, K. Yoshii, S.-T. Myung, I. Nakai, and S. Komaba, *J. Am. Chem. Soc.*, **133**, 4404 (2011).
103. M. Metzger, B. Strehle, S. Solchenbach, and H. A. Gasteiger, *J. Electrochem. Soc.*, **163**, A1219 (2016).
104. R. Jung, M. Metzger, F. Maglia, C. Stinner, and H. A. Gasteiger, *J. Electrochem. Soc.*, **164**, A1361 (2017).
105. M. Metzger, J. Sicklinger, D. Haering, C. Kavakli, C. Stinner, C. Marino, and H. A. Gasteiger, *J. Electrochem. Soc.*, **162**, A1227 (2015).
106. J. Zheng, P. Xu, M. Gu, J. Xiao, N. D. Browning, P. Yan, C. Wang, and J.-G. Zhang, *Chem. Mater.*, **27**, 1381 (2015).
107. E. Rossen, J. Reimers, and J. Dahn, *Solid State Ion.*, **62**, 53 (1993).
108. B. Shi, J. Gim, L. Li, C. Wang, A. Vu, J. R. Croy, M. M. Thackeray, and E. Lee, *Chem. Comm.*, **57**, 11009 (2021).

Supporting Information

Effect of Three-in-one Surface Modification of Spherical, Co-free Li-rich Cathode Material for Li-Ion Batteries ($Li_{1.2}Mn_{0.6}Ni_{0.2}O_2$) with Citric Acid

Florian Klein,[a] Claudia Pfeifer,[a] Joachim Bansmann,[b] Zenonas Jusys,[c] R. Jürgen Behm,[c,e] Margret Wohlfahrt-Mehrens,[a,e] Mika Lindén[z,d] and Peter Axmann[z] [a]

[z] E-Mail: mlinden@uni-ulm.de, Peter.Axmann@zsw-bw.de

[a] F. Klein, C. Pfeifer, Dr. M. Wohlfahrt-Mehrens, Dr. P. Axmann
Zentrum für Sonnenenergie- und Wasserstoffforschung Baden-Württemberg (ZSW)
Helmholtzstrasse 8, D-89081 Ulm (Germany)

[b] Dr. J. Bansmann
Institute of Surface Chemistry and Catalysis, Ulm University
Albert-Einstein-Allee 47, D-89081 Ulm (Germany)

[c] Dr. Z. Jusys, Prof. Dr. R. J. Behm
Institute of Theoretical Chemistry, Ulm University
Albert-Einstein-Allee 11, D-89081 Ulm (Germany)

[d] Prof. Dr. M. Lindén
Institute for Inorganic Chemistry II, Ulm University
Albert-Einstein-Allee 11, D-89081 Ulm (Germany)

[e] Prof. Dr. R. J. Behm, Dr. M. Wohlfahrt-Mehrens
Helmholtz Institute Ulm Electrochemical Energy Storage (HIU),
Helmholtzstraße 11, D–89081 Ulm (Germany)

Table S1. Results of elemental analysis by ICP-OES given as molar ratios (Li + Mn + Ni = 2).

	Li	Mn	Ni
C0	1.205	0.585	0.210
C1	1.198	0.592	0.210
C2	1.200	0.589	0.211
C3	1.202	0.588	0.209

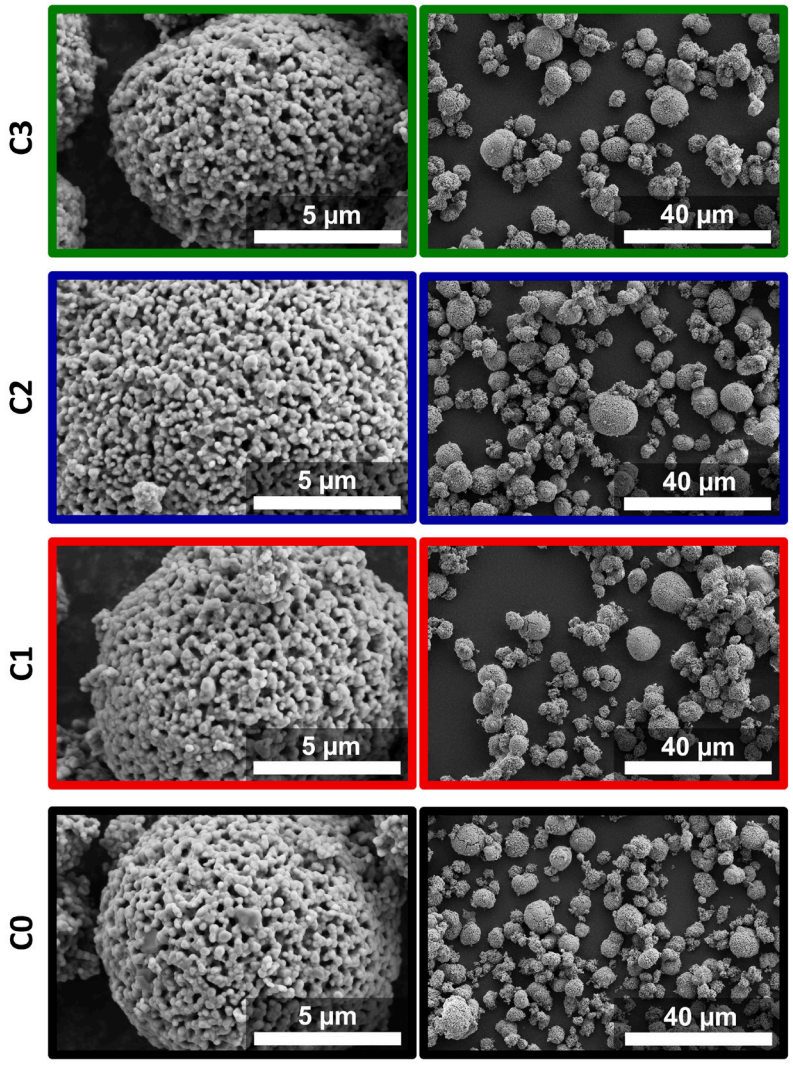

Figure S1. SEM images (SE detector, accelerating voltage 5 kV) of C0 (black), C1 (red), C2 (blue) and C3 (green).

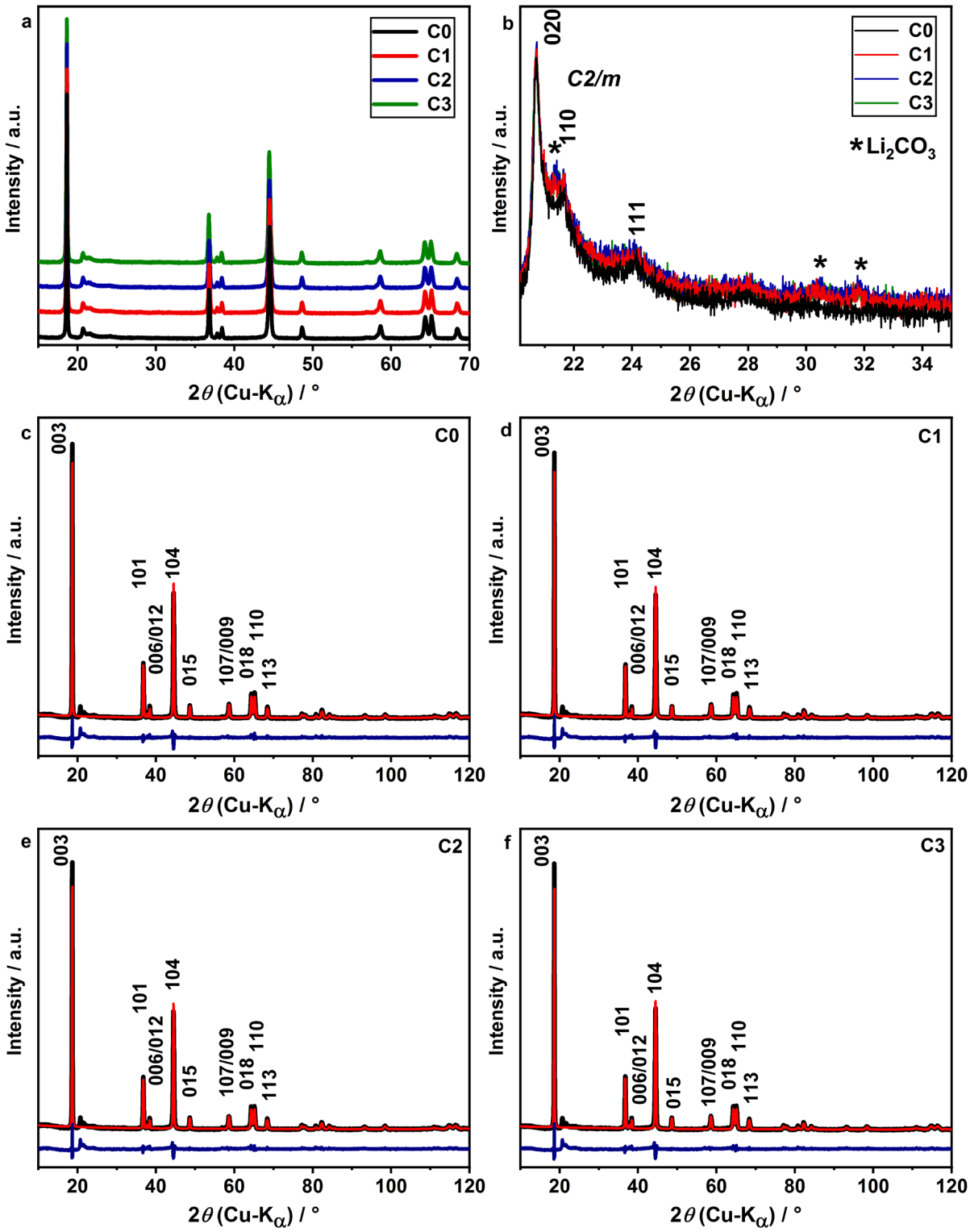

Figure S2. Evaluation of the XRD results a) overview over the XRD pattern of C0 (black), C1 (red), C2 (blue) and C3 (green); b) proof of Li_2CO_3 traces and indexing of the related peaks (*) for C0-C3 and detailed plots from Rietveld refinement with difference (blue) between the calculated (red) and the experimental (black) pattern for c) C0, d) C1, e) C2 and f) C3.

Table S2. Rietveld refinement results (TOPAS V6, Bruker) based on the structural model for $Li_{1.2}Mn_{0.6}Ni_{0.2}O_2$ of Fell et al.[1]: space group, lattice parameters, cell volume V, cation occupancies, atom coordinate z of the oxide ions, the estimated crystallite size (integral breadth), isotropic microstrain ε_0 and the R factor.

	C0	**C1**	**C2**	**C3**
Space group	*R-3m* (166)	*R-3m* (166)	*R-3m* (166)	*R-3m* (166)
***a* / Å**	2.862	2.863	2.864	2.865
***c* / Å**	14.260	14.262	14.267	14.270
V / Å³	101.1	101.2	101.3	101.4
Li_{Li} (3a: 0, 0, 0)	0.98	0.98	0.98	0.98
Ni_{Li} (3a: 0, 0, 0)	0.02	0.02	0.02	0.02
Li_{TM} (3b: 0, 0, 1/2)	0.22	0.22	0.22	0.22
Mn_{TM} (3b: 0, 0, 1/2)	0.59	0.59	0.59	0.59
Ni_{TM} (3b: 0, 0, 1/2)	0.18	0.18	0.18	0.18
***z* [O (6c: 0, 0, z)]**	0.242	0.242	0.241	0.241
Crystallite Size / nm	116	114	116	109
ε_0	0.0011	0.0011	0.0011	0.0011
R_{wp} / %	7.2	7.1	7.0	7.5

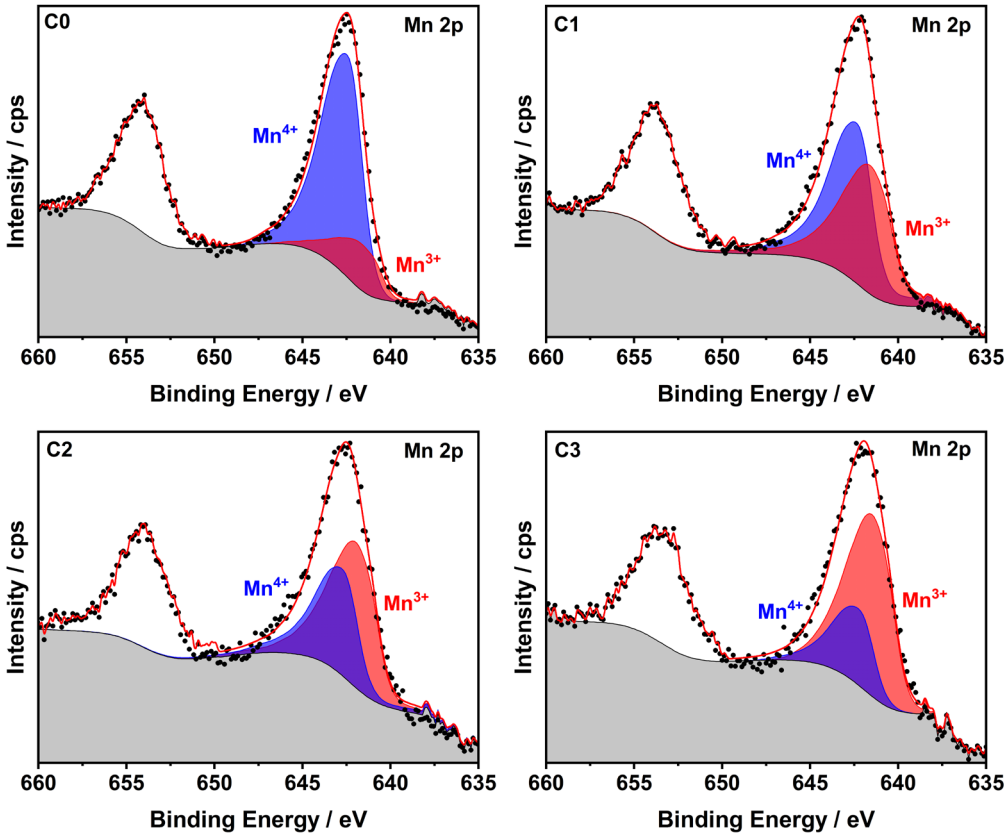

Figure S3. Deconvoluted Mn 2p XPS spectra of all powders (C0-C3).

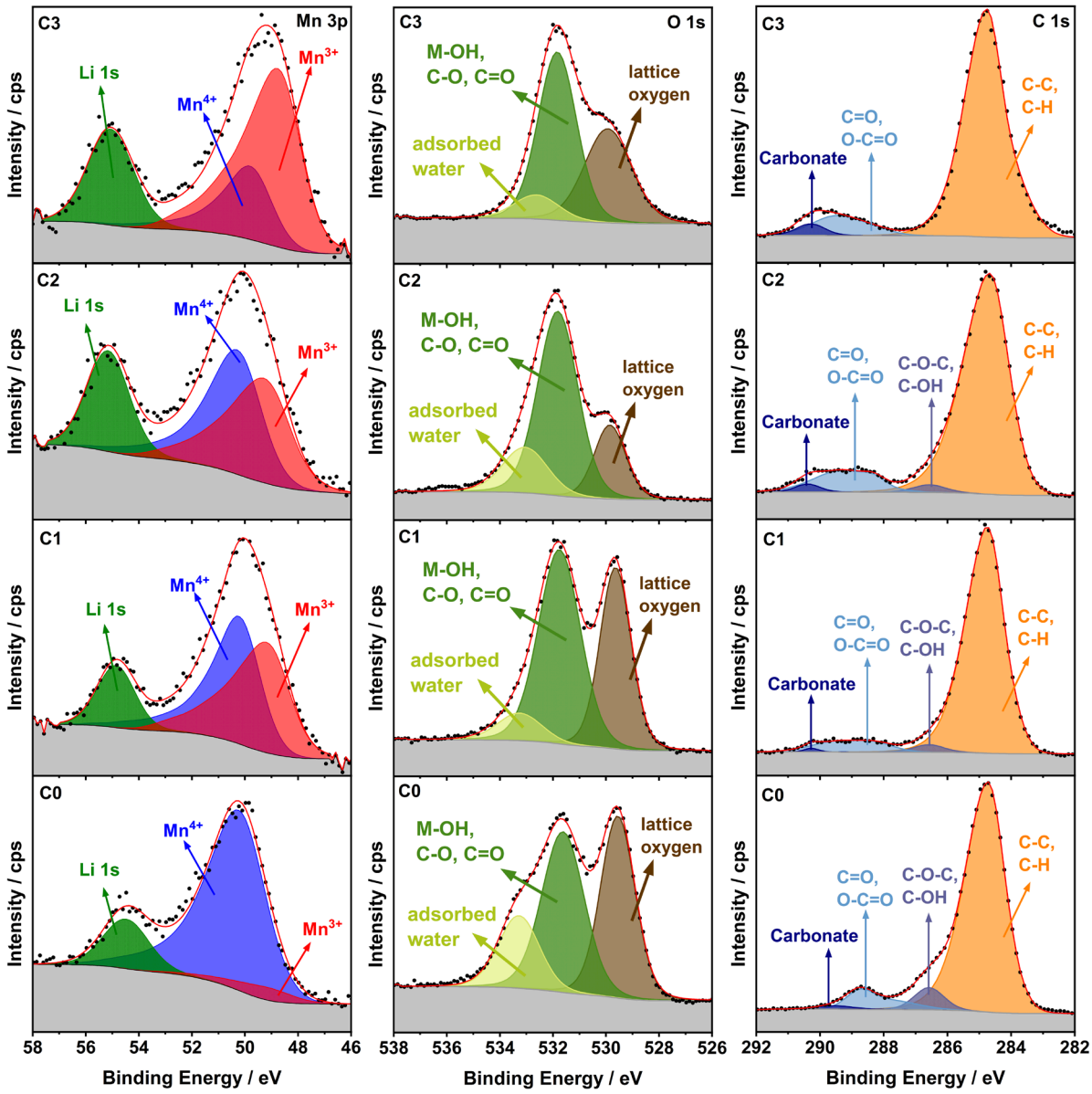

Figure S4. Deconvoluted XPS spectra of all investigated powders (C0-C3): Mn 3p (left column), O 1s (middle column) and C 1s (right column).

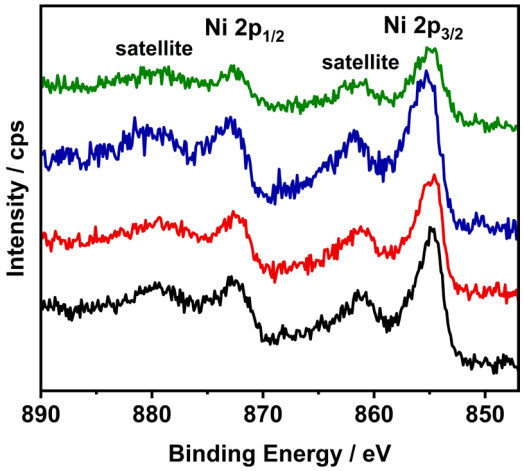

Figure S5. Ni $2p_{3/2}$ and Ni $2p_{1/2}$ XPS spectra of C0 (black), C1 (red), C2 (blue) and C3 (green) with their corresponding satellite peaks.

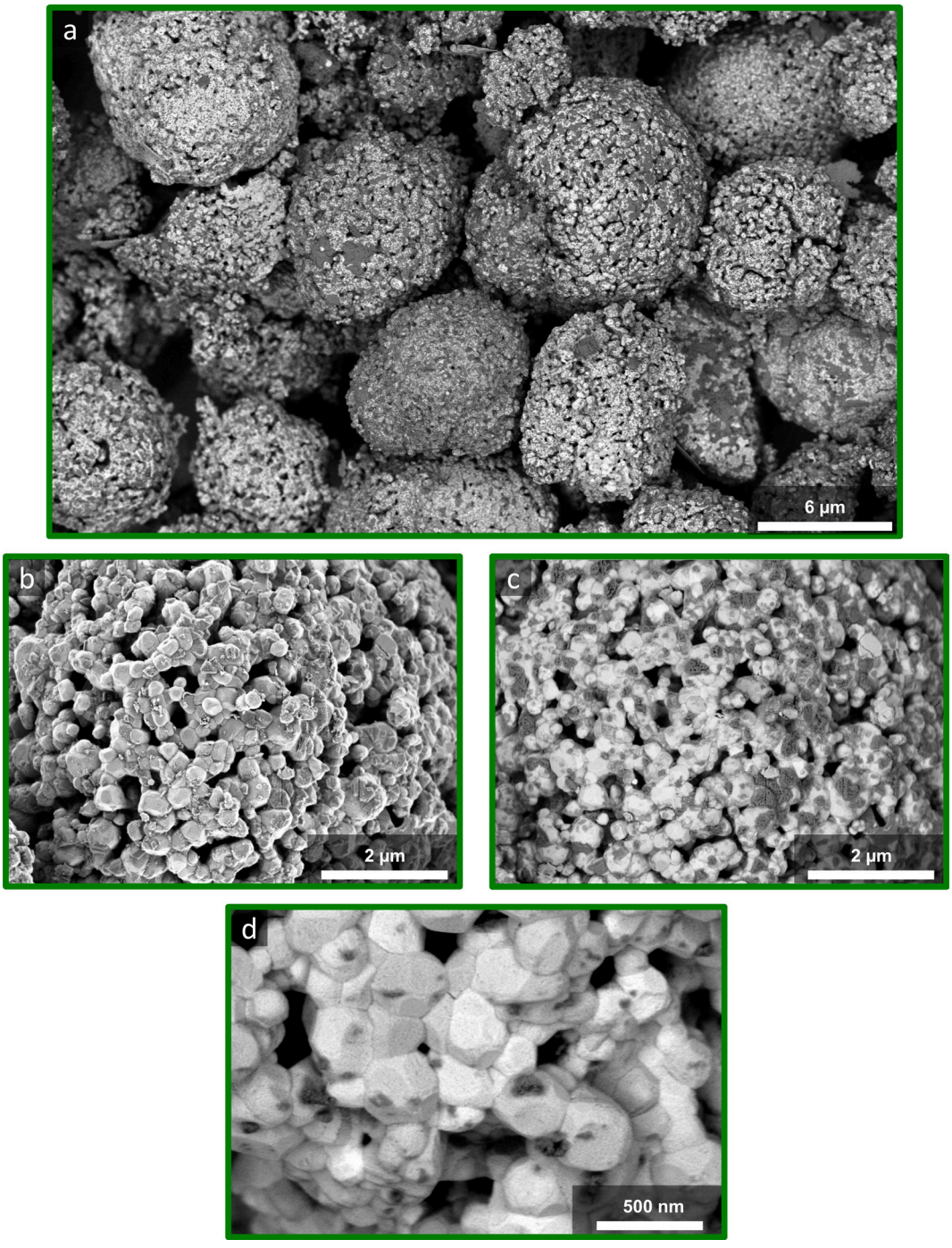

Figure S6. SEM images of C3 with an accelerating voltage of 0.8 kV. a) EsB overview image presenting the distribution of the carbon species, comparison between b) inlens SE image and c) EsB image of the same area, and d) EsB high magnification image showing surface allocation with very small carbon particles.

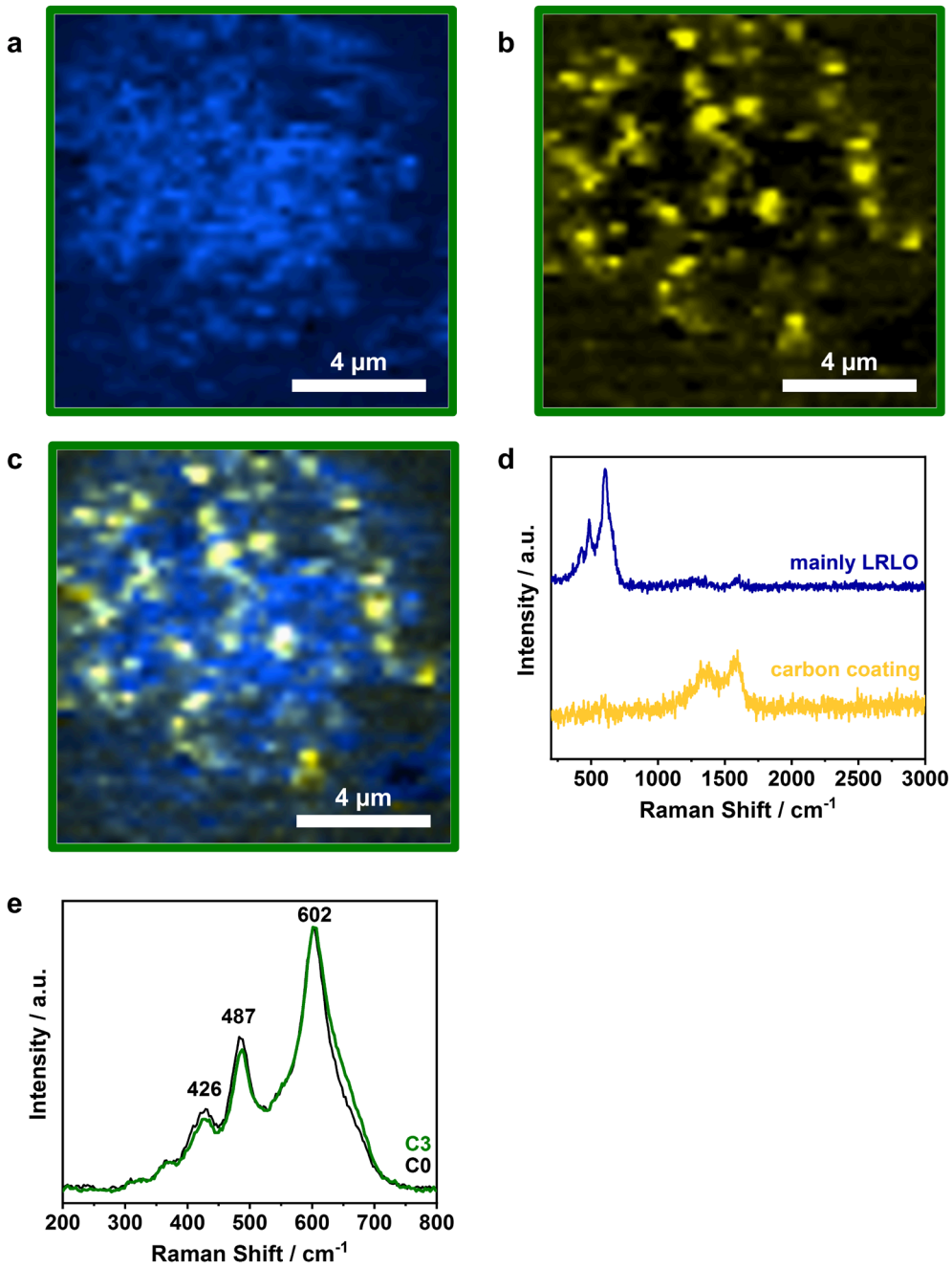

Figure S7. Confocal Raman microscopy results of the particle surface of C3 after spectral demixing: a) demixed map of the LRLO signal, b) demixed map of carbon coating signal, c) combined map of a) and b) as well as d) corresponding Raman spectra of the demixed components, LRLO and the carbon coating. Additionally, the overview spectra of C0 and C3 (Figure 4f) are presented in higher magnification in e), focused on the M-O-vibration bands.

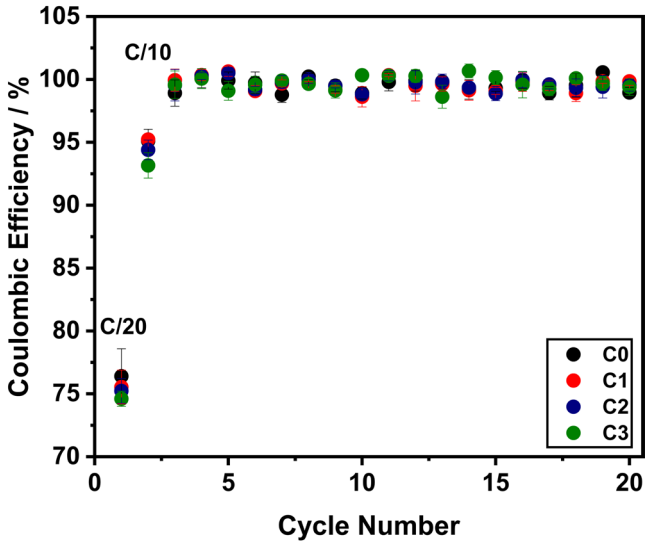

Figure S8. Coulombic efficiency of the cycling experiment presented in Figure 5: C0 (black), C1 (red), C2 (blue), and C3 (green).

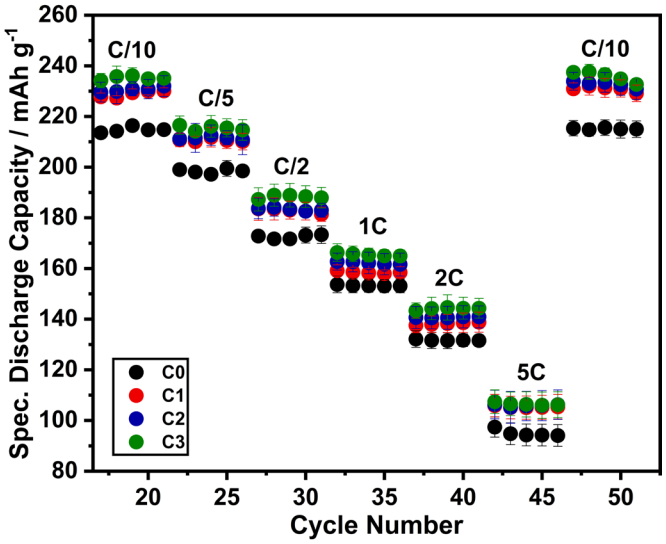

Figure S9. Rate performance of the investigated materials: C0 (black), C1 (red), C2 (blue), and C3 (green) in the voltage range of 2.5 to 4.8 V under symmetrical charge and discharge conditions.

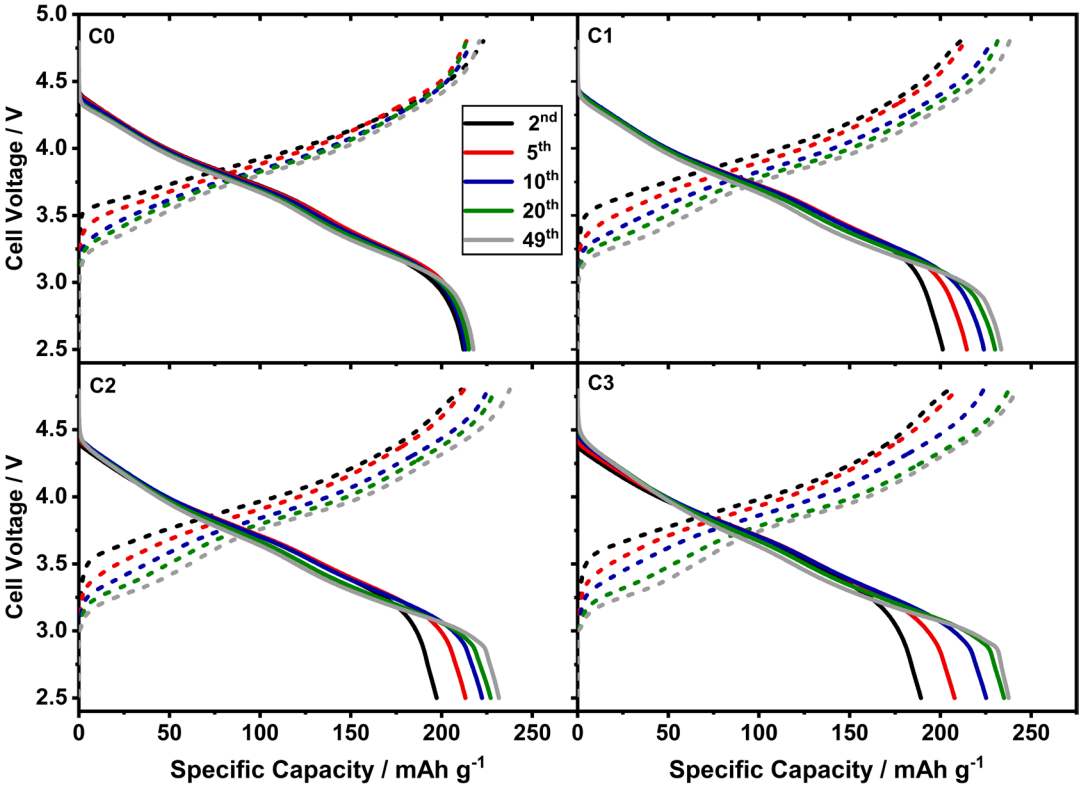

Figure S10. Corresponding potential profiles of the d*Q*/d*V* plots in Figure 5.

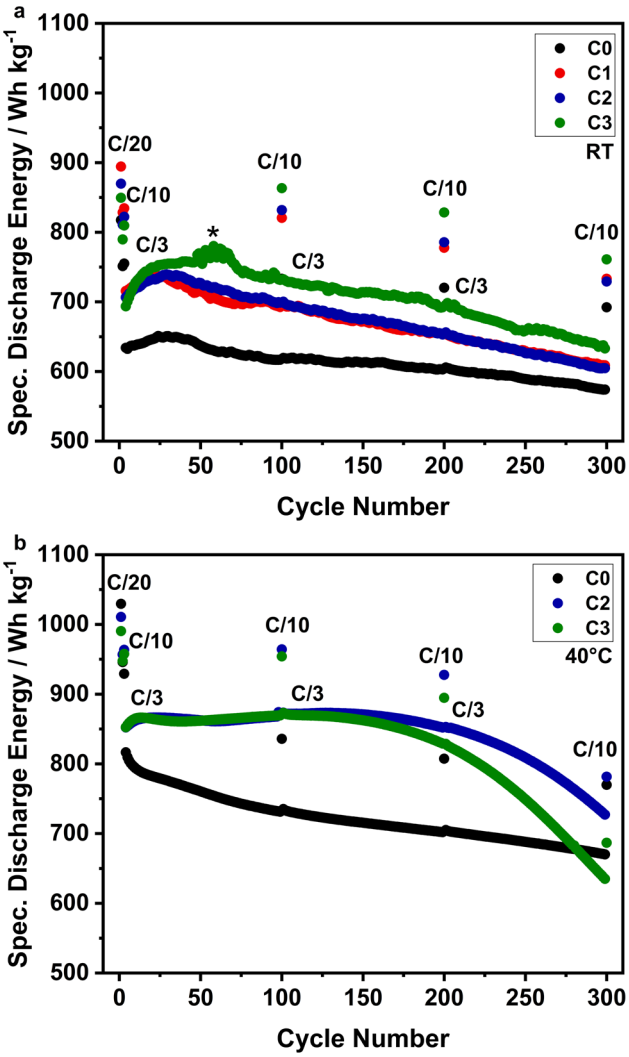

Figure S11. Specific discharge energy of the long-term stability tests a) of C0 (black), C1 (red), C2 (blue) and C3 (green) at RT and b) of C0, C2 and C3 (same color code) at 40°C. The peaks marked with a star (*) of C3 and C0 are artefacts from temporarily slightly increased RT (ΔT ≈ 3°C).

References

[1] C. R. Fell, D. Qian, K. J. Carroll, M. Chi, J. L. Jones and Y. S. Meng, *Chem. Mater.,* **25**(9), 1621–1629 (2013).

In-depth structural characterization of the influence of Li^+ excess on spherical, Co-free layered $LiMn_{0.5}Ni_{0.5}O_2$ cathode material using correlative Raman-SEM microscopy

Reproduced with permission from:

F. Klein, C. Pfeifer, P. Scheitenberger, L. F. Pfeiffer, D. Zimmer, M. Wohlfahrt-Mehrens, M. Lindén, P. Axmann, *J. Mater. Chem. A* **2023**, *11*, 5135, DOI: 10.1039/D2TA05957F.

© 2023 The Authors. Journal of Materials Chemistry A is © by the Royal Society of Chemistry. This open access article is reproduced under the terms of the Creative Commons Attribution 3.0 Unported License CC BY 3.0 (https://creativecommons.org/licenses/by/3.0/).

Journal of Materials Chemistry A

ROYAL SOCIETY OF CHEMISTRY

PAPER

View Article Online
View Journal | View Issue

Check for updates

Cite this: J. Mater. Chem. A, 2023, 11, 5135

In-depth structural characterization of the influence of Li^+ excess on spherical, Co-free layered $LiMn_{0.5}Ni_{0.5}O_2$ cathode material using correlative Raman–SEM microscopy†

Florian Klein, [a] Claudia Pfeifer,[a] Philipp Scheitenberger,[b] Lukas Pfeiffer, [a] Dominik Zimmer,[c] Margret Wohlfahrt-Mehrens,[a] Mika Lindén *[b] and Peter Axmann *[a]

A series of different spherical Co-free $Li_{1+x}(Mn_{0.5}Ni_{0.5})_{1-x}O_2$ powders with $0 \leq x \leq 0.16$ was synthesized to investigate the effect of excess Li^+ on the host structure of $LiMn_{0.5}Ni_{0.5}O_2$. Structural investigation with XRD shows less Li^+/Ni^{2+} disordering and strong broadening of the pattern indicating phase separation with increasing x. A deeper understanding of the structural changes was gained from a combined approach of SEM, EDX and Raman microscopy. A phase separation into Ni-rich and Li-/Mn-rich layered oxide domains could be proven. In the investigated series, the best electrochemical performance was obtained for $Li_{1.07}(Mn_{0.5}Ni_{0.5})_{0.93}O_2$ with a stable specific discharge capacity of 173 mAh g^{-1} (658 Wh kg^{-1}, 12 mA g^{-1}) after 40 cycles. The presented results strongly highlight the strength of correlating chemical (EDX), structural (Raman) and morphological (SEM) information with sub-micrometer lateral resolution for the development and understanding of future battery materials.

Received 27th July 2022
Accepted 21st December 2022

DOI: 10.1039/d2ta05957f

rsc.li/materials-a

This article is licensed under a Creative Commons Attribution 3.0 Unported Licence.

Introduction

State-of-the-art layered lithium transition metal oxides, *e.g.* $Li(Ni_{1-x-y}Mn_xCo_y)O_2$ (NMC) with high Ni content, are the most popular cathode material class for lithium ion battery (LIB) application.[1] In 2001, several important papers were published by Dahn and Lu on $Li(Ni_xCo_{1-2x}Mn_x)O_2$ ($x = 1/4, 3/8$) as well as by Ohzuku on $LiNi_{1/3}Mn_{1/3}Co_{1/3}O_2$ and $LiMn_{0.5}Ni_{0.5}O_2$ with promising cycling performance.[2–5] Particularly, the work of Ohzuku demonstrated the possibility to reduce the Ni compared to nowadays state-of-the-art Ni-rich compounds and to remove Co from the structure with stable discharge capacities of approximately 200 mAh g^{-1} for $LiMn_{0.5}Ni_{0.5}O_2$, which will both reduce cost and critical raw material demand.[3,6–9] Therefore, it is very important to further investigate and understand the structural diversity of the materials, represented in the Li–Ni–Mn–O phase diagram.[10] In the past, many groups have intensively studied different regions of the phase diagram. Besides the spinel material with a general formula of $Li(Ni_x-Mn_{2-x})O_4$ ($0 \leq x \leq 0.5$),[11,12] there are two further noteworthy cathode material classes in the ternary phase diagram with layered structures (Fig. 1): $Li(Ni_{1-y}Mn_y)O_2$ ($0 \leq y \leq 0.5$, red line)[13–16] and $z\ Li_2MnO_3 \cdot (1-z)\ LiMn_{0.5}Ni_{0.5}O_2$ ($0 \leq z \leq 1.0$, LRLO, green line).[17–19] Obviously, the material with a composition of $LiMn_{0.5}Ni_{0.5}O_2$ seems to be highly important for both layered systems and is from a structural point of view the end

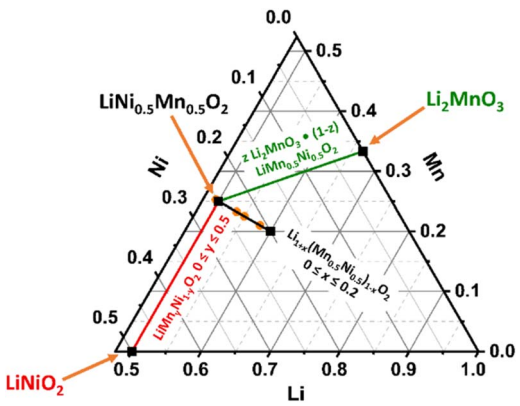

Fig. 1 Schematic compositional diagram of the Li–Mn–Ni–O ternary system (Li + Mn + Ni = 1) with selected structures: $Li(Ni_{1-x}Mn_x)O_2$ ($0 \leq x \leq 0.5$, red), $z\ Li_2MnO_3 \cdot (1-z)\ LiMn_{0.5}Ni_{0.5}O_2$ ($0 \leq z \leq 0.5$, green) and $Li_{1+x}(Mn_{0.5}Ni_{0.5})_{1-x}O_2$ ($0 \leq x \leq 0.2$, black). The elemental compositions of the powders investigated in this study are dotted in orange.

[a]Zentrum für Sonnenenergie- und Wasserstoffforschung Baden-Württemberg (ZSW), Helmholtzstrasse 8, Ulm D-89081, Germany. E-mail: peter.axmann@zsw-bw.de

[b]Institute for Inorganic Chemistry II, Ulm University, Albert-Einstein-Allee 11, Ulm D-89081, Germany. E-mail: mika.linden@uni-ulm.de

[c]Oxford Instruments GmbH, Borsigstr. 15A, Wiesbaden 65205, Germany

† Electronic supplementary information (ESI) available: Further SEM images, XRD overview and more detailed pattern, analysis of Li^+/Ni^{2+} disorder, specific capacity analysis of the first cycle, EBSD data and further Raman evaluation. See DOI: https://doi.org/10.1039/d2ta05957f

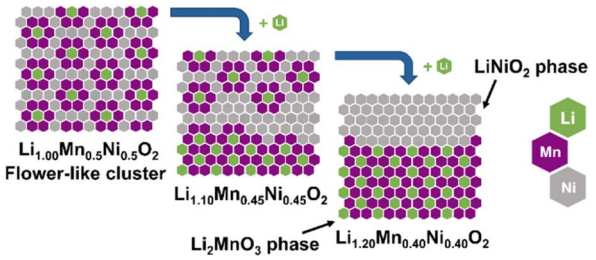

Fig. 2 Schematic illustration of a hypothetical complete phase separation in the transition metal layer with increased Li^+ content in $Li_{1+x}(Mn_{0.5}Ni_{0.5})_{1-x}O_2$. The proposed flower-like structure is based on first-principle calculations by the group of Ceder.[23]

member of the solid solution of $Li(Ni_{1-y}Mn_y)O_2$ ($0 \le y \le 0.5$, red line), which is isostructural to the α-$NaFeO_2$ type with the space group $R\bar{3}m$.[13] Up to 50% of the Ni sites of $LiNiO_2$ can be replaced by redox inactive Mn^{4+} ions without changing the structure.[13,14,16] For charge compensation each Mn^{4+} ion requires an equivalent amount of Ni^{2+}, thereby stabilizing the host structure.[20] Consequently, $LiMn_{0.5}Ni_{0.5}O_2$ is the most stable phase containing only Ni^{2+} and Mn^{4+} ions in its solid solution.[16] Unfortunately, the Li^+/Ni^{2+} cation disorder is particularly pronounced for $LiMn_{0.5}Ni_{0.5}O_2$ ($\approx$10%).[21] In the literature, the combination of the high amount of Ni^{2+} ions in the structure and the high affinity of Mn and Li to each other is reported to be the reason for the formation of flower-like clusters in the TM layer (Fig. 2, left scheme).[22–25] As a consequence of the clustering, $LiMn_{0.5}Ni_{0.5}O_2$ shows a lower electrochemical performance due to the resulting kinetic limitations.[16,19,26,27] Nevertheless, high specific discharge capacities are reported in a broad range from 150 to 200 mAh g^{-1}.[3,18,21,26,28–32]

In general, the synthesis route for $LiMn_{0.5}Ni_{0.5}O_2$, including the calcination procedure, temperature[26,28,33,34] and the used Li^+/TM ratio during the synthesis,[28,32,34–36] significantly influences the electrochemical performance. The Li^+/TM ratio is reported to be a prominent key factor for this material.[37,38] Therefore, it is important to understand the reason for the increased specific capacity of $LiMn_{0.5}Ni_{0.5}O_2$ with Li^+ excess in the structure, which is represented by the chemical formula of $Li_{1+x}(Mn_{0.5}Ni_{0.5})_{1-x}O_2$ ($0 \le x \le 0.2$, Fig. 1, black line).[32,35,38,39] Myung *et al.* showed with neutron diffraction that the excess Li^+ was completely incorporated into the structure ($0 \le x \le 0.06$).[38] In the following years, it was shown by XRD that the Li^+/Ni^{2+} cation disordering decreases with increasing Li^+ excess and that Li^+ excess can suppress layer–layer composite formation during synthesis ($0.06 \le x \le 0.16$), which increases the specific discharge capacity.[10,37]

Nevertheless, a critical view on the diffraction patterns of Bian *et al.*[32] shows a broadening of the reflections with increasing Li^+ excess, which likely could indicate a phase separation into related crystallographic phases with similar lattice parameters, such as $LiMn_{0.5}Ni_{0.5}O_2$ related layered stoichiometric (red line) and layered Li–Mn-rich oxides (green line). It is debatable whether the excess Li^+ ions are incorporated in the TM layer in the form of a solid solution of Li, Mn and Ni ions or if there is an excess Li^+ induced phase separation. Unfortunately, the SEM images of powders with high Li^+ excess are rare to prove a possible macroscopic phase separation.[35,40] However, the images of Kurilenko *et al.* indicate homogeneous crystallite morphology for $x \approx 0.13$–0.16 after calcination at 900 °C using pelletized samples.[35]

Overall, the discussion shows the structural complexity of the $Li_{1+x}(Mn_{0.5}Ni_{0.5})_{1-x}O_2$ system and the strong influence of the synthesis route. Therefore, the possibility of a Li^+ induced phase separation needs to be considered from a structural point of view: increasing the excess Li^+ x in the stoichiometric formula $Li_{1+x}(Mn_{0.5}Ni_{0.5})_{1-x}O_2$ leads to a higher Li^+ content in the TM layer and thereby theoretically to more Li_2MnO_3 clusters.[25] The cluster formation concentrates the Mn ions locally and consequently creates a Mn depletion in the directly surrounding area, forming Ni-enriched areas.[32] This hypothesis is described by eqn (1) below with the end members $LiMn_{0.5}Ni_{0.5}O_2$ ($p = 0$, equates to $x = 0$) and 0.5 $Li_2MnO_3 \cdot 0.5$ $LiNiO_2$ ($p = 0.25$, equates to $x = 0.2$) (Fig. 2):

$$\begin{aligned} &LiMn_{0.5}Ni_{0.5}O_2 + p\ Li_2O + \frac{p}{2}\ O_2 \rightarrow Li_{1+2p}Mn_{0.5}Ni_{0.5}O_{2+2p} \ \text{ or} \\ &2p\ Li_2MnO_3 \cdot (1-2p)\ LiMn_{(0.5-2p)/(1-2p)}Ni_{0.5/(1-2p)}O_2 (0 \le p \le 0.25) \end{aligned} \quad (1)$$

To the best of our knowledge the length scale of this possible phase separation, whether it is on atomic scale within the lattice, on the microstructure level or on macroscopic scale, has not been fully investigated yet. In this work, the influence of excess Li^+ on the structural homogeneity of $Li_{1+x}(Mn_{0.5}Ni_{0.5})_{1-x}O_2$ for a spherical shaped precursor was investigated, using a combination of different microscopy techniques to analyze the local structure and particle morphology with respect to a possible phase separation. The structural characterization was combined with electrochemical measurements to fully interpret the results.

Experimental

Synthesis of the powders

The $Mn_{0.5}Ni_{0.5}(OH)_2$ precursor powder was synthesized *via* a scalable coprecipitation route. In a continuous stirred tank reactor (CSTR, V = 500 mL) a solution of $Ni(NO_3)_2 \cdot 6\ H_2O$ and $Mn(NO_3)_2 \cdot 4\ H_2O$ (both Roth) was mixed under vigorous stirring with a NH_4OH (Roth) and NaOH (Roth) solution. The pH of the suspension was kept constant at $\approx$10. The excess suspension

This article is licensed under a Creative Commons Attribution 3.0 Unported Licence.

 This journal is © The Royal Society of Chemistry 2023

This article is licensed under a Creative Commons Attribution 3.0 Unported Licence.

Table 1 Results of the elemental analysis by ICP-OES given as molar ratios (Li + Mn + Ni = 2), mean oxidation state of the transition metals (TM = Mn + Ni) by cerimetric redox titration, lattice parameters and the Li^+/Ni^{2+} displacement of the materials as well as the theoretical Li–TM stoichiometry after impregnation of the precursor

	Theoretical Li content	ICP-OES			Mean TM OS	Lattice parameters		Li^+/Ni^{2+}/%
		Li	Mn	Ni		a/Å	c/Å	
$Li_{1.00}$	1.00	**0.99**	**0.50**	**0.50**	3.02	2.890	14.306	10
$Li_{1.07}$	1.06	**1.07**	**0.46**	**0.46**	3.17	2.880	14.289	8
$Li_{1.10}$	1.11	**1.10**	**0.45**	**0.45**	3.27	2.874	14.272	7
$Li_{1.16}$	1.20	**1.16**	**0.42**	**0.42**	3.33	2.867	14.255	6

was removed from the reactor and filtered continuously. The obtained spherical precursor powder (Mn/Ni = 1.00 : 1.00) was washed extensively with deionized water and dried. Subsequently, the precursor material was mixed with various stoichiometric amounts of $LiOH \cdot H_2O$ (Roth, for the Li/M ratio see the theoretical values given in Table 1). After a pre-calcination step at 600 °C (4 h), the final calcination step was conducted at 1000 °C (12 h) under air.

Chemical and structural characterization

The chemical characterization of the powders was conducted *via* the inductively coupled plasma optical emission spectroscopy (ICP-OES) of a diluted aqua regia digestion (Spectro Arcos SOP) and cerimetric redox titration. The latter was divided into two steps: (a) determination of the amount of transition metal in the powders *via* complexometric back titration of Na–EDTA with a Cu(II) solution, buffering the pH with NH_4^+/NH_3 buffer and (b) digestion of the powders in an acidic $(NH_4)_2Fe(SO_4)_2$ solution under nitrogen. The remaining Fe(II) was back titrated with acidic $Ce(SO_4)_2$ solution. Powder X-ray diffraction (XRD) measurements were performed using a D8 Advance diffractometer (Bruker AXS, Bragg–Brentano geometry in reflection mode, Cu-K_α radiation, LYNXEYE_XE detector). The diffraction patterns of the materials were refined using TOPAS V6 (Bruker) based on the structural model of $LiMn_{0.5}Ni_{0.5}O_2$ of Bréger *et al.* and the model of Stephens.[41,42] Scanning electron microscopy (SEM) was carried out using a Leo 1530VP (Zeiss) microscope equipped with a Schottky thermal emitter field. Images were taken at an acceleration voltage of 5 kV with an Everhart–Thornley detector. The elemental distribution was analyzed with energy dispersive X-ray spectroscopy (EDX, X-Max50, Oxford Instruments). The particle cross-sections were prepared by mixing the powders with an epoxy resin, depositing the mixture on a support substrate and polishing the surface with a broad Ar^+ ion beam milling system (IM4000Plus, Hitachi). Raman investigations of the powders and the cross-sections were carried out with an alpha300 R confocal Raman microscope (WITec) over a spectral range between −70 and 1108 rel. cm^{-1}. An Nd:YAG laser with an excitation wavelength of 532 nm was used. The laser power was adjusted to 1.5 mW after microscope transit. The spectrometer was equipped with a grating of 1800 lines mm^{-1} and a CCD-camera (1600 × 200 pixels). An objective with a magnification of 100× (Zeiss) was used. The particle mappings were evaluated with the software Project FIVE (WITec). For the evaluation of the peak positions, all spectra were fitted with up to three Lorentzian peak profiles.

More detailed chemical and crystallographic investigation of the $Li_{1.16}$ microstructure was performed *via* SEM in combination with EDX and electron backscatter diffraction (EBSD). The measurements were conducted on a Zeiss GeminiSEM 450 field-emission (FE) SEM (Zeiss), equipped with an Ultim Max 170 (Oxford Instruments) large area silicon drift detector (SDD) for EDX and a fiber optic-based CMOS EBSD camera Symmetry S2 (Oxford Instruments).

Simultaneous EBSD/EDX mappings were performed at 15 kV accelerating voltage, a beam current of 4 nA, a step size of 30 nm, a total pixel count of about 1.5 million pixels, an electron backscatter diffraction pattern (EBSP) resolution of 622 × 512 pixels and an illumination time per pattern of 1.4 ms (electron dose 5.6 nAms). For indexation, 11 bands were taken into account using Hough-space-based indexation with a resolution of 1.06° per pixel in the theta direction. The dataset was indexed based on the crystal structure of $LiMn_{0.5}Ni_{0.5}O_2$ (SG 166, $R\bar{3}m$, a = 2.8879 Å, c = 14.269 Å).[41] The EBSD results were further improved using a pattern matching method, as implemented in the AztecCrystal MapSweeper Software (Oxford Instruments). Here each experimental EBSD pattern is matched to simulated pattern templates based on full dynamical pattern simulations in order to improve the angular precision of the orientation measurement and to correct for systematic indexing errors.

Electrochemical characterization

For each powder, a homogeneous slurry of active material, conductive carbon SuperP (Timcal) and polyvinylidene difluoride (PVdF, Solef 5130, Solvay) (dry ratio of 91 : 5 : 4), dispersed in an adequate amount of *N*-methyl-2-pyrrolidinone, (NMP, Sigma Aldrich) was coated on an aluminum foil using the doctor blade technique. After drying under vacuum, the electrodes were calendered to a thickness of approximately 70 μm, disk electrodes with a diameter of 12 mm were punched, dried overnight under dynamic vacuum (120 °C) and were transferred directly without contact to air into an argon-filled glovebox (MBraun, O_2 and H_2O < 0.1 ppm). Coin cells (CR2032, Hohsen) were assembled with a disk electrode, two glass fiber separators (16 mm diameter, Whatman), a lithium metal foil (450 μm, 12 mm diameter) and ethylene carbonate (EC) and dimethyl carbonate (DMC) containing electrolyte (150 μL, 1 M $LiPF_6$ in EC : DMC = 1 : 1 by wt). The electrodes have a typical active

This article is licensed under a Creative Commons Attribution 3.0 Unported Licence.

material loading between 9 and 10 mg. The cells were cycled between 2.5 and 4.7 V at room temperature with an applied current of 12 mA g^{-1} using a BaSyTec galvanostat. The specific capacities are mean values of at least three cells. The optimization of the electrolyte was conducted using two further mixtures containing ethyl methyl carbonate (EMC) and vinylene carbonate (VC) (both 150 μL, 1 M $LiPF_6$): EC : EMC (3 : 7 by wt) and EC : EMC (3 : 7 by wt) + 2 wt% VC. Long-term cycling performance was investigated with an applied current of 32 mA g^{-1} in combination with repetitive cycles at 12 mA g^{-1}. After constant current delithiation up to the upper cut-off voltage, a constant voltage step at 4.7 V was conducted with a current limit of 12 mA g^{-1} and 8 mA g^{-1}, respectively.

Results and discussion

Chemical and structural characterization

The investigated powders were synthesized *via* calcination of a dense, coprecipitated $(Mn_{0.5}Ni_{0.5})(OH)_2$ precursor with spherical morphology (Fig. S1, ESI†), using different amounts of Li^+ (Li/TM = 1, 9/8, 5/4, 3/2). ICP-OES measurements were used to analyze the Li^+–TM ratio and to quantify the Li^+ loss during synthesis (Table 1). The as-prepared samples are abbreviated following their Li^+ stoichiometry after synthesis, *e.g.*, $Li_{1.10}$ corresponds to $Li_{1.10}(Mn_{0.5}Ni_{0.5})_{0.9}O_2$. Up to $Li_{1.10}$ the Li^+ content of the synthesized powders matches closely with the lithium content during synthesis, while for $Li_{1.16}$ the Li^+ content strongly decreased during the heat-treatment from 1.20 to 1.16. The Mn/Ni ratio remained constant for all materials. The reason for the loss of Li^+ during calcination is well known and can be assigned to the evaporation of surface Li_2O.[43,44] Interestingly, only the sample with the highest Li^+ content showed a significant Li^+ loss. This indicates that the incorporation of extra Li^+ is more hindered with increased Li^+ content. Possible impurities on the particle surface, originating from structurally not incorporated Li^+ and the preservation of the spherical particle morphology, were investigated *via* SEM (Fig. 3). Generally, the spherical particle shape of the hydroxide precursors is well preserved after thermal lithiation. Nevertheless, there are morphological differences between the different powders, dependent on their Li^+ content. The samples with stoichiometric Li^+ content or a small excess, $Li_{1.00}$ and $Li_{1.07}$, exhibited relatively smooth surfaces with defined primary particles of a few-hundred nanometers in size. The primary particles themselves did not have specific crystal facets, but have kind of a molten appearance. The samples with a higher Li^+ excess, $Li_{1.10}$ and $Li_{1.16}$, show more heterogeneous surfaces and partially strong agglomeration of the secondary particles. This is in accordance with the mechanical characteristics of the freshly calcined samples: While $Li_{1.00}$ and $Li_{1.06}$ were received as powders, $Li_{1.10}$ and especially $Li_{1.16}$ sintered strongly and had to be ground intensively before further characterization.

In addition, some of the particles of $Li_{1.16}$ indicate areas with strong crystal growth and primary particles in the micrometer-size range. These observations suggest that Li^+ excess plays an important role during the conversion of the precursor into the lithiated layered oxides.

The incorporation of excess Li^+ into the structure was investigated by XRD and cerimetric redox back-titration. The latter method was used to analyze the mean TM oxidation state (OS) of the powders (Fig. 4a, Table 1). Theoretically, the average TM OS has to increase with the amount of incorporated Li^+ ions into the lattice, in order to maintain charge neutrality. Plotting the mean OS of the TM against the amount of Li^+ per formula (ICP-OES), an increase of the OS in the range of the theoretically calculated ones (red line) is observable. Further structural analysis of the materials was carried out by XRD (Fig. 4b and c). The complete patterns are presented in the ESI (Fig. S2a†). Generally, the powders show a typical layered oxide pattern of the α-$NaFeO_2$ type. Consequently, most of the reflections can be assigned to a hexagonal crystal structure with the space group $R\bar{3}m$. Impurities like Li_2CO_3 were not observable. Additional reflections were visible in the 2θ range between 20 and 25°. The presence of these additional reflections is indicative of $LiMn_6$ clustering in the transition metal (TM) layer, *e.g.*, in Li_2MnO_3 type materials, and the flower-like clustering of $Li_{1.00}$, as already reported by the group of Ceder.[23] The intensity of the honeycomb superstructure reflections increased and all reflections shifted towards higher 2θ angles with increased amount of excess Li^+ in the lattice. This indicates an increased amount of Li^+ in the TM layer as well as a decrease of at least one lattice parameter. The lattice parameters were determined by Rietveld refinement using TOPAS V6 and a $LiMn_{0.5}Ni_{0.5}O_2$ structure model, which allows incorporating Ni^{2+} ions on Li sites and *vice versa* (Fig. S3, Table S1†).[41,46,47] All excess Li^+ was assumed to be incorporated into the TM layer (3b) and its occupancy (3b) was fixed to a value of one. Both lattice parameters decrease with a higher Li^+ content in the structure (Fig. 4c, Table 1). This is in accordance with trends reported in the literature.[32,38] A comparison of the single lattice parameters of $LiMn_{0.5}Ni_{0.5}O_2$ (a = 2.891 Å, c = 14.301 Å),[21] Li_2MnO_3 (a = 2.843 Å, c = 14.220 Å)‡[48] and $LiNiO_2$ (a = 2.875 Å, c = 14.18 Å)[49] supports these shifts.

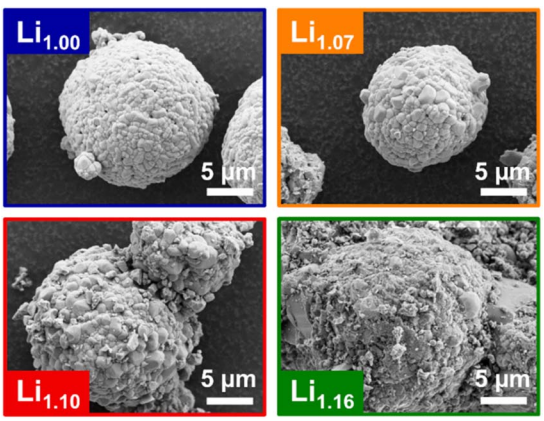

Fig. 3 SEM images of the synthesized powders $Li_{1.00}$ (blue), $Li_{1.07}$ (orange), $Li_{1.10}$ (red) and $Li_{1.16}$ (green) showing the agglomeration behavior and the increase of surface heterogeneities.

‡ Lattice parameters were approximately converted to the hexagonal lattice, using the formula of Ohzuku *et al.*[18]

 This journal is © The Royal Society of Chemistry 2023

This article is licensed under a Creative Commons Attribution 3.0 Unported Licence.

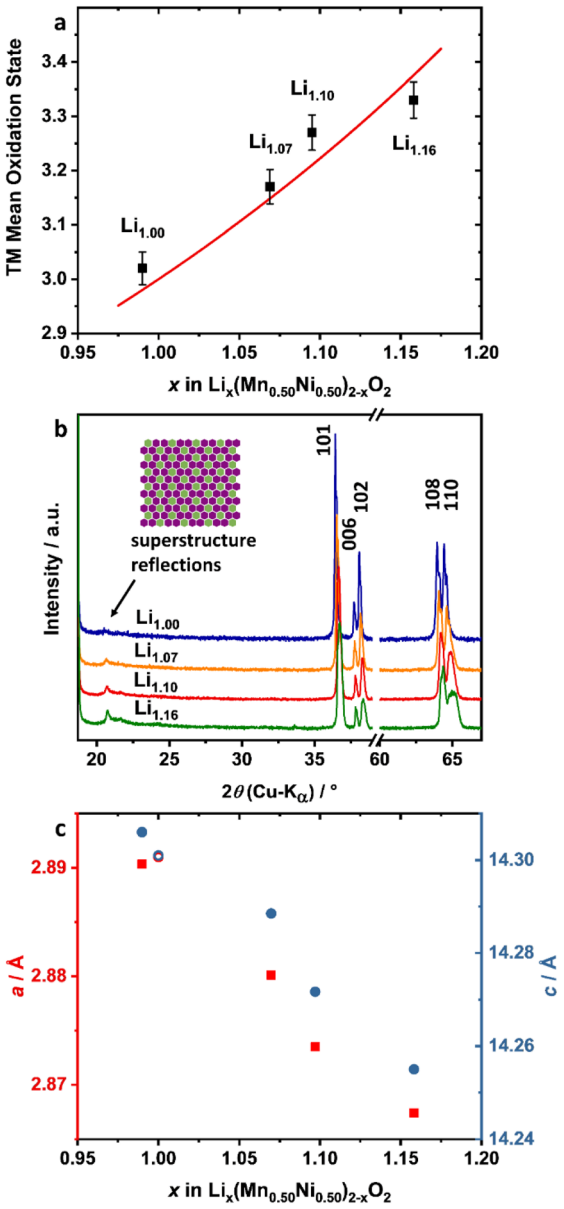

Fig. 4 Analysis of the incorporation of excess Li^+: (a) experimental (black dots) and theoretical calculated (red line) mean TM OS as a function of the Li^+ content of $Li_x(Mn_{0.50}Ni_{0.50})_{2-x}O_2$, (b) detailed XRD pattern of $Li_{1.00}$ (blue), $Li_{1.07}$ (orange), $Li_{1.10}$ (red) and $Li_{1.16}$ (green) and (c) lattice parameters *a* (red squares) and *c* (blue circles) as a function of the Li^+ content. As a comparison, lattice parameters of $LiMn_{0.50}Ni_{0.50}O_2$ reported by Makimura *et al.* are presented in (c) (hollow circles).[21]

With the incorporation of excess Li^+ into the crystal lattice, the decrease of the *a* parameter is dominated by the increase of the Li^+ content in the TM layer, while the decrease of the *c* parameter can be influenced by both the increase of Li_2MnO_3 domains and a possible enrichment of Ni in the layered domains. The decrease of the lattice parameters in combination with the increase of the superstructure reflections and the mean TM OS strongly indicates that excess Li^+ is structurally incorporated into the material.

Li^+/Ni^{2+} displacement is a crucial material issue for layered oxides.[47,50] Due to the similar ion radii of Ni^{2+} and Li^+,[46] some of the Ni^{2+} ions are incorporated into the Li^+ layer of the hexagonal crystal lattice.[47] For $LiMn_{0.5}Ni_{0.5}O_2$ this is more pronounced compared to, *e.g.*, NMC, because Li–Mn-clustering in the TM layer is thermodynamically favored.[23,51] In general, a high amount of Ni^{2+} ions in the Li^+ layer leads to slower kinetics of Li^+ diffusion, strongly affected by the lower Li slab space (Ni^{2+}: stronger O–metal–O interactions) and the blocking of Li^+ diffusion pathways.[47,52,53] A Li^+/Ni^{2+} displacement of 9.5% was obtained for $Li_{1.00}$ from Rietveld refinement, which is comparable to reported values for $LiMn_{0.5}Ni_{0.5}O_2$.[41] With increasing excess Li^+, the displacement shows a nearly linear decrease (Table 1, Fig. S4†). The main reason for the decreasing Li^+/Ni^{2+} disordering is most probably the increase of the Ni^{3+} content in the structure. X-ray absorption spectroscopy (XAS) measurements of Yoon *et al.* showed that in $LiMn_{0.5}Ni_{0.5}O_2$ most of the Ni ions are in the divalent state, whereas the Mn ions are tetravalent.[54] Increasing the mean TM OS with excess Li^+, which was shown to be the case by cerimetry, leads to an increase of the Ni OS, while the Mn OS can be assumed to be constant at +IV in an octahedral environment. The decreasing Li^+/Ni^{2+} displacement is therefore consistent with both higher mean TM OS and higher lithium content.

For layered type oxides, the separation of the (006) and (102) as well as the (108) and (110) reflections can be used to evaluate the quality of the structure.[55] Both pairs are well defined and separated for the $Li_{1.00}$ sample (Fig. 4b, Fig. S2b†). With increasing Li^+ excess, the reflections become broader and smoother. This effect is mostly pronounced for $Li_{1.16}$. For instance, a shoulder on the low-angle side of the (108) reflection and a strong broadening of the (110) reflection is observable. A comparable behavior for most of the other reflections of $Li_{1.16}$ is evident, which suggests a phase separation into regions with different Ni, Mn and Li stoichiometries. Due to the similar symmetry and comparable lattice parameters, a conclusive assignment of the XRD pattern to the three endmembers $LiMn_{0.5}Ni_{0.5}O_2$, $LiNiO_2$ and Li_2MnO_3 in terms of domains or mixtures thereof is not possible with the applied XRD measurement even for $Li_{1.16}$.

Investigation of the microstructure

Based on the XRD results no conclusive statement about the extent of the phase separation or size of the domains can be made. Therefore, the powders were investigated with a combination of SEM, EDX and confocal Raman microscopy, so called correlative SEM–Raman microscopy (Fig. 5).[56] SEM images taken with secondary electron (SE) detectors show crystallographic and material contrast and further contain topographical information.[57] EDX provides additional information about the elemental composition, and Raman microscopy about the local structure of the excited volumes, different coordination geometries and oxidation states.[58,59]

The SEM images of the prepared cross-sections (CS) shown in Fig. 5 clearly depict the particle microstructure, the embedding agent (black background) and a small part of the

This article is licensed under a Creative Commons Attribution 3.0 Unported Licence.

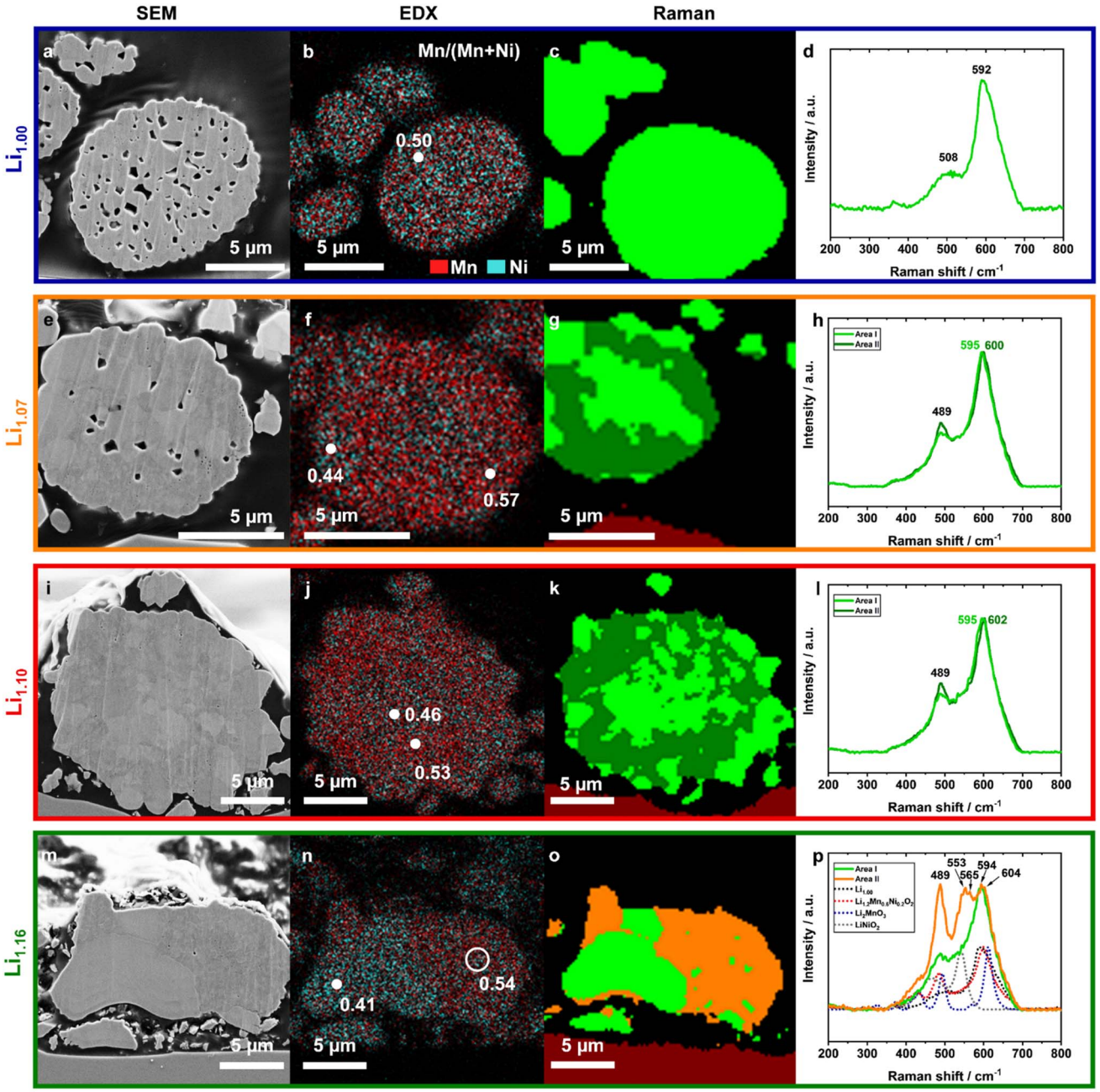

Fig. 5 SEM–Raman imaging of $Li_{1.00}$ (blue), $Li_{1.07}$ (orange), $Li_{1.10}$ (red) and $Li_{1.16}$ (green) comparing the results of the different techniques SEM (1st column, (a), (e), (i), and (m)), EDX (2nd column, (b), (f), (j), and (n)) and Raman (3rd & 4th column, (c)–(d), (g)–(h), (k)–(l), and (o)–(p)) investigated on the same particle cross-section. In the EDX mappings the distribution of Mn (red) and Ni (turquoise) as well as the ratio of Mn/(Mn + Ni) are presented. The colored Raman maps show areas with similar Raman spectra. The resulting spectra are presented with the corresponding color in the 4th column.

supporting substrate (red colored in the Raman mapping). Due to the applied preparation method, particles are not necessarily cut through the particle center – therefore direct particle size information gets lost. The curtaining effect of the surface can be assigned to the ion milling process. This artefact is more pronounced for the powders with a higher number of pores, but the surface was still plain enough for the applied methods.

An increasing excess of Li^+ led to significant decreases in the pore sizes and in the amount of pores. Compared to $Li_{1.10}$ and $Li_{1.16}$, $Li_{1.00}$ exhibited a high internal porosity in the secondary particle architecture, which is in agreement with the Li^+ content dependent particle morphology changes (Fig. 3). In $Li_{1.00}$ the microstructure is homogeneous and single primary particles cannot be identified. For $Li_{1.07}$, primary particles are observable from different shadings, indicating either different orientations of the crystallites or deviations in their composition. With further increased Li^+ content, the grain boundaries become more pronounced, too. For $Li_{1.16}$, both shape and

 This journal is © The Royal Society of Chemistry 2023

This article is licensed under a Creative Commons Attribution 3.0 Unported Licence.

microstructure change significantly, as also seen in the SEM top view images of the original particles (Fig. 3). Most of the particles (Fig. S5†) lose their spherical morphology, become more irregular and partially agglomerate with other particles. An additional compositional segregation was observable, as indicated by the different coloring originating from local differences in electron densities,[57,60] being well pronounced in the presented particle (Fig. 5m). The particle can be divided into two areas: one brighter part, which likely consists of two large crystallites and a darker part, which is dominated by smaller crystallites and bright grain boundaries.

In order to quantify the elemental distribution in the specific areas, EDX mappings and point analyses were conducted. The Mn signal (red) was overlaid with the Ni (turquoise) signal in the presented images to illustrate their lateral distribution (Fig. 5b, f, j and n). The distribution strongly differs between the investigated samples. $Li_{1.00}$ has a homogeneous distribution of Mn and Ni, while $Li_{1.16}$ indicates a Ni enrichment on the left side and a Mn enrichment on the opposite. Furthermore, the Ni-enriched areas have exactly the same shape and location like the bright crystallites in the SEM image. Local quantification of the Mn/(Mn + Ni) ratio shows that there is still a lot of Mn (Mn/(Mn + Ni) ≈ 0.41) inside. For the stoichiometries of $Li_{1.07}$ and higher, local differences in the Mn/(Mn + Ni) ratios are evident, which were not seen for $Li_{1.00}$.

EBSD measurements were conducted for $Li_{1.16}$ in order to quantify the size distribution and the orientation of the crystallites (Fig. 6). The single crystallites can be identified with the band contrast map (Fig. 6a). They were divided into Mn- and Ni-enriched areas for further computational analysis of the data with the help of EDX measurements (Fig. 6b, S6a and b†). Computational analysis confirms the differences in crystallite size distribution (Fig. 6d). Whereas the Mn-enriched crystallites have an area-weighted mean area of 0.5 μm^2 (maximum 1.9 μm^2), the Ni-enriched ones have a value of 5.2 μm^2 (maximum 13.4 μm^2). Furthermore, the assignment of each single pixel to one of the two groups indicates strong differences in the grey values of the band contrast. The pixels in the Mn-enriched areas are shifted to lower numbers, which can be an indicator of higher defect density (Fig. 6c). However, we should note that due to the larger crystallite size, the ratio of dark grain boundaries with lower grey values is lower for the Ni-enriched crystallites compared to the small ones, influencing the distribution. The orientation of the crystallites was successfully determined using the crystal structure of $LiMn_{0.5}Ni_{0.5}O_2$ (space group: $R\bar{3}m$) for indexing the EBSD patterns. Orientation plots, pole figures and the correlation of the Mackenzie plot with random pair distribution are presented in the ESI (Fig. S6c–h†), indicating a random orientation of the crystallites.

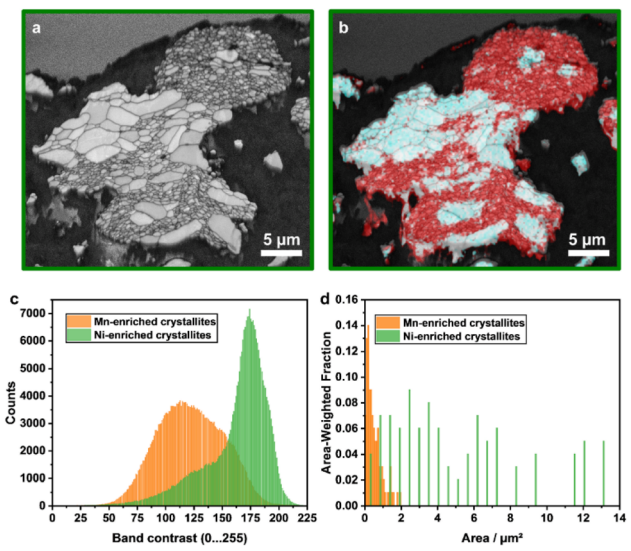

Fig. 6 EBSD results of $Li_{1.16}$: mappings of (a) band contrast and (b) elemental distribution with Ni-enriched (turquoise) and Mn-enriched (red) areas. Both the Mn- and Ni-enriched crystallites were analyzed *via* a data post-processing procedure in more detail with respect to (c) the frequency distribution of the grey values of the band contrast and (d) their size distribution at the surface of the particle cross-section.

In order to shed more light on the observed local differences, confocal Raman microscopy measurements were performed (lateral resolution ≈ 300 nm). Similar Raman spectra were clustered together into groups, using the software Project FIVE (WITec) and plotted as a colored map (Fig. 5c, g, k and o). A first comparison of the Raman maps with the SEM images and the EDX data is self-consistent.

The Raman spectrum of $Li_{1.00}$ contains one strong band at 592 cm^{-1} and a broad shoulder with a plateau between 480 cm^{-1} and 540 cm^{-1}. All Raman shifts are similar to reported literature values of Kumar *et al.* and can be assigned to the $LiMn_{0.5}Ni_{0.5}O_2$ structure.[61] Based on the factor group analysis, layered Li–TM-oxide materials with the space group $R\bar{3}m$ have two Raman-active vibration modes, A_{1g} and E_g, assuming a perfect crystallographic lattice. The vibration band 592 cm^{-1} represents the signal of the out-of-plane M–O stretching vibration of the A_{1g} mode, which vibrates parallel to the *c*-axis, while the E_g mode is an in-plane O–M–O bending vibration parallel to the Li/TM layers (480 cm^{-1}).[58,62,63]

However, both the asymmetry in the peak at 592 cm^{-1} and the plateau indicate that the spectrum consists of several signals with various chemical environments. One reason is most probably the high amount of Li^+/Ni^{2+} disordering in the system, already shown in the XRD analysis, which implies the presence of Li_2MnO_3 domains. Li_2MnO_3 has a lower symmetry ($C/2m$) resulting in a higher amount of active vibration modes as shown in the reference spectrum (Fig. 5p, blue dots). They are located at 612 (A_g), 568, 493, 438, 413, 369, 332, 308 and 248 cm^{-1}.[64] But it is important to note that local structural differences, due to the presence of Ni and, *e.g.*, the layered domains in Li-rich compounds, lead to peak broadening of all vibration bands and to lower intensities of the peaks below 440 cm^{-1}.[65] Therefore, the resulting Li_2MnO_3 domains of the honeycomb superstructure would explain both broadening of the vibration band at 592 cm^{-1} and the additional small vibration band at ≈362 cm^{-1}.[61]

With increasing amount of excess Li^+ up to $Li_{1.10}$, a second cluster of spectra was detectable and is marked in dark green (Fig. 5h and l). The average spectrum of the second cluster is similar in shape to $Li_{1.00}$, but has slightly higher Raman shifts of

This article is licensed under a Creative Commons Attribution 3.0 Unported Licence.

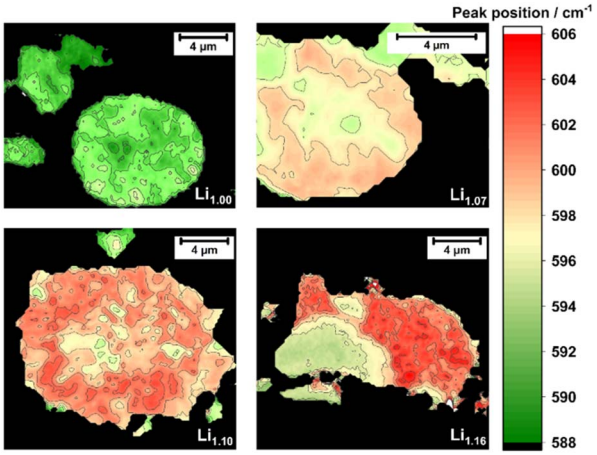

Fig. 7 Fitted peak position of the A_{1g} vibration band for different amounts of Li^+ excess: $Li_{1.00}$, $Li_{1.07}$, $Li_{1.10}$ and $Li_{1.16}$.

the A_{1g} mode. Additionally, both average spectra (indicated as dark and light green) have a more pronounced peak at 489 cm^{-1} as compared to the spectra measured for $Li_{1.00}$, which likely indicates a higher structural order in the system. This might be in accordance with the decrease of Li^+/Ni^{2+} disordering in the powders as observed in the XRD. The minor blue-shift of the most intense peak from the light green (595 cm^{-1}) to the dark green area (600 and 602 cm^{-1}, respectively) indicates contributions of Li_2MnO_3 domains from the incorporation of excess Li^+ into the dark green region of the mappings.[66] Fitting each single spectrum of the Raman mappings with Lorentzian peak profiles allows the determination of the specific peak position and their frequency distribution (Fig. 7). The color change from $Li_{1.00}$ to $Li_{1.16}$ indicates a systematical shift of the peak maximum with increasing excess Li^+ as well as the beginning of the phase separation, which is underlined by the frequency distribution provided in the ESI (Fig. S7†). This shows that the peak position of the vibration band at approximately 600 cm^{-1} can be used as an indicator for the local Li^+ content in the structure.

Comparing the Raman results with the color changes in the SEM images and EDX mappings, it can be assumed that the Mn-enriched areas overlap with the dark green areas and dark crystallites, whereas the Ni-rich ones overlap with the light green areas and the brighter particles in the SEM images. Together, they clearly indicate the beginning of phase separation into a stoichiometric layered Ni-enriched oxide and a Li–Mn-enriched layered oxide. Furthermore, a closer look at the light green spectrum of $Li_{1.10}$ (Fig. 5l) shows that this already contains contributions of the dark green spectrum. This implies that the length-scale of phase separation is smaller than the lateral resolution of the Raman microscope, which is limited by the diffraction limitation of the used laser wavelength.

The selected particle of $Li_{1.16}$ can be separated as well into two parts (Fig. 5p). The light green spectrum has two peaks with a Raman shift of 489 and 594 cm^{-1}, but the latter peak is broader compared to the other samples. This is likely related to the higher Ni content of this particle (EDX, Fig. 5n) and indicates that the larger particles consist of a layered phase with no or only a slight Li^+ excess. The spectrum of the orange area differs strongly from the others. Besides the maxima at 489, 594 and 604 cm^{-1}, a further main peak with three local maxima at 544, 553 and 565 cm^{-1} is visible. Particularly, the vibration band at approx. 550 cm^{-1} indicates the presence of a $LiNiO_2$ species or a comparable compound with slight incorporation of Mn. Further shoulders between 400 and 450 cm^{-1} as well as 498 cm^{-1} and the relatively large blue-shift of the A_{1g} vibration band indicate a strong local increase of Li_2MnO_3 domains in this area. The multitude of new vibration bands suggest a significant change in the structure.

More differentiated clustering of the spectra in the orange area of $Li_{1.16}$ (Fig. 5p) visualizes the observed phase separation in the microstructure in more detail (Fig. 8). For the other samples with lower Li^+ excess a further similar separation into sub-clusters was not possible. In the Mn-enriched region of the $Li_{1.16}$ particle, the intensity ratios of the peaks at approximately 488, 552 and 604 cm^{-1} differ strongly between the sub-clusters. The spectral overlap of both a Li-rich and a Ni-rich composition leads to the strong increase of intensity ratio between the peak at 489 cm^{-1} and approximately at 600 cm^{-1}. The relative increase of the intensity at 488 cm^{-1} is explainable with the decrease of the band intensity at 604 cm^{-1}, due to the splitting of the signal into two main peaks. Interestingly, the intensity of the peak at approximately 552 cm^{-1}, which was already assigned to a Ni-rich layered compound, deviates strongly in the intensity depending on the location of the sub-cluster. The correlation of both SEM image and Raman mapping suggests a higher intensity of the peak at 552 cm^{-1} at the bright grain boundaries in the Mn-enriched area. The influence of different

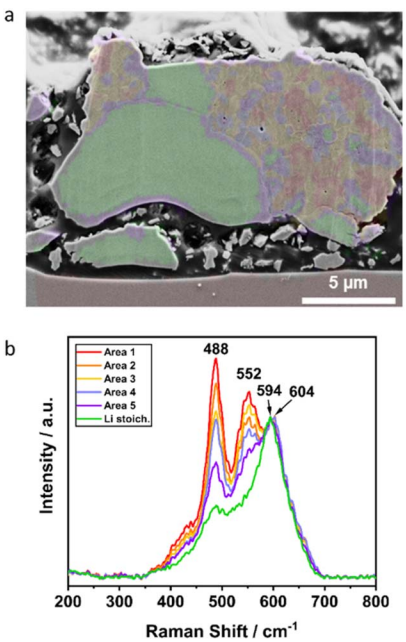

Fig. 8 Detailed investigation of $Li_{1.16}$: (a) correlation of SEM image with Raman mapping and (b) corresponding Raman spectra of the colored, clustered areas with similar Raman spectra.

 This journal is © The Royal Society of Chemistry 2023

This article is licensed under a Creative Commons Attribution 3.0 Unported Licence.

orientations of the crystallites on the intensity ratios of the bands due to the random orientation as shown by EBSD is very unlikely. Further interpretation of the mapping would need an even higher lateral resolution of the Raman microscope beyond the diffraction limit.

Overall, the specific combination of the three methods, SEM, EDX and Raman, provides a deep insight into the complex structural situation inside the spherical particles, helps to understand the cause of the broadening of the XRD reflections and to prove the phase separation with increasing amount of excess Li^+ in the particle into a Ni-enriched and a Li–Mn-enriched layered compound, respectively. The phase separation is differently pronounced, while for $Li_{1.00}$ only one phase was detected, for $Li_{1.07}$ and $Li_{1.10}$ local differences in the Mn/Ni ratio and the Li^+ content in the structure appeared. For $Li_{1.16}$ a fundamental rearrangement of the primary particles during the calcination process can be assumed. This might be supported by the larger amount of Li^+ salts outside of the secondary particles, acting as a flux, most probably due to the limited access into the secondary particle structure. This leads to a separation into layered stoichiometric Ni-enriched particles and a Li–Mn-enriched area, with further phase separation on local scale into Ni-rich and Li–Mn-rich layered oxides. Furthermore, a faster growth of the Ni-enriched crystallites likely leads to a more pronounced phase separation in the spherical material due to the extraction and chemical binding of Ni-ions.

It can be concluded that $Li_{1.07}$ has the best balance between structural incorporation of the excess Li^+ and the phase separation. Compared to the other materials, the incorporation of the excess Li^+ was more homogeneously distributed as shown in the Raman mappings (Fig. 5 and 6) and the Mn/Ni separation was reduced to a minimum (Fig. 5). Additionally, it was underlined that the interpretation of the powder diffraction data without analyzing the samples by further methods is not sufficient to distinguish between macroscopic segregation (mixture of particles with different compositions), phase separation in the microstructure or defects in the lattice.

Electrochemical behavior

The influence of the excess Li^+ on the electrochemical behavior was investigated in a voltage range between 2.5 and 4.7 V to activate possible Li_2MnO_3 domains, which become electrochemically accessible at higher potentials (Fig. 9). All powders have a similar cycling characteristic with respect to their capacity loss over cycling. During the first few cycles, a fast capacity fade is observable, which stabilizes after approximately 10 cycles except for $Li_{1.00}$ and $Li_{1.16}$. In contrast to the cycling characteristics, the specific discharge capacity differs strongly. While $Li_{1.07}$ and $Li_{1.10}$ have initial discharge capacities of 173 and 171 mAh g^{-1}, $Li_{1.00}$ and $Li_{1.16}$ have significantly lower capacities of 157 and 150 mAh g^{-1}. Similar effects are observed in long-term cycling experiments of the better performing materials $Li_{1.07}$ and $Li_{1.10}$ (Fig. S8†). After a strong capacity fade in the beginning of the cycling experiments, both materials show stable cycling performance between cycles 50 and 200.

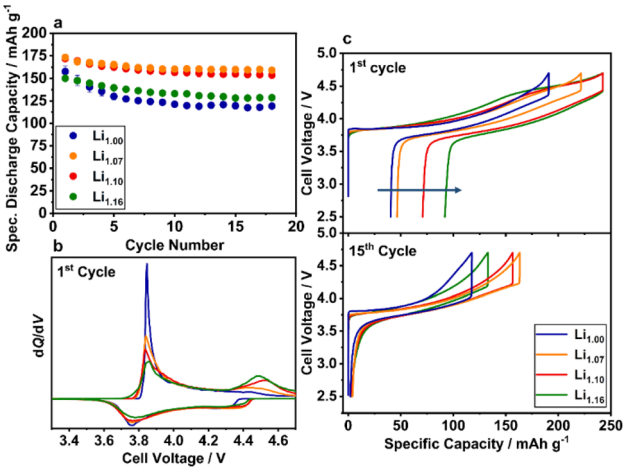

Fig. 9 Electrochemical characterization of $Li_{1.00}$ (blue), $Li_{1.07}$ (orange), $Li_{1.10}$ (red) and $Li_{1.16}$ (green): (a) specific discharge capacities of the initial cycles (12 mA g^{-1}), (b) dQ/dV plot and (c) voltage profiles of the 1st and 15th cycle.

For a better understanding of the differences in the initial capacities, an in-depth analysis of the voltage curve is necessary (Fig. 9c). The blue curve of $Li_{1.00}$ shows a smooth, for solid solutions typical, monotone progression after the voltage jump from the open circuit voltage (OCV) to an initial cell voltage of 3.84 V. A detailed mechanism and the involved Ni oxidation states have been suggested elsewhere.[67,68] Specific plateaus, that would indicate phase transitions or electrochemical activation as in Li_2MnO_3-containing LRLO materials, are not present.[45,69] The voltage profiles of the other electrodes show a slightly different behavior in the voltage region beyond 4.4 V. With higher amount of excess Li^+, a plateau region is observable with increasing length, concomitant with decreasing charge capacity below 4.4 V. Furthermore, the first cycle irreversible capacity loss increases. A detailed analysis is presented in the ESI (Fig. S9†). The additional plateau region indicates the electrochemical activation of Li_2MnO_3 domains,[70] which were identified during the structural analysis of the materials. Consequently, the initial voltage curves of $Li_{1.07}$, $Li_{1.10}$ and $Li_{1.16}$ are most likely influenced by a cationic redox reaction in the lower voltage region (Ni-redox) and an anionic redox reaction at higher voltage (O-redox).[71] Both reactions are visible in the corresponding dQ/dV plot as well (Fig. 9b). During initial delithiation the peak at 3.8 V can be assigned to the oxidation reaction of the TM and the peak at ≈4.5 V to the electrochemical activation of the Li_2MnO_3 domains.[38] Furthermore, the intensity of the latter peak increases with higher Li/Mn ratios, which is in agreement with the systematical blue-shift of the A_{1g} Raman vibration band and the other structural investigations, suggesting an increased number of Li_2MnO_3 domains. Nevertheless, compared to LRLO materials (Fig. 1, green line) with a strongly distinct plateau at ≈4.5 V,[45,72–75,79] the plateau in the voltage profile of the presented powders is less pronounced, likely due to the higher Li/Mn ratio and very dense particle morphology ($Li_{1.10}$ and $Li_{1.16}$) of the investigated materials. Based on the SEM images, we additionally estimate

This article is licensed under a Creative Commons Attribution 3.0 Unported Licence.

a low specific surface area, which strongly influences the activation of the Li_2MnO_3 domains as well. Similar morphological influences were recently reported by the Gasteiger group for LRLO materials.[76]

At the beginning of lithiation in the 1st cycle, significant differences in the size of the voltage drop (IR-drop) can be observed in the order of $Li_{1.07} \approx Li_{1.10} < Li_{1.16} \ll Li_{1.00}$. Particularly, the increased voltage drop of $Li_{1.00}$ is likely ascribed to the strong Li^+/Ni^{2+} disordering due to the honeycomb superstructure and the resulting lower Li^+ diffusion kinetics. For $Li_{1.16}$, most probably the macroscopic phase separation shown by SEM, EDX, EBSD and Raman limits the diffusion. During further lithiation, there is a pronounced peak at approximately 3.75 V, which is mainly attributed to the reduction reaction of the cationic redox system. Based on the microstructural and electrochemical findings, there are probably three main factors influencing the capacity induced by the excess Li^+ in the structure: (a) Li^+/Ni^{2+} disorder, (b) additional capacity from the oxygen redox and (c) structural inhomogeneity in the lattice. The lower performance of $Li_{1.00}$ compared to the other investigated materials with higher Li/Mn ratios was already reported in the literature and ascribed to the high amount of Ni^{2+} ions in the Li^+ layer and the local collapse of the structure during cycling, hindering the (de)lithiation process.[38] The local collapse is likely the reason for the high voltage drop at the beginning of the electrochemical lithiation already after 15 cycles of $Li_{1.00}$ (Fig. 9c). Bian *et al.* reported that the capacity fade of $Li_{1.00}$ is independent of the high discharge voltage and as well observable at lower cut-off potentials.[32] We observed similar results for $Li_{1.00}$, but with a decreasing extent at lower cut-off voltages most probably due to less side-reactions like electrolyte decomposition or other parasitic side-reactions (Fig. S10†).[77] $Li_{1.07}$ and $Li_{1.10}$ are most probably in an ideal compositional range, where the Li^+/Ni^{2+} disorder is already reduced due to the higher amount of Ni^{3+} and the irreversible capacity loss, originating mainly from the oxygen release during the activation of the Li_2MnO_3 domains,[70] is comparatively low. For $Li_{1.16}$, the benefit of the excess Li^+ is overcompensated likely by the phase segregation in the microstructure and the high irreversible capacity loss, which result in low discharge capacity.

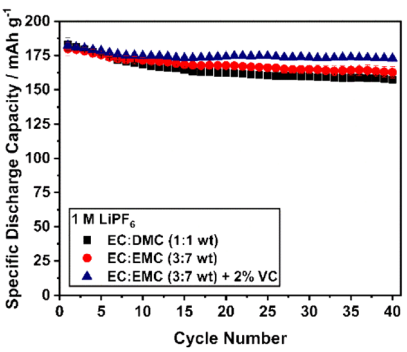

Fig. 10 Cycling performance (12 mA g^{-1}) of $Li_{1.07}$ using different electrolytes (1M $LiPF_6$): EC : DMC (1 : 1 by wt, black), EC : EMC (3 : 7 by wt, red) and EC : EMC (3 : 7 by wt) + 2 wt% VC (blue) at RT.

The pronounced capacity loss during the first cycles is accompanied by an increase of the polarization mainly in the high voltage region, which is clearly indicated by the dQ/dV curves of the initial cycles (Fig. S11†). The increasing overpotential mainly indicates the formation and growth of a cathode electrolyte interface (CEI). In the beginning, the growing process is most probably very fast and slows down during cycling due to the self-passivation of the surface. This effect was also observed by Dupré *et al.* suggesting interfacial effects between the particle surface and the electrolyte as the main reason for this phenomenon.[78] The choice of the electrolyte may influence the CEI formation. Consequently, different electrolytes were screened with respect to their influence on the cycling behavior of $Li_{1.07}$ (Fig. 10). For all electrolytes, the principal characteristic of the cycling curve remains unaffected. Reducing the ethylene carbonate (EC) content increases the discharge capacity, but not the cycling stability of the material. However, significant stabilization can be observed for the vinylene carbonate (VC) containing electrolyte with a specific discharge capacity after the first 10 cycles of approximately 175 mAh g^{-1}. Finally, it was shown that the $Li_{1.07}$ material has a stable discharge capacity of 173 mAh g^{-1} (658 Wh kg^{-1}) even after 40 cycles using an improved electrolyte composition.

Conclusions

In this work, different powders with various amounts of Li^+ excess in the structure $Li_{1+x}(Mn_{0.5}Ni_{0.5})_{1-x}O_2$ ($0 \leq x \leq 0.16$) have been investigated with respect to microstructural changes induced by the additional Li^+. Increasing the Li^+ excess in the structure leads to a decrease of both lattice parameters and a broadening of the diffraction patterns. Furthermore, the intensity of superstructure reflections, indicating the presence of Li_2MnO_3 domains, increases, too. The study shows that the incorporation of a certain amount of excess Li^+ helps to improve the structural and electrochemical properties, with lower Li^+/Ni^{2+} disorder and anionic redox activity. Further addition of Li^+ leads to electrochemical deactivation. The ideal composition in the investigated system was found for $x = 0.07$, with a stable discharge capacity of 173 mAh g^{-1} (658 Wh kg^{-1}) after 40 cycles. The influence of excess lithium on microstructural features turned out to be very complex. XRD does not give a full view of the structural details and a misinterpretation of the pattern with its broad reflections as a single structure with high amounts of lattice defects is possible if no complementary analysis techniques are employed. Therefore, a powerful combination of SEM imaging (microstructure), EDX (elemental mapping), EBSD and Raman microscopy (structural information) was applied to identify the effect on the particle microstructure driven by excess Li^+. While the stoichiometric material ($x = 0$) exhibits a homogeneous particle composition, a strong segregation was observable for $x = 0.16$. In the latter, the particle microstructure is dominated by two levels of segregation: (a) large homogeneous crystallites with slightly increased Ni-content and (b) areas composed of small Li–Mn-rich crystallites surrounded by Ni-rich layered compounds along the grain boundaries. Integrating these findings into the

 This journal is © The Royal Society of Chemistry 2023

This article is licensed under a Creative Commons Attribution 3.0 Unported Licence.

information obtained from XRD, ICP and cerimetry allows deriving a conclusive understanding of the Li^+ excess impact on the secondary particle architecture. The results clearly show that Li^+ excess can induce a complex macroscopic phase segregation on particle level. For the reported materials, we assume that the macroscopic phase separation is driven by a kinetically retarded access of the Li^+ into the grain structure during calcination, where a part of the Li^+ can remain unreacted for a certain time span and act as an intermediary fluxing agent. This effect is strongly pronounced for higher Li^+ excess beyond $x \approx 0.10$. In the frame of literature reported results, this study helps as well to interpret methodical differences of calcination procedures on the product quality. Overall, the presented combination of the three analyzing techniques (SEM, EDX, and Raman) will help in the future to generate a deeper understanding of battery materials and their structural and electrochemical behavior.

Conflicts of interest

There are no conflicts to declare.

Acknowledgements

This work was supported by the German Federal Ministry of Education and Research (BMBF) in the project ExcellBattMat (03XP0257A and 03XP0257C). The authors thank Wolfgang Weirather for his support during the synthesis process, Gisela Arnold for the ICP measurements, Ivan Trentin for providing the $LiNiO_2$ reference material (all ZSW) and Patrick Trimby for support with EBSD pattern matching (Oxford Instruments).

Notes and references

1 J. Dunn, M. Slattery, A. Kendall, H. Ambrose and S. Shen, *Environ. Sci. Technol.*, 2021, **55**, 5189, DOI: 10.1021/acs.est.0c07030.
2 Z. Lu, D. D. MacNeil and J. R. Dahn, *Electrochem. Solid-State Lett.*, 2001, **4**, A200, DOI: 10.1149/1.1413182.
3 T. Ohzuku and Y. Makimura, *Chem. Lett.*, 2001, **30**, 744, DOI: 10.1246/cl.2001.744.
4 J. H. Yang, H. Kim and G. Ceder, *Molecules*, 2021, **26**, 3173, DOI: 10.3390/molecules26113173.
5 T. Ohzuku and Y. Makimura, *Chem. Lett.*, 2001, **30**, 642, DOI: 10.1246/cl.2001.642.
6 L.-P. He, K. Li, Y. Zhang and J. Liu, *ACS Appl. Mater. Interfaces*, 2020, **12**, 28253, DOI: 10.1021/acsami.0c06824.
7 B. E. Murdock, K. E. Toghill and N. Tapia-Ruiz, *Adv. Energy Mater.*, 2021, **11**, 2102028, DOI: 10.1002/aenm.202102028.
8 S. Lee and A. Manthiram, *ACS Energy Lett.*, 2022, **7**, 3058, DOI: 10.1021/acsenergylett.2c01553.
9 M. Greenwood, M. Wentker and J. Leker, *J. Power Sources Adv.*, 2021, **9**, 100055, DOI: 10.1016/j.powera.2021.100055.
10 E. McCalla, A. W. Rowe, R. Shunmugasundaram and J. R. Dahn, *Chem. Mater.*, 2013, **25**, 989, DOI: 10.1149/2.047308jes.
11 Q. Zhong, A. Bonakdarpour, M. Zhang, Y. Gao and J. R. Dahn, *J. Electrochem. Soc.*, 1997, **144**, 205, DOI: 10.1149/1.1837386.
12 K. Amine, H. Tukamoto, H. Yasuda and Y. Fujita, *J. Power Sources*, 1997, **68**, 604, DOI: 10.1016/S0378-7753(96)02590-6.
13 E. Rossen, C. Jones and J. R. Dahn, *Solid State Ionics*, 1992, **57**, 311, DOI: 10.1016/0167-2738(92)90164-K.
14 D. Caurant, N. Baffler, V. Bianchi, G. Grégoire and S. Bach, *J. Mater. Chem.*, 1996, **6**, 1149, DOI: 10.1039/JM9960601149.
15 M. E. Spahr, P. Novák, B. Schnyder, O. Haas and R. Nesper, *J. Electrochem. Soc.*, 1998, **145**, 1113, DOI: 10.1149/1.1838425.
16 Y.-K. Sun, D.-J. Lee, Y. J. Lee, Z. Chen and S.-T. Myung, *ACS Appl. Mater. Interfaces*, 2013, **5**, 11434, DOI: 10.1021/am403684z.
17 H. Yu and H. Zhou, *J. Phys. Chem. Lett.*, 2013, **4**, 1268, DOI: 10.1021/jz400032v.
18 T. Ohzuku, M. Nagayama, K. Tsuji and K. Ariyoshi, *J. Mater. Chem.*, 2011, **21**, 10179, DOI: 10.1039/c0jm04325g.
19 Z. Lu, L. Y. Beaulieu, R. A. Donaberger, C. L. Thomas and J. R. Dahn, *J. Electrochem. Soc.*, 2002, **149**, A778, DOI: 10.1149/1.1471541.
20 H. Kobayashi, H. Sakaebe, H. Kageyama, K. Tatsumi, Y. Arachi and T. Kamiyama, *J. Mater. Chem.*, 2003, **13**, 590, DOI: 10.1039/B211558A.
21 Y. Makimura and T. Ohzuku, *J. Power Sources*, 2003, **119–121**, 156, DOI: 10.1016/S0378-7753(03)00170-8.
22 J. Bréger, N. Dupré, P. J. Chupas, P. L. Lee, T. Proffen, J. B. Parise and C. P. Grey, *J. Am. Chem. Soc.*, 2005, **127**, 7529, DOI: 10.1021/ja050697u.
23 A. van der Ven and G. Ceder, *Electrochem. Commun.*, 2004, **6**, 1045, DOI: 10.1016/j.elecom.2004.07.018.
24 Z. Hu, J. Zheng, C. Xin, G. Teng, Y. Zuo and F. Pan, *J. Phys. Chem. C*, 2018, **122**, 4125, DOI: 10.1021/acs.jpcc.7b10968.
25 W.-S. Yoon, S. Iannopollo, C. P. Grey, D. Carlier, J. Gorman, J. Reed and G. Ceder, *Electrochem. Solid-State Lett.*, 2004, **7**, A167, DOI: 10.1149/1.1737711.
26 K. Kang, Y. S. Meng, J. Bréger, C. P. Grey and G. Ceder, *Science*, 2006, **311**, 977, DOI: 10.1126/science.1122152.
27 H. Kobayashi, Y. Arachi, H. Kageyama, H. Sakaebe, K. Tatsumi, D. Mori, R. Kanno and T. Kamiyama, *Solid State Ionics*, 2004, **175**, 221, DOI: 10.1016/j.ssi.2003.12.027.
28 N. Yabuuchi, Y.-C. Lu, A. N. Mansour, S. Chen and Y. Shao-Horn, *J. Electrochem. Soc.*, 2010, **158**, A192, DOI: 10.1149/1.3526309.
29 J. R. Croy, K. G. Gallagher, M. Balasubramanian, B. R. Long and M. M. Thackeray, *J. Electrochem. Soc.*, 2014, **161**, A318, DOI: 10.1149/2.049403jes.
30 S.-H. Kang, I. Belharouak, Y.-K. Sun and K. Amine, *J. Power Sources*, 2005, **146**, 650, DOI: 10.1016/j.jpowsour.2005.03.084.
31 A. Abdel-Ghany, K. Zaghib, F. Gendron, A. Mauger and C. M. Julien, *Electrochim. Acta*, 2007, **52**, 4092, DOI: 10.1016/j.electacta.2006.11.044.
32 X. Bian, R. Zhang and X. Yang, *Inorg. Chem.*, 2020, **59**, 17535, DOI: 10.1021/acs.inorgchem.0c02766.

This article is licensed under a Creative Commons Attribution 3.0 Unported Licence.

33 B. Ammundsen and J. Paulsen, *Adv. Mater.*, 2001, **13**, 943, DOI: 10.1002/1521-4095(200107)13:12/13<943::AID-ADMA943>3.0.CO;2-J.
34 N. Phattharasupakun, M. M. E. Cormier, Y. Liu, C. Geng, E. Zsoldos, I. Hamam, A. Liu, M. B. Johnson, M. Sawangphruk and J. R. Dahn, *J. Electrochem. Soc.*, 2021, **168**, 110502, DOI: 10.1149/1945-7111/ac3157.
35 K. A. Kurilenko, O. A. Shlyakhtin, O. A. Brylev and O. A. Drozhzhin, *Electrochim. Acta*, 2015, **152**, 255, DOI: 10.1016/j.electacta.2014.11.045.
36 T. Gao, G. Yang, B. Yang and Y. Dai, *J. Alloys Compd.*, 2016, **680**, 694, DOI: 10.1016/j.jallcom.2016.04.187.
37 E. McCalla, J. Li, A. W. Rowe and J. R. Dahn, *J. Electrochem. Soc.*, 2014, **161**, A606, DOI: 10.1149/2.083404jes.
38 S.-T. Myung, S. Komaba, K. Kurihara, K. Hosoya, N. Kumagai, Y.-K. Sun, I. Nakai, M. Yonemura and T. Kamiyama, *Chem. Mater.*, 2006, **18**, 1658, DOI: 10.1021/cm052704j.
39 S. Myung, S. Komaba and N. Kumagai, *Solid State Ionics*, 2004, **170**, 139, DOI: 10.1016/j.ssi.2003.09.006.
40 L. Guo, X. Tan, D. Mao, T. Zhao, L. Song, Y. Liu, X. Kang, H. Wang, L. Sun and W. Chu, *Electrochim. Acta*, 2021, **370**, 137808, DOI: 10.1016/j.electacta.2021.137808.
41 J. Bréger, Y. S. Meng, Y. Hinuma, S. Kumar, K. Kang, Y. Shao-Horn, G. Ceder and C. P. Grey, *Chem. Mater.*, 2006, **18**, 4768, DOI: 10.1021/cm060886r.
42 P. W. Stephens, *J. Appl. Crystallogr.*, 1999, **32**, 281, DOI: 10.1107/S0021889898006001.
43 T. Sata, *Ceram. Int.*, 1998, **24**, 53, DOI: 10.1016/S0272-8842(96)00077-6.
44 E. McCalla, G. H. Carey and J. R. Dahn, *Solid State Ionics*, 2012, **219**, 11, DOI: 10.1016/j.ssi.2012.05.007.
45 F. Klein, J. Bansmann, Z. Jusys, C. Pfeifer, P. Scheitenberger, M. Mundszinger, D. Geiger, J. Biskupek, U. Kaiser, R. J. Behm, M. Lindén, M. Wohlfahrt-Mehrens and P. Axmann, *ChemSusChem*, 2022, **15**, e202201061, DOI: 10.1002/cssc.202201061.
46 R. D. Shannon, *Acta Crystallogr., Sect. A: Cryst. Phys., Diffr., Theor. Gen. Crystallogr.*, 1976, **32**, 751, DOI: 10.1107/S0567739476001551.
47 J. Zheng, Y. Ye, T. Liu, Y. Xiao, C. Wang, F. Wang and F. Pan, *Acc. Chem. Res.*, 2019, **52**, 2201, DOI: 10.1021/acs.accounts.9b00033.
48 J. Bréger, M. Jiang, N. Dupré, Y. S. Meng, Y. Shao-Horn, G. Ceder and C. P. Grey, *J. Solid State Chem.*, 2005, **178**, 2575, DOI: 10.1016/j.jssc.2005.05.027.
49 K. Hirakawa, H. Kadowaki and K. Ubukoshi, *J. Phys. Soc. Jpn.*, 1985, **54**, 3526, DOI: 10.1143/JPSJ.54.3526.
50 X. Zhang, W. J. Jiang, A. Mauger, Qilu, F. Gendron and C. M. Julien, *J. Power Sources*, 2010, **195**, 1292, DOI: 10.1016/j.jpowsour.2009.09.029.
51 Y. Hinuma, Y. S. Meng, K. Kang and G. Ceder, *Chem. Mater.*, 2007, **19**, 1790, DOI: 10.1021/cm062903i.
52 Y. Su, Q. Zhang, L. Chen, L. Bao, Y. Lu, S. Chen and F. Wu, *J. Energy Chem.*, 2022, **65**, 236, DOI: 10.1016/j.jechem.2021.05.048.
53 J. Wang, X. Lu, Y. Zhang, J. Zhou, J. Wang and S. Xu, *J. Energy Chem.*, 2022, **65**, 681, DOI: 10.1016/j.jechem.2021.06.017.
54 W.-S. Yoon, Y. Paik, X.-Q. Yang, M. Balasubramanian, J. McBreen and C. P. Grey, *Electrochem. Solid-State Lett.*, 2002, **5**, A263, DOI: 10.1149/1.1513001.
55 M. H. Rossouw and M. M. Thackeray, *Mater. Res. Bull.*, 1991, **26**, 463, DOI: 10.1016/0025-5408(91)90186-P.
56 T. L. Burnett and P. J. Withers, *Nat. Mater.*, 2019, **18**, 1041, DOI: 10.1038/s41563-019-0402-8.
57 H. Seiler, *J. Appl. Phys.*, 1983, **54**, R1–R18, DOI: 10.1063/1.332840.
58 C. Julien, *Solid State Ionics*, 2000, **136–137**, 887, DOI: 10.1016/S0167-2738(00)00503-8.
59 R. Fitzgerald, K. Keil and K. F. Heinrich, *Science*, 1968, **159**, 528, DOI: 10.1126/science.159.3814.528.
60 G. E. Lloyd, *Mineral. Mag.*, 1987, **51**, 3, DOI: 10.1180/minmag.1987.051.359.02.
61 P. Senthil Kumar, A. Sakunthala, M. Prabu, M. V. Reddy and R. Joshi, *Solid State Ionics*, 2014, **267**, 1, DOI: 10.1016/j.ssi.2014.09.002.
62 E. Flores, P. Novák, U. Aschauer and E. J. Berg, *Chem. Mater.*, 2020, **32**, 186, DOI: 10.1021/acs.chemmater.9b03202.
63 M. Inaba, Y. Iriyama, Z. Ogumi, Y. Todzuka and A. Tasaka, *J. Raman Spectrosc.*, 1997, **28**, 613, DOI: 10.1002/(SICI)1097-4555(199708)28:8<613::AID-JRS138>3.0.CO;2-T.
64 C. M. Julien and M. Massot, *Mater. Sci. Eng., B*, 2003, **100**, 69, DOI: 10.1016/S0921-5107(03)00077-1.
65 H. Koga, L. Croguennec, P. Mannessiez, M. Ménétrier, F. Weill, L. Bourgeois, M. Duttine, E. Suard and C. Delmas, *J. Phys. Chem. C*, 2012, **116**, 13497, DOI: 10.1021/jp301879x.
66 P. Lanz, C. Villevieille and P. Novák, *Electrochim. Acta*, 2014, **130**, 206, DOI: 10.1016/j.electacta.2014.03.004.
67 S. Venkatraman and A. Manthiram, *Chem. Mater.*, 2003, **15**, 5003, DOI: 10.1021/cm034757b.
68 Y. Arachi, H. Kobayashi, S. Emura, Y. Nakata, M. Tanaka, T. Asai, H. Sakebe, K. Tatsumi and H. Kageyama, *Solid State Ionics*, 2005, **176**, 895, DOI: 10.1016/j.ssi.2004.10.024.
69 Z. Lu, Z. Chen and J. R. Dahn, *Chem. Mater.*, 2003, **15**, 3214, DOI: 10.1021/cm030194s.
70 N. Guerrini, L. Jin, J. G. Lozano, K. Luo, A. Sobkowiak, K. Tsuruta, F. Massel, L.-C. Duda, M. R. Roberts and P. G. Bruce, *Chem. Mater.*, 2020, **32**, 3733, DOI: 10.1021/acs.chemmater.9b04459.
71 R. A. House, G. J. Rees, M. A. Pérez-Osorio, J.-J. Marie, E. Boivin, A. W. Robertson, A. Nag, M. Garcia-Fernandez, K.-J. Zhou and P. G. Bruce, *Nat. Energy*, 2020, **5**, 777, DOI: 10.1038/s41560-020-00697-2.
72 Z. He, Z. Wang, Z. Huang, H. Chen, X. Li and H. Guo, *J. Mater. Chem. A*, 2015, **3**, 16817, DOI: 10.1039/C5TA04424C.
73 S. Alagar, C. Karuppiah, R. Madhuvilakku, S. Piraman and C.-C. Yang, *ACS Omega*, 2019, **4**, 20285, DOI: 10.1021/acsomega.9b02766.
74 S. Gao, Y. Zhang, H. Zhang, D. Song, X. Shi and L. Zhang, *New J. Chem.*, 2017, **41**, 10048, DOI: 10.1039/C7NJ01759F.
75 X. Zhang, M. Lengyel and R. L. Axelbaum, *AIChE J.*, 2014, **60**, 443, DOI: 10.1002/aic.14287.

 This journal is © The Royal Society of Chemistry 2023

76 B. Strehle, J. Yoon, F. Friedrich and H. A. Gasteiger, *J. Electrochem. Soc.*, 2022, **169**, 60521, DOI: **10.1149/1945-7111/ac766c**.
77 P. K. Nayak, J. Grinblat, M. Levi, Y. Wu, B. Powell and D. Aurbach, *J. Electroanal. Chem.*, 2014, **733**, 6, DOI: **10.1016/j.jelechem.2014.09.005**.
78 N. Dupré, J.-F. Martin, J. Oliveri, P. Soudan, A. Yamada, R. Kanno and D. Guyomard, *J. Power Sources*, 2011, **196**, 4791, DOI: **10.1016/j.jpowsour.2010.07.049**.
79 F. Klein, C. Pfeifer, J. Bansmann, Z. Jusys, R. J. Behm, M. Wohlfahrt-Mehrens, M. Lindén and P. Axmann, *J. Electrochem. Soc.*, 2022, **169**, 120533, DOI: **10.1149/1945-7111/acaa5c**.

This article is licensed under a Creative Commons Attribution 3.0 Unported Licence.

Electronic Supplementary Material (ESI) for Journal of Materials Chemistry A.
This journal is © The Royal Society of Chemistry 2022

Electronic Supporting Information (ESI)

In-depth structural characterization of the influence of Li^+ excess on spherical, Co-free layered $LiMn_{0.5}Ni_{0.5}O_2$ cathode material using correlative Raman-SEM microscopy

Florian Klein,[a] Claudia Pfeifer,[a] Philipp Scheitenberger,[b] Lukas Pfeiffer,[a] Dominik Zimmer,[c] Margret Wohlfahrt-Mehrens,[a] Mika Lindén*,[b] and Peter Axmann*,[a]

[a]Zentrum für Sonnenenergie- und Wasserstoffforschung Baden-Württemberg (ZSW),
Helmholtzstrasse 8, D-89081 Ulm (Germany).
e-mail: peter.axmann@zsw-bw.de

[b]Institute for Inorganic Chemistry II, Ulm University,
Albert-Einstein-Allee 11, D-89081 Ulm (Germany).
e-mail: mika.linden@zsw-bw.de

[C]Oxford Instruments GmbH,
Borsigstr. 15A, 65205 Wiesbaden (Germany)

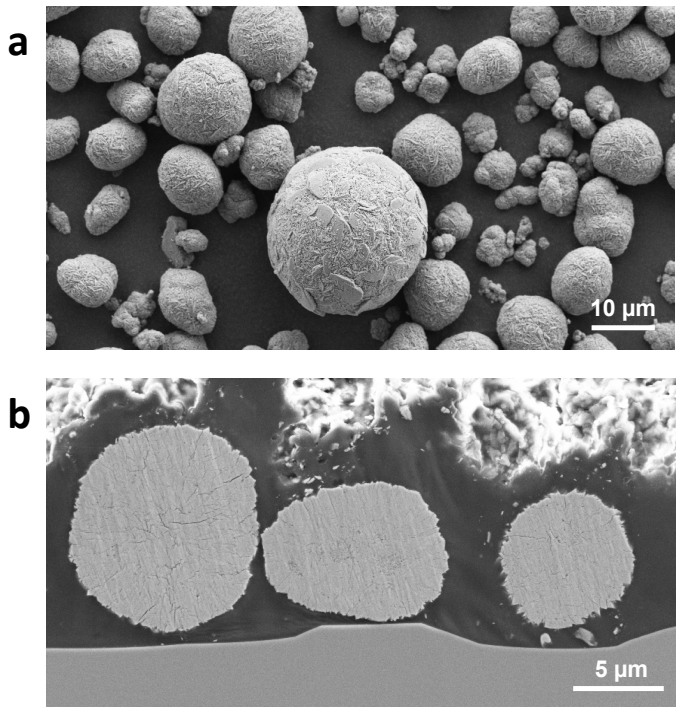

Figure S1. SEM images of the $(Mn_{0.5}Ni_{0.5})(OH)_2$ precursor: a) top view of spherical particle morphology and b) particle cross-section of dense spheres.

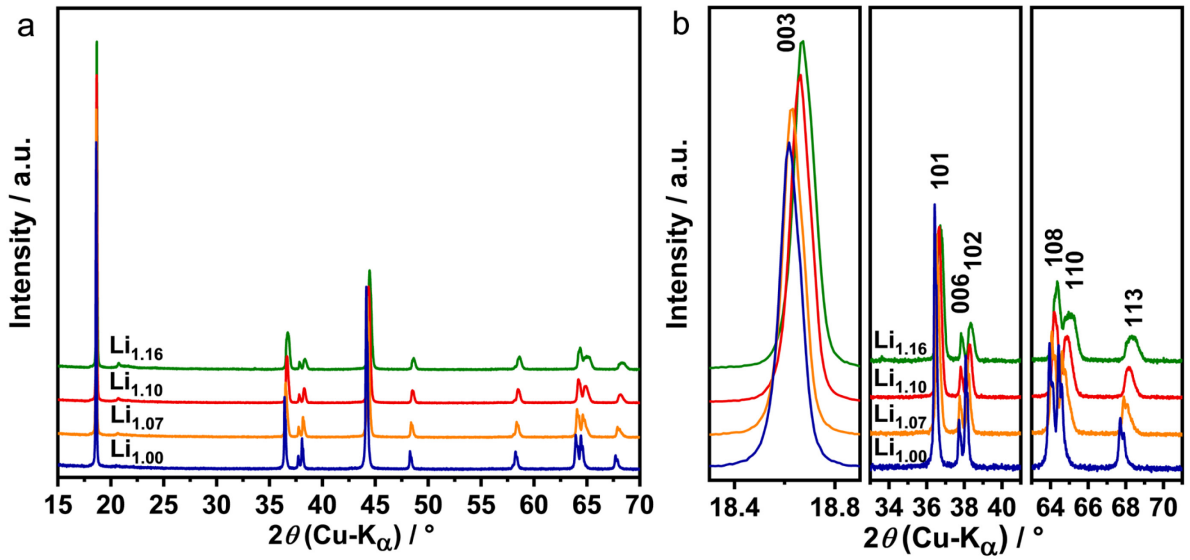

Figure S2. XRD pattern of $Li_{1.00}$ (blue), $Li_{1.07}$ (orange), $Li_{1.10}$ (red) and $Li_{1.16}$ (green): a) overview and b) details of selected reflections.

Table S1. Calculated Rietveld refinement parameters based on the structural model for $LiMn_{0.5}Ni_{0.5}O_2$ of Bréger *et al.*[1]: space group, lattice parameters, Cell Volume *V*, cation occupancies, atom coordinate *z* of the oxide ions, the estimated crystallite size (integral breadth) and the *R* factor.

	$Li_{1.00}$	$Li_{1.07}$	$Li_{1.10}$	$Li_{1.16}$
Space group	$R\bar{3}m$ (166)	$R\bar{3}m$ (166)	$R\bar{3}m$ (166)	$R\bar{3}m$ (166)
***a* / Å**	2.890	2.880	2.874	2.867
***c* / Å**	14.306	14.289	14.272	14.255
V / Å³	103.5	102.6	102.1	101.5
Li_{Li} (3a: 0, 0, 0)	0.91	0.92	0.93	0.94
Ni_{Li} (3a: 0, 0, 0)	0.09	0.08	0.07	0.06
Li_{TM} (3b: 0, 0, 1/2)	0.09	0.08	0.07	0.06
Mn_{TM} (3b: 0, 0, 1/2)	0.50	0.50	0.50	0.50
Ni_{TM} (3b: 0, 0, 1/2)	0.41	0.42	0.43	0.44
***z* [O (6c: 0, 0, z)]**	0.242	0.243	0.243	0.243
Crystallite Size / nm	149	385	284	293
R_{wp} / %	5.8	5.9	4.6	5.3

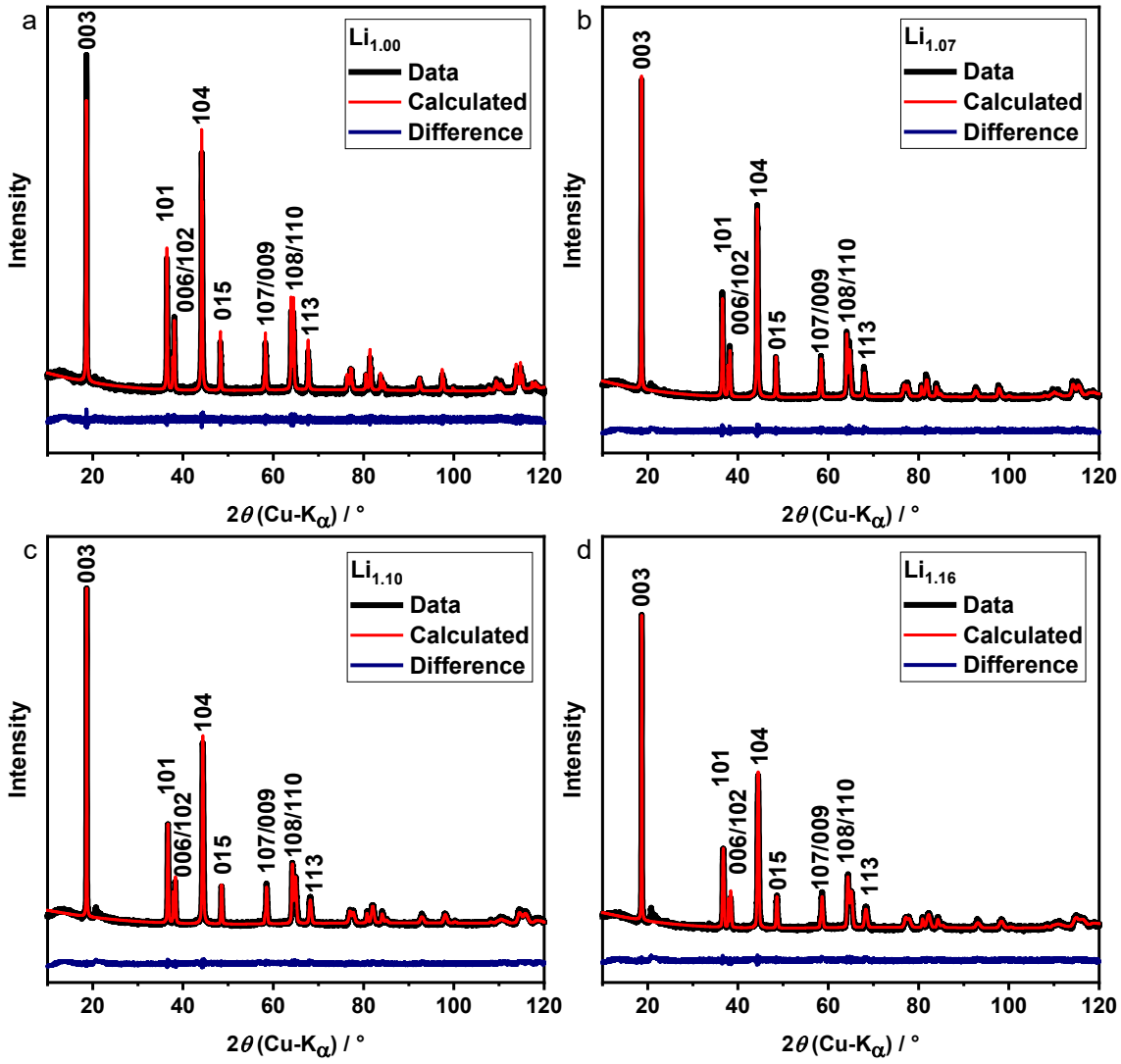

Figure S3. XRD pattern (black) of a) $Li_{1.00}$, b) $Li_{1.07}$, c) $Li_{1.10}$ and d) $Li_{1.16}$ in comparison with the calculated pattern from Rietveld refinement (red) and the difference between both (blue).

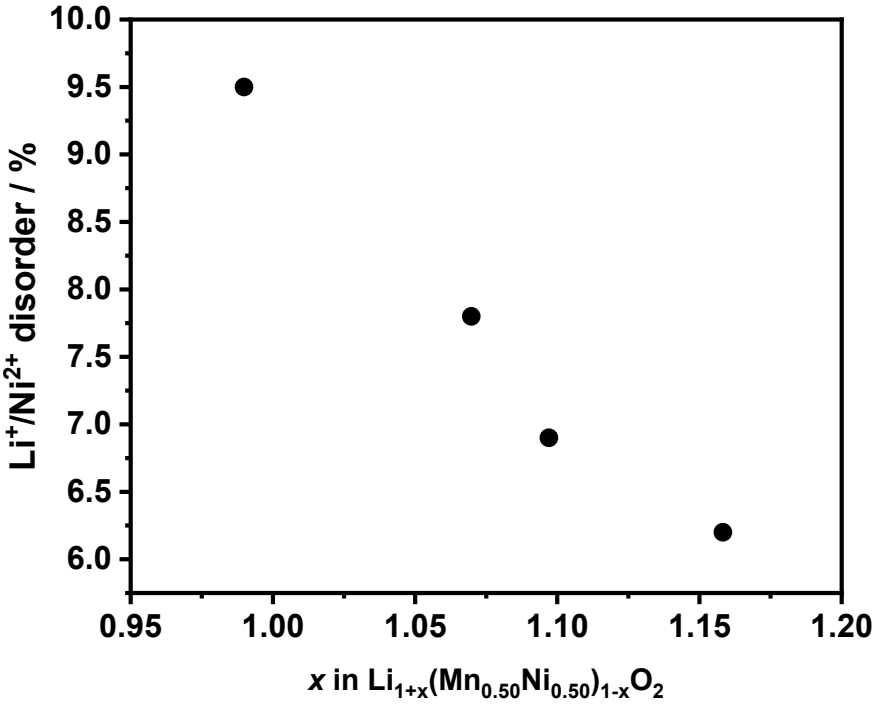

Figure S4. Li/Ni disorder as a function of the amount of excess Li^+ in the structure determined via Rietveld refinement.

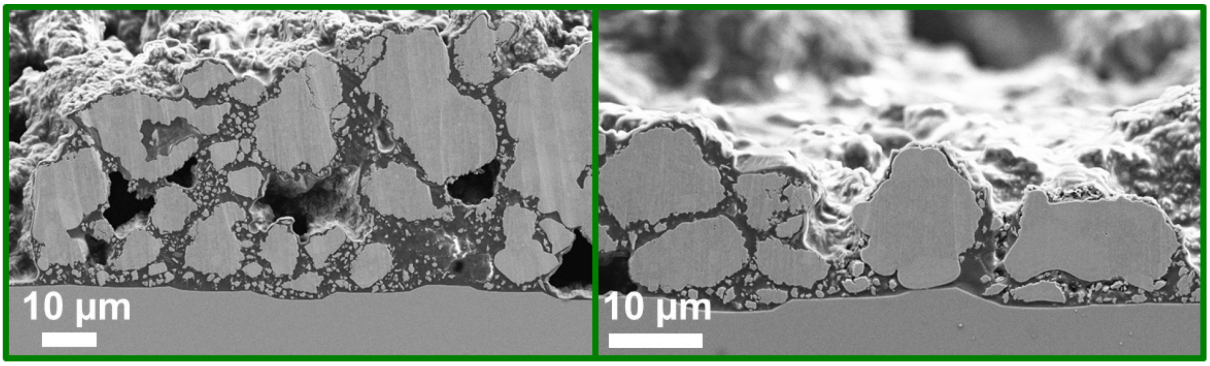

Figure S5. Overview SEM images of $Li_{1.16}$ particle cross section showing an irregular morphology and the local phase separation.

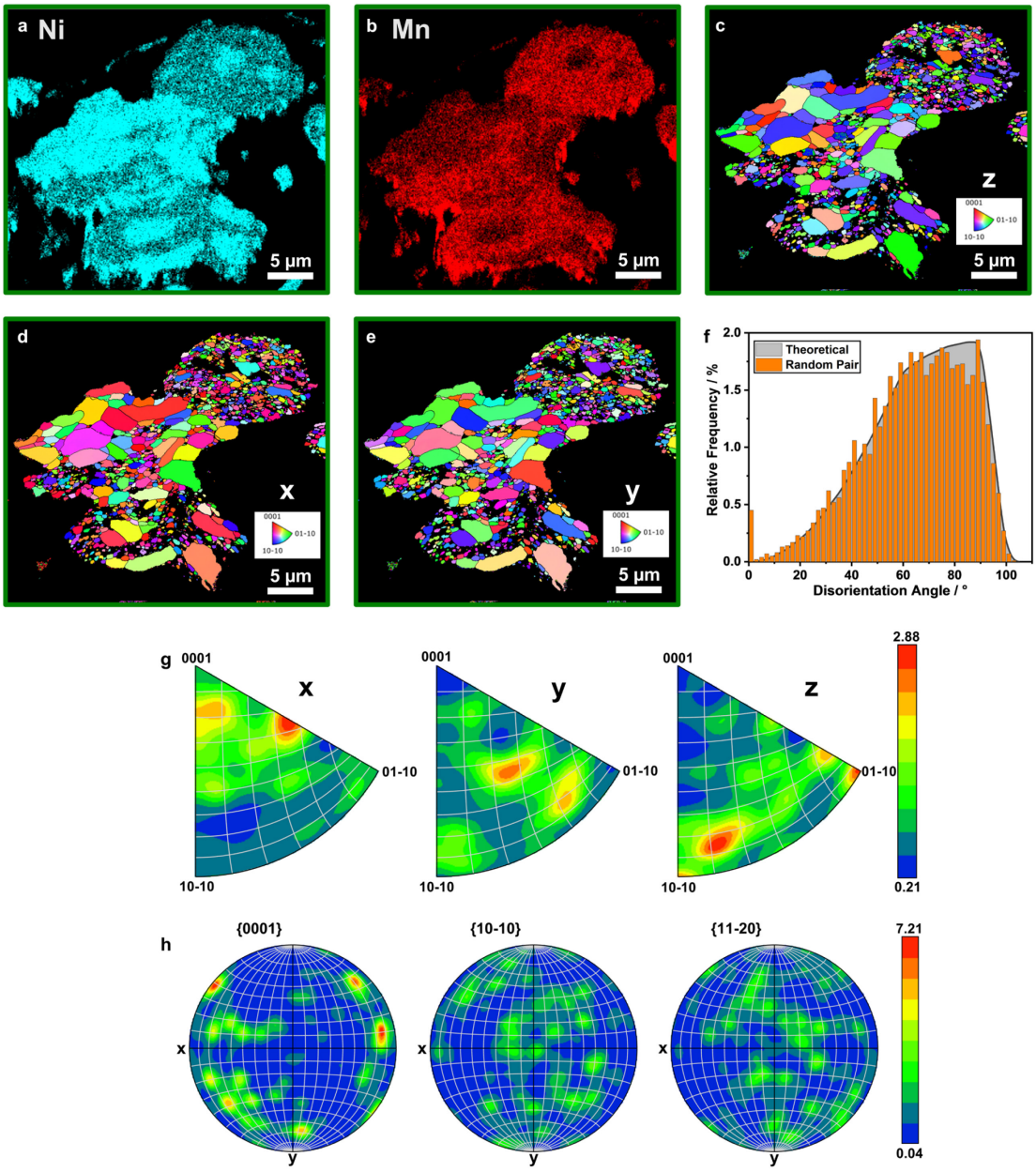

Figure S6. EBSD results of $Li_{1.16}$: EDX mapping of a) Ni and b) Mn, orientation distribution maps with inverse pole figure color key in direction c) Z, d) X and e) Y with respect to the acquisition system. The specimen is located in the X-Y plane and is oriented perpendicularly to the Z-axis. Furthermore, g) the inverse pole figures for the three directions X, Y and Z and h) pol figures for the families {0001}, {10-10} and {11-20} indicating both no significant preferred crystallographic orientation of the crystallites. This is confirmed by f) the correlation of the Mackenzie plot (grey) with the random pair distribution (orange) of 99 % and an M-index of 0.1, where a M-index of 1 represents a single crystal and a value of 0 represents a purely random orientation distribution.[2]

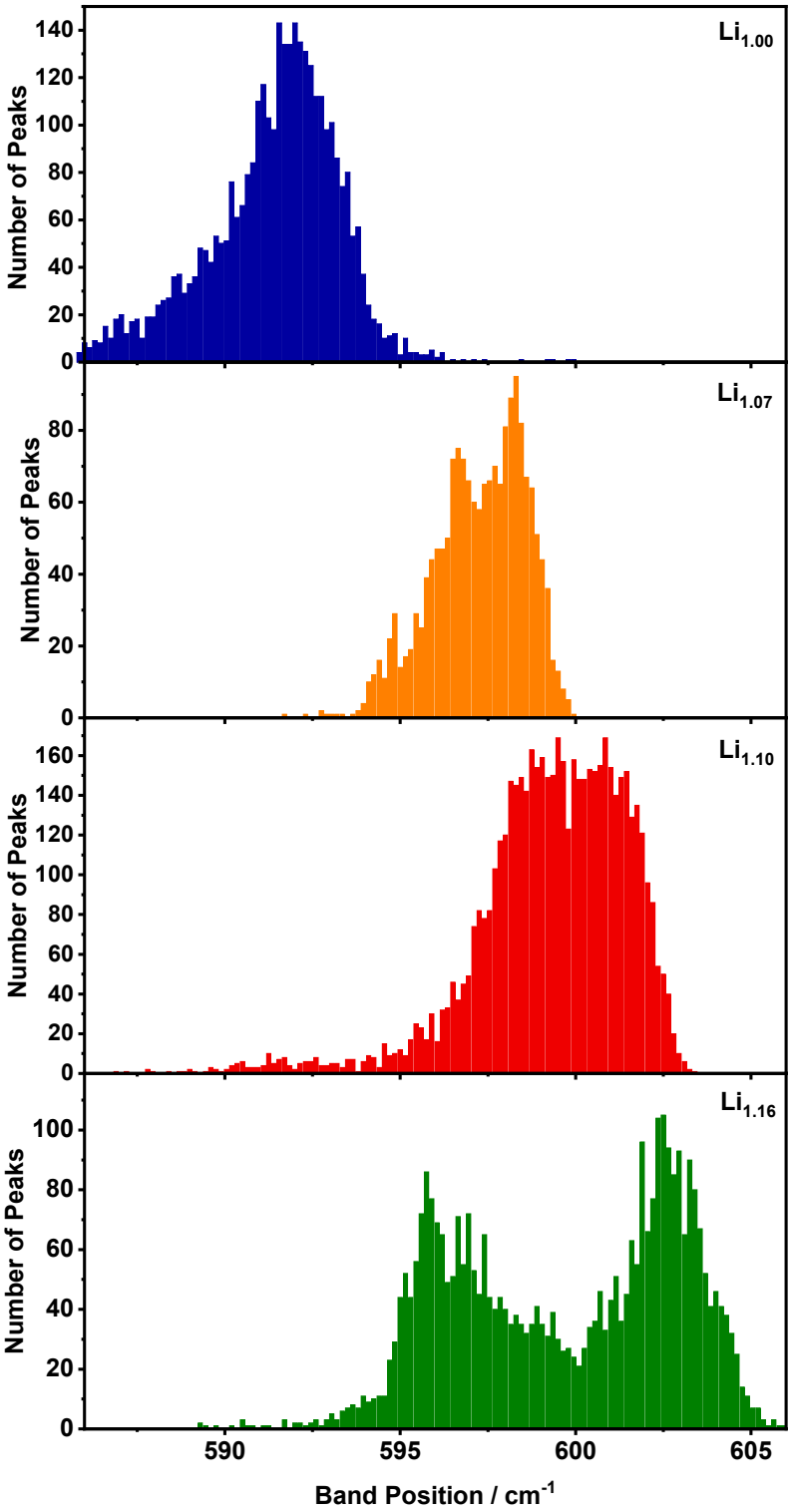

Figure S7. Histograms of the fitted position of the Raman vibration band at approximately 600 cm^{-1} of $Li_{1.00}$ (blue), $Li_{1.07}$ (orange), $Li_{1.10}$ (red) and $Li_{1.07}$ (green).

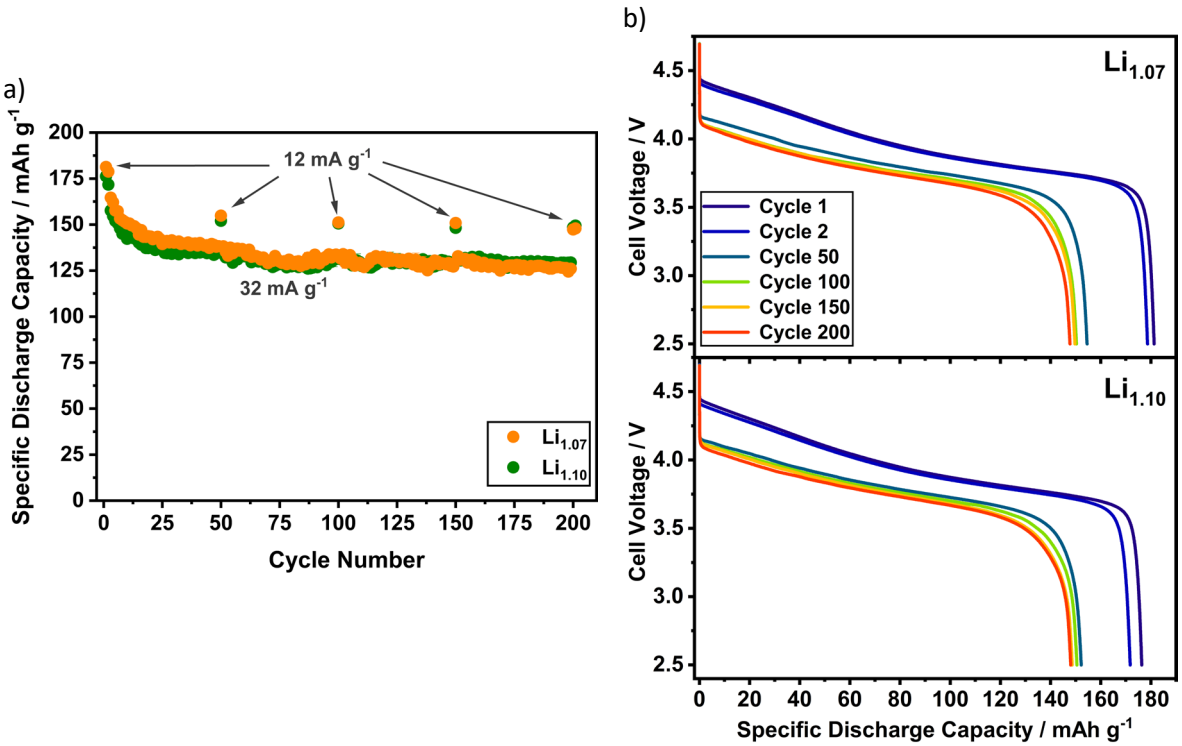

Figure S8. Long-term cycling performance of $Li_{1.07}$ and $Li_{1.10}$ at RT (2.5 - 4.7 V): a) Specific discharge capacities and b) discharge voltage profiles of cycles with lower discharge current (12 mA g^{-1}). The small fluctuation of the data points in a) is related to slight variations of the room temperature.

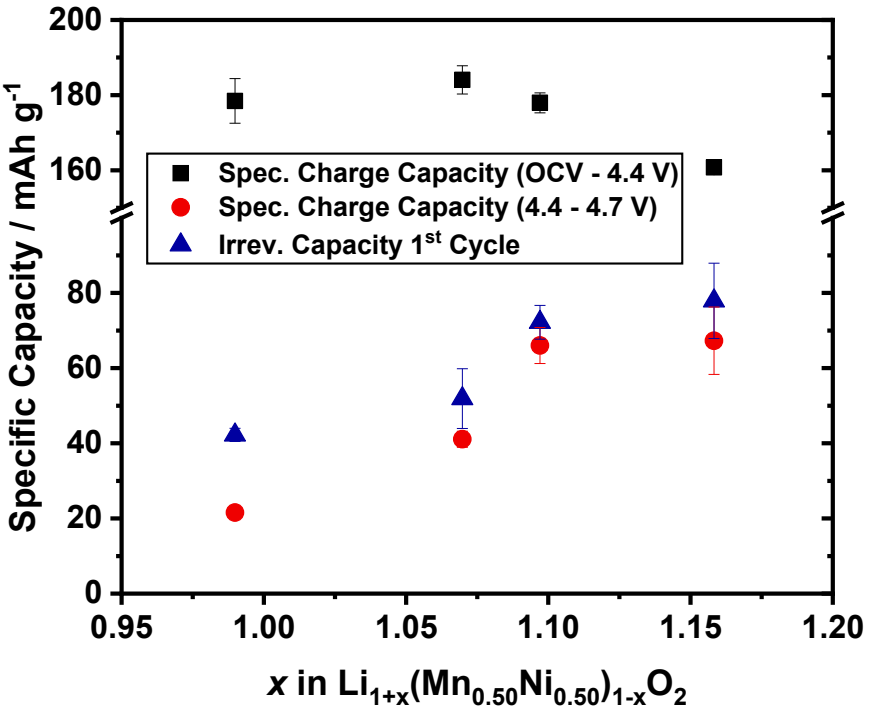

Figure S9. Electrochemical analysis of the 1st cycle specific capacity behavior in different voltage ranges: OCV – 4.4 V (black) and 4.4 – 4.7 V (red) as well as the irreversible initial capacity loss. The given numbers are mean values of three cells.

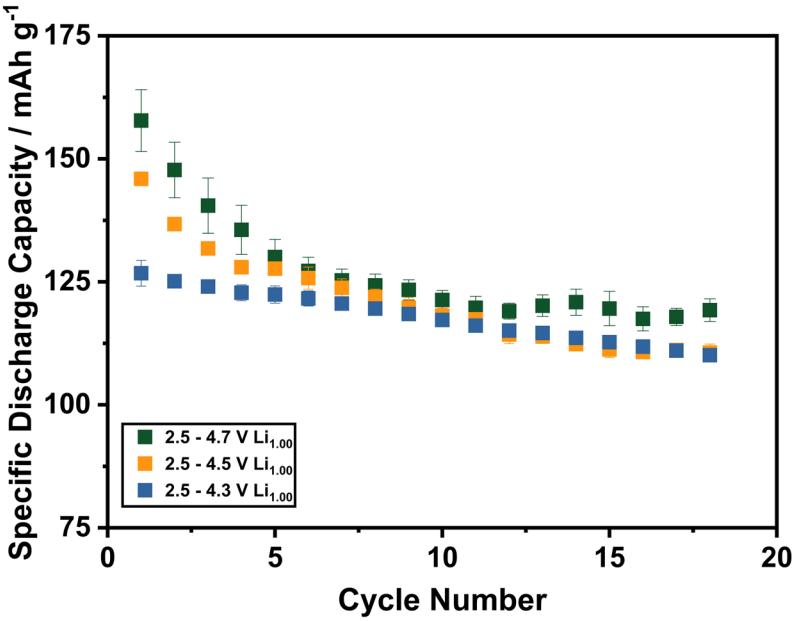

Figure S10. Comparison of the discharge capacity development during cycling (12 mA g^{-1}) of $Li_{1.00}$ using different upper cut-off voltages: 4.3 V (blue), 4.5 V (yellow) and 4.7 V (green).

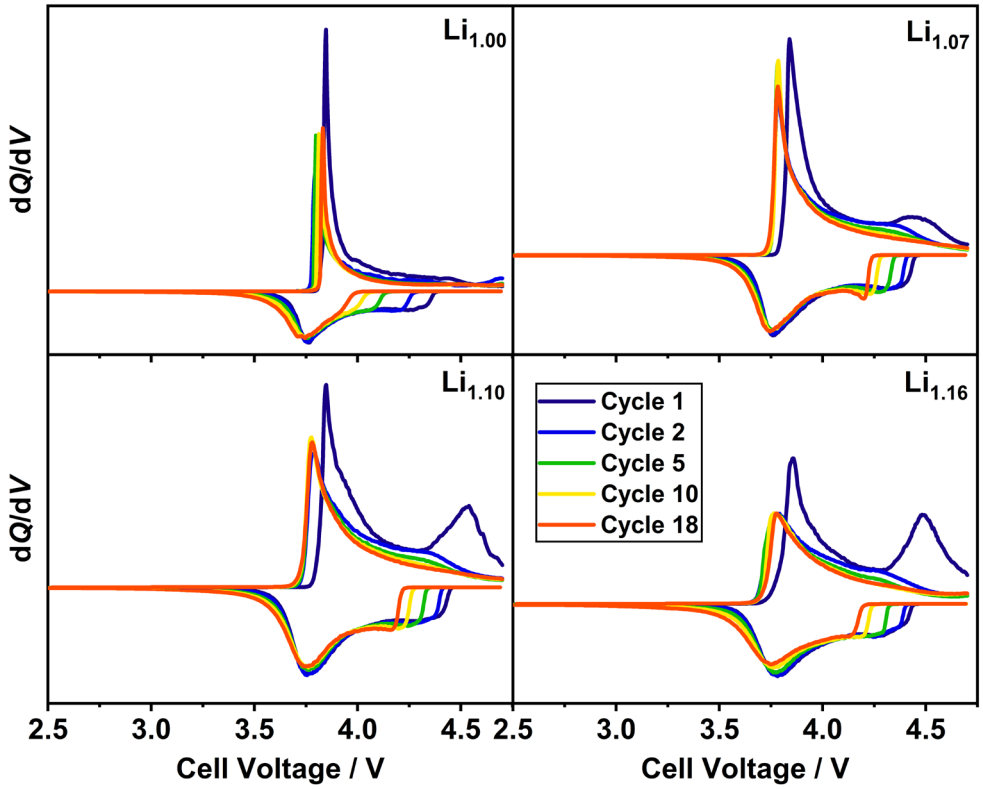

Figure S11. Electrochemical characterization of $Li_{1.00}$, $Li_{1.07}$, $Li_{1.10}$ and $Li_{1.16}$ during the initial cycles (12 mA g^{-1}): supplementary d*Q*/d*V* plots of the cycling data presented in Figure 9.

References

1 J. Bréger, Y. S. Meng, Y. Hinuma, S. Kumar, K. Kang, Y. Shao-Horn, G. Ceder and C. P. Grey, *Chem. Mater.*, 2006, **18**, 4768.

2 P. Skemer, I. Katayama, Z. Jiang and S. Karato, *Tectonophysics*, 2005, **411**, 157.